Observation of Feshbach resonances in an ultracold gas of ^{52}Cr

Von der Fakultät Mathematik und Physik der Universität Stuttgart
zur Erlangung der Würde eines Doktors der
Naturwissenschaften (Dr. rer. nat.) genehmigte Abhandlung

Vorgelegt von

Jörg Werner

aus Kaufbeuren

Hauptberichter:	Prof. Dr. T. Pfau
Mitberichter:	Prof. Dr. U. Schumacher
Tag der mündlichen Prüfung:	14. Juni 2006

Physikalisches Institut der Universität Stuttgart

2006

Bibliografische Information Der Deutschen Bibliothek
Die Deutsche Bibliothek verzeichnet diese Publikation in der Deutschen Nationalbibliografie; detaillierte bibliografische Daten sind im Internet über **http://dnb.ddb.de** abrufbar.

ISBN 3-89963-384-9

D93

Sternstr. 18, 80538 München
Tel.: 089/66060798
www.dr.hut-verlag.de

Die Informationen in diesem Buch wurden mit großer Sorgfalt erarbeitet. Dennoch können Fehler, insbesondere bei der Beschreibung des Gefahrenpotentials von Versuchen, nicht vollständig ausgeschlossen werden. Verlag, Autoren und ggf. Übersetzer übernehmen keine juristische Verantwortung oder irgendeine Haftung für eventuell verbliebene fehlerhafte Angaben und deren Folgen.

1. Auflage 2006

Druck und Bindung: printy, München (www.printy.de)

To Brigitte, Lena-Sophie and Simon Per.

Contents

Zusammenfassung

Die erstmalige Realisierung eines Bose-Einstein-Kondensats in verdünnten atomaren Gasen im Jahr 1995 [6, 25, 47] hat eine faszinierende Forschungsrichtung eröffnet: das Studium makroskopischer Quantenzustände als eine neue Form der Materie. In den neuesten Experimenten spielt die interatomare Wechselwirkung eine entscheidende Rolle für die große Vielfalt der beobachteten Phänomene [19]. Die exakte Kenntnis der Wechselwirkungs-Potenziale zwischen zwei Atomen ist eine der Grundvoraussetzungen für diese Experimente. Eine sehr präzise Methode zur Vermessung der Wechselwirkungs-Potenziale nutzt die Existenz von magnetisch induzierten Streu-Resonanzen sog. Feshbach-Resonanzen aus. Durch ein extern angelegtes Magnetfeld lässt sich in der Nähe dieser Streuresonanzen die Wechselwirkung zwischen zwei Atomen beliebig variieren. Dieser Effekt ist experimentell messbar. Aus den Positionen der Feshbach-Resonanzen lassen sich weitreichende Rückschlüsse über die Wechselwirkungs-Potenziale ziehen.

Thema der vorliegenden Arbeit ist die erstmalige Beobachtung von vierzehn magnetisch-induzierten Feshbach-Resonanzen bei Stößen zwischen optisch gespeicherten ultrakalten ^{52}Cr Atomen. Untersucht wurde dabei der Magnetfeldbereich zwischen 4 und 600 G. Die Variation der Streulänge nahe einer Feshbach-Resonanz wurde anhand der Teilchenverluste aufgrund der resonant überhöhten inelastischen Stoßprozesse beobachtet. Die Kalibration der Magnetfelder erfolgte mittels Mikrowellenspektroskopie und erlaubte eine absolute Genauigkeit von unter 100 mG.

Vor dieser Arbeit war nur wenig über das Wechselwirkungs-Potenzial zwischen zwei ^{52}Cr Atomen bekannt. In Zusammenarbeit mit Dr. Andrea Simoni und Dr. Eite Tiesinga vom National Institute of Standards and Technology (NIST), Gaithersburg, USA gelang es uns, dreizehn der vierzehn experimentell beobachteten Resonanzen zu identifizieren und die entsprechenden Quantenzahlen zuzuordnen. Die elf stärksten Feshbach-Resonanzen bilden einen kompletten Satz von Resonanzen. Diese entstehen aufgrund der Kopplung des s-Wellen Eingangskanals an die gebundenen Molekülzustände. Für die Kopplung ist die starke Dipol-Dipol-Wechselwirkung bei ^{52}Cr verantwortlich, welche bis zur zweiten Ordnung berücksichtigt werden muss, um die elf stärksten Resonanzen zu erklären. Weitere zwei Resonanzen konnten der Ankopplung des *d*-Wellen-Eingangskanals an die gebundenen Zustände zugeordnet werden. Mit Hilfe der experimentellen Resonanz-Positionen und der Kenntnis

der zugehörigen Quantenzahlen gelang es erstmalig, einen Parametersatz für die Born-Oppenheimer Potenziale $^{13,9,5}\Sigma_g^+$ mit hoher Genauigkeit anzugeben. Die Abweichungen zwischen den mit diesem Parametersatz theoretisch vorhergesagten und experimentell beobachteten Positionen liegen im Mittel bei 10 G. Bei Berücksichtigung der Dipol-Dipol-Wechselwirkung in der Theorie beträgt die mittlere Abweichung unter 0,6 G. Dies zeigt, dass die Dipol-Dipol-Wechselwirkung für Stöße zwischen ultrakalten Chromatomen eine entscheidende Rolle spielt.

Die genaue Kenntnis der Molekülpotenziale eröffnet viele neue Perspektiven. Auf Basis der Molekülpotenziale lassen sich präzise Aussagen über die Kollisionseigenschaften in anderen Eingangskanälen und weiterer Chrom-Isotope treffen. Möglicherweise führen diese neuen Ergebnisse auch zu einem besseren Verständnis der Bindungsmechanismen des Cr_2-Moleküls, welche noch nicht im Detail verstanden sind.

Für weitere Experimente mit ultrakalten Chromatomen ist vor allem die Variation der Wechselwirkungsstärke nahe bei einer Feshbach-Resonanz von Interesse. Dies erlaubt es, das Verhältnis zwischen der anisotropen Dipol-Dipol-Wechselwirkung und der isotropen Kontaktwechselwirkung beliebig einzustellen. Auch können die gefundenen Feshbach-Resonanzen ausgenutzt werden, um ultrakalte Moleküle zu erzeugen.

Abstract

The first realization of Bose-Einstein condensation (BEC) in dilute atomic gases in the year 1995 [6, 25, 47] has pioneered the exploration of an exciting new form of matter: the macroscopic quantum state. In many of the more recent experiments the interatomic interaction is responsible for the astonishing variety of observed phenomena [19]. The exact knowledge of the interaction potentials between two atoms is one of the prerequisites for these kind of experiments. A very precise method for determining the interaction potentials exploits the existence of magnetically induced Feshbach resonances. For certain values of the applied external magnetic field the interaction can be arbitrarily tuned. From the positions of these Feshbach resonances one can deduce many details of the acting interaction potentials.

The topic of this thesis is the first observation of fourteen magnetically induced Feshbach resonances in collisions between optically trapped ultracold ^{52}Cr atoms. The search for Feshbach resonances was performed for magnetic fields between 4 and 600 G. A calibration of the magnetic field was done for each observed resonance slightly above and below the resonance using rf-spectroscopy. This allowed us to determine the positions of the resonances with an accuracy of below 100 mG.

Up to now, not much was known about the interaction potentials between two ^{52}Cr atoms. Due to a close collaboration with Andrea Simoni and Eite Tiesinga of the National Institute of Standards and Technology, Gaithersburg, USA we succeeded in identifying thirteen of the fourteen experimentally observed resonances and to assign the relevant quantum numbers. The eleven strongest Feshbach resonances build a complete set of all possible resonances up to second-order in the magnetic dipole-dipole coupling for the deca-triplett s-wave entrance channel. The two remaining identified resonances are resonances with a d-wave entrance channel and are thus much weaker. From the experimental resonance positions and knowing the corresponding quantum numbers allowed us to calculate a set of parameters describing the Born-Oppenheimer potentials $^{13,9,5}\Sigma_g^+$ with unprecedent precision. The average difference between theoretical and experimental resonance positions is only ≈ 0.6 G. Neglecting the spin-spin dipole interaction in our calculations leads to an average deviation of about 10 G. This is a clear sign, that the dipole-dipole interaction plays an important role in collisions between ultracold chromium atoms.

The precise knowledge of the molecular potentials opens up new vistas. Based on the measured molecular potentials we can predict the collisional properties in other entrance channels and even for other chromium isotopes. Maybe these new results will lead to a better understanding of the bonding mechanisms of the chromium dimer, which is not yet fully understood in detail.

Concerning further experiments with ultracold chromium atoms, the possibility to vary the interaction strength by using a Feshbach resonance is of interest. This will allow to change the strength of the isotropic contact interaction in relation to the anisotropic dipole-dipole interaction. The observed Feshbach resonances can even be used to create ultracold molecules.

Chapter 1

Introduction

For thousands of years people have asked, "What is the world made of?" and "What holds it together?" The idea that matter should be made out of fundamental *building blocks* is more then 2000 years old. The blocks were assumed to be simple and structureless and not made of anything smaller:

> "...the nature of the perpetual things consist of small particles infinite in number...the particles are so small as to be imperceptible to us, and take all kinds of shapes and all kinds of forms and differences of size. Out of them, like out of elements (earth, air, fire, water) he now lets combine and originate the visible and perceptible bodies..."
>
> 450 B.C. Democritus [11]

Today we know that according to *The Standard Model* [44], the world is made out of six quarks[1] and six leptons[2] and is held together by four fundamental forces[3]. Much of our understanding of the fundamental nature of particles and their underlying microscopic interactions has been derived from scattering experiments. In the year 1909 Ernest Rutherford scattered alpha particles off a thin gold foil [94]. From the observed distribution of backscattered particles, he inferred the presence of a charged massive core concentrated within a tiny spatial region. He thus discovered the nucleus and proposed a celestial model for the atom, with electrons orbiting a massive nucleus. In the quest of a deeper understanding of matter and the basic interactions, more and more complex scattering experiments were performed. During the last century the collision energy between two colliding particles was further and further increased to successfully verify the predictions made by the standard model.

But not only very high collision energies are of interest. Extremely low collision energies imply that the two particles interact with one another for a long time during

[1] top,bottom,strange,charm,up and down quark
[2] electron, muon, tau and the corresponding neutrinos
[3] electromagnetism, gravity, strong and weak interaction.

a collision event. This makes the study of ultracold collisions an ideal method for understanding the weak long-range forces that atoms exert on one another. The preparation of an ultracold atomic sample was driven by the quest to create a Bose-Einstein condensate [20, 62] for which temperatures below 1 μK are typically required. In the year 1995 three different groups [6, 25, 47] successfully created a Bose-Einstein condensate. This was the first advancement into the degenerate regime of a weakly interacting quantum gas. By now, there are many groups worldwide who have realized a Bose-Einstein condensate, most of them working with alkalis due to their simple level structure [19], but also more complex elements like metastable helium [194, 204] or ytterbium were condensed [234]. Due to the specific collisional properties of each element, appropriate trap types and cooling procedures are required for the realization of a Bose-Einstein condensate. In experiments with rubidium and sodium atoms a BEC can be achieved by laser cooling [39, 42, 178] and subsequent rf-evaporation in magnetic traps [137], while Hydrogen has been cooled with cryogenic methods and evaporative cooling below the critical condensation temperature.

The effectiveness of the evaporative cooling step, critically depends on the collision rate of the atoms and thus the interaction potential of two atoms. The same holds true for the properties of a Bose-Einstein condensate. Even though the creation of a Bose-Einstein condensate is theoretically possible for non-interacting atoms, many interesting effects occur due to the existence of an interaction between the atoms. Already 1995 it was observed that for ^{7}Li the condensate is stable only below a critical number of atoms due to the attractive interaction between the atoms [24]. But also for repulsive interactions many interesting phenomena can be observed. The experiments performed range — without claiming completeness — from the study of elementary excitations like acoustic waves and phonons [149, 219, 220], the creation of solitons [27, 54] and the realization of condensate spin mixtures [159, 208, 226], over the creation of atom lasers [4, 16, 93, 150], the setup of atom interferometers [96] with condensates and the demonstration of matter wave amplification [109, 126] to the examination of superfluidity in condensates [34, 140, 185] and in particular the observation of quantized vortices [1, 110, 139, 145] and solitons [5, 27, 54]. BEC in optical lattices have been investigated [4, 28, 125, 174] and quantum phase transitions have been demonstrated [81]. From many of these experimental results a rough estimate of the interaction potentials can be extracted.

The most accurate method to determine the interaction potentials though, is to perform Feshbach resonance spectroscopy. Feshbach resonances have been observed for the first time in nuclear physics [70] and have recently become an important tool in atomic physics, allowing to tune the magnitude and sign of the interaction by controlling an external parameter e. g. the magnetic field. Feshbach resonances have been observed in different atomic gases [36, 37, 45, 108, 143, 195, 197, 198, 199, 244]. The fruitful interplay between theoretical calculations [107, 131, 155, 241] and experimental work has lead to an excellent understanding of the relevant interaction potentials.

Moreover, interspecies Feshbach resonances [217, 222], Feshbach resonances between atoms in different states [63] were observed.

After the successful creation of a Bose-Einstein condensate the next big challenge was the creation of ultracold molecules of even a molecular BEC. Due to the additional vibrational and rotational energy levels of molecules, no practical approach has been found to laser-cool molecules. Therefore, alternative methods were explored to create ultracold molecules. One possibility which has been demonstrated with CaH [247], is sympathetic cooling of molecules with a buffer gas of cryogenically cooled helium. In other approaches, polar molecules could be slowed in oscillating electric fields by using the DC Stark-effect [14, 117]. In a similar experiment, ammonia-molecules were successfully loaded into an electrostatic trap. The achieved temperatures were also of the order of a few 10 mK [15]. A completely different approach is to form cold molecules from laser-cooled atomic ensembles. Using laser-induced photoassociation, homonuclear molecules in their electronic ground state with translational temperatures below 1 mK could be produced [75, 164, 165, 258]. In particular, the experiments in the groups of D. Heinzen [258] with ^{87}Rb and R. Hulet [75] with ^{7}Li show that the creation of molecules works very well if the atomic ensemble is already quantum degenerate. The success of this technique stems from the small Doppler-broadening (a few kHz) of the transition from the molecular to the atomic state at extremely low temperatures. Both approaches though, never achieved to cool molecules into the quantum degenerate regime.

This changed in the past two years, when researchers succeed to adiabatically transfer ultracold colliding atoms from an open channel into a molecular bound state of a closed channel by ramping the magnetic offset field slowly over the position of a Feshbach resonance towards lower fields. This synthesis of ultracold molecules gases generated of bosonic [58, 61, 104, 199, 245, 259] and fermionic [56, 115, 188] degenerate quantum gases was reported and dissociation of these molecules was studied. While the lifetime of molecules formed by bosonic atoms is due to a high three-body loss-coefficient of approximately $L_3 \approx 10^{-25}\,\mathrm{cm}^6/\mathrm{s}$ extremely short [68, 197, 225, 246], the lifetime of molecules created by fermionic atoms is sufficiently long to allow evaporative cooling of the molecules and to generate molecular BECs [82, 116, 266]. Moreover, the BEC-BCS crossover regime has been investigated in the latter system. This leads to the observation of strongly correlated fermionic gases [190] and the observation of a pairing gap in a strongly interacting Fermi gas [38].

The interaction in BECs realized up to now is dominated by the isotropic and short-range contact interaction. In contrast to the contact interaction, the dipole-dipole interaction is long-range and anisotropic. If the dipole moment is high enough, the resulting dipole-dipole force can influence or even completely change the properties of a Bose-Einstein condensate. Properties of these dipolar gases have been theoretically investigated [9]. Due to the character of the interaction, the stability of the condensate is expected to depend on the trapping geometry [89, 205]. Changes in the excitation

spectrum are predicted [87, 260] and under certain conditions a dispersion law which acquires a roton-maxon spectrum [170, 206] can be obtained. Dipolar gases in optical lattices may lead to new phase transitions [90]. Moreover, there are theoretical proposals for realizing a fast and robust quantum computer with permanent dipole moments [52]. In degenerated dipolar Fermi gases an anisotropy in the gap parameter in the Cooper Pair formation is predicted [10].

Promising candidates [9] for observing the influence of the dipole-dipole interaction on the dynamics of a BEC are atomic gases with high magnetic moments, e. g. chromium (μ=6μ_B) and europium (μ=7μ_B). Other possibilities are molecules which display either a high electric moment in electric fields [14] or electric dipole moments by exciting them to Rydberg states [205]. Another alternative is to laser-induce dipole-dipole interactions [169].

Similar to the Feshbach resonances, there is a possibility to change the magnitude and sign of the dipole-dipole interaction by applying time varying magnetic fields [77] as it is done in NMR. This makes it possible to map the dependence of the effects described above on the strength of the dipolar interaction. In contrast to a Feshbach resonance, tuning the dipolar interaction is a non-resonant effect, so there are no excessive losses to be expected.

The phase transition to a Bose-Einstein condensate leads to a non-zero value of the scalar order parameter, i. e. the condensate wave function. For atoms with multiple (e. g. magnetic) sub-states, a quantum fluid consisting of multiple — distinguishable — components can be created. In a magnetic trap only the low-field-seeking components can be trapped, which limits the number of suitable states. Moreover, there are high losses due to exothermic collisions which change the sub-state. Due to a fortunate near-equality of the singlet and triplet scattering lengths for ^{87}Rb the exothermic collisions are suppressed. This allowed experiments with multi-component condensates of ^{87}Rb in a magnetic trap e. g. probing the spatial separation [95, 159] and the stability of the relative phase in presence of dissipation [96] between the two components. Also investigated were the nature of multi-component condensates in the presence of continuous resonant and non-resonant rf-coupling between the components [144, 145, 252, 253, 254]. In an optical dipole-trap atoms in all sub-states can be trapped. Thus, spinor condensates consisting of a mixture of internal sub-states can be created. In spinor condensates the order parameter is no longer a scalar, but rather a vector which can rotate in the space spanned by the sub-states. In various experiments the ground state of such a spinor condensate in external magnetic fields [226], the dynamics [208], the formation and persistence of meta-stable spin-domains [154] and the transport over spin-domain borders by quantum-tunneling [221] have been investigated. There are theoretical calculations on ferromagnetism in a lattice of Bose-Einstein condensates, in which the dipole-dipole interaction leads to a spontaneous magnetization [184] or the excitation of spin-waves [265].

In this thesis, I report the observation of fourteen magnetically induced Feshbach resonances in ultracold ^{52}Cr. The resonance positions were determined by monitoring the increased three body loss-rate close to a Feshbach resonance. Through a close collaboration with theory, we were able to infer from the experimental results the interaction potentials of the $^{13,9,5}\Sigma_g^+$ states. Our results form the most precise determination of the ^{52}Cr interaction potentials up-to-date. The precise knowledge of the potentials may lead to a better understanding of the bonding mechanisms of the chromium dimer, which is not yet fully understood theoretically [200]. In addition, the existence of Feshbach resonances will allow to change the value of the contact interaction. The adjustability of both, the dipole-dipole interaction and the contact interaction, along with seven Zeeman-substates makes chromium an ideal candidate for exploring the properties of dipolar condensates and spinor-physics. Finally, due to the absence of the hyperfine-structure, ^{52}Cr forms an ideal candidate for the theoretical investigation of Feshbach resonances; it is an ideal "text-book" example for discussing Feshbach resonances.

This thesis is organized as follows:

Chapter 2 and 3 are dedicated to introducing the theoretical framework used to describe Feshbach resonances. The idea behind these two chapters is to form a compilation of all the theoretical aspects about Feshbach resonances in a very concise manner. Chapter 2 is a short repetition of the well known basic scattering theory. The presentation follows not the commonly encountered approach found in textbooks though, but uses "formal" scattering theory. This approach is much more powerful and will allow us to introduce the Feshbach resonance theory in Chapter 3 much more elegantly. Before turning our attention to this task, I apply the "formal" scattering theory to solve the scattering problem at a square-well potential. After a phenomenological introduction of Feshbach resonances at the beginning of Chapter 3, I then derive the behavior of the scattering length close to a Feshbach resonance. This is done using the approach of Feshbach [70], which uses the "formal" scattering theory from the previous chapter. Following this abstract derivation, I now extend our previous example to include two square-well potentials. When a coupling is introduced between these two potentials I can reproduce all properties of Feshbach resonances already with this quite simple example. Since an analytic solution of the Schrödinger equation is not possible any more for real world potentials, Feshbach resonance calculations need to resort to numerical methods. I present two popular methods for solving the Schrödinger equation. The chapter closes with an overview of the different possibilities to experimentally observe the diverging scattering length at a Feshbach resonance. Chapter 4 gives a summary of the physical and spectroscopic properties of chromium for this work. There I also review some results of our earlier measurements of the elastic and inelastic cross-sections of ^{52}Cr and ^{50}Cr. Of particular interest for this work are the results of the cross-dimensional relaxation measurements. From this measurement I could determine the elastic cross-section

of the $^{13}\Sigma_g^+$ state of ^{52}Cr, which serves as a comparison to our obtained value. The setup of our experiment is described in Chapter 5. Since the experiment has grown quite complex over time, only the new parts which were realized during this thesis are discussed in detail. These are the setup of the optical dipole trap, optical pumping laser-system and the computer control system. The experimental observation of the Feshbach resonances is treated in Chapter 6. First I review all steps involved in preparing the necessary ultracold atomic sample of ^{52}Cr. This is followed by the presentation of the experimental results of the Feshbach measurements. The Feshbach resonances were detected by looking for the inelastic loss features which accompany the diverging scattering length. To obtain the interaction potentials from the measured positions we need to construct the model potentials which reproduce the experimental results. The precise knowledge of these potentials allows to infer the outcome of several follow-up experiments which are investigated at the end of this chapter. The thesis concludes with a summary and future perspectives in Chapter 7.

Chapter 2

Basic collision theory

In this first chapter, I introduce the basic physical concepts of collision theory with an emphasis on cold and ultracold collisions. I do not intend to give a full derivation of the theoretical formalism but rather stress the — sometimes less precise — underlying physical pictures and interpretations. For the full derivations see for example [202]. After introducing the theoretical formalism used to describe the scattering process, I'll explain the scattering of a square-well potential. Using this example, I'll also highlight some special features of low energy scattering. The material in this chapter will establish the basis for the discussion of the Feshbach resonance-theory in the next chapter.

2.1 The scattering problem

Here we will consider the non-relativistic collision process between two distinguishable, moving particles interacting via a finite-range scalar potential $V(\mathbf{r_1} - \mathbf{r_2})$. We shall not take into account the possible internal structure of the particles, thereby ignoring inelastic scattering phenomena. Also, we shall assume that the target is thin enough to enable us to neglect multiple scattering processes. Because the interaction potential $V(\mathbf{r_1} - \mathbf{r_2})$ depends only on the relative positions $\mathbf{r_1} - \mathbf{r_2}$ of the particles, one can most conveniently solve this problem in the center-of-mass reference frame. Thus the problem reduces to the study of the scattering problem of a single particle by the potential $V(\mathbf{r})$. The reduced mass m_μ of this particle is then given by $m_\mu = \frac{m_1 m_2}{m_1 + m_2}$. In quantum mechanics, particles are usually described as wave packets. The incident particle is described by a wave packet $\phi(\mathbf{r})$ which is a superposition of plane waves $e^{i\mathbf{kr}}$:

$$\phi(\mathbf{r}) = \int d\mathbf{k} e^{i\mathbf{kr}} A_{\mathbf{k_0}}(\mathbf{k}) \,, \tag{2.1}$$

where $A_{\mathbf{k_0}}(\mathbf{k})$ is sharply peaked about the particle momentum $\mathbf{k_0}$. $E(k)$ is the energy of a free particle with momentum $k = |\mathbf{k}|$; in the case of a non-relativistic particle

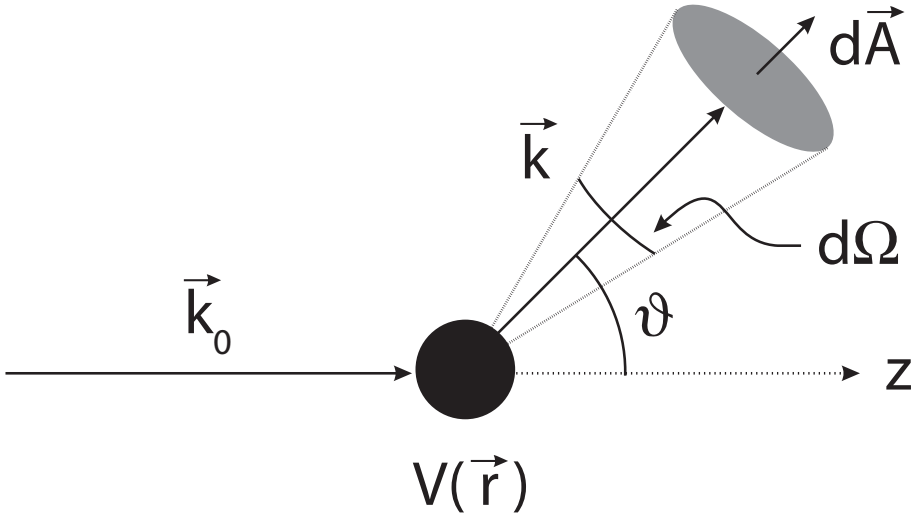

Figure 2.1: Basic scattering problem: an incident plane wave with wave vector $\mathbf{k_0}$ is scattered by a potential $V(\mathbf{r})$. The scattered wave is detected in the shaded area along a direction $\mathbf{k}$ under the solid angle $d\Omega$.

$E(k) = \frac{\hbar^2 k^2}{2m_\mu}$. It is therefore sufficient to solve the scattering problem for a plane wave $e^{i\mathbf{kr}}$. This simplified scattering problem is sketched in Figure 2.1. An incident plane wave with wave vector $\mathbf{k_0}$ is scattered by a potential $V(\mathbf{r})$. The scattering of the plane wave is described by the time independent Schrödinger equation

$$\left[\frac{\hbar^2 \hat{\mathbf{k}}^2}{2m_\mu} + V(\mathbf{r})\right] \phi(\mathbf{r}) = E\phi(\mathbf{r})\,. \tag{2.2}$$

The solution of this equation in the far field consists out of two components: the incident plane wave and a spherical wave with wave vector k modulated by the angle-dependent scattering amplitude $f(\vartheta, \phi)$:

$$\phi(\mathbf{r}) \xrightarrow[\mathbf{r}\to\infty]{} e^{i\mathbf{kr}} + f(\vartheta,\phi)\frac{e^{ikr}}{r}\,. \tag{2.3}$$

For elastic scattering, energy conservation requires $k = |\mathbf{k_0}|$. The main goal of scattering theory is to derive an expression for the scattering cross-section σ_{tot} which tells us how many scattering events per unit time and incident particle flux take place. The detector in the setup which is depicted in Fig. 2.1 can only observe a fraction of the total scattered wave. This leads to the definition of the differential scattering cross-section

$$d\sigma(E,\vartheta,\phi) = |f(E,\vartheta,\phi)|^2 d\Omega\,, \tag{2.4}$$

which is a measure for scattering probability of a single particle into the solid angle $d\Omega$ normalized to the incident particle current density. Integration of Eq. (2.4) yields the total scattering cross-section

$$\sigma_{\text{tot}}(E) = \int |f(E, \vartheta, \phi)|^2 d\Omega \,. \tag{2.5}$$

All the information about the collision process can therefore be obtained from the scattering amplitude.

Finally one can derive the optical theorem:

$$\sigma_{\text{tot}}(E) = \frac{4\pi}{k} \text{Im} f(E, \vartheta = 0) \,. \tag{2.6}$$

It arises because of the destructive interference between the incident and the scattered waves behind the scattering region ($\vartheta \approx 0$). In other words, the "shadow" cast by the target in the forward direction reduces the intensity of the incident beam, so that the scattered particles are removed from it in an amount proportional to σ_{tot} [202]. Most books now continue by introducing the partial wave expansion. The partial wave expansion approach simplifies calculations and allows to gain a faster insight into the physical properties of the scattering process (see for example [40]). We will in the following solve the scattering problem in a more formal way, using the framework of the Lippmann-Schwinger equation which is much more powerful. It also enables us to describe the theory of collisions involving Feshbach resonances in the next chapter more elegantly.

2.2 Lippmann–Schwinger equation

We assume that the scattering Hamiltonian can be decomposed in the following way:

$$\hat{H} = \hat{H}_0 + \hat{V} \,, \tag{2.7}$$

where $\hat{H}_0$ is the kinetic-energy operator and $\hat{V}$ the scattering potential operator. In the absence of a scatterer, $\hat{V}$ would be zero and an energy eigenstate would be just a free particle state $\mathbf{k}$. However, if the scattering process is to be elastic we are interested in obtaining a solution to the full Schrödinger equation with the same eigenvalue. More specifically, let $|\,\phi\,\rangle$ be the energy eigenket of $\hat{H}_0$:

$$\hat{H}_0 |\,\phi\,\rangle = E |\,\phi\,\rangle \,. \tag{2.8}$$

So the basic Schrödinger equation we need to solve is

$$\hat{H} |\,\psi\,\rangle = (\hat{H}_0 + \hat{V}) |\,\psi\,\rangle = E |\,\psi\,\rangle \,, \tag{2.9}$$

or slightly rewritten

$$(E - \hat{H}_0)|\,\psi\,\rangle = \hat{V}|\,\psi\,\rangle\,. \tag{2.10}$$

This linear inhomogeneous differential equation can be solved using Green's functions [71] or in this case operators. A formal solution is given by:

$$|\,\psi^{(\pm)}\,\rangle = |\,\phi\,\rangle + \hat{G}_0^{(\pm)}\hat{V}|\,\psi^{(\pm)}\,\rangle\,. \tag{2.11}$$

This is the so called Lippmann-Schwinger equation, where

$$\hat{G}_0^{(\pm)} = \frac{1}{E - \hat{H}_0 \pm i\epsilon}\,. \tag{2.12}$$

The Lippmann-Schwinger equation can be formally derived by multiplying Eq. (2.10) with $(E - \hat{H}_0)^{-1}$, which results in

$$|\,\psi\,\rangle = (E - \hat{H}_0)^{-1}V|\,\psi\,\rangle\,. \tag{2.13}$$

To make this solution meaningful, we must define the inverse operator if E happens to be an eigenvalue of $\hat{H}_0$. We avoid the singularity by adding/subtracting an infinitesimally small imaginary part $i\epsilon$ to the energy[1] E. For completeness and to match the complete scattering experiment boundary conditions, the full solution must also include $|\,\phi\,\rangle$, the solution to the homogeneous equation[2]. The physical meaning of the $\pm$ in the Lippmann-Schwinger equation is to be discussed in a moment when we look at the space representation of the solution, i.e. $\langle\,\mathbf{r}\,|\,\psi^{(\pm)}\,\rangle$.

First note that the Lippmann-Schwinger equation is an integral equation which replaces the Schrödinger Eq. (2.10) plus the boundary condition Eq. (2.3) which is incorporated through the choice of Green's operator Eq. (2.12). To verify the correct asymptotic behavior, one can calculate the space representation of the Lippmann-Schwinger equation in the limit[3] $\mathbf{r} \to \infty$. Green's Operator in space representation is given by:

$$G^{(\pm)}(\mathbf{x}, \mathbf{x}') = -\frac{1}{4\pi}\frac{e^{\pm i\mathbf{k}|\mathbf{r}-\mathbf{r}'|}}{|\mathbf{r} - \mathbf{r}'|}\,, \tag{2.14}$$

which is nothing else than Green's function for the Helmholtz equation [71, 112]. This now enables us to calculate the asymptotic solution of the Lippmann-Schwinger

[1] Some authors add a $\lim_{\epsilon\to 0}$ to make this more explicit and mathematically correct. We choose to omit it here for readability reasons.

[2] A more rigorous derivation of this expression for Green's operator can be found in Appendix B on page 135.

[3] for most real potentials the condition is less stringent, $\mathbf{r}$ has to be only far outside the range of the potential. But the range of the Coulomb potential for example is infinite. Solving the scattering problem for a Coulomb potential requires thus special care and is described in [114].

equation in space representation [202]:

$$\langle \mathbf{r} \,|\, \psi^{(\pm)} \rangle \xrightarrow[\mathbf{r}\to\infty]{} = \langle \mathbf{r} \,|\, \phi \rangle - \frac{1}{4\pi}\frac{2m}{\hbar^2}\frac{e^{\pm ikr}}{r}\int d\mathbf{r}' e^{-i\mathbf{k}'\mathbf{r}'} V(\mathbf{r}') \langle \mathbf{r}' \,|\, \psi^{(\pm)} \rangle = \\ = \frac{1}{(2\pi)^{3/2}}\left(e^{i\mathbf{k}\mathbf{r}} + f(\mathbf{k},\mathbf{k}')\frac{e^{\pm ikr}}{r}\right) . \quad (2.15)$$

This form makes it very clear that we have the original plane wave in propagation direction $\mathbf{k}$ plus an outgoing (+) or incoming (-) spherical wave with amplitude $f(\mathbf{k},\mathbf{k}')$ given by

$$f(\mathbf{k},\mathbf{k}') = -\frac{1}{4\pi}(2\pi)^3 \frac{2m}{\hbar^2} \langle \pm\mathbf{k}' \,|\, \hat{V} \,|\, \psi^{(\pm)} \rangle . \quad (2.16)$$

The implicit Eq. (2.11) can be rewritten to only depend on $|\,\phi\,\rangle$ by multiplying from the left with $(E - \hat{H}_0 + i\epsilon)$, adding on both sides $\hat{V}|\,\phi\,\rangle$ and again multiplying from the left $(E - \hat{H} + i\epsilon)^{-1}$, to give

$$|\,\psi^{(\pm)}\,\rangle = |\,\phi\,\rangle + \frac{1}{E - \hat{H} \pm i\epsilon}\hat{V}|\,\phi\,\rangle = |\,\phi\,\rangle + \hat{G}^{(\pm)}\hat{V}|\,\phi\,\rangle . \quad (2.17)$$

Here we have defined

$$\hat{G}^{(\pm)} = \frac{1}{E - \hat{H} \pm i\epsilon} . \quad (2.18)$$

Compared with Eq. (2.11) the full Hamilton operator appears now in Green's operator. One can define the so called "Møller operators" $\hat{\Omega}^{(+)}$ and $\hat{\Omega}^{(-)}$

$$\hat{\Omega}^{(\pm)} = 1 + \hat{G}^{(\pm)}V , \quad (2.19)$$

through which Eq. (2.17) may be rewritten as,

$$|\,\psi^{(\pm)}\,\rangle = \hat{\Omega}^{(\pm)}|\,\phi\,\rangle . \quad (2.20)$$

In other words $\hat{\Omega}^{(+)}$ is just the operator which transforms the unperturbed initial state $|\,\phi\,\rangle$ into the scattering state $|\,\psi^{(+)}\,\rangle$. $\hat{\Omega}^{(-)}$ transforms $|\,\phi\,\rangle$ into the unphysical state $|\,\psi^{(-)}\,\rangle$, whose significance lies in the number of important results in which it occurs.

It is helpful to define the transition operator $\hat{T}$, such that

$$\hat{V}|\,\psi^{(+)}\,\rangle = \hat{T}|\,\phi\,\rangle . \quad (2.21)$$

Using this definition, the scattering amplitude of Eq. (2.16) can now be expressed using Eq. (2.21)

$$f(\mathbf{k},\mathbf{k}') = -\frac{1}{4\pi}(2\pi)^3 \frac{2m}{\hbar^2} \langle \mathbf{k}' \,|\, \hat{T} \,|\, \mathbf{k} \rangle . \quad (2.22)$$

Multiplying the Lippmann-Schwinger Eq. (2.11) by $\hat{V}$ and using that the eigenkets $|\,\phi\,\rangle$ are complete, results in

$$\hat{T} = \hat{V} + \hat{V}\frac{1}{E - \hat{H}_0 + i\epsilon}\hat{T}\,. \tag{2.23}$$

We can obtain an iterative solution for $\hat{T}$ as follows

$$\hat{T} = \hat{V} + \hat{V}\frac{1}{E - \hat{H}_0 + i\epsilon}\left(\hat{V} + \hat{V}\frac{1}{E - \hat{H}_0 + i\epsilon}\left(\hat{V} + \hat{V}\frac{1}{E - \hat{H}_0 + i\epsilon}\left(\hat{V} + \cdots\right)\right)\right)\,. \tag{2.24}$$

Using this iterative solution to calculate the scattering amplitude with the help of Eq. (2.22) gives the well known Born approximation [167].

On the other hand we can multiply Eq. (2.17) with $\hat{V}$ from the left to get a formal solution for $\hat{T}$

$$\hat{T} = \hat{V} + \hat{V}\frac{1}{E - \hat{H} + i\epsilon}\hat{V}\,. \tag{2.25}$$

After insertion of the complete set of eigenstates $|\,\psi^{(+)}\,\rangle$ of $\hat{H}$ we have

$$\hat{T}(E) = \hat{V} + \sum_{\nu}\hat{V}\frac{|\,\psi^{(+)}\,\rangle\langle\,\psi^{(+)}\,|}{E - \epsilon_\nu}\hat{V}\,, \tag{2.26}$$

where the summation over ν is discrete for the bound-state energies $\epsilon_\nu < 0$, and represents an integration for positive energies that correspond to scattering solutions. From this equation we see that the two-body T-matrix has poles, which correspond to the bound states of the potential[4].

Finally we define the S-Operator as $\hat{S} = \hat{\Omega}^{(-)\dagger}\hat{\Omega}^{(+)}$. Let us now calculate the S-Matrix in the basis of the asymptotic states $|\,\phi_\mu\,\rangle$:

$$\begin{aligned} S_{\mu\nu} &= \langle\,\phi_\mu\,|\,\hat{\Omega}^{(-)\dagger}\hat{\Omega}^{(+)}\,|\,\phi_\nu\,\rangle = \langle\,\psi_\mu^{(-)}\,|\,\psi_\nu^{(+)}\,\rangle = \\ &= \langle\,\phi_\mu\,|\,U(+\infty,-\infty)\,|\,\phi_\nu\,\rangle\,. \end{aligned} \tag{2.27}$$

In the last step we have used that the Møller operators can be expressed by the time evolution operator $\hat{U}(t,t')$ as shown in Appendix B on page 135. Now the physical interpretation of the S-Matrix is clear. It gives the asymptotical transition probabilities between two free states $|\,\phi_\mu\,\rangle$ and $|\,\phi_\nu\,\rangle$. One can derive a more explicit expression for the S-Matrix elements [114, Chapter 14], which relates the S- and T-Matrix.

$$\begin{aligned} S_{\mu\nu} &= \delta(\mu-\nu) - 2\pi i\delta(E_\mu - E_\nu)\langle\,\phi_\mu\,|\,\hat{V}\,|\,\psi_\nu^{(+)}\,\rangle \\ &= \delta(\mu-\nu) - 2\pi i\delta(E_\mu - E_\nu)\langle\,\phi_\mu\,|\,\hat{T}\,|\,\phi_\nu\,\rangle\,. \end{aligned} \tag{2.28}$$

[4]While all bound states occur at poles of $\hat{T}$, not all poles of $\hat{T}$ are bound states. True bound states are only poles where $\mathbf{k}$ is located along the positive imaginary axis of the complex $\mathbf{k}$ plane. Other poles may correspond to resonances, virtual states, or kinematic effects [162]. This also holds true for the S-matrix.

2.3 Partial wave decomposition

If we assume that the potential is spherically symmetric, the transition operator $\hat{T}$ commutes with $\hat{L}^2$ and $\hat{L}$. In other words, $\hat{T}$ is a scalar operator. Thus the solution of the Schrödinger equation Ψ can be separated into a radial part $^1/_r u_\ell(r)$ and an angular part[5] $P_\ell(\theta)$. We can now expand the scattering amplitude Eq. (2.22) in spherical functions $|\, E\,\ell\, m\,\rangle$:

$$\begin{aligned} f(\mathbf{k},\mathbf{k}') &= -\frac{1}{4\pi}(2\pi)^3\frac{2m}{\hbar^2}\langle\, \mathbf{k}'\,|\,\hat{T}\,|\,\mathbf{k}\,\rangle = \\ &= -\frac{1}{4\pi}(2\pi)^3\frac{2m}{\hbar^2}\sum_{\ell,\ell',m,m'}\iint dE\,dE'\langle\, \mathbf{k}'\,|\,E'\,\ell'\,m'\,\rangle\langle\, E'\,\ell'\,m'\,|\,\hat{T}\,|\,E\,\ell\,m\,\rangle\langle\, E\,\ell\,m\,|\,\mathbf{k}\,\rangle = \\ &= -\frac{4\pi}{k}\sum_{l,m} T_\ell(E)\Big|_{E=\hbar^2k^2/2m} Y_\ell^m(\mathbf{k}')Y_\ell^{m\dagger}(\mathbf{k})\,. \end{aligned} \tag{2.29}$$

Together with the customary definition

$$f_\ell(k) = -\frac{\pi T_\ell(E)}{k}\,, \tag{2.30}$$

and the properties of the spherical harmonic functions, we then have

$$f(\mathbf{k},\mathbf{k}') = f(\vartheta) = \sum_{\ell=0}^{\infty}(2\ell+1)f_\ell(k)P_\ell(\cos\vartheta)\,. \tag{2.31}$$

To appreciate the physical significance of $f_\ell(k)$, we have to study again the large-distance behavior of the wave function $\langle\, \mathbf{r}\,|\,\psi^{(+)}\,\rangle$ given by Eq. (2.15). Using the expansion of a plane wave in terms of spherical waves [114] and Eq. (2.31) gives

$$\begin{aligned} \langle\, \mathbf{r}\,|\,\psi^{(+)}\,\rangle &\xrightarrow[\mathbf{r}\to\infty]{} \frac{1}{(2\pi)^{3/2}}\left(e^{i\mathbf{k}\mathbf{r}} + f(\mathbf{k},\mathbf{k}')\frac{e^{ikr}}{r}\right) = \\ &= \frac{1}{(2\pi)^{3/2}}\sum_\ell \frac{(2\ell+1)}{2ik}P_\ell(\cos\vartheta)\left[(1+2ikf_\ell(k))\frac{e^{ikr}}{r} - \frac{e^{-i(kr-\ell\pi)}}{r}\right]. \end{aligned} \tag{2.32}$$

The physics of scattering process becomes now clear. When the scatterer is absent, we can analyze the plane wave as the sum of a spherically outgoing $^{e^{ikr}}/_r$ and a spherically incoming $-^{e^{-i(kr-\ell\pi)}}/_r$ wave for each ℓ. The presence of a scatterer changes only the coefficient of the outgoing wave. The incoming wave is completely unaffected. It is now convenient to define[6] $S_\ell(k)$ to be

$$S_\ell(k) = (1+2ikf_\ell(k)) = e^{2i\delta_\ell(k)}\,. \tag{2.33}$$

[5] P_ℓ denotes the Legendre polynomials

[6] $S_\ell(k)$ can also be regarded as the ℓ-th diagonal element of the $\hat{S}$ operator.

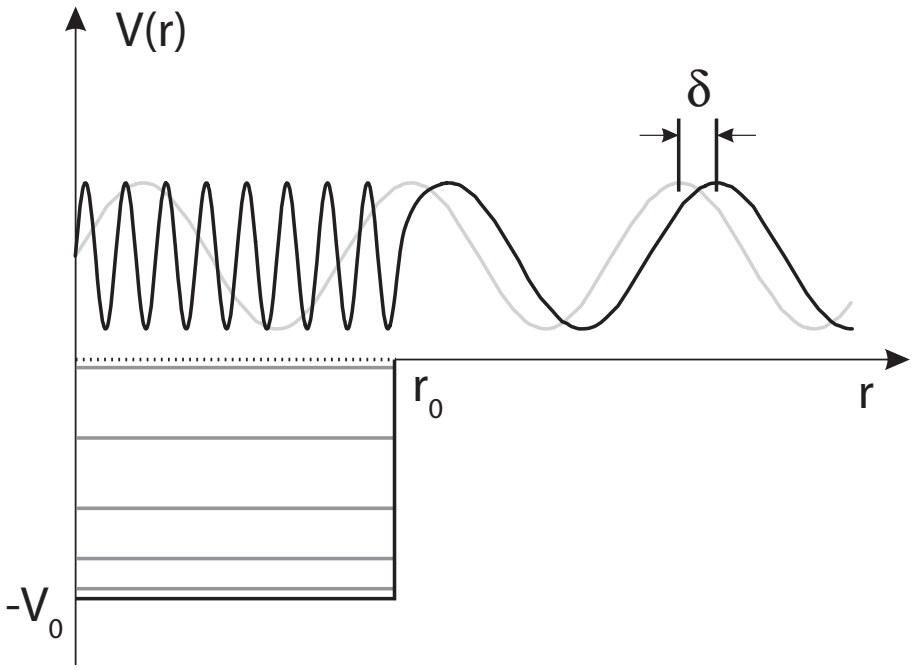

Figure 2.2: Schematic representation of the phase shift $\delta_\ell(k)$. The wave function Eq. (2.32) when the scattering potential is absent is drawn in gray, while the wave function with the scattering potential present is drawn in black. The phase difference between these two wave functions far away from the scattering region determines the phase shift $\delta_\ell(k)$ (in this case for ℓ=0).

Using this definition we can rewrite Eq. (2.32) in a more convenient form

$$\langle \mathbf{r} \,|\, \psi^{(+)} \rangle \xrightarrow[\mathbf{r}\to\infty]{} \frac{1}{(2\pi)^{3/2}} \sum_\ell (2\ell+1) P_\ell(\cos\vartheta) i^\ell e^{i\delta_\ell(k)} \frac{\sin(kr - \frac{1}{2}\ell\pi + \delta_\ell(k))}{kr} \tag{2.34}$$

Because of the probability flux conservation one can deduce that $|S_\ell(k)| = 1$, that is, the most that can happen is a change in the phase of the outgoing wave. This is expressed by the second equality in Eq. (2.33), where we have introduced $\delta_\ell(k)$, the so called phase shift of the ℓ-th partial wave. A schematic representation of the phase shift is given in Fig. 2.2. We can now express $f_\ell(k)$ explicitly in terms of $\delta_\ell(k)$:

$$f_\ell(k) = \frac{S_\ell(k) - 1}{2ik} = \frac{e^{2i\delta_\ell(k)} - 1}{2ik} = \frac{e^{i\delta_\ell(k)} \sin\delta_\ell(k)}{k} = \frac{1}{k\cot\delta_\ell(k) - ik}\,. \tag{2.35}$$

For the full scattering amplitude we have finally:

$$f(\vartheta,\phi) = \frac{1}{k}\sum_l (2l+1) e^{i\delta_\ell(k)} \sin\delta_\ell(k) P_l(\cos\vartheta)\,. \tag{2.36}$$

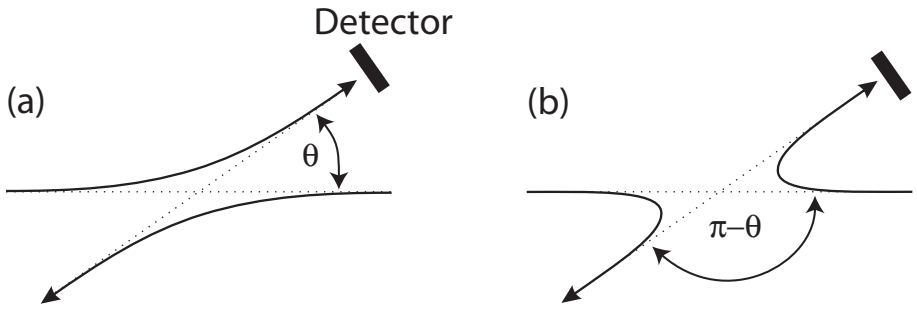

Figure 2.3: For identical particles, it is impossible to tell if we are observing a scattered beam particle (a) or a recoiling target particle (b).

The differential cross section can now be obtained from Eq. (2.4) and σ_{tot} can be obtained by performing the integration over the solid angle Eq. (2.5), which gives

$$\sigma_{\text{tot}}(k) = \frac{4\pi}{k^2} \sum_l (2\ell + 1) \sin^2 \delta_\ell(k) = \sum_l \sigma_\ell(k) \,. \tag{2.37}$$

The maximum contribution of a specific partial wave to the total cross-section is reached in the so called *unitarity limit* ($\sin^2 \delta_\ell(k) = 1$) and increases with angular momentum according to

$$\sigma_\ell(k) = \frac{4\pi(2\ell + 1)}{k^2} \,. \tag{2.38}$$

Comparing the scattering amplitude in forward direction, $f(\vartheta = 0)$ with Eq. (2.37), directly yields the optical theorem given in Eq. (2.6).

We have now reduced the solution of a specific scattering problem to the determination of the corresponding partial wave phase shifts $\delta_\ell(k)$. These are obtained by solving the full Schrödinger Eq. (2.10) — numerically if necessary. The solution is then compared to the asymptotic solution of Eq. (2.32) to determine the scattering phase $\delta_\ell(k)$. From the $\delta_\ell(k)$ all other physically interesting quantities can be calculated.

2.4 Identical particles

In quantum mechanics there is no way of keeping track of each particle individually when the wave functions of two identical particles overlap. It is therefore impossible to identify in a scattering event, which particle scatters and which is the scatterer. A detector can either detect the scattered particle or the recoiling target particle as shown in Fig. 2.3. The symmetrization postulate [40] requires that the wave function is either completely symmetric (for bosons) or completely antisymmetric

(for fermions) with respect to permutation of these particles ($\mathbf{r} \to -\mathbf{r}$[7], $r \to -r$, $\vartheta \to \pi - \vartheta$, $\phi \to \pi + \phi$). To achieve this, we need to (anti-)symmetrize the asymptotic wave function from Eq. (2.3),

$$\phi(\mathbf{r}) \xrightarrow[\mathbf{r}\to\infty]{} e^{i\mathbf{kr}} \pm e^{-i\mathbf{kr}} + \left[f(\vartheta,\phi) \pm f(\pi-\vartheta,\pi+\phi)\right] \frac{e^{ikr}}{r}\,, \tag{2.39}$$

where the plus sign applies for bosons and the minus sign for fermions. This results in a differential cross section,

$$\begin{aligned} \frac{d\sigma}{d\Omega} &= \left|f(\vartheta,\phi) \pm f(\pi-\vartheta,\pi+\phi)\right| = \\ &= \left|f(\vartheta,\phi)\right|^2 + \left|f(\pi-\vartheta,\pi+\phi)\right|^2 \pm 2\Re\left[f(\vartheta,\phi)f^\dagger(\pi-\vartheta,\pi+\phi)\right]\,. \end{aligned} \tag{2.40}$$

We note that in the classical limit, where the particles are distinguishable, the interference term $2\Re\left[f(\vartheta,\phi)f^\dagger(\pi-\vartheta,\pi+\phi)\right]$ disappears. The total cross section σ_{tot} needs to be divided by a factor of two, since we count each scattering event twice during the integration. If we now use the partial wave decomposition Eq. (2.31) to calculate the differential cross section we immediately see that odd partial waves interfere destructively for bosons, whereas for fermions all even partial waves vanish due to the symmetry properties of the Legendre polynomials. Integration gives the total scattering cross section:

$$\sigma_{\text{tot}}(k) = \frac{8\pi}{k^2} \sum_{\substack{\ell \text{ even, bosons} \\ \ell \text{ odd, fermions}}} (2l+1)\sin^2\delta_\ell(k)\,. \tag{2.41}$$

In the limit $k \to 0$, i.e. when only s-wave collisions are still possible, collisions between identical fermions are "frozen out".

2.5 Elastic s-wave collisions

At low energies — or, more precisely, when $1/k$ is comparable to or larger than the range R of the potential — partial waves for higher ℓ are, in general, unimportant. This point may be obvious classically because the particle cannot penetrate the centrifugal barrier[8]; as a result the potential inside has no effect. In terms of quantum mechanics, the effective potential for the l-th partial wave is given by[9]

$$V_{\text{eff}}(r) = V(r) + \frac{\hbar^2}{2m_\mu}\frac{\ell(\ell+1)}{r^2}\,. \tag{2.42}$$

[7] To see that this operation really is a permutation of both particles, please remember that $\mathbf{r}$ is the relative position of the particles

[8] a semi-classical argument gives that substantial scattering only occurs for $\ell \simeq \sqrt{\ell(\ell+1)} \lesssim kR$, where R is the range of the potential.

[9] If the potential is strong enough to accommodate $l \neq 0$ bound states near $E \simeq 0$ the atoms can tunnel through the potential barrier and couple resonantly to a bound state. This is a so called shape resonance [114].

The behavior of the radial wave function $u_\ell(r)$ is then largely determined by the centrifugal barrier term. We can estimate the behavior of the phase shift by writing Eq. (2.11) using the partial wave expansion of Green's operator Eq. (2.14) [128, Chap. 8] which gives the following Integral equation for the scattering amplitude/phase:

$$f_\ell(k) = \frac{e^{i\delta_\ell(k)} \sin \delta_\ell(k)}{k} = -\frac{2m}{\hbar^2} \int_0^\infty j_\ell(kr) V(r) u_\ell(r) r dr \,. \tag{2.43}$$

If $u_\ell(r)$ is not to different from the solution[10] $j_\ell(kr)$ for a free particle and $1/k$ is much larger than the range of the potential, the right hand side would vary as $k^{2\ell}$; for small $\delta_\ell(k)$ the left-hand side must vary as $\delta_\ell(k)/k$ Eq. (2.33)[11]. Hence the phase shift k goes to zero as

$$\delta_\ell(k) \xrightarrow[k\to 0]{} k^{2\ell+1} \text{ modulo } \pi, \tag{2.44}$$

for[12] $\ell > 0$. This is known as threshold behavior[13]. It is therefore obvious that at low energies with a finite range potential, all partial cross sections except the s-wave contribution σ_0 vanish as $k^{4\ell}$, which can be written

$$\lim_{k\to 0} \sigma_0(k) = 8\pi a^2, \tag{2.45}$$

where the *scattering length* a is defined by

$$a = -\lim_{k\to 0} \frac{\tan \delta_0(k)}{k}. \tag{2.46}$$

So low energy scattering can be described by a single parameter, the scattering length. To understand the physical significance of the scattering length we will look at the asymptotic behavior of the radial wave function for $r \to 0$. For s-wave scattering ($\ell = 0$) at low energies $k \simeq 0$, the Schrödinger equation outside the range of the potential $r > R$ is given by

$$\frac{d^2 u_0(r)}{dr^2} = 0 \,. \tag{2.47}$$

The obvious solution is $u_0(r) = c(r - a)$, so just a straight line! This can be understood if we look at the behavior of the asymptotic s-wave function in the limit $k \to 0$. It is given by $\lim_{k\to 0} u_0(r) = \sin[k(r + \delta_\ell(k)/k)]$ which shows identical

[10] $j_\ell(z)$ are the spherical Bessel functions and assume the values $j_\ell(z) \xrightarrow[z\to 0]{} \frac{z^l}{(2\ell+1)!!}$

[11] For non-negligible values of $\delta_\ell(k)$ the scattering amplitude is complex. This is best visualized using a so called Argand plot [114, 128, 202, 235]

[12] $j_0(z) \xrightarrow[z\to 0]{} 1$, thus the s-wave scattering amplitude assumes a constant value.

[13] We should be aware here that our argumentation is not very strict. A more careful derivation shows that for power law potentials $U(r) \propto r^{-n}$ Eq. (2.44) is valid only if $2l + 3 < n$. So for $n \leq 3$ (e.g. the dipole-dipole interaction) all partial waves will contribute [127, §124].

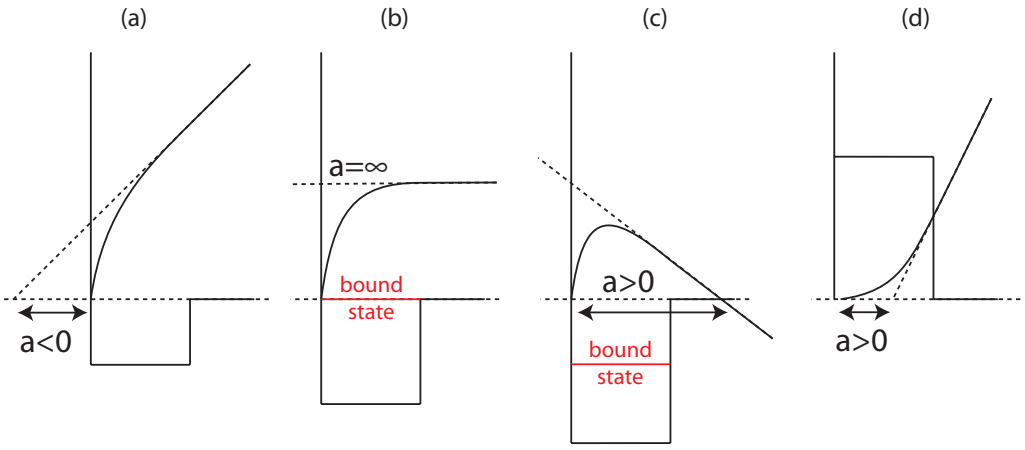

Figure 2.4: The scattering length of a potential can be determined from the intercept of the asymptotic wave function. (a,b,c) attractive potential with increasing depth. In case (a) the potential supports no bound state, thus the scattering length is negative. (b) the potential is now deep enough to start to support one bound state, the scattering length diverges. (c) an even deeper potential increases the curvature of the wave function even further, so the asymptote intersects the zero energy line for positive energies. (d) for a repulsive potential the curvature is always away from the r-axis, so the scattering length is always positive.

behavior. We are now interested in the intercept of the s-wave function, which can be calculated by linear extrapolation of $u_0(r)$ from a point $r = r_0$ onwards

$$u_0(r) \stackrel{!}{=} 0 \Rightarrow r = r_0 - \frac{u_0(r_0)}{u_0'(r_0)} = r_0 - \frac{\tan\left[k(r_0 + \frac{\delta_0(k)}{k})\right]}{k} \xrightarrow[k\to 0]{} a\,. \tag{2.48}$$

Now, from the intercept of the asymptotic wave function we can directly read of the scattering length of the potential. This is shown schematically for different potentials in Fig. 2.4.

Sometimes we are not only interested in the behavior for $k \to 0$, but in the whole low temperature region. To investigate the cross section in the small k region we expand $k\cot(\delta_0(k))$ from Eq. (2.46) to higher order[14] [114]:

$$k\cot(\delta_0(k)) = -\frac{1}{a} + \frac{1}{2} r_{\text{eff}} k^2 + \dots\,, \tag{2.49}$$

where the effective range r_{eff} is defined by

$$r_{\text{eff}} = 2\int_0^\infty \left[v_0(r)^2 - u_0(r)^2\right] dr\,. \tag{2.50}$$

[14]The effective range expansion can only be performed for any potential vanishing faster than $1/r^5$ [158]

Here $u_0(r)$ and $v_0(r)$ are the solutions of the radial Schrödinger equation with and without the potential $V(\mathbf{r})$ present, respectively. The effective range expansion is valid provided the energy dependent term satisfies $\frac{1}{2}k^2 a r_{\text{eff}} < 1$. The effective range can be interpreted as a second-order correction to the phase shift, reducing or enlarging the effective width of the scattering potential. The cross section one obtains using the effective range expansion is given by

$$\sigma_0(k) = \frac{8\pi a^2}{k^2 a^2 + (\frac{1}{2}k^2 r_{\text{eff}} a - 1)^2}\,, \tag{2.51}$$

which of course reduces to $8\pi a^2$ for $k \to 0$. Two other things are of interest here. First, the scattering length appears linearly in this equation, so the temperature behavior will depend on the sign of a. Second, the approximation is not sufficient to reproduce oscillations in the cross section, like the Ramsauer-Townsend effect (see Figure 2.6).

2.6 Example: Square well potential

To illustrate the results from the previous section, we now explicitly calculate the results for the simple case that the interaction potential is a square-well potential of the form:

$$V(r) = \begin{cases} -V_0 & \text{if } r < R. \\ 0 & \text{if } r > R. \end{cases} \tag{2.52}$$

The general solution of the Schrödinger Eq. (2.10) for this potential assuming $\ell = 0$ and $E > 0$ is

$$u^<(r) = Ae^{ik^< r} + Be^{-ik^< r} \quad \text{if } r < R, \tag{2.53a}$$
$$u^>(r) = Ce^{ikr} + De^{-ikr} \quad \text{if } r > R, \tag{2.53b}$$

with $k^< = \sqrt{k^2 - 2m_\mu V_0/\hbar^2}$. Since the wave function has to obey the Schrödinger equation at the origin, we have to require that $u^<$ vanishes at the origin. This immediately gives the boundary condition $B = -A$. Comparing the wave function $u^>$ to the s-wave component of the general scattering wave function for $r \to \infty$ Eq. (2.32), we find that

$$e^{2\delta_0(k)} = -\frac{C}{D}\,. \tag{2.54}$$

Requiring that the wave functions for $r < R$ and $r > R$ join smoothly leads to the following result for the scattering phase:

$$\delta_0(k) = -kR + \arctan\left(\frac{k}{k^<}\tan(k^< R)\right)\,. \tag{2.55}$$

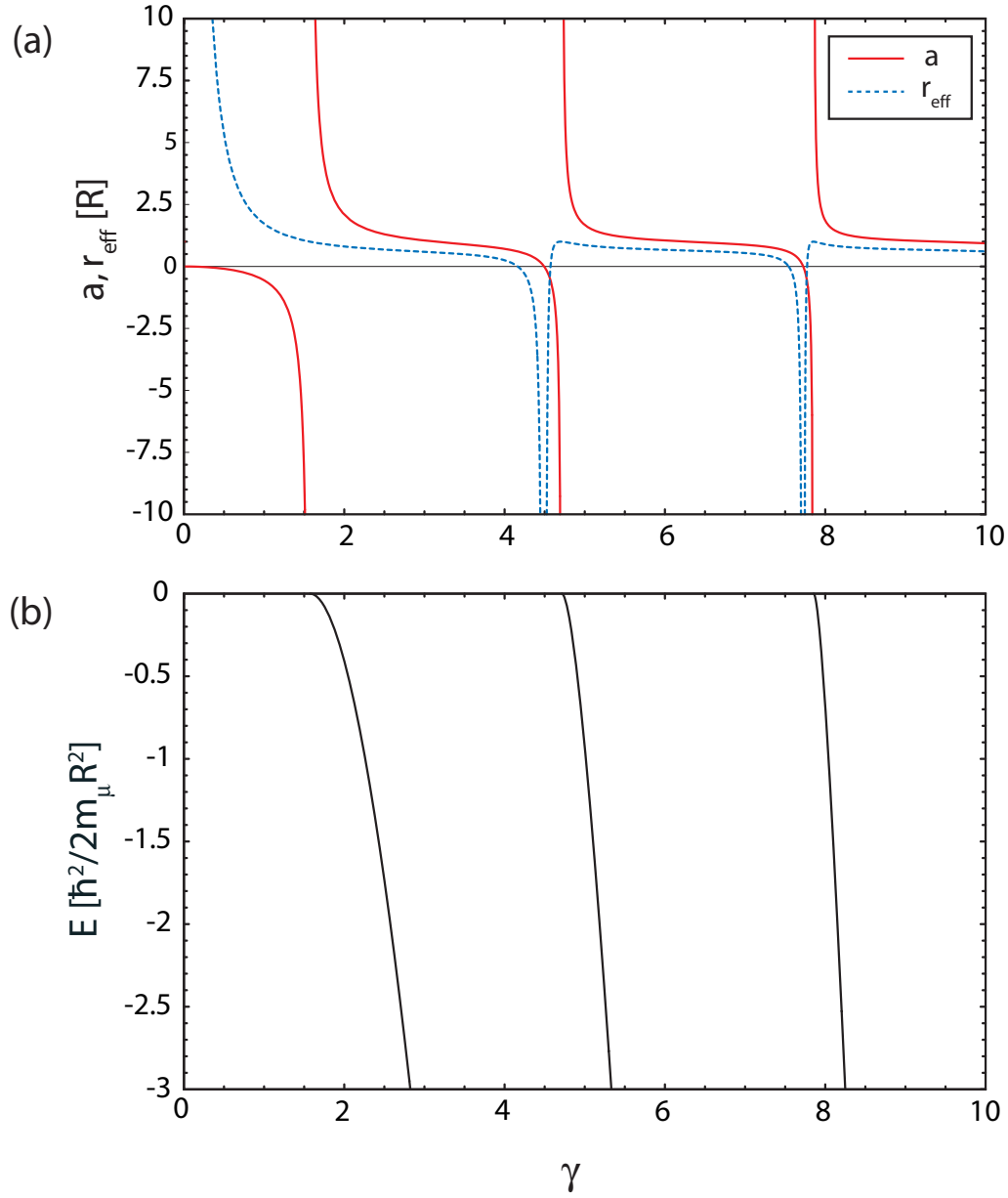

Figure 2.5: (a) shows the behavior of the scattering length a and the effective range r_{eff} with increasing well-depth γ. (b) The formation of the first three bound states with increasing well-depth is shown. Every time the potential supports a new bound state, the scattering length diverges. This is a so called *zero energy resonance*. Please note that the lower plot was done under the assumption $R = 1$.

From this result we can now explicitly determine an analytical expression for the scattering length

$$a = R(1 - \frac{\tan\gamma}{\gamma}), \text{ where } \gamma = R\sqrt{\frac{2m_\mu|V_0|}{\hbar^2}}\,. \tag{2.56}$$

and the effective range

$$r_{\text{eff}} = R\left[1 + \frac{3\tan\gamma - \gamma(3+\gamma^2)}{3\gamma(\gamma - \tan\gamma)^2}\right]\,, \tag{2.57}$$

using Eq. (2.49). Their behavior with increasing well depth γ is shown in Fig. 2.5. For $\gamma = (n + 1/2)\pi$ the scattering length diverges and changes sign. This behavior is called a *zero energy resonance* and in fact occurs each time the potential is just deep enough to support a new bound state[15]. If a potential is just about to support another bound state (a so called virtual bound state) the scattering length goes to $-\infty$ and returns from $+\infty$ the moment the bound state is really supported by the potential (see also Fig. 2.4). The effective range diverges if the scattering length becomes equal to zero because the effective range expansion is ill defined for $a = 0$. Also of interest is the dependence of the cross sections $\sigma_\ell(k)$ on the collision energy which is shown in Fig. 2.6 on the next page. As predicted by Eq. (2.44) higher partial cross sections "freeze out" according to $k^{4\ell}$ for low k.

It turns out, that there is an important relationship between the energy of the last bound state and the scattering length. To derive this relation, we first need the positions of the last bound state. Therefore we need to solve the Schrödinger equation for negative energy. This leads to

$$u^<(r) = A(e^{ik^< r} - e^{-ik^< r}) \quad \text{if } r < R, \tag{2.59a}$$
$$u^>(r) = Be^{-\kappa r} \quad \text{if } r > R, \tag{2.59b}$$

with $k^< = \sqrt{2m_\mu(E - V_0)/\hbar^2}$ and $\kappa = \sqrt{2m_\mu|E|/\hbar^2}$. Again we demand the solutions to smoothly join at $r = R$. This gives the following equation for the bound-state energies

$$\sqrt{\frac{2m_\mu}{\hbar^2}\,|E_m|} = -\sqrt{\frac{2m_\mu}{\hbar^2}(E_m - V_0)}\,\cot\left(\sqrt{\frac{2m_\mu}{\hbar^2}(E_m - V_0)}\right)\,. \tag{2.60}$$

One can show that a potential with a well-depth of V_0 supports n bound states, where n is given by

$$(n - 1/2)\pi < \gamma < (n + 1/2)\pi\,. \tag{2.61}$$

[15] Also the phase shift jumps by π each time a new bound state is supported. The number of bound states a potential supports can be obtained according to Levinson's theorem [128]

$$\delta_0(k = 0) - \delta_0(k = \infty) = n\pi\,. \tag{2.58}$$

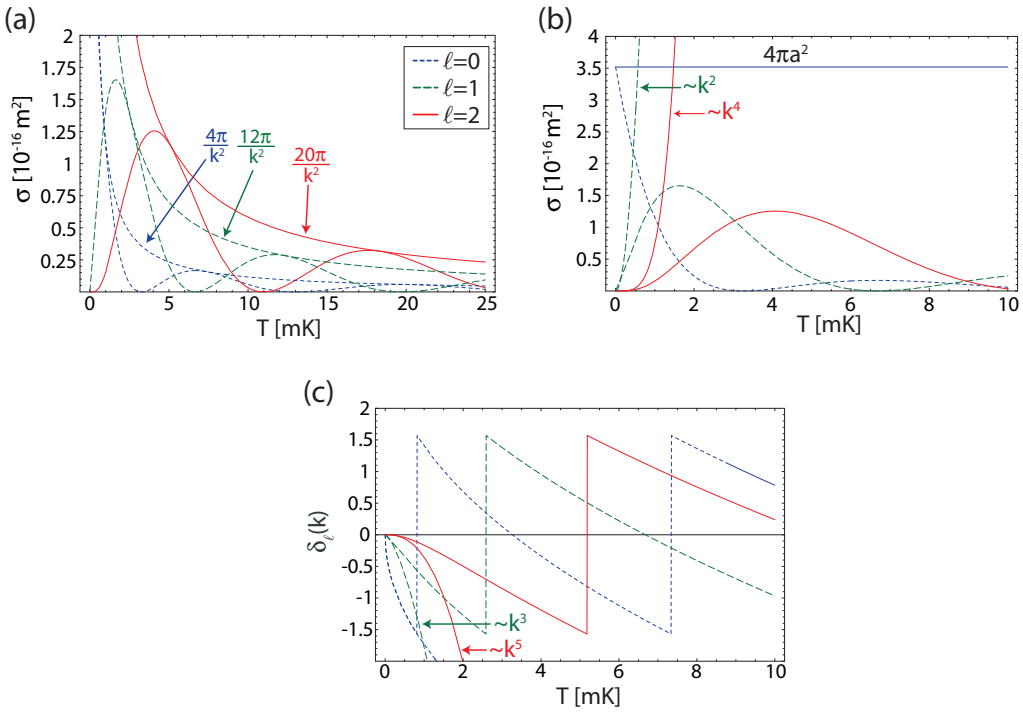

Figure 2.6: Temperature dependence of the partial cross sections $\sigma_{\ell=0,1,2}(k)$ for a square well potential of width $r = 100\,\mathrm{a_0}$ and a depth $V_0 = 1.02 \cdot 10^{-21}\,\mathrm{J}$ which supports 150 bound states. (a) With increasing temperature the partial cross-sections oscillate between zero and the unitarity limit. The phenomenon that for certain ℓ and k the cross section vanishes is called the *Ramsauer-Townsend effect*. It has been observed in low-energy collisions of electrons with rare-gas atoms. (b) The partial cross sections for $\ell > 0$ show the expected $k^{4\ell}$ behavior and "freeze out" with decreasing temperature, while σ_0 approaches the finite value of $4\pi a^2$ for small k. (c) Behavior of the scattering phase $\delta_\ell(k)$ over the temperature. Also shown is the low temperature behavior $\delta_\ell(k) = k^{2\ell+1}$.

For small binding energy $|E_m| \ll |V_0|$ we have from Eq. (2.60):

$$\sqrt{\frac{2m_\mu}{\hbar^2}\,|E_m|} \simeq -\gamma \cot \gamma/R \simeq 1/a \quad \text{or} \quad E_m = -\frac{\hbar^2}{2m_\mu a^2}\,. \tag{2.62}$$

It turns out, that this relation is quite general and does not depend on the specific details of the potential. Any potential with a large positive scattering length has a bound state just below the continuum threshold.

Chapter 3

Theory of Feshbach resonances

After introducing the "formal" scattering theory in the last chapter, I'll now turn to describing Feshbach resonances. First an informal, phenomenological description of the properties of Feshbach resonances is given. After an initial understanding of the phenomenon has been formed, I'll turn to the theoretical description of Feshbach resonances. There, the relevant Schrödinger equation will be solved with the help of formal scattering theory. In the following, I'll extend the previous square-well example to include Feshbach resonances. For realistic potentials only numerical solutions are possible. Two different numerical multi-channel calculation methods are presented. The chapter closes with an overview of the different possibilities to experimentally observe a Feshbach resonance.

Feshbach resonances were introduced in nuclear physics to describe the narrow resonances observed in the total cross section for a neutron scattering of a nucleus [70]. These very narrow resonances are the result of the formation of a long-lived compound nucleus during the scattering process, with a binding energy close to that of the incoming neutron. The defining feature of a Feshbach resonance is that the bound state responsible for the resonance exists in another part of the quantum-mechanical Hilbert space than the part associated with the incoming particles. Stwalley [232] discussed for the first time the existence of Feshbach resonances in collisions of spin-polarized Hydrogen and Deuterium and the possibility to magnetically tune those Feshbach resonances. Those resonances were experimentally found by Reynolds et al. [191] and Silvera et al. [215]. Tiesinga et al. [238, 239] predicted the existence of Feshbach resonances in ultracold collisions of Cs and their usefulness to determine the long-range interaction potentials of the involved atoms. Following the first observation of Feshbach resonances in ^{23}Na by Inouye et al. [108], they have now been observed in various bosonic atomic species [45, 143, 195, 228, 244], as well as a number of fermionic isotopes [21, 57, 173, 187]. Feshbach resonances between different atomic species have also been theoretically predicted [217], and were quite recently experimentally observed [111, 222]. If the interaction between the two colliding

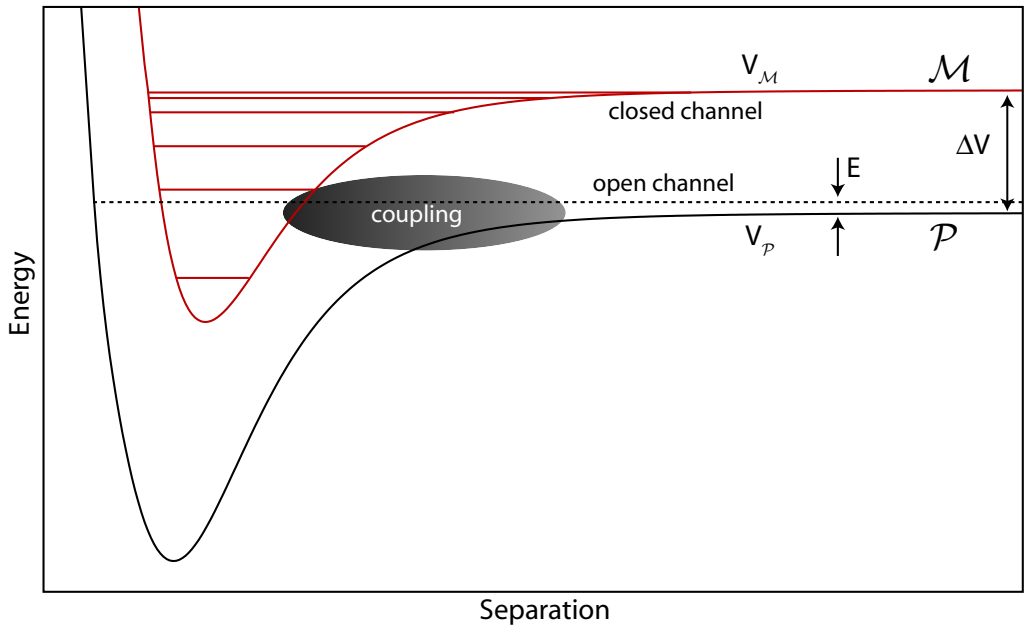

Figure 3.1: Basic principle of a Feshbach resonance. Shown are the molecular interaction potentials $V_{\mathcal{P}}$ and $V_{\mathcal{M}}$ for two colliding atoms in two different internal states, labeled $\mathcal{P}$ and $\mathcal{M}$, respectively. The $\mathcal{M}$-state supports at least one or more bound states. The energy difference between the two interaction potentials ΔV can be changed by experimental means. The collision occurs in the energetically open channel $\mathcal{P}$ with a collision energy E. Due to the energy being lower than the asymptotic energy of the $\mathcal{M}$-state, the atoms cannot collide in this state and it is called a closed channel. A Feshbach resonance now occurs if the energy of the open channel is (almost) degenerate with a bound state of the molecular state $\mathcal{M}$ *and* a coupling between the two states exists. This allows a temporary occupation of the bound state and thus modifies the scattering properties drastically.

atoms is not isotropic, one Feshbach resonance can split up into a multiplett [237]. Finally, an entertaining introduction to Feshbach resonances and their application can be found in [123].

3.1 Phenomenological description

In the preceding chapter we discussed the scattering of two atoms in some detail. What we neglected in the preceding chapter was the internal structure of the atoms. The different internal states of the atoms give rise to many different molecular interaction potentials. In addition, we need to take the coupling between the different internal states into account. The situation with which we are dealing now is sketched in Fig. 3.1. To keep our picture simple, we have limited ourselves to two internal

states for our colliding atoms which we call $\mathcal{P}$ and $\mathcal{M}$. The corresponding molecular interaction potentials are denoted by $V_\mathcal{P}$ and $V_\mathcal{M}$, respectively. The energy of the two colliding atoms is slightly above the asymptotic value of $V_\mathcal{P}$. Since their energy E is less than the asymptotic value of $V_\mathcal{M}$, the collision products can never be in state $\mathcal{M}$. This is why $\mathcal{M}$ is often called a closed and $\mathcal{P}$ an open channel. The closed channel $\mathcal{M}$ supports at least one, if not more bound states as shown in the figure. So, up to now the scattering could be still described along the lines of the previous chapter, since there is yet nothing different from the one channel case. The situation changes when we allow for the existence of a coupling between the open and the closed channel. If the energy of the open channel is close to the energy of a bound state of $\mathcal{M}$, the two colliding atoms can undergo a Landau-Zener [264] type transition from $\mathcal{P}$ to a bound state of $\mathcal{M}$ mediated by the coupling. A diatomic quasi-molecule is formed, whose lifetime is limited due to the coupling to the continuum-states of channel $\mathcal{P}$. Due to the formation and the decay of the quasi-molecule the scattering process will be modified drastically. Since the situation is similar as in Chapter 2.6 for the zero-energy resonance we expect a resonance behavior for the scattering length depending on the position of the bound state.

The only remaining question is how to change the energy difference ΔV between the two molecular interaction potentials and thus the position of the bound states. In the most common case the two different internal states are different spin configurations of the two atoms and thus their magnetic moment is different. By applying a magnetic field both molecular potentials shift differently, thereby changing ΔV. Figure 3.2 on the following page shows the position of the open channel and the bound states with increasing magnetic field, together with the resulting scattering length. Each time the energy of a bound state is slightly below the energy of the incoming channel, the scattering length diverges to positive infinity, only to return again from minus infinity slightly above. Far away from resonance the scattering length returns to the value a_{nr} of the $\mathcal{P}$-state alone. The strength of the coupling between the two involved states determines the width of the Feshbach resonance. The width of a Feshbach resonance is defined as the difference between the positions where the scattering length diverges and where it crosses zero. Also shown in the lower figure is the Landau-Zener behavior of the energy levels, i.e. in the diagonalized basis.

Alternative coupling schemes for inducing Feshbach resonances have been proposed. The use of radio frequency [156] and static electric fields [141] was suggested but never experimentally applied to control atomic interactions. Fedichev et al. [67] came up with the possibility to induce Feshbach resonances using optical fields, which was theoretically analyzed further in [18, 124]. To optically modify the scattering length, one can use laser light tuned close to a photo-association resonance which couples the continuum state of the incoming free atoms to an excited molecular level. So here the *external* laser-field is responsible for the coupling of the two states. The coupling also leads to an atomic loss, due to spontaneous decay via the molecular state. The

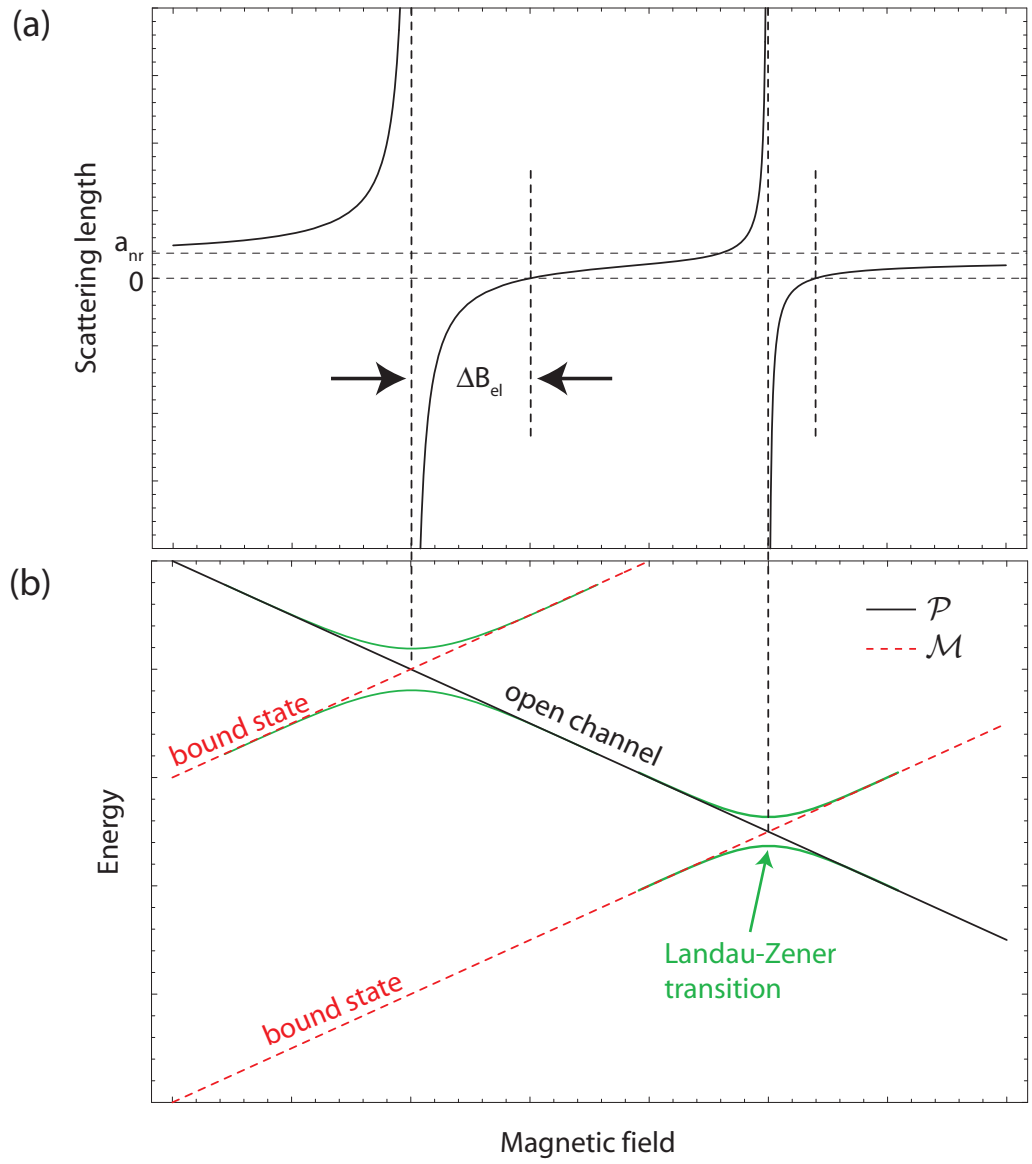

Figure 3.2: Magnetically induced Feshbach resonances. The upper plot (a) shows the behavior of the scattering length over the magnetic field, while the lower (b) shows the energy of the open channel and the bound states with increasing magnetic field. The scattering length diverges each time when a bound state crosses the open channel. Far away from resonance the scattering length returns to its non-resonant value a_{nr}. Due to the coupling between the open channel and the bound states a Landau-Zener transition allows to adiabatically transfer the atomic state of the two colliding atoms into a molecular state and back. The strength of the coupling is reflected by the width ΔB_{el} of the resonance which is defined as the difference between the positions where the scattering length diverges and where it crosses zero.

scattering length can be tuned by changing the frequency of the photo-association laser. The strength of the coupling, and thereby the width of the resonance can be changed through the laser intensity. Inducing Feshbach resonances with optical fields offers experimental advantages compared to magnetic fields. The intensity and frequency of optical fields can be rapidly changed. Furthermore, complex spatial intensity distributions can be easily produced which result in corresponding scattering length patterns across the sample. Experimentally this has been successfully demonstrated for Na by Fatemi et al. [66] and ^{87}Rb by Theis et al. [236].

3.2 Theoretical description

3.2.1 Formal solution

Here we will investigate a particularly elegant solution to the problem of *resonance scattering* which is due to Feshbach [70]. Originally devised to study nuclear collision processes, the Feshbach method can also be applied to atomic collisions.

Again the starting point is the Schrödinger equation which describes the collision of two atoms with the energy $E = \frac{\hbar^2 k^2}{2m_\mu}$

$$(\hat{H} - E)|\,\psi\,\rangle = 0\,, \tag{3.1}$$

where $\hat{H} = \hat{H}_0 + \hat{V}$. The potential operator now describes the incident scattering channel $\mathcal{P}$ and the closed[1] molecular channel $\mathcal{M}$ (see Fig. 3.2) and the coupling between those two channels[2]. We can now define two projection operators $\hat{\mathcal{P}}$ and $\hat{\mathcal{M}}$ that denote respectively, the projections onto the Hilbert subspace of the incident channel and the subspace of the (closed) molecular channels. For $\mathbf{r} \to \infty$ the collision process is solely described by the potential of the open channel $\mathcal{P}$, or using the operator formalism $\hat{\mathcal{P}}|\,\psi\,\rangle \xrightarrow[r\to\infty]{} |\,\psi\,\rangle$. In addition these projection operators satisfy the usual projection operator properties:

$$\hat{\mathcal{M}}\hat{\mathcal{P}} = \hat{\mathcal{P}}\hat{\mathcal{M}} = 0 \tag{3.2a}$$

$$\hat{\mathcal{M}}^2 = \hat{\mathcal{M}} \tag{3.2b}$$

$$\hat{\mathcal{P}}^2 = \hat{\mathcal{P}} \tag{3.2c}$$

$$\hat{\mathcal{M}} = 1 - \hat{\mathcal{P}}\,. \tag{3.2d}$$

The wave function $|\,\psi\,\rangle$ can now be decomposed according to

$$|\,\psi\,\rangle = \hat{\mathcal{M}}|\,\psi\,\rangle + \hat{\mathcal{P}}|\,\psi\,\rangle = |\,\psi_{\mathcal{M}}\,\rangle + |\,\psi_{\mathcal{P}}\,\rangle\,. \tag{3.3}$$

[1] This channel is closed because the energy of the colliding atoms is assumed to be smaller than the asymptotic value of the $\mathcal{M}$ channel.

[2] This means that $\hat{V}$ in the ($\mathcal{P}$,$\mathcal{M}$) basis contains off-diagonal elements.

Using this, we may write the Schrödinger Eq. (3.1) as

$$(\hat{H} - E)(\hat{\mathcal{P}} + \hat{\mathcal{M}})|\,\psi\,\rangle = 0\,. \tag{3.4}$$

Acting on this equation with $\hat{\mathcal{P}}$ and $\hat{\mathcal{M}}$ and using the projection operator properties (3.2) we get:

$$(\hat{H}_{\mathcal{P}\mathcal{P}} - E)|\,\psi_{\mathcal{P}}\,\rangle + \hat{H}_{\mathcal{P}\mathcal{M}}|\,\psi_{\mathcal{M}}\,\rangle = 0 \text{ and} \tag{3.5a}$$

$$(\hat{H}_{\mathcal{M}\mathcal{M}} - E)|\,\psi_{\mathcal{M}}\,\rangle + \hat{H}_{\mathcal{M}\mathcal{P}}|\,\psi_{\mathcal{P}}\,\rangle = 0\,, \tag{3.5b}$$

where

$$\hat{H}_{\mathcal{P}\mathcal{P}} = \hat{\mathcal{P}}\hat{H}\hat{\mathcal{P}},\ \hat{H}_{\mathcal{M}\mathcal{M}} = \hat{\mathcal{M}}\hat{H}\hat{\mathcal{M}},\ \hat{H}_{\mathcal{P}\mathcal{M}} = \hat{\mathcal{P}}\hat{H}\hat{\mathcal{M}},\ \hat{H}_{\mathcal{M}\mathcal{P}} = \hat{\mathcal{M}}\hat{H}\hat{\mathcal{P}}\,. \tag{3.6}$$

The two Eqs. (3.5) may be decoupled by formally solving Eq. (3.5b) using Green's operator $\hat{G}^{(+)}_{\mathcal{M}\mathcal{M}} = \frac{1}{E - \hat{H}_{\mathcal{M}\mathcal{M}} + i\epsilon}$ for $|\,\psi_{\mathcal{M}}\,\rangle$:

$$|\,\psi_{\mathcal{M}}\,\rangle = \hat{G}^{(+)}_{\mathcal{M}\mathcal{M}}\hat{H}_{\mathcal{M}\mathcal{P}}|\,\psi_{\mathcal{P}}\,\rangle\,, \tag{3.7}$$

and inserting this result into Eq. (3.5a), so that

$$(E - \hat{H}_{\mathcal{P}\mathcal{P}} - \hat{H}'_{\mathcal{P}\mathcal{P}})|\,\psi_{\mathcal{P}}\,\rangle = 0\,. \tag{3.8}$$

Here the term $\hat{H}'_{\mathcal{P}\mathcal{P}} = \hat{H}_{\mathcal{P}\mathcal{M}}\hat{G}^{(+)}_{\mathcal{M}\mathcal{M}}\hat{H}_{\mathcal{M}\mathcal{P}}$ represents an effective interaction in the $\mathcal{P}$ subspace due to transitions from that subspace to the $\mathcal{M}$ subspace, time evolution in the $\mathcal{M}$ subspace and a transition back to the $\mathcal{P}$ subspace.

Now let us imagine that we have solved the eigenvalue problem in the $\mathcal{M}$ subspace

$$\hat{H}_{\mathcal{M}\mathcal{M}}|\,\chi_{\mathcal{M},\nu}\,\rangle = \epsilon_\nu|\,\chi_{\mathcal{M},\nu}\,\rangle\,, \tag{3.9}$$

for all ϵ_ν, $|\,\chi_{\mathcal{M},\nu}\,\rangle$. Since the energy in our problem is below the excitation threshold, the eigenvalues ϵ_ν are discrete and the $|\,\chi_{\mathcal{M},\nu}\,\rangle$ are the bound states of the molecular potential. Due to the completeness of the set $|\,\chi_{\mathcal{M},\nu}\,\rangle$ in the $\mathcal{M}$ subspace we are allowed to write

$$\hat{\mathcal{M}} = \sum_\nu |\,\chi_{\mathcal{M},\nu}\,\rangle\langle\,\chi_{\mathcal{M},\nu}\,|\,. \tag{3.10}$$

This in turn allows us to write $\hat{H}'_{\mathcal{P}\mathcal{P}}$ using Eq. (3.2) as

$$\begin{aligned}
\hat{H}'_{\mathcal{P}\mathcal{P}} &= \hat{H}_{\mathcal{P}\mathcal{M}}\hat{G}^{(+)}_{\mathcal{M}\mathcal{M}}\hat{H}_{\mathcal{M}\mathcal{P}} = \\
&= \sum_\nu \hat{H}_{\mathcal{P}\mathcal{M}}\hat{G}^{(+)}_{\mathcal{M}\mathcal{M}}|\,\chi_{\mathcal{M},\nu}\,\rangle\langle\,\chi_{\mathcal{M},\nu}\,|\hat{H}_{\mathcal{M}\mathcal{P}} = \\
&= \sum_\nu \hat{H}_{\mathcal{P}\mathcal{M}}\frac{|\,\chi_{\mathcal{M},\nu}\,\rangle\langle\,\chi_{\mathcal{M},\nu}\,|}{E - \epsilon_\nu}\hat{H}_{\mathcal{M}\mathcal{P}}\,,
\end{aligned} \tag{3.11}$$

so that Eq. (3.8) becomes

$$\left(E - \hat{H}_{\mathcal{P}\mathcal{P}} - \sum_{\nu} \hat{H}_{\mathcal{P}\mathcal{M}} \frac{|\,\chi_{\mathcal{M},\nu}\,\rangle\langle\,\chi_{\mathcal{M},\nu}\,|}{E-\epsilon_\nu} \hat{H}_{\mathcal{M}\mathcal{P}}\right) |\,\psi_{\mathcal{P}}\,\rangle = 0\,. \tag{3.12}$$

If the resonances may be considered as isolated, so that the ϵ_ν are well separated from each other, it is clear that only one term of the sum, say $\mu = \nu$ will become large when E gets close to ϵ_μ. This particular term is now isolated

$$\left(E - \underbrace{\hat{H}_{\mathcal{P}\mathcal{P}} - \sum_{\nu\neq\mu} \hat{H}_{\mathcal{P}\mathcal{M}} \frac{|\,\chi_{\mathcal{M},\nu}\,\rangle\langle\,\chi_{\mathcal{M},\nu}\,|}{E-\epsilon_\nu} \hat{H}_{\mathcal{M}\mathcal{P}}}_{=\hat{H}_{\mathrm{nr}}\approx\hat{H}_{\mathcal{P}\mathcal{P}}}\right) |\,\psi_{\mathcal{P}}\,\rangle =$$

$$= \hat{H}_{\mathcal{P}\mathcal{M}} \frac{|\,\chi_{\mathcal{M},\mu}\,\rangle\langle\,\chi_{\mathcal{M},\mu}\,|}{E-\epsilon_\mu} \hat{H}_{\mathcal{M}\mathcal{P}} |\,\psi_{\mathcal{P}}\,\rangle\,. \tag{3.13}$$

$\hat{H}_{\mathrm{nr}}$ is that part of the effective Hamiltonian which varies slowly with energy and therefore gives rise to the non-resonant part of the scattering. To solve the last equation, we first consider the solution $|\,\chi_{\mathcal{P}}\,\rangle$ of the corresponding homogeneous equation, namely $(\hat{H}_{\mathcal{P}\mathcal{P}} - E)|\,\chi_{\mathcal{P}}\,\rangle = 0$ which describes non-resonant scattering. Let us now assume that we have been able to find outgoing spherical wave solutions of this equation, which we denote by $|\,\chi^{(+)}_{\mathcal{P}}\,\rangle$. We can now again formally solve Eq. (3.13) using Green's operator $\hat{G}^{(+)}_{\mathcal{P}\mathcal{P}} = \frac{1}{E-\hat{H}_{\mathcal{P}\mathcal{P}}+i\epsilon}$ and thus get

$$|\,\psi^{(+)}_{\mathcal{P}}\,\rangle = |\,\chi^{(+)}_{\mathcal{P}}\,\rangle + \hat{G}^{(+)}_{\mathcal{P}\mathcal{P}} \frac{\hat{H}_{\mathcal{P}\mathcal{M}}|\,\chi_{\mathcal{M},\mu}\,\rangle\langle\,\chi_{\mathcal{M},\mu}\,|\hat{H}_{\mathcal{M}\mathcal{P}}|\,\psi^{(+)}_{\mathcal{P}}\,\rangle}{E-\epsilon_\mu}\,. \tag{3.14}$$

The matrix element $\langle\,\chi_{\mathcal{M},\mu}\,|\,\hat{H}_{\mathcal{M}\mathcal{P}}\,|\,\psi^{(+)}_{\mathcal{P}}\,\rangle$ may be obtained by multiplying Eq. (3.14) from the left with $\langle\,\chi_{\mathcal{M},\mu}\,|\,\hat{H}_{\mathcal{M}\mathcal{P}}$ and then solving for $\langle\,\chi_{\mathcal{M},\mu}\,|\,\hat{H}_{\mathcal{M}\mathcal{P}}\,|\,\psi^{(+)}_{\mathcal{P}}\,\rangle$. Substituting this expression into Eq. (3.14) again, leads to

$$|\,\psi^{(+)}_{\mathcal{P}}\,\rangle = |\,\chi^{(+)}_{\mathcal{P}}\,\rangle + \hat{G}^{(+)}_{\mathcal{P}\mathcal{P}} \frac{\hat{H}_{\mathcal{P}\mathcal{M}}|\,\chi_{\mathcal{M},\mu}\,\rangle\langle\,\chi_{\mathcal{M},\mu}\,|\,\hat{H}_{\mathcal{M}\mathcal{P}}\,|\,\chi^{(+)}_{\mathcal{P}}\,\rangle}{E-(\epsilon_\mu+\Delta_\mu)+\frac{1}{2}i\Gamma_\mu}\,, \tag{3.15}$$

with

$$\Delta_\mu = \Re\langle\,\chi_{\mathcal{M},\mu}\,|\hat{H}_{\mathcal{M}\mathcal{P}}\hat{G}^{(+)}_{\mathcal{P}\mathcal{P}}\hat{H}_{\mathcal{P}\mathcal{M}}|\,\chi_{\mathcal{M},\mu}\,\rangle \text{ and} \tag{3.16}$$

$$\frac{1}{2}\Gamma_\mu = -\Im\langle\,\chi_{\mathcal{M},\mu}\,|\hat{H}_{\mathcal{M}\mathcal{P}}\hat{G}^{(+)}_{\mathcal{P}\mathcal{P}}\hat{H}_{\mathcal{P}\mathcal{M}}|\,\chi_{\mathcal{M},\mu}\,\rangle\,. \tag{3.17}$$

Finally we need to obtain the $\hat{T}$ Matrix. Using Eq. (3.5a) and the two-potential theorem[3] one ends up with the following expression

$$T_{\mathrm{fi}} = T_{\mathrm{fi}}^{(\hat{\mathcal{P}})} + T_{\mathrm{fi}}^{(\hat{\mathcal{P}}\hat{\mathcal{M}})} = \langle\, \phi_f^{(-)} \,|\, \hat{H}_{\mathcal{P}\mathcal{P}} \,|\, \chi_{\mathcal{P}}^{(+)} \,\rangle + \langle\, \chi_{\mathcal{P}}^{(-)} \,|\, \hat{H}_{\mathcal{P}\mathcal{M}} \,|\, \psi_{\mathcal{P}}^{(+)} \,\rangle\,. \tag{3.20}$$

Using Eq. (3.15) we retrieve the final result

$$T_{\mathrm{fi}}^{(\hat{\mathcal{P}}\hat{\mathcal{M}})} = \frac{\langle\, \chi_{\mathcal{P}}^{(-)} \,|\, \hat{H}_{\mathcal{P}\mathcal{M}} \,|\, \chi_{\mathcal{M},\mu} \,\rangle \langle\, \chi_{\mathcal{M},\mu} \,|\, \hat{H}_{\mathcal{M}\mathcal{P}} \,|\, \chi_{\mathcal{P}}^{(+)} \,\rangle}{E - (\epsilon_\mu + \Delta_\mu) + \frac{1}{2} i \Gamma_\mu}\,. \tag{3.21}$$

The last expression clearly exhibits a resonance behavior. We see that the term Δ_μ gives rise to a shift in the position of the resonance from ϵ_μ, while the quantity Γ_s controls the width of the resonance.

We are now interested in the asymptotic behavior of $\langle\, \mathbf{r} \,|\, \psi_{\mathcal{P}}^{(+)} \,\rangle$ (using $|\, \psi_{\mathcal{P}}^{(+)} \,\rangle$ from Eq. (3.15)) for $\mathbf{r} \to \infty$. By comparing the result with Eq. (2.32) we can directly infer the scattering phase $\delta_\ell(k)$ and the scattering matrix $S_\ell(k)$. Since in our application only s-wave scattering plays an important role and it greatly simplifies our calculations, we will limit us in the following to the case $l = 0$. We now investigate each term of

$$\lim_{\mathbf{r}\to\infty} \langle\, \mathbf{r} \,|\, \psi_{\mathcal{P}}^{(+)} \,\rangle = \lim_{\mathbf{r}\to\infty} \left(\langle\, \mathbf{r} \,|\, \chi_{\mathcal{P}}^{(+)} \,\rangle + \frac{\langle\, \mathbf{r} \,|\, \hat{G}_{\mathcal{P}\mathcal{P}}^{(+)} \hat{H}_{\mathcal{P}\mathcal{M}} \,|\, \chi_{\mathcal{M},\mu} \,\rangle \langle\, \chi_{\mathcal{M},\mu} \,|\, \hat{H}_{\mathcal{M}\mathcal{P}} \,|\, \chi_{\mathcal{P}}^{(+)} \,\rangle}{E - (\epsilon_\mu + \Delta_\mu) + \frac{1}{2} i \Gamma_\mu} \right), \tag{3.22}$$

separately. The first term can be directly expressed using Eq. (2.34) using a non-resonant scattering phase δ_{nr}. The second term is evaluated by expanding $\hat{G}_{\mathcal{P}\mathcal{P}}^{(+)}$ in eigenfunctions $|\, \chi_{\mathcal{P},\nu} \,\rangle$ of $\hat{H}_{\mathcal{P}\mathcal{P}}$

$$\begin{aligned} &\lim_{\mathbf{r}\to\infty} \langle\, \mathbf{r} \,|\, \hat{G}_{\mathcal{P}\mathcal{P}}^{(+)} \hat{H}_{\mathcal{P}\mathcal{M}} \,|\, \chi_{\mathcal{M},\mu} \,\rangle = \\ &\quad = \lim_{\mathbf{r}\to\infty} \sum_{\nu,\nu'} \langle\, \mathbf{r} \,|\, \chi_{\mathcal{P},\nu} \,\rangle \langle\, \chi_{\mathcal{P},\nu} \,|\, \hat{G}_{\mathcal{P}\mathcal{P}}^{(+)} \,|\, \chi_{\mathcal{P},\nu'} \,\rangle \langle\, \chi_{\mathcal{P},\nu'} \,|\, \hat{H}_{\mathcal{P}\mathcal{M}} \,|\, \chi_{\mathcal{M},\mu} \,\rangle = \\ &\quad = \lim_{\mathbf{r}\to\infty} \sum_{\nu} \langle\, \mathbf{r} \,|\, \chi_{\mathcal{P},\nu} \,\rangle \frac{1}{E - E_\nu + i\epsilon} \langle\, \chi_{\mathcal{P},\nu} \,|\, \hat{H}_{\mathcal{P}\mathcal{M}} \,|\, \chi_{\mathcal{M},\mu} \,\rangle\,. \end{aligned} \tag{3.23}$$

[3] The two-potential theorem is due to Gell-Mann and Goldberger [74]. Suppose one has the Hamiltonian $\hat{H} = \hat{H}_0 + \hat{V}_1 + \hat{V}_2$, with the equations

$$(E - \hat{H}_0) |\, \phi^{(\pm)} \,\rangle = 0 \tag{3.18a}$$

$$(E - \hat{H}_0 - \hat{V}_1) |\, \chi^{(\pm)} \,\rangle = 0 \tag{3.18b}$$

$$(E - \hat{H}_0 - \hat{V}_1 - \hat{V}_2) |\, \psi^{(\pm)} \,\rangle = 0 \tag{3.18c}$$

being satisfied. One can then prove that the transition matrix element for the complete Hamiltonian $\hat{H}$ is given by:

$$T_{\mathrm{fi}} = \langle\, \phi_f^{(-)} \,|\, \hat{T} \,|\, \phi_i^{(+)} \,\rangle = \langle\, \phi_f^{(-)} \,|\, \hat{V}_1 + \hat{V}_2 \,|\, \psi_i^{(+)} \,\rangle = \langle\, \phi_f^{(-)} \,|\, \hat{V}_1 \,|\, \chi_i^{(+)} \,\rangle + \langle\, \chi_f^{(-)} \,|\, \hat{V}_2 \,|\, \psi_i^{(+)} \,\rangle\,. \tag{3.19}$$

The first term of this equation is again given by Eq. (2.34), so what remains to be calculated is $\langle \chi_{\mathcal{P},\nu} | \hat{H}_{\mathcal{PM}} | \chi_{\mathcal{M},\mu} \rangle$. Since we are again only interested in the asymptotic limit we find

$$\langle \chi_{\mathcal{P},\nu} | \hat{H}_{\mathcal{PM}} | \chi_{\mathcal{M},\mu} \rangle \approx \frac{e^{-i\delta_{\mathrm{nr}}}}{\sqrt{\Omega}} \underbrace{\int u(r) \hat{H}_{\mathcal{PM}} \chi_{\mathcal{M},\mu}(\mathbf{r}) d\mathbf{r}}_{=\alpha} = \frac{e^{-i\delta_{\mathrm{nr}}}}{\sqrt{\Omega}} \alpha \,. \tag{3.24}$$

where Ω represents the macroscopic volume to which the binary atom system is confined. Note that the de-Broglie wavelength $(2\pi/k)$ in our case $\mathbf{k} \to 0$, vastly exceeds the range L of the inter-atomic potential. So in a range $L < r < 1/k$ $u(r)$ can be approximated by $u(r) \approx 1 + \delta_{\mathrm{nr}}/kr \approx 1 - a/r$, so $u(r)$ and thus α are thus independent of the collision energy. Using this we get

$$\lim_{\mathbf{r}\to\infty} \langle \mathbf{r} | \hat{G}^{(+)}_{\mathcal{PP}} \hat{H}_{\mathcal{PM}} | \chi_{\mathcal{M},\mu} \rangle \approx \alpha \frac{1}{\Omega} \sum_{\nu} \langle \mathbf{r} | \chi_{\mathcal{P},\nu} \rangle \frac{u(r)}{E - E_\nu + i\epsilon} \,. \tag{3.25}$$

Using the same approximations $\langle \chi_{\mathcal{M},\mu} | \hat{H}_{\mathcal{MP}} | \chi^{(+)}_{\mathcal{P}} \rangle \approx \alpha^\dagger e^{i\delta_{\mathrm{nr}}}/\sqrt{\Omega}$ and thus

$$\begin{aligned} \lim_{\mathbf{r}\to\infty} \langle \mathbf{r} | \hat{G}^{(+)}_{\mathcal{PP}} \hat{H}_{\mathcal{PM}} | \chi_{\mathcal{M},\mu} \rangle \langle \chi_{\mathcal{M},\mu} | \hat{H}_{\mathcal{MP}} | \chi^{(+)}_{\mathcal{P}} \rangle \approx \\ \approx \frac{e^{i\delta_{\mathrm{nr}}}}{\Omega^{3/2}} |\alpha|^2 \sum_{\nu} \frac{u(r)}{E - E_\nu + i\epsilon} = -\frac{e^{2i\delta_{\mathrm{nr}}}}{\sqrt{\Omega}} \frac{e^{ikr}}{r} \gamma_\mu \quad \text{with} \quad \gamma_\mu = |\alpha|^2 \frac{m}{4\pi\hbar^2} \,, \end{aligned} \tag{3.26}$$

where in the last step we've converted the sum to an integral and evaluated it using the residue theorem. We've also introduced the *reduced width* γ_μ. The connection between the width of a resonance and γ_μ becomes obvious if one reformulates Eq. (3.17):

$$\begin{aligned} \frac{1}{2}\Gamma_\mu &= -\Im \langle \chi_{\mathcal{M},\mu} | \hat{H}_{\mathcal{MP}} \hat{G}^{(+)}_{\mathcal{PP}} \hat{H}_{\mathcal{PM}} | \chi_{\mathcal{M},\mu} \rangle = \\ &= -\Im \sum_{\nu} \langle \chi_{\mathcal{M},\mu} | \hat{H}_{\mathcal{MP}} | \chi_{\mathcal{P},\nu} \rangle \frac{1}{E - E_\nu + i\epsilon} \langle \chi_{\mathcal{P},\nu} | \hat{H}_{\mathcal{PM}} | \chi_{\mathcal{M},\mu} \rangle = \\ &= \sum_{\nu} \left| \langle \chi_{\mathcal{M},\mu} | \hat{H}_{\mathcal{MP}} | \chi_{\mathcal{P},\nu} \rangle \right|^2 \frac{\epsilon}{(E - E_\nu)^2 + \epsilon^2} \approx \\ &\approx |\alpha|^2 \frac{1}{\Omega} \sum_{\nu} \delta(E - E_\nu) = \\ &= \gamma_\mu k \,. \end{aligned} \tag{3.27}$$

Here we explicitly see, that the width of the Feshbach resonance is k-dependent.

Now we put everything together, by substituting Eqs. (3.26) and (2.34) into (3.23). We finally get for the asymptotic behavior of $\langle \mathbf{r} \,|\, \psi_{\mathcal{P}}^{(+)} \rangle$:

$$\begin{aligned}\lim_{\mathbf{r}\to\infty} \langle \mathbf{r} \,|\, \psi_{\mathcal{P}}^{(+)} \rangle &= \lim_{\mathbf{r}\to\infty} \langle \mathbf{r} \,|\, \chi_{\mathcal{P}}^{(+)} \rangle - \frac{1}{2ik\sqrt{\Omega}} e^{2i\delta_{\mathrm{nr}}} \frac{e^{ikr}}{r} \frac{i\Gamma_\mu/2}{E-(\epsilon_\mu+\Delta_\mu)+\frac{1}{2}i\Gamma_\mu} = \\ &= -\frac{1}{2ik\sqrt{\Omega}} \left(\frac{e^{-ikr}}{r} - e^{2i\delta_{\mathrm{nr}}} \left[1 - \frac{i\Gamma_\mu/2}{E-(\epsilon_\mu+\Delta_\mu)+\frac{1}{2}i\Gamma_\mu} \right] \frac{e^{ikr}}{r} \right) .\end{aligned} \tag{3.28}$$

By identifying the factor in square brackets with the scattering matrix $\hat{S}$ (see Eqs. (2.32) and (2.33)), we obtain

$$S = e^{-2ika_{\mathrm{nr}}} \underbrace{\left[1 - \frac{i\Gamma_\mu/2}{E-(\epsilon_\mu+\Delta_\mu)+\frac{1}{2}i\Gamma_\mu} \right]}_{=e^{-2ika_{\mathrm{r}}}} = e^{-2ik(a_{\mathrm{nr}}+a_{\mathrm{r}})} = e^{-2ika_{\mathrm{eff}}} , \tag{3.29}$$

where we used that $\delta_{\mathrm{nr}} = -ka_{\mathrm{nr}}$ and defined $a_{\mathrm{eff}} = a_{\mathrm{nr}} + a_{\mathrm{r}}$.

$$\begin{aligned} a_{\mathrm{eff}} &= a_{\mathrm{nr}} + \frac{1}{2k} \arctan\left(\frac{\Gamma_\mu(E-\epsilon_\mu-\Delta_\mu)}{(E-\epsilon_\mu-\Delta_\mu)^2+\Gamma_\mu^2/4} \right) = \\ &= a_{\mathrm{nr}} - \frac{\gamma_\mu}{\epsilon_\mu+\Delta_\mu-E} = \text{for } k\to 0 \\ &= a_{\mathrm{nr}} \left(1 - \frac{\Delta E_{\mathrm{el}}}{\epsilon_\mu+\Delta_\mu-E} \right) \quad \text{with} \quad \Delta E_{\mathrm{el}} = \frac{\gamma_\mu}{a_{\mathrm{nr}}} . \end{aligned} \tag{3.30}$$

One can see from the second line, that even though E and $\Gamma_\mu = 2\gamma_\mu k$ vanish for $k \to 0$, the effective scattering length a_{eff} tends to a well defined value.

From Eq. (3.30) we can see that the scattering length can be varied, if the energy of the bound state ϵ_μ can be varied relative to the incoming energy E of the colliding atoms. This can be achieved in different ways. The most common method is to apply a homogeneous magnetic field which shifts the energy of both channels $\mathcal{P}$ and $\mathcal{M}$ by different values. Near a resonance the "detuning" of both channels $\Delta E = \epsilon_\mu + \Delta_\mu - E$ can be expanded in a Taylor series around the resonance value B_0:

$$\Delta E(B) = \left. \frac{\partial \Delta E}{\partial B} \right|_{B=B_0} \times (B - B_0) + \cdots \quad . \tag{3.31}$$

Together with Eq. (3.30) the dependency of the scattering length on the magnetic field can be expressed as

$$a_{\mathrm{eff}} = a_{\mathrm{nr}}(1 - \frac{\Delta B_{\mathrm{el}}}{B - B_0}) \quad \text{with} \quad \Delta B_{\mathrm{el}} = \frac{\gamma_\mu}{a_{\mathrm{nr}} \partial \Delta E/\partial B|_{B_0}} . \tag{3.32}$$

The dependence of a_{nr} and γ_μ on the magnetic field is so weak, that it can be neglected for our purposes. One also sees that the width of the resonances is determined by the coupling strength between both channels given through ΔB_{el} and thus by Eq. (3.17). The width of a resonance can be directly seen in a plot of the scattering length over the B-field, it is the distance between the resonance position and the zero crossing of the scattering length (see Fig. 3.2).

3.2.2 Example: Square well potential

To get a more intuitive picture of a Feshbach resonance, it is helpful to consider an example. The derivation of this example is based on Duine and Stoof [60]. Building on the example of a square-well potential in section 2.6, we now use two square-well potentials,

$$V_{\mathrm{T,S}}(r) = \begin{cases} -V_{\mathrm{T,S}} & \text{if } r < R\,, \\ 0 & \text{if } r > R\,, \end{cases} \tag{3.33}$$

where $V_{\mathrm{T,S}} > 0$. Furthermore, we assume that the potentials are such that $V_{\mathrm{T}} < V_{\mathrm{S}}$ and V_{S} supports at least one bound state. The resulting potentials are shown in Fig. 3.3 on the next page.

We now introduce a coupling V_{C} between the two square-well potentials V_{T} and V_{S}. For the strength of the coupling we assume that $0 < V_{\mathrm{C}} \ll V_{\mathrm{T}}, V_{\mathrm{S}}, \Delta\mu B$. The Schrödinger Eq. (3.1) we need to solve, is given by

$$(\hat{H} - E)\vec{\Psi} = \begin{pmatrix} -\frac{\hbar^2\nabla^2}{2m} + V_{\mathrm{T}}(\mathbf{r}) - E & V_{\mathrm{C}} \\ V_{\mathrm{C}} & -\frac{\hbar^2\nabla^2}{2m} + \Delta\mu B + V_{\mathrm{S}}(\mathbf{r}) - E \end{pmatrix} \begin{pmatrix} \psi_T(\mathbf{r}) \\ \psi_S(\mathbf{r}) \end{pmatrix} = 0\,. \tag{3.34}$$

It is now again advisable to diagonalize the Hamiltonian $\hat{H}$ for $r < R$ ($\hat{H}^<$) and $r > R$ ($\hat{H}^>$) separately. $\hat{H}^<$ and $\hat{H}^>$ are given by[4]

$$\hat{H} = \begin{cases} \begin{pmatrix} 0 & V_{\mathrm{C}} \\ V_{\mathrm{C}} & \Delta\mu B \end{pmatrix} & \text{for } r > R, \\ \begin{pmatrix} -V_{\mathrm{T}} & V_{\mathrm{C}} \\ V_{\mathrm{C}} & \Delta\mu B - V_{\mathrm{S}} \end{pmatrix} & \text{for } r < R, \end{cases} \tag{3.35}$$

and can be diagonalized by using the following (unitary) matrix

$$Q(\theta) = \begin{pmatrix} \cos(\theta) & \sin(\theta) \\ -\sin(\theta) & \cos(\theta) \end{pmatrix}, \tag{3.36}$$

[4] Since the kinetic energy operator is diagonal in the internal space of the atoms, we can omit it here.

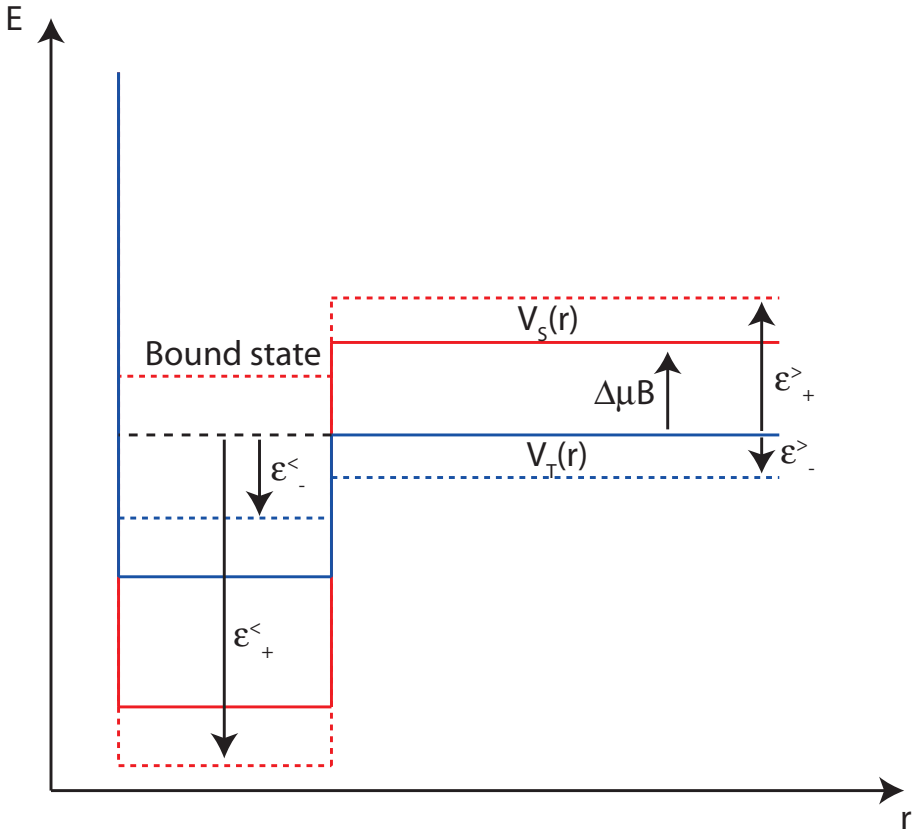

Figure 3.3: Feshbach resonance in a two-channel system with square-well interaction potentials. The solid lines indicate the singlet and triplet potentials when no coupling is present. Due to the Zeeman interaction with the magnetic field, the energy difference between the singlet and triplet potential is equal to $\Delta\mu B$. The dashed lines show how the potentials shift when a coupling is applied. The singlet potential supports a bound state which is responsible for the existence of the Feshbach resonance.

which gives

$$Q(\theta^{\gtrless})\hat{H}Q^{-1}(\theta^{\gtrless}) = \begin{cases} \begin{pmatrix} \epsilon_-^> & 0 \\ 0 & \epsilon_+^> \end{pmatrix} & \text{for } r > R \text{ using } \tan(2\theta^>) = -\frac{2V_\mathrm{C}}{\Delta\mu B}. \\ \begin{pmatrix} \epsilon_-^< & 0 \\ 0 & \epsilon_+^< \end{pmatrix} & \text{for } r < R \text{ using } \tan(2\theta^<) = \frac{2V_\mathrm{C}}{V_\mathrm{S}-V_\mathrm{T}-\Delta\mu B}. \end{cases} \tag{3.37}$$

The $\epsilon_\pm^{\gtrless}$ are given by

$$\begin{aligned} \epsilon_\pm^> &= \frac{\Delta\mu B}{2} \pm \frac{1}{2}\sqrt{(\Delta\mu B)^2 + (2V_\mathrm{C})^2} \text{ and} \\ \epsilon_\pm^< &= \frac{\Delta\mu B - V_\mathrm{T} - V_\mathrm{S}}{2} \mp \frac{1}{2}\sqrt{(V_\mathrm{S} - V_\mathrm{T} - \Delta\mu B)^2 + (2V_\mathrm{C})^2}\,. \end{aligned} \tag{3.38}$$

Physically, this means that due to the coupling of the singlet and the triplet potentials, the energies in the coupled basis are shifted. In Fig. 3.3 the dashed lines show the energies in the coupled basis. The square-well of the triplet potential gets shallower, while the singlet well depth increases, thereby shifting the position of the bound state and thus the resonance position. The solutions for the wave functions in the coupled basis $\uparrow\uparrow$, $\downarrow\downarrow$ are given by

$$\begin{pmatrix} u^{>}_{\uparrow\uparrow} \\ u^{>}_{\downarrow\downarrow} \end{pmatrix} = \begin{pmatrix} Ce^{ikr} + De^{-ikr} \\ Fe^{-\kappa r} \end{pmatrix} \text{ and } \begin{pmatrix} u^{<}_{\uparrow\uparrow} \\ u^{<}_{\downarrow\downarrow} \end{pmatrix} = \begin{pmatrix} A\sin(ik^{<}_{\uparrow\uparrow} r) \\ B\sin(ik^{<}_{\downarrow\downarrow} r) \end{pmatrix}, \tag{3.39}$$

where $\kappa = \sqrt{2m_\mu(\epsilon^{>}_{+} - \epsilon^{>}_{-})/\hbar^2 - k^2}$, $k^{<}_{\uparrow\uparrow} = \sqrt{2m_\mu(\epsilon^{>}_{-} - \epsilon^{<}_{-})/\hbar^2 + k^2}$, and $k^{<}_{\downarrow\downarrow} = \sqrt{2m_\mu(\epsilon^{>}_{-} - \epsilon^{<}_{+})/\hbar^2 + k^2}$. In order to determine the phase shift we have to join the solution for $r < R$ and $r > R$ smoothly. This is done most easily by transforming back to the singlet/triplet basis. Demanding the solution to be continuously differentiable leads to the equations:

$$\begin{aligned} Q^{-1}(\theta^{<}) \begin{pmatrix} u^{<}_{\uparrow\uparrow}(R) \\ u^{<}_{\downarrow\downarrow}(R) \end{pmatrix} &= Q^{-1}(\theta^{>}) \begin{pmatrix} u^{>}_{\uparrow\uparrow}(R) \\ u^{>}_{\downarrow\downarrow}(R) \end{pmatrix} \\ \frac{\partial}{\partial r} Q^{-1}(\theta^{<}) \begin{pmatrix} u^{<}_{\uparrow\uparrow}(r) \\ u^{<}_{\downarrow\downarrow}(r) \end{pmatrix}\Bigg|_{r=R} &= \frac{\partial}{\partial r} Q^{-1}(\theta^{>}) \begin{pmatrix} u^{>}_{\uparrow\uparrow}(r) \\ u^{>}_{\downarrow\downarrow}(r) \end{pmatrix}\Bigg|_{r=R}. \end{aligned} \tag{3.40}$$

These equations determine the coefficients A, B, C, D and F up to a normalization factor. Therefore, also the phase shift and the scattering length is given. Normally one determines A through the incoming probability current[5] $J = \hbar k/m|A|^2$, and solves for the remaining variables. An analytic solution for the scattering length (see Eq. (2.54)) is possible, but the resulting expression is rather formidable and is thus omitted here. The resulting dependence of the scattering length on the magnetic field is shown in Fig. 3.4 on the following page for $V_\mathrm{S} = 10\,\hbar^2/2m_\mu R^2$, $V_\mathrm{T} = 1\,\hbar^2/2m_\mu R^2$, $V_\mathrm{C} = 0.1\,\hbar^2/2m_\mu R^2$ and $E = 1 \cdot 10^{-5}\,\hbar^2/2\mathrm{m}_\mu\mathrm{R}^2$. The resonant behavior is due to the energy of the bound state of the singlet potential V_S becoming comparable to the incoming energy. Using Eq. (2.60) to determine the binding energy of a square-well potential of depth V_S gives $E_\mu \approx 4.6242\,\hbar^2/2\mathrm{m}_\mu\mathrm{R}^2$, which is approximately the position of the resonance in Fig. 3.4. As we already know from the discussion in the previous section, the scattering length behaves as expected by Eq. (3.30). The non-resonant scattering length a_nr is approximately equal to the scattering length expected from Eq. (2.56) for $V_\mathrm{T} = 1\,\hbar^2/2\mathrm{m}_\mu\mathrm{R}^2$ which gives $a_\mathrm{nr} = -0.5574\,{}^1\!/_\mathrm{R}$.

Next, we calculate the energy dependency of the molecular state state on the magnetic field. In the absence of the coupling between the open and closed channel, we simply have that $\epsilon_\mu = E_\mu + \Delta\mu B$. Here, E_μ is the energy of the bound state responsible for the Feshbach resonance, that is determined by Eq. (2.60) for a single square-well.

[5] The incoming plane wave cannot be normalized.

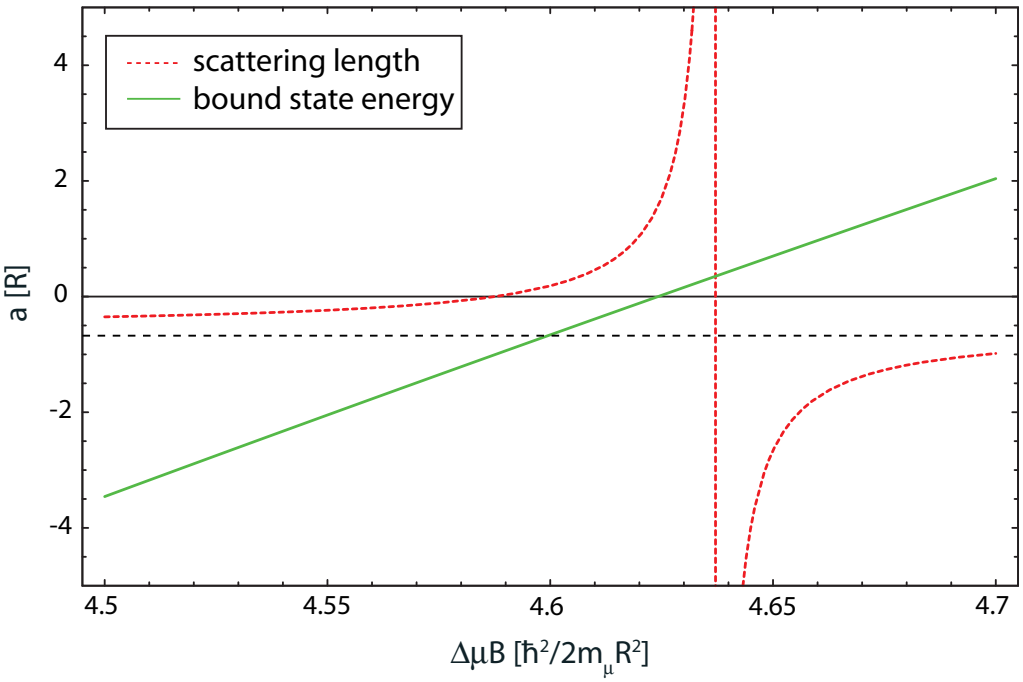

Figure 3.4: Scattering length for two coupled square-well potentials and energy of the corresponding bound state (scaled by a factor of 20) as a function of $\Delta\mu B$. The dotted line shows the background scattering length $a_{\mathrm{nr}} = -0.5574\,{}^{1}/_{\mathrm{R}}$ which results from the triplet potential alone. While the resonance occurs at approx. $4.6371\,\hbar^2/2m_\mu R^2$, the bound state is degenerate with the incoming energy at about $4.6242\,\hbar^2/2m_\mu R^2$. The depth of the triplet and singlet channel potentials is $V_{\mathrm{T}} = 1\,\hbar^2/2m_\mu R^2$ and $V_{\mathrm{S}} = 10\,\hbar^2/2m_\mu R^2$, respectively. The coupling is $V_{\mathrm{C}} = 0.1\,\hbar^2/2m_\mu R^2$.

This bound-state energy as a function of the magnetic field is shown as a dashed line in Fig. 3.5. A non-zero coupling drastically changes this result. To calculate the bound-state energy with the coupling present, we solve the Schrödinger Eq. (2.10) for negative energy. Here we change Eqs. (3.39) accordingly and again require the solution to be continuously differentiable at R (see Eq. (3.40)). Since we are looking for bound states, Eq. (3.40) can only be solved for energies where a bound state is present. To retrieve these energies, one writes Eq. (3.40) in the form $Mx = 0$, where $x = (A, B, C, D)$[6]. This equation only has solutions when $\det(M) = 0$, which can be solved for the energies of the bound states. The position of the bound state over the applied magnetic field is shown as a solid line in Fig. 3.5. As expected already from our previous derivation Eq. (3.30) the position of the resonance is shifted compared to the case without coupling. Additionally, the dependence of the bound-state energy

[6] In this case, there are only four constants for the wave functions, because for $r > R$ all wave functions decay exponentially for $E < 0$.

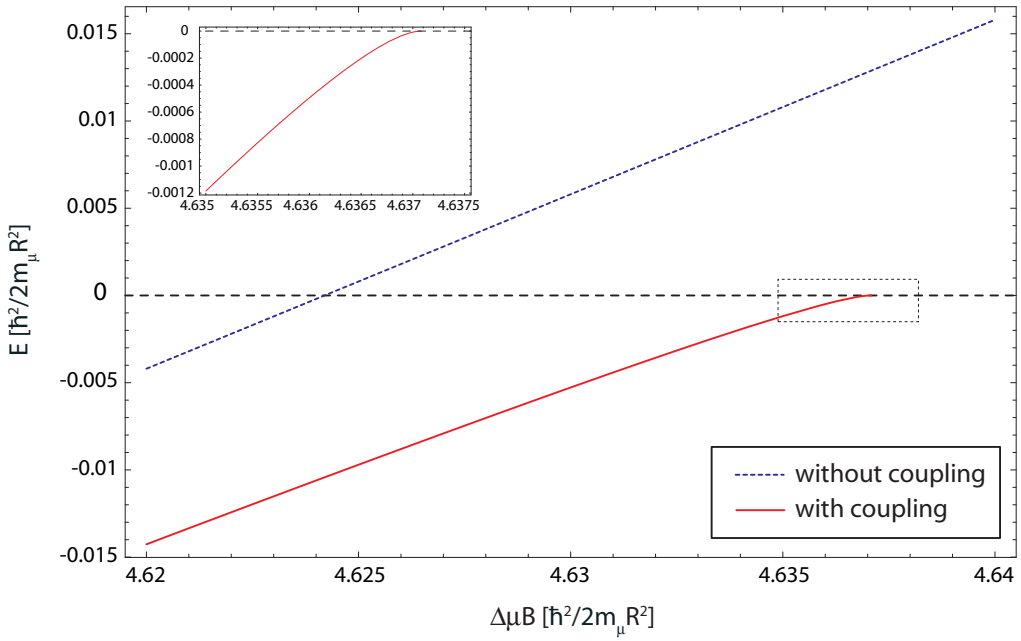

Figure 3.5: Bound-state energy of the molecular state near a Feshbach resonance for two coupled square-well interaction potentials. Shown are the results for $V_C = 0.1\,\hbar^2/2m_\mu R^2$ and for the uncoupled case. The inset is a close up of the crossing region. Here, due to the influence of the coupling an avoided crossing occurs. The parameters are the same as in Fig. 3.4.

on the magnetic field is no longer linear close to resonance, but quadratic as seen in the inset of Fig. 3.5. For fields above the resonance a bound state no longer exists and due to the coupling the molecule can now decay into two free atoms, because its energy is above the two-atom continuum threshold. Similar to the single-channel case, close to resonance the energy of the molecular state turns out to be related to the scattering length by

$$\epsilon_\mu(B) = -\frac{\hbar^2}{2m_\mu[a(B)]^2}\,. \tag{3.41}$$

This directly results from the T-Matrix, which has a pole at energy ϵ_μ [60].

To underpin the statement that a quasi-molecule is created in the bound state, we will look in the following at the probability density function of the bound state close to a resonance. As already explained earlier, we assume a constant incoming probability current, which thus determines the constant A. Using the solutions for $E > 0$ we can then determine the wave functions and occupation probabilities for all r. It is convenient to calculate the wave functions in the $\uparrow\uparrow$, $\downarrow\downarrow$ basis[7] for $r > R$,

[7] Since we use the unitary matrix from Eq. (3.36) for all basis transformations, the probability current is conserved.

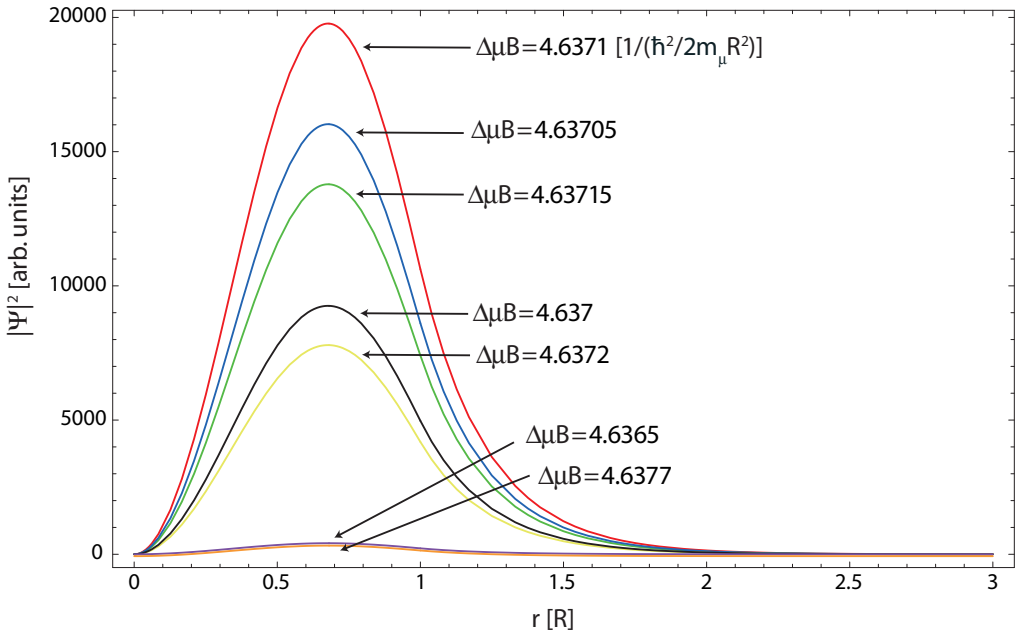

Figure 3.6: Resonantly enhanced occupation of a quasi-bound state for different magnetic fields close to resonance. The depicted wave function $u_{\downarrow\downarrow}$ was calculated in the $\uparrow\uparrow$, $\downarrow\downarrow$ basis for $r > R$, so the wave function decays exponentially for $r > R$. For magnetic field values close to the resonance value, the occupation of the quasi-bound state is two orders of magnitude higher, than already slightly off resonance. The parameters are again the same as in Fig. 3.4.

since in this basis the wave function[8] $u_{\downarrow\downarrow}$ will decay exponentially for $r > R$. In Fig. 3.6 the resulting probability density is plotted for magnetic fields around the resonance. It can be clearly seen that the probability density is resonantly enhanced close to the resonance, while already only a little bit off the resonance it sharply decays. This means in other words, that the probability for two atoms forming a (quasi-)molecule and thus populating the bound state is very high on resonance.

Finally, we investigate the dependence of the shift and the width of a resonance on the coupling. From Eq. (3.30) and the definition of γ_μ (3.26) we expect the width of the resonance ΔE_{el} to vary quadratically with the strength of the coupling. This is well reproduced in Fig. 3.7. It also shows the increasing shift of the resonance position with increasing coupling strength. In the limit of a weak coupling the resonance position coincides with the position of the bound state in a square-well potential.

[8]The wave function $u_{\downarrow\downarrow}$ is the only one we are interested in because it contains the bound state.

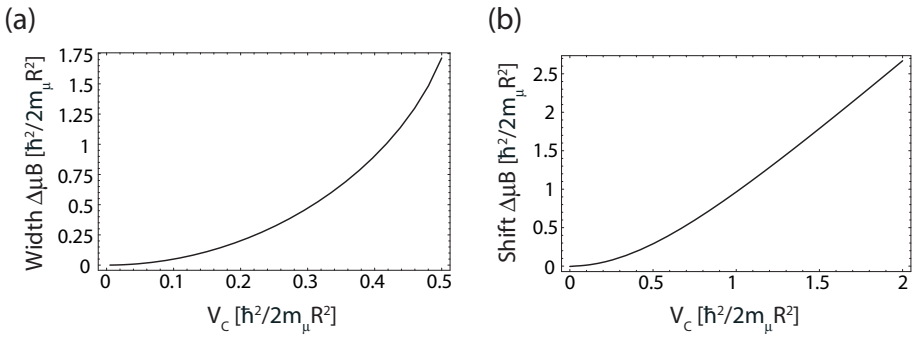

Figure 3.7: (a) Width of the position of the Feshbach resonance as function of the strength of the coupling. (b) Shift of the position of the Feshbach resonance as function of the strength of the coupling.

3.3 Multi-channel calculations

As was seen in the previous section, for the special case of two coupled square-well potentials we could solve the Schrödinger equation analytically. However, in the general case, which includes more than two coupled states and involves realistic potentials, we have to resort to numerical methods. Solving such coupled linear differential equations numerically is a problem found in all branches of physics and as such, extensive literature exists on the subject [182]. One can divide these numerical methods broadly into two categories, explicit (also called "propagators") and implicit approaches. Both approaches divide the domain of the independent variable into grids or sectors. Explicit methods require the value of the dependent variable at the previous grid point, to calculate the value at the next adjacent point. Examples of explicit methods are the algorithms from Numerov [168] and Gordon [79]. Implicit methods take not only the previous, but also the future values of the dependent variable into account. This approach leads to a large set of linear equations (or an eigensystem), which can be solved using linear algebra methods. One thus determines the value at all grid points simultaneously. A typical example for an implicit algorithm is the finite-elements method (FEM) [251]. Another example are methods which involve the representation of a continuous function by a finite set of sampling points, commonly called discrete variable representations (DVRs) [43, 135].

The different algorithms are compared in [186] regarding their accuracy and the required computing time for solving a coupled channel Schrödinger equation.

For the calculation of Feshbach resonance positions in ^{52}Cr two different methods have been used. The DVR method was employed to determine the position of the bound states in the absence of a coupling, while Gordon's method was used for the "full" scattering calculations which included the coupling between different scattering channels. So what follows is a closer look at these two methods.

3.3.1 Gordon's method

The method proposed by Gordon [79] is one of the most popular and well established methods, due to its intuitive and straightforward implementation. It is also accurate enough for most applications, even though it is inferior to other methods [186]. The method is thoroughly outlined in Gordan's lucid papers. Our description is based on the slightly modified method suggested by Mies [152].

Gordon's method solves the Schrödinger equation over some specified range of $\mathbf{r}$. The initial values for the propagation are given by the boundary conditions. The total range is now divided into a number of intervals $d\mathbf{r}$. Then the potential matrix $V(\mathbf{r})$ is approximated by an averaged constant potential in each interval $d\mathbf{r}$ and the resulting matrix is subsequently diagonalized. In the diagonalized interval $d\mathbf{r}$ the wave function is represented in each channel[9] n by $\Psi_n = A_n(\mathbf{r})\sin(\mathbf{k}_n\mathbf{r}) + B_n(\mathbf{r})\cos(\mathbf{k}_n\mathbf{r})$, and the vectors of the coefficients A and B are calculated by integrating a system of first-order coupled differential equations involving the difference between the true and the averaged potential matrix for $\mathbf{r}$ to $\mathbf{r} + d\mathbf{r}$. The diagonalization is then reversed to obtain the wave function and its first derivative at $\mathbf{r} + d\mathbf{r}$. This procedure is repeated and thus the solution is propagated toward some predetermined distance $\mathbf{r}_{\max}$. Consequently no large linear system needs to be evaluated in the Gordon algorithm and hence the method is not memory limited. The step size of each propagation is calculated on the fly according to an accuracy criterion. Closed channels are removed from the propagation when the corresponding amplitude of the channel wave function has become smaller than a threshold parameter. The influence of these components on the scattering properties of the asymptotically accessible channel is then negligible. The physical boundary conditions for the solution are obtained by first calculating N linear independent solutions from different initial slopes at the origin, and then constructing appropriate linear combinations of these solutions. For a bound state $\psi(\mathbf{r}_{\max}) = 0$ has to hold, while for a scattering state they must approach the asymptotic form given by Eq. (2.32). The resulting $\hat{S}$ matrix contains everything to predict the result of any scattering experiment.

3.3.2 Discrete variable representation (DVR)

The discrete variable representation approach to quantum-scattering is described in [43, 135, 136] and a nice review is given by Light and Carrington [134]. The description of this method is based on this review and [216].

[9] which are the solutions for the Schrödinger equation for a constant potential and positive local energy. If the local energy is negative then $\exp(\pm\mathbf{kr})$ is used instead. In the intervals where some of the local energies are negative, the undesired exponentially increasing functions are minimized by a "triangularization" method developed by Gordon.

Since we are interested in the calculation of the bound state energies, we only need to solve the Schrödinger equation in a finite interval $[0, r]$, as the bound state wavefunction decays exponentially at large distances. The smaller the binding energy of the bound state, the larger the interval has to be chosen. In a first step we choose a finite, n-dimensional, orthogonal basis for the Hilbert space which reflects the symmetry of the problem under consideration. This is called the finite basis representation (FBR), and the basis functions are usually orthogonal polynomials[10]. Commonly used are a trigonometric basis (Fourier-series), particle in a box states (i.e. Chebyshev polynomials), harmonic oscillator functions (Hermite polynomials), and Legendre or Laguerre polynomials. In our case particles in a box states are used, since they have the needed vanishing boundary conditions required for bound states. One could try to solve the whole problem in the FBR, but this would require to compute the matrix elements of the potential onto this basis, i.e. the numerical calculation of lots of integrals. The kinetic energy operator instead is usually simple to evaluate analytically in the FBR. For instance, on the trigonometric basis it is trivially diagonal. The problem of calculating the integrals of the potential on the FBR is bypassed by introducing a second basis set, the discrete variable representation (DVR).

The idea is to use Gaussian quadrature to evaluate these integrals[11] which leads to a new basis representation, the DVR. Harris et al. [97] showed that by diagonalizing the matrix representation of the position operator $\hat{x}$ in the FBR, the DVR can be constructed much more easily. The eigenvalues of the matrix U which diagonalizes $\hat{x}$ are the quadrature points, while the eigenvectors constitute the new basis set that defines the DVR.

These new basis functions, as they reduce the $\hat{x}$ position operator to diagonal form, look quite much like bell-shaped functions, centered around the quadrature points. The larger n, the more they will look like delta-functions. This is why one can approximate the matrix representing the potential on the DVR basis as being

[10] Generally the complete basis has an infinite number of basis functions. But since we are only interested in states up to a certain energy, we can restrict us to a finite basis.

[11] A quadrature rule is an approximation of the definite integral of a function, usually stated as a weighted sum of function values at specified points within the domain of integration. An n-point Gaussian quadrature rule, named after Carl Friedrich Gauss, is a quadrature rule constructed to yield an exact result for polynomials of degree $2n-1$, by a suitable choice of the n points x_i and n weights w_i such that

$$\int_a^b \omega(x) f(x)\, dx \approx \sum_{i=1}^{n} w_i f(x_i)\,. \tag{3.42}$$

It can be shown [182] that the evaluation points are just the roots of a polynomial belonging to a certain class of orthogonal polynomials depending on the choice of the weight function $\omega(x)$ and the integration interval $[a, b]$. Knowing the evaluation points, the associated weights are easily calculated [182].

diagonal, with elements equal to the potential evaluated at the quadrature points. The larger n, the better the approximation.

Of course the problem is now to express the kinetic energy in the DVR. This is easily done, because we know the orthogonal matrix U that diagonalizes $\hat{x}$. The matrix U is the orthogonal transformation that connects DVR and FBR:

$$T_{\mathrm{DVR}} = U \cdot T_{\mathrm{FBR}} \cdot U^T \,. \tag{3.43}$$

Now that we have expressed all parts of the Hamiltonian in the DVR, we just need to diagonalize the resulting matrix to get the energies and wave functions of the bound states.

3.4 Detecting Feshbach resonances experimentally

We have seen in the preceding parts of this chapter, that the scattering length a diverges on a Feshbach resonance. The remaining part of this chapter will be concerned with what methods we can use to determine the scattering length. The methods in question, can be roughly divided into three different categories, according to the physical quantity which is measured:

- Elastic collision rate

  Looking back at Chapter 2, we see that the elastic cross-section is directly related to the scattering length through Eq. (2.45) for vanishing k, and by Eq. (2.51) for small k. The elastic collision rate is then given by

  $$\Gamma_{\mathrm{coll}} = \bar{n}(t) < \sigma(v) v >_{\mathrm{therm}} \,, \tag{3.44}$$

  where $\sigma(v)$ is the velocity dependent s-wave elastic cross-section, $<\cdot>_{\mathrm{therm}}$ denotes thermal averaging and $\bar{n} = \int n^2(\mathbf{r}) dV / \int n(\mathbf{r}) dV$ is the mean density. A limited redistribution of energy in the collision process requires each atom to scatter more than once before an athermal atomic cloud reaches thermal equilibrium. The relaxation rate for this thermalization process can be related to the collision rate by $\Gamma_{\mathrm{coll}} = \alpha \Gamma_{\mathrm{rel}}$, where α is in general a temperature dependent factor [8, 119, 157, 160, 257]. The idea of the cross-dimensional rethermalization method is now to prepare an athermal atomic cloud, by adiabatically compressing the trap in only one direction. If this is done on a faster time scale than the collision rate, the temperature in the compressed direction will be higher, than in the other two. Due to elastic collisions the atomic cloud will relax to a new (higher) equilibrium temperature. From the measured relaxation rate it is then possible to determine the elastic cross-section and thus the magnitude of a, but not the sign, through Eq. (2.45)

[8, 17, 51, 106, 157, 161, 193, 196]. If one can measure the temperature dependence of the relaxation rate according to Eq. (2.51) it is also possible to determine the sign of a like for ^{52}Cr by Schmidt et al. [212]. In Chapter 4 we will shortly review this measurement and the obtained results, to be able to compare them to the values for the scattering length obtained in this thesis.

Another possibility to detect the variations in the scattering length a and thus σ_{el} is to allow atoms in the high-energy tail of the thermal distribution to leave a shallow trap. Elastic collisions again replenish these states, leading to a continued evaporation loss that is determined by the collision rate. Although this loss is a nonlinear function of the elastic cross section, it can still be used to find minima in σ_{el} (and accordingly a) with high precision. This method has been successfully applied for finding Feshbach resonances in Cs [36].

- Inelastic collision rate

  With increasing scattering length not only the probability for an elastic collision increases, but also the chances for three-body inelastic collisions go up. The recombination event rate can be parametrized as $\Gamma_{\mathrm{rec}} = \alpha n^3$, where α is the recombination constant and n is the density of the gas. Dimensional analysis under the assumption that a is bigger than the size of the atoms implies that

$$\alpha = C\frac{\hbar a^4}{m}\,. \tag{3.45}$$

  C is a dimensionless constant and generally consists out of two contributions. One contribution is from recombination into a shallow s-wave state, which is only possible for $a > 0$. For either sign of a, there can also be recombination into deep molecular bound states. The three-body recombination into the shallow bound state has been studied in [69, 163] and into the deep states in [13, 23, 64, 240]. These theoretical investigations predict values between 0 and 70 for C. A review of this topic is given by Braaten and Hammer [22].

  The three body loss rate is connected to the recombination rate, by n_l the number of atoms lost from the trap due to a three body collision:

$$L_3 = n_l\alpha = n_l C\frac{\hbar a^4}{m}\,. \tag{3.46}$$

  The value of n_l depends on the details of the experiment. In the recombination process, the molecular binding energy is set free as kinetic energy. Since the kinetic energy is large compared to the trapping potential depth, both molecule and the third atom are expelled from the trap, setting $n_l = 3$. However, the binding energy of the weakly bound last energy level of the dimer is given by Eq. (3.41), and at very large scattering length values the kinetic energy of the third atom may be below the trap depth and thus cannot escape. If

the potential of the atom trap does not confine the molecule, the dimer is lost and n_l=2. If, however, the molecule is trapped and stays within the atom cloud, it may quickly quench its high vibrational excitation in an inelastic collision with a fourth trapped atom. The large amount of energy released in this situation expels the collision partners, making $n_l = 3$. In either case, the kinetic energy of the remaining atom is distributed in the ensemble, giving rise to recombination heating.

Yurovsky and Ben-Reuven [262] use a different approach for modeling the three-body loss. They treat it as a two-stage reaction, using Breit-Wigner theory. The first stage is the formation of a resonant diatomic molecule, and the second one is its deactivation by inelastic collisions with other atoms. For a non-condensed atom sample, they obtain for α the following dependence

$$\alpha = \frac{36\pi\hbar^2 k_d \, |a_{\mathrm{nr}}\mu| \, \Delta}{m\left[\mu^2(B-B_0)^2 + \hbar^2\Gamma_e^2/4\right]}\,, \tag{3.47}$$

where k_d is the two body rate coefficient, a_{nr} the non-resonant cross-section, μ the difference of the magnetic momenta, Δ the Feshbach resonance width and Γ_e the resonance width for the formation of the molecule. Of special interest is here the dependence of α on the resonance width, i.e. the three-body loss rate is proportional to the width of the Feshbach resonance. A similar expression can be derived for a BEC [263], though the rate coefficient is six times smaller than the corresponding rate for the non-condensed case. This difference, due to the effects of quantum statistics, has been predicted [118] and observed in experiments [29].

Both theoretical approaches predict that the highest three-body loss rate occurs when the scattering length diverges. This has been experimentally verified with high accuracy for ^{87}Rb, where a discrepancy of only 60 mG was observed [242]. It is though justified to infer the location of a Feshbach resonance from the position of the maximum of the three-body loss rate.

- Thomas-Fermi radius of a Bose-Einstein condensate.

  Once a Bose-Einstein condensate has been created, the scattering length can be deduced from the measured density distribution of the BEC. If the thermal de-Broglie wavelength is on the order of the inter-particle separation and much larger than the potential range, the interaction between the condensate atoms can be described by an effective interaction $V_{\mathrm{eff}}(\mathbf{r}) = g\delta(\mathbf{r})$, where $\mathbf{r}$ is the particle separation and $g = 4\pi\hbar^2 a/m$ is the coupling constant [46]. The stationary Schrödinger equation including particle interactions becomes nonlinear and is called the *Gross-Pitaevskii equation* (GPE)

$$\left[-\frac{\hbar^2}{2m}\nabla^2 + V_{\mathrm{trap}}(\mathbf{r}) + g|\Psi(\mathbf{r})|^2\right]\Psi(\mathbf{r}) = i\hbar\frac{\partial}{\partial t}\Psi(\mathbf{r})\,, \tag{3.48}$$

where $\Psi(\mathbf{r})$ is the condensate wave function.

If we put a large enough number of atoms N_0 into the condensate, the repulsive interactions will dominate over the kinetic energy term of the GPE. This is the so called Thomas-Fermi regime [32]. The shape of the condensate density mirrors the trapping potential and is given for a harmonic trap by [121]

$$n(\mathbf{r}) = \frac{\mu}{N_0 g}\left(1 - \sum_{\alpha=x,y,z} \frac{r_\alpha^2}{R_\alpha^2}\right) \text{ where } R_\alpha^2 = \frac{2\mu}{m\omega_\alpha^2} = \frac{8\pi\hbar^2 a n_0}{m^2\omega_\alpha^2}\,, \tag{3.49}$$

μ is the chemical potential, ω_α are the trap frequencies and n_0 is the peak density. As can be clearly seen, the Thomas-Fermi radius depends on a. The main uncertainty in this measurement comes from the difficulty in determining the density accurately. For negative scattering lengths, the condensate is stable only below a critical number of atoms. From this instability, a value for the negative scattering length can be deduced.

Chapter 4

Chromium

This chapter will give a short overview over the physical, electronic and spectroscopic properties of chromium relevant to this work. I'll also shortly recapitulate the results of previous experiments conducted by our group, regarding the elastic and inelastic cross sections of ^{52}Cr.

4.1 General properties

The general scope of this project is the investigation of quantum statistical effects in bosons and fermions. A natural choice are two different isotopes of the same element. Chromium offers three bosonic (I=0) and one fermionic isotope (I=3/2) with high natural abundances. Table D.1 in Appendix D summarizes the natural abundance and nuclear spin for the stable chromium isotopes.

For operating a magneto-optical trap chromium vapor is necessary. At room temperature chromium is a very hard metal with a body-centered cubic crystalline structure. It has a very high melting point of 1850 °C. The boiling point is at around 2200 °C. Sublimation under vacuum conditions results in a vapor pressure of $6 \cdot 10^{-7}$ mbar at a temperature of 1500 °C [233], which is sufficient for operating a MOT.

For efficient laser cooling the spectroscopic properties of the considered atom are of importance. Figure 4.1 on the next page shows the relevant part of the level scheme for bosonic ^{52}Cr and fermionic ^{53}Cr. A more complete scheme can be found in Fig. D.1 on page 144. All bosonic isotopes share a similar level scheme, except for slightly different transition frequencies due to isotope shifts. This is contrasted by the fermionic isotope where each level splits up into four, due to the hyperfine interaction. We operate the Zeeman-slower and the magneto-optical trap on the strong transition connecting the ground state $^7S_3$ with the excited state $^7P_4$ in the blue at a wavelength of 425.555 nm[1]. Atoms in the excited ^{7}P manifold can undergo

[1] All wavelengths given in this thesis are vacuum wavelengths from [166], unless otherwise noted.

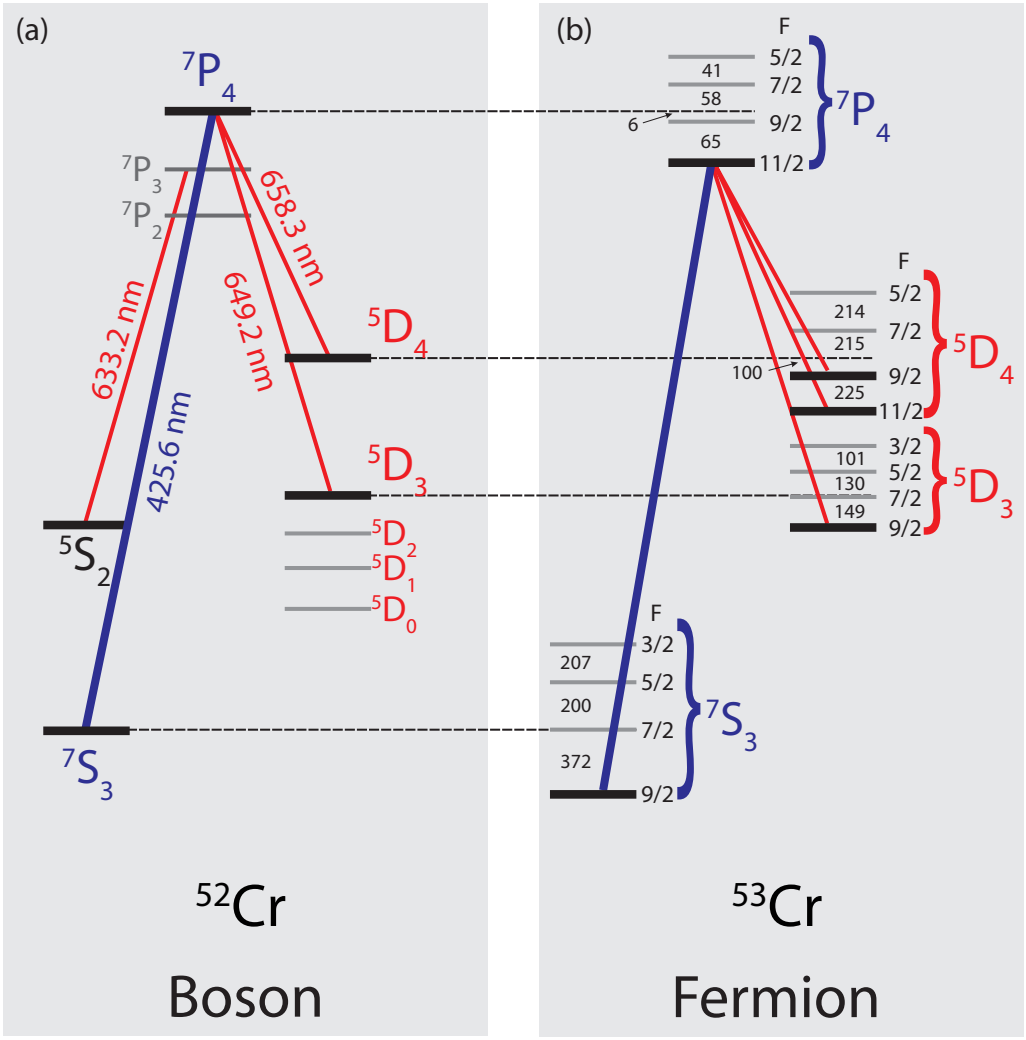

Figure 4.1: Part of the level schemes for (a) bosonic ^{52}Cr and (b) fermionic ^{53}Cr. Also shown are the relevant transitions together with their respective wavelength. The hyperfine-splittings and the shifts between the bosonic and fermionic isotope are given in MHz.

a transition to the metastable ^{5}D manifold via intercombination lines. Due to the high magnetic moment of the ^{5}D manifold states, atoms in these states are trapped in a magnetic trap (see Chapter 6.1.1). We use a repumper laser on the $^5D_4 \leftrightarrow {}^7P_3$ line to pump the atoms back into the ground state, since this transition is faster than the $^5D_4 \leftrightarrow {}^7P_4$ transition, and dark state resonances on the latter transition are absent [230]. One disadvantage is that the $^7P_3$ state can also decay into the $^5S_2$ state instead of the ground state $^7S_3$ with a branching ratio of 1:1000. For optical pumping the atoms from the m_s =+3 into the -3 state we use the transition $^7S_3 \leftrightarrow {}^7P_3$ with a wavelength of 425.600 nm. All relevant transitions for this work and their widths are summarized in Appendix D.

Compared to the alkalis, chromium has six valence electrons instead of one, which leads to a much more complicated electron configuration. In the ground state $^7S_3$, the electrons are in a hybridized $[Ar]3d^54s^1$ electronic configuration. The alignment of all electron spins leads to a strong magnetic moment in the $^7S_3$ ($6\mu_B$) ground and metastable $^5D_4$ ($6\mu_B$), $^5D_3$ ($4.5\mu_B$) states. This allows to build magnetic traps with a strong confinement, necessary for evaporative cooling. The large magnetic moment is also responsible for a very strong anisotropic spin-spin dipole interaction between two $^7S_3$ ^{52}Cr atoms. In fact, when compared to alkali-metal atoms, which have a maximum magnetic moment of 1 μ_B, it is 36 times stronger.

The number of electrons also has profound consequences on the complexity of ultracold elastic collisions, which will be seen in Chapter 6.

4.2 Elastic cross section measured in a magnetic trap

From the measurements of the Feshbach resonance positions for ^{52}Cr which are presented in Chapter 6 of this thesis, precise model potentials can be constructed which allow an exact determination of the $^{13,9,5}\Sigma_g^+$ scattering lengths. Our group already performed a scattering length measurement of the deca-triplet state $^{13}\Sigma_g^+$ of ^{52}Cr [209, 212] in a magnetic trap, employing the cross-dimensional relaxation method described in section 3.4. To compare both methods, the results of the cross-dimensional relaxation method will be summarized here. The latter was performed in a temperature range which covers almost two orders of magnitude to be able to not only give an absolute value for the scattering length, but to also determine the sign of the scattering length. Figure 4.2 on the next page shows the measured density normalized relaxation rate $\Gamma_{rel}/\bar{n}$ versus the mean temperature. Four theory curves are plotted together with the data. The blue lines are a fit of the thermal average $\Gamma_{rel} = \bar{n}(t) < \sigma(v)v >_{therm}$, where σ is given by the effective range approximation Eq. (2.51). The magnitude of the scattering length is most accurately determined from the low temperature elastic collisional properties. Thus for fitting we only considered data points below 25 μK. The fits were done once under the assumption

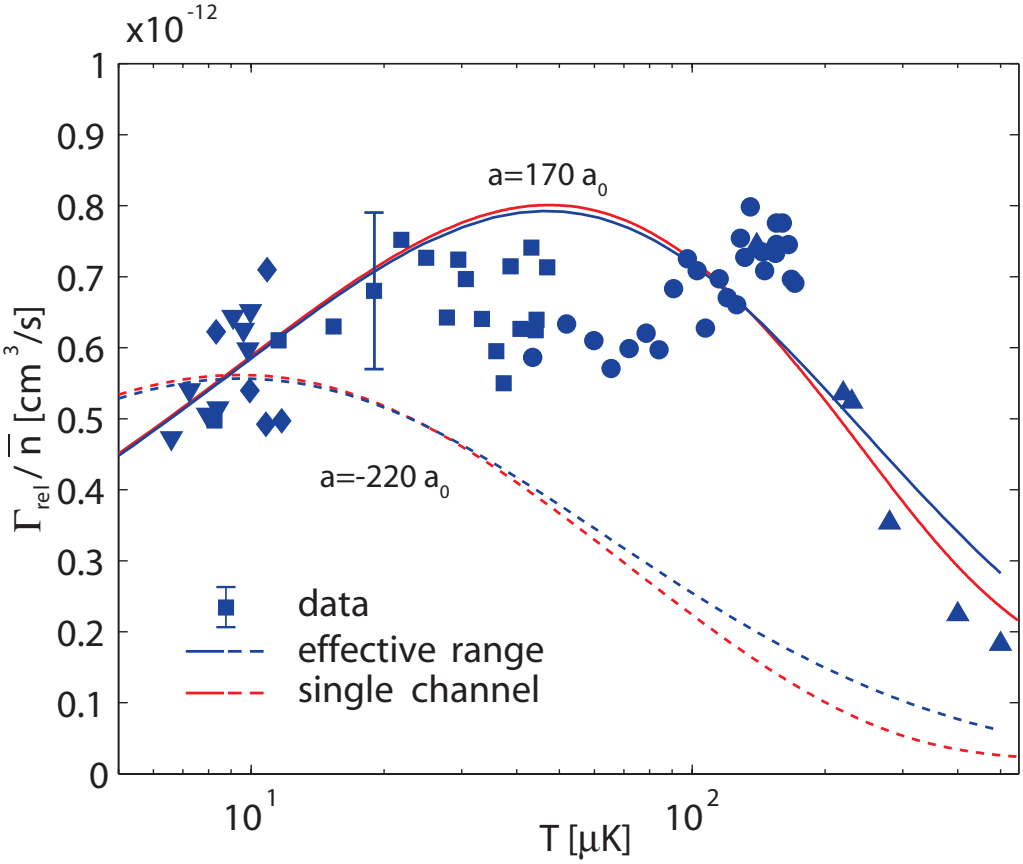

Figure 4.2: Temperature dependence of the density normalized relaxation rate for ^{52}Cr. The blue lines are a fit of $\Gamma_{\rm rel} = \bar{n}(t) < \sigma(v)v >_{\rm therm}$ to the data, while the red lines are numerical single channel calculations. The fits were done under the assumption of a positive/negative scattering length. They result in a positive scattering length of $a(^{52}\mathrm{Cr}) = 170 \pm 39\,\mathrm{a_0}$ and a negative scattering length of $a(^{52}\mathrm{Cr}) = -220\,\mathrm{a_0}$. The error bars are derived from statistical and calibration uncertainties. Data from different runs are labeled by the plot symbols [212].

of a positive and once for a negative scattering length. The reader clearly sees that the high energy tail of the curve for $a(^{52}\mathrm{Cr}) = 170 \pm 39\,\mathrm{a_0}$ follows the experimental data, in contrast to the best fit for a negative scattering length of $a(^{52}\mathrm{Cr}) = -220\,\mathrm{a_0}$. The red lines are the results of numerical single channel calculations using model potentials which exhibit the same scattering lengths.

We also investigated the deca-triplet scattering length of ^{50}Cr using the same method. In Fig. 4.3 we have plotted the results of the relaxation experiment for ^{50}Cr. All theory curves are obtained from numerical single-channel calculation. The solid curve is a fit to the ^{50}Cr data resulting in a scattering length of $a(^{50}\mathrm{Cr}) = 40 \pm 15\,\mathrm{a_0}$. For the

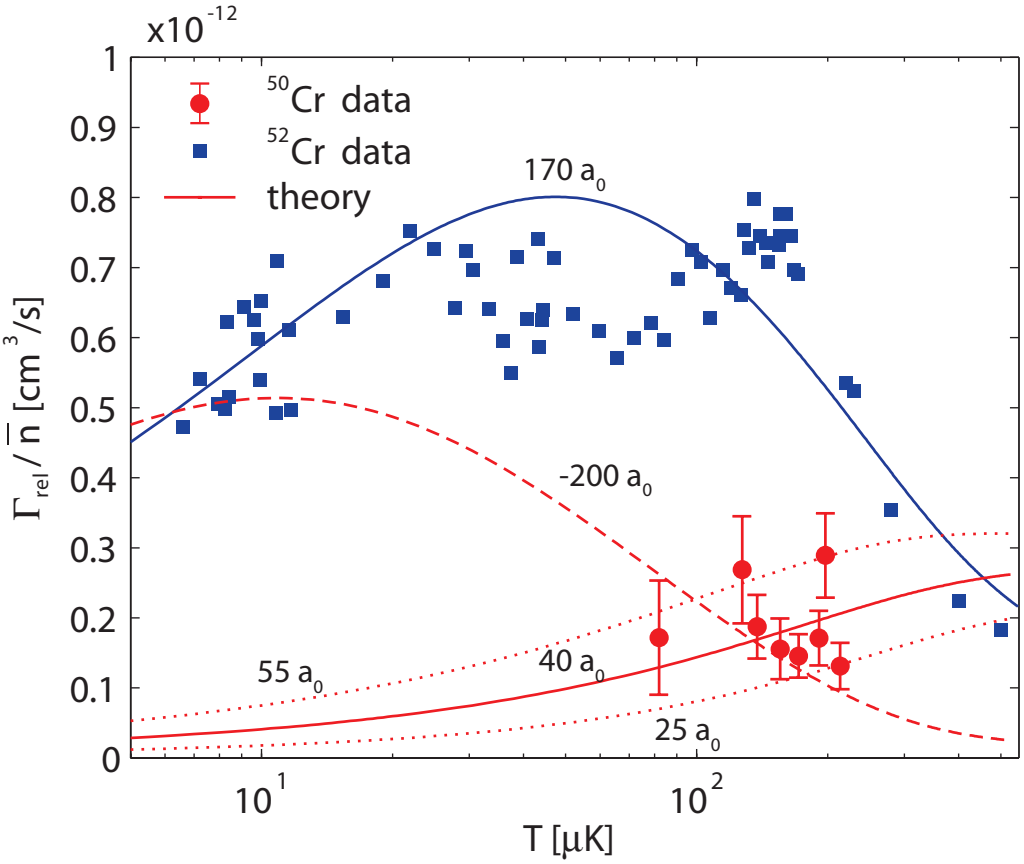

Figure 4.3: Density normalized cross-dimensional relaxation rates for ^{52}Cr (squares) and ^{50}Cr (circles). The red lines are plots with $a = 25\,a_0$, $40\,a_0$, $55\,a_0$ and $-200\,a_0$, respectively [212].

dashed curve, we have assumed a negative scattering length, where $a(^{50}\mathrm{Cr}) = -200\,a_0$ gave the best agreement with the data. The Cr_2 molecular potential constructed from C_6 and $a(^{52}\mathrm{Cr})$ can be used to obtain a scattering length for ^{50}Cr by mass scaling. We find that negative scattering lengths $a(^{50}\mathrm{Cr}) \approx -200\,a_0$ are not compatible with reasonable changes in our best potential, thus providing very strong evidence for a positive sign of $a(^{50}\mathrm{Cr})$.

4.3 Inelastic cross section measured in a magnetic trap

As a consequence of Maxwell's equations it is impossible to create a maximum of a static magnetic field in a region where external currents are absent. For this

reason atoms are usually magnetically trapped in the energetically highest Zeeman sub-level (weak-field-seeking state). The trap lifetime of these atoms is mainly limited by collisions. Aside from background gas collisions and three-body recombination, the atoms undergo spin-exchange and dipolar relaxation collisions. In contrast to spin-exchange collisions, in which the total spin is conserved, the spin is flipped in a dipolar relaxation process, since the dipole–dipole interaction does not preserve the total spin, but rather the total angular momentum. Therefore, if one considers a cloud of fully polarized ^{52}Cr atoms in the energetically highest state $m_s = +3$, only spin relaxation that does not conserve the total spin i.e. the dipolar relaxation, leads to atom loss from the magnetic trap. During a dipolar relaxation process either one or both colliding atoms can relax to the $m_s = +2$ state. The gained Zeeman-energy leads to heating of the atomic cloud. Furthermore, the existence of atoms in the $m_s = +2$ states opens new collision channels which now also include spin-changing collisions. Atoms whose energy exceeds the magnetic trap depth or which reach states with $m_s < +1$ are lost from the trap. Previous attempts to Bose-Einstein condense ^{52}Cr in a magnetic trap using evaporative cooling, showed that the dipolar relaxation limits the maximum attainable phase-space density in a magnetic trap to $\rho = 10^{-2}$ [100].

To be able to quantify the dipolar relaxation rate β_{dr} of ^{52}Cr our group measured the dependence of β_{dr} on the magnetic offset field using three different experimental methods [100, 102]. We find a typical dipolar relaxation rate constant of $\beta_{\mathrm{dr}} = 4 \cdot 10^{-12}\,\mathrm{cm^3/s}$ at a magnetic offset field of $B_0 = 1\,\mathrm{G}$. Thus, even at low magnetic fields, the loss coefficient for chromium is one order of magnitude larger than that reported for Cs in the lowest hyperfine level (F=3) [86] and another three orders of magnitude larger than that for Na [92]. The values predicted by a theoretical calculation [102] are in good agreement with the experimentally observed values. These findings are especially important for experiments that aim to produce high-density samples of atoms and molecules with high magnetic or electric dipole moments in magnetostatic or electrostatic traps [15, 247, 248]. Large inelastic two-body collision rates are to be expected with increasing dipole–dipole interaction. As has already been pointed out by Guéry-Odelin et al. [86], dipolar relaxation can be almost totally suppressed by polarizing the sample in the energetically lowest spin state, which requires different trapping schemes, for example optical dipole traps (see Chapter 5.4). In this state neither dipolar relaxation nor spin-exchange collisions are possible at a reasonable offset field. The only expected loss mechanisms in this case are three-body recombination and background gas collisions.

Chapter 5

Experimental setup and methods

Before covering the Feshbach experiments in detail in the next chapter, this chapter will give an overview of our experimental setup. Since the design and characterization of many parts of our setup were already the subject of earlier theses [83, 100, 209, 230, 250], the description will be kept very concise. For further details the cited references should be consulted. The optical dipole trap, the optical pumping laser system and the computer control system were not contained in earlier theses and are thus described more thoroughly.

5.1 The vacuum system

The ultra-high vacuum (UHV) system for our experiments consists out of three chambers, see Fig. 5.1. The core is the science chamber, where the atoms are captured, accumulated and manipulated. Right next to the science chamber the pumping chamber is attached. The lower oven-chamber (see Fig. 5.2) is attached through a 800 mm long Zeeman-slower to the science chamber. Using a high temperature effusion cell[1], chromium is sublimated at temperatures around 1873 K. We use commercially available chromium granulate[2] which is deposited in a CaO stabilized zirconium dioxide crucible[3], which in turn is placed inside a tungsten crucible[4]. This is necessary, because chromium forms a low-melting alloy with tungsten [233], while zirconium dioxide crucibles tend to react with the tantalum rods holding the crucibles (or even break). The crucibles are heated using tungsten wires. An aperture with a diameter of 1 mm, which is put into the crucible, collimates the chromium beam. This prevents that chromium is deposited onto the cooler molybdenum apertures

[1] VTS Schwarz GmbH, model HT-TA-35-10/W (special design)
[2] Chromium 99.99%, granulate 0.7-3.5 mm. Unaxis, Article Nr. BD481138-T
[3] Haldenwanger, special design
[4] VTS Schwarz, model W-T-HTC-UK-802

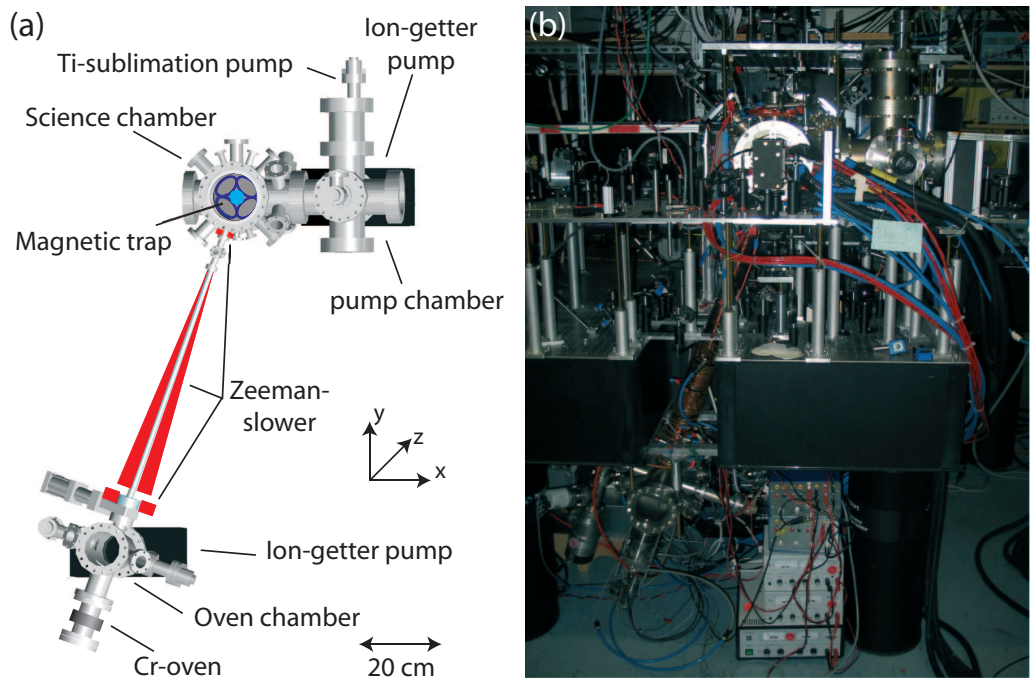

Figure 5.1: Setup of the ultra-high vacuum system. (a) CAD-Drawing of the vacuum chamber. Shown are the science- (top), pumping- (top right) and oven-chamber (bottom). The oven and the science chamber are interconnected by the Zeeman-slower. (b) Photo of the vacuum chamber setup. The chamber is surrounded by the necessary optics for the different required laser beams. Also easily spotted are the power cables and the cooling water tubes for the magnetic trap. See text for details.

above, which serve as heat shield. The chromium beam can be switched on and off in approximately 200 ms using a rotatable metal plate which is operated by a stepper motor through a mechanical feed-through. The vacuum in the oven chamber is maintained by an ion pump[5] at a pressure of around 10^{-10} mbar.

The velocity distribution for atoms coming out of the oven has a peak at around 950 m/s. A typical MOT has a capture velocity of approximately 30 m/s. To accumulate enough atoms in a MOT, the atoms need to be slowed down longitudinally. This is done using a spin-flip Zeeman-slower [83, 100, 230, 256]. The Zeeman-slower tube with an inner diameter of 1.5 cm also acts as a differential pumping stage. This allows a pressure difference between the oven and science chamber of more than two orders of magnitude [83].

The details of the science- and pumping-chamber are shown in Fig. 5.3. The pump-

[5] Varian, VacIon 75-Diode and MiniVac-Controller

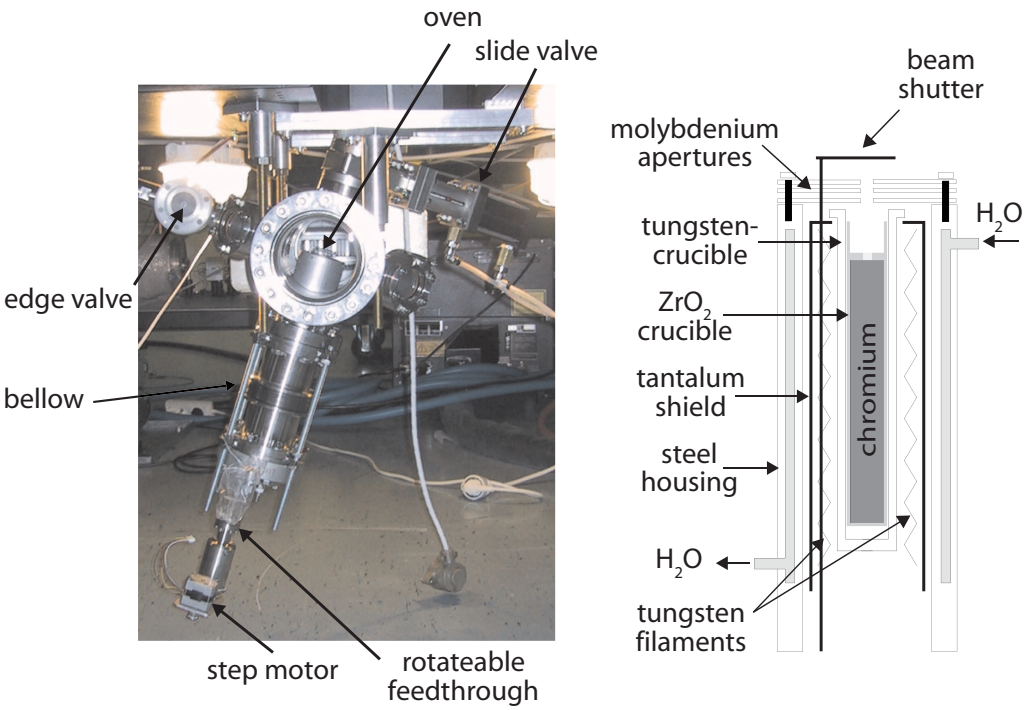

Figure 5.2: View of the realized oven chamber. (a) Photo of the complete oven chamber. (b) Schematic view of the high temperature effusion cell.

chamber is a 6-way vacuum cross, where an ion pump[6] and a Ti:sublimation[7] pump are attached. Both together yield a pressure below 10^{-11} mbar. This is also helped by the fact, that chromium itself is a very good getter material, so all surfaces coated by chromium will improve the vacuum. To create the initial vacuum a turbo-molecular pump can be attached to the 6-way cross through an edge valve. By doing away with mechanical pumps, we avoid vibrations and thus a heating of the atomic cloud.

The science chamber is dominated by two inverted CF160 flanges which are opposite to each other. These inverted flanges house the magnetic coil packets. The distance between the two inverted flanges is 26 mm. In the center of each inverted flange a glass window is mounted, allowing to shine in the z-beams. In star formation around the inverted flanges, two CF100 flanges and 10 smaller flanges can be found. One of the two big CF100 flanges connects to the pumping cross and one small flange interconnects with the Zeeman-Slower, while all the others are used for optical access through viewports. The purpose of each flange is found in Fig. 5.3. Additionally, there exist four CF40 supply flanges which are used for electrical feed-throughs (for the RF-coils) and a vacuum gauge[8].

[6] Varian, VacIon 75-Diode and MiniVac-Controller
[7] Varian TSP-cartridge
[8] Varian, UHV-24, range up to $1 \cdot 10^{-11}$ mbar

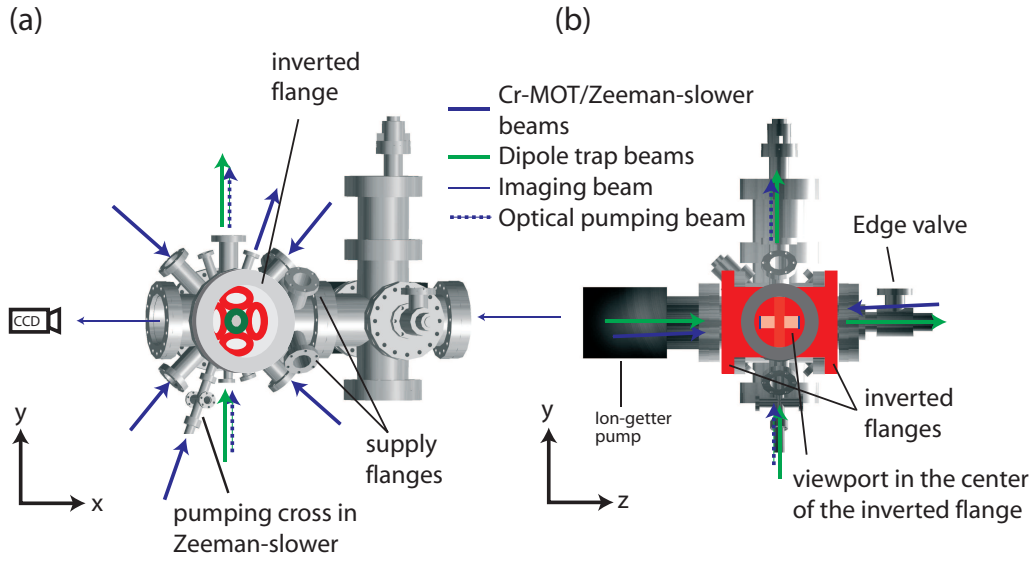

Figure 5.3: Details of the science-, and pumping chamber. (a) in z-direction, (b) in x-direction. Shown are the directions of the necessary trapping beams. See text for details.

5.2 The laser system

5.2.1 Cooling laser

For cooling and trapping of ^{52}Cr atoms the $^7S_3 \leftrightarrow {}^7P_4$ transition with a wavelength of 425.6 nm is used. The laser light for this transition is generated by frequency doubling the output of a Ti:sapphire-laser[9] which is in turn pumped by an Ar^+-ion laser[10] with a power of 16 W (see Fig. 5.4). A self-made external, pump beam resonant cavity using a brewster cut LBO crystal converts 2 W of fundamental power into approximately 300 mW of blue light. Further details about the design and characterization of the frequency doubling system can be found in my diploma thesis [250]. Since the brewster angle of the LBO crystal is only correct for the pumping light, approximately 19 % or 80 mW of the converted blue light is reflected at the exit face of the crystal. The light from this reflex is used for the imaging beam and the spectroscopy.

For actively stabilizing the blue laser light on the $^7S_3 \leftrightarrow {}^7P_4$ transition we use a Doppler-free polarization spectroscopy [53] on chromium gas (beam II), produced by a cold gas discharge in a chromium tube under an argon atmosphere [230]. By applying a magnetic field, the resonance frequency can be fine-tuned by Zeeman-shifting the transition energy. We achieve a long term stability of ≈ 1 MHz. The

[9] Coherent, model MBR-110
[10] Coherent, model Sabre 25 TSM, multi-line visible mode (MLVIS)

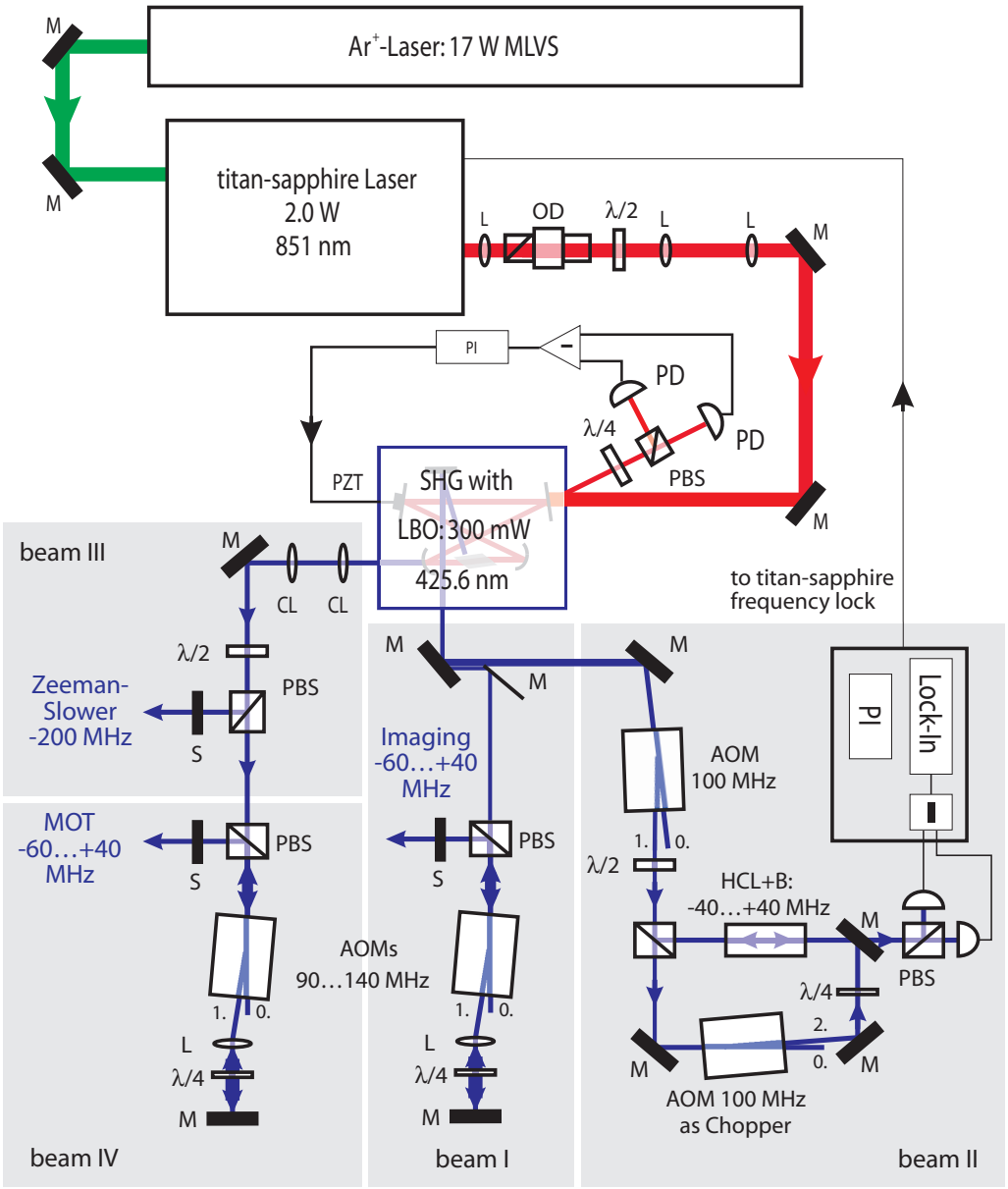

Figure 5.4: Sketch of the setup for the cooling laser system showing laser light generation, frequency stabilization (beam II) and beam preparation for absorption imaging (beam I), Zeeman-slower (beam III) and magneto-optical trap (beam IV). The frequencies of the beams are relative to the atomic resonance. L: lens, OD: optical diode, $\lambda/2$, $\lambda/4$: half and quarter-wave plate, respectively, M: mirror, PBS: polarizing beam splitter, PD: photo diode, PI: proportional-integral servo, PZT: piezo transducer, CL: cylindrical lens, S: mechanical shutter, AOM: acousto-optic modulator, HCL: hollow cathode lamp.

generated lock signal is fed back to the Ti:sapphire laser. Due to the additional AOMs in the spectroscopy setup the frequency of the laser light coming out of the frequency doubling cavity is 200 MHz red detuned to the atomic resonance. For the absorption imaging light a double-pass AOM and a VCO are used to shift the light back close to resonance and allow for fast switching (beam I). The imaging beam is coupled into a single-mode fiber to guide it to the science chamber. Using a fiber improves the transversal mode quality and beam pointing stability. The main fraction of the blue light ($\approx$ 120 mW) is allotted to the Zeeman-Slower beam (beam III), whose frequency is fixed to -200 MHz. The remaining power of 60 mW is used for the retro-reflected MOT beams (beam IV). Again a double pass AOM is used to allow for flexible frequency shifts of the MOT light by a few linewidths around the atomic resonance and also to control the power in the MOT beams.

5.2.2 Repumping laser

During laser cooling, atoms can decay from the $^7P_4$ state into the metastable $^5D_4$ and $^5D_3$ states instead of the ground state. Those atoms can be transferred back into the ground state by pumping them into the $^7P_3$ state, from which they then spontaneously decay with high probability into the ground state[11]. To achieve this, two commercially available diode laser systems[12] in Littrow configuration [192] have been set up. The setup is sketched in Fig. 5.5. The first diode laser system is resonant with the $^5D_3 \leftrightarrow {}^7P_3$ transition at a wavelength of 663.2 nm and provides a power of approximately 5 mW. Optionally, the power can be increased to 15 mW by injection locking to a slave laser. The second system is responsible for the $^5D_4 \leftrightarrow {}^7P_3$ transition at 654.0 nm. Both lasers are stabilized onto a 1 m long, passive Fabry-Perot reference cavity made out of Zerodur and Invar, using the Pound-Drever-Hall sideband modulation technique [59]. The resonator is evacuated and temperature stabilized, to minimize drifts. To obtain frequencies between two cavity fringes, double pass AOMs are used to shift the frequencies. We experience frequency drifts of about 2 $^{\mathrm{MHz}}/_{\mathrm{h}}$, which can be mostly attributed to temperature drifts. More details can be found in [101].

5.2.3 Optical pumping laser

To generate the laser light with a wavelength of 427.6 nm necessary for optical pumping on the transition $^7S_3 \leftrightarrow {}^7P_3$ a new laser system had to be set up. Since the required optical power necessary for optical pumping is below 1 mW, we decided

[11] There exists a probability of 1:1000 that the atoms decay into the metastable $^5S_2$, which can be neglected in our applications.
[12] Toptica, model DL100

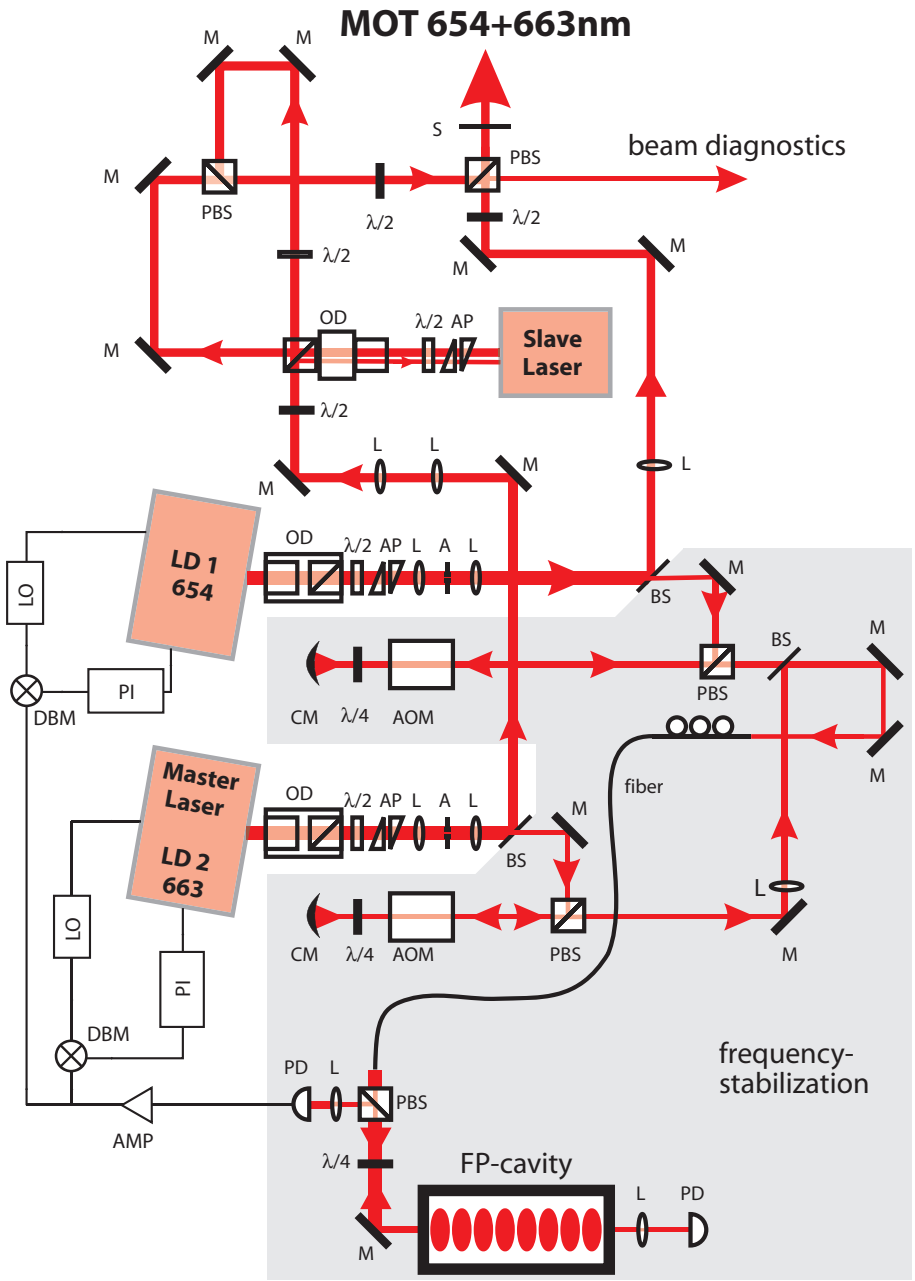

Figure 5.5: Sketch of the setup for the repumping laser system showing both master laser diode systems, the slave system for the 663 nm laser, frequency stabilization and beam preparation. L: lens, OD: optical diode, $\lambda/2$, $\lambda/4$: half and quarter-wave plate, M: mirror, CM: curved mirror, PBS: polarizing beam splitter, BS: beam splitter, PD: photo diode, LO: local oscillator, DBM: double balanced mixer, PI: proportional-integral servo, PZT: piezo transducer, CL: cylindrical lens, S: mechanical shutter, AOM: acousto-optic modulator.

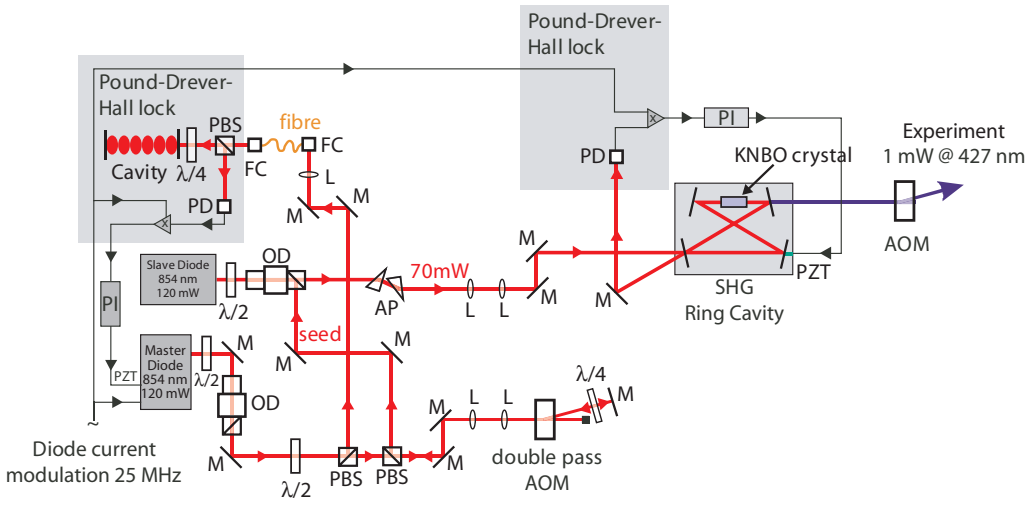

Figure 5.6: Sketch of the setup for the optical pumping laser system. Shown are the master/slave laser diode system which is frequency stabilized onto an external resonator and the SHG ring cavity using KNbO. L: lens, OD: optical diode, $\lambda/2$, $\lambda/4$: half and quarter-wave plate, respectively, M: mirror, PBS: polarizing beam splitter, PD: photo diode, PI: proportional-integral servo, PZT: piezo transducer, AOM: acousto-optic modulator, AP: anamorphic prism pair, FC: fiber coupler.

to build a frequency doubling resonator employing KNbO as non-linear material. KNbO is well suited for frequency doubling in the low power regime (output power below 200 mW). It has a very high non-linear coefficient (20.3 $^{\mathrm{pm}}/_{\mathrm{V}}$) and adverse effects like the high absorption coefficient for the fundamental and frequency doubled light which lead to a thermal lens or even BLIIRA[13] [138] only play a role in the high power regime. It is also not necessary to use a brewster cut crystal, since the circulating power in the resonator is typically below 1 W and thus the power density on the crystal surfaces is well below the damage threshold of the anti-reflection coating. To generate the necessary pump power, we use a self built master/slave laser-diode system using commercially available high power diodes[14]. The complete setup is shown in Fig. 5.6. The master laser-diode system is in Littrow configuration and stabilized also onto the Fabry-Perot resonator which is already used for the repumping laser system (see section 5.2.2). For stabilization we use again the Pound-Drever-Hall [59] stabilization technique. The necessary sidebands are generated by modulating the master laser-diode current. To tune the frequency arbitrarily between two cavity fringes, a double-pass AOM is shifting the frequency between the master and the slave diode laser. Approximately 70 mW of optical pumping power reach the frequency doubling resonator. Since the sidebands of the master laser system are

[13] Blue Light Induced Infrared Absorption
[14] Roithner Laser

also imprinted on the slave laser we can stabilize the frequency doubling resonator with the proven Pound-Drever-Hall technique. Phase-matching in the KNbO-crystal is achieved by tuning the temperature of the crystal. Due to non-optimal impedance matching and a very old KNbO crystal, the conversion efficiency is not optimal, but the output power of about 2 mW is sufficient for our purposes. The design of the frequency doubling resonator is described in [223], for similar setups see [146, 210]. To be able to switch the optical pumping laser on short timescales an AOM is used for switching, supplemented by a mechanical shutter.

5.3 The magnetic trap

For magnetically trapping ^{52}Cr atoms we have implemented a Ioffe-Pritchard (IP) trap [80, 183] in the cloverleaf configuration[15] [148]. All IP trap configurations produce a translationally invariant 2D quadrupole field in the radial direction and a quadratically increasing magnetic "curvature" field along the axial direction of the trap. The advantage of the cloverleaf configuration is that it offers 2π optical and mechanical access in radial direction, in contrast to the other trap types. Our coil setup is shown in Fig. 5.7 on the following page. Four pairs of cloverleaf coils generate the required radial gradient, while the two dipole coils produce the axial curvature. Cloverleaf and dipole coils are located in the same plane to achieve maximum radial gradient without scarifying axial curvature. The offset coils are placed behind the cloverleafs and produce an almost homogeneous field canceling the field of the dipole coils at the center of the trap. The actual shape of the cloverleaf coils is not circular but rather elliptical to fill the available space most efficiently. All coils are made out of hollow copper tubing to allow for water cooling. To mechanically fix the position of the coils, they were glued into a tightly fitting plastic form using two component low expansion epoxy glue. The resulting coil packets were then inserted into the reentrance buckets of the vacuum chamber. They are held in position by four screws from the backside. Table 5.1 lists the typical parameters of our magnetic trap. A detailed explanation of the magnetic trap design can be found in [83, 100]. To be able to compensate stray magnetic fields in all spatial directions three pairs of coils in Helmholtz configuration are used.

We use a power supply[16] with 16.8 V/300 A for the dipole and offset compensation coils which are connected in series to achieve common mode rejection of current noise. To generate the homogeneous offset field needed for observing the Feshbach resonances, we use an additional power supply 20 V/500 A over the pinch coils [17]. It is decoupled from the rest of the circuit through two diodes. For compensating

[15] Other configurations are the baseball trap [159], 4-Dee trap [98] and the QUICK-trap [65].
[16] Agilent technology, model HP 6682A
[17] Power Ten, model P63C-20500

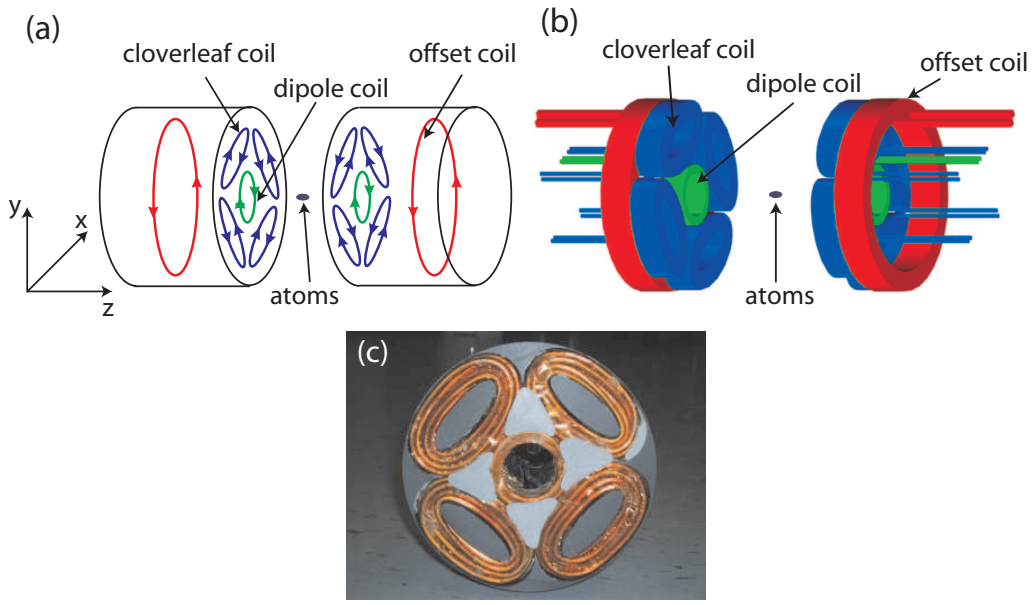

Figure 5.7: Coil setup for the cloverleaf magnetic trap. (a) Sketch of the coil configuration. Arrows indicate the direction of the current in the coils. (b) Rendered image of the implementation. Each dipole coil is surrounded by four clover-leaves. The offset coil is placed behind the leaves. (c) Photo of one coil package, before the coils were fixed into place using epoxy glue.

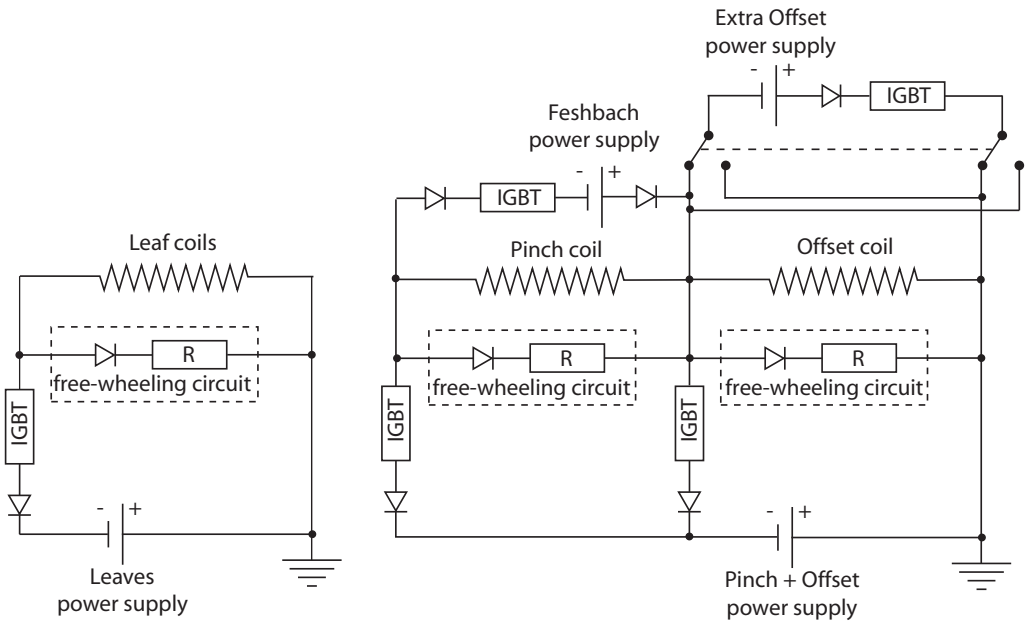

Figure 5.8: Electrical supply circuit for the magnetic coils.

Property	Value
radial gradient $\frac{\partial B'_r}{\partial I}$	0.67 G/(cmA)
maximum radial gradient B'_r at 300 A	201 G/cm
axial curvature $\frac{\partial B''_z}{\partial I}$	1.08 G/(cm^{2}A)
maximum axial curvature B''_z at 300 A	324 G/cm^2
instability points position z_{inst} at 300 A	0.62 cm
axial trap frequency at 300 A	73 Hz
radial trap frequency at 300 A and B_0 =1 G	808 Hz

Table 5.1: Calculated properties of our magnetic trap.

small offset fields a power supply [18] over the offset coils is used. The polarity of the power supply can be reversed to compensate fields in both directions. The cloverleafs are powered by a separate current supply[19] with 30 V/300 A. Fast switching of all the currents is accomplished by using IGBT's[20] and carefully designed free wheeling circuits. We achieve switching times below 50 μs. Residual eddy currents in the steel chamber can prolong the magnetic field switching time up to 5 ms. The complete electrical circuit is drawn in Fig. 5.8. The currents of all power supplies are set by the computer control through the analog inputs.

5.4 The dipole trap

5.4.1 Atom-light interaction

To understand the mechanisms behind an optical dipole trap we have to investigate how a two-level atom with ground state $|\,g\,\rangle$ and excited state $|\,e\,\rangle$ interacts with a monochromatic light field $\mathbf{E}(\mathbf{r},t) = \hat{\mathbf{e}}E_0(\mathbf{r})\cos(\omega_l t - \Phi(\mathbf{r}))$ of frequency ω_l, phase $\Phi(\mathbf{r})$, amplitude E_0 and polarization $\hat{\mathbf{e}}$. The electric field couples to the induced electric dipole moment $\mathbf{d}$ of the atom giving rise to an interaction term $H_{\mathrm{WW}} = -\mathbf{d}\cdot\mathbf{E}$. From this interaction term and by considering the spontaneous emission one can derive the time averaged force on a resting atom [41, 147, 151], which has two

[18] EA-PS 3016-10
[19] Power Ten, model P63D-30330
[20] Insulated Gate Bipolar Transistor, from Semikron

contributions: The conservative dipole force term arising from energy shifts of the atomic states in the light field (ac stark shift) is proportional to ∇I. The second contribution is the dissipative radiation pressure force and arising from momentum transfer of scattered photons. It is proportional to the phase gradient $\nabla\Phi$. As we are only interested in the dipole force, we will restrict the following discussion to it.

The dipole force shows a dispersive behavior. This can be understood in the classical Lorentz model [71, 112]. If the frequency of the laser field ω_l is lower (higher) than the transition frequency of the two-level system ω_a (i.e. the detuning $\delta = \omega_l - \omega_a$ is negative (positive)) the induced electric dipole and the driving electric field oscillate in phase (180° out of phase). For the induced dipole it is now energetically preferable to stay in regions of the light field with high (low) intensity. This classical derivation [85] gives the same results as a semi-classical [214] or even quantum-mechanical derivation [85] for the dipole potential U_{dip} and the scattering rate Γ_{sc}:

$$U_{\mathrm{dip}}(\mathbf{r},t) = -\frac{3\pi c^2\Gamma}{2\omega_a^3}\left(\frac{1}{\omega_a-\omega_l}+\frac{1}{\omega_a+\omega_l}\right) I(\mathbf{r},t) \tag{5.1}$$

$$\Gamma_{\mathrm{sc}}(\mathbf{r},t) = \frac{3\pi c^2\Gamma^2}{2\hbar\omega_a^3}\left(\frac{\omega_l}{\omega_a}\right)^3\left(\frac{1}{\omega_a-\omega_l}+\frac{1}{\omega_a+\omega_l}\right)^2 I(\mathbf{r},t), \tag{5.2}$$

Here the line-width of the two-level transition is denoted by Γ.

For $|\delta| = |\omega_l - \omega_a| \ll \omega_a$ the second term in the equations can be neglected (rotating-wave approximation) and one can set $\omega_l/\omega_a \approx 1$. This leads to

$$U_{\mathrm{dip}}(\mathbf{r},t) = -\frac{3\pi c^2}{2\omega_a^3}\left(\frac{\Gamma}{\delta}\right) I(\mathbf{r},t) \tag{5.3}$$

$$\Gamma_{\mathrm{sc}}(\mathbf{r},t) = \frac{3\pi c^2}{2\hbar\omega_a^3}\left(\frac{\Gamma}{\delta}\right)^2 I(\mathbf{r},t), \tag{5.4}$$

Obviously, a simple relation exists between the scattering rate and the dipole potential

$$\hbar\Gamma_{\mathrm{sc}} = \frac{\Gamma}{\delta}U_{\mathrm{dip}} \quad . \tag{5.5}$$

This means that while the dipole potential scales as I/δ, the scattering rate scales as I/δ^2. Therefore, optical dipole traps usually use large detunings and high intensities to keep the scattering rate as low as possible at a certain potential depth.

For a very far detuned laser $\omega_l \ll \omega_a$, both terms of (5.1) contribute with almost the same amount to the potential to give

$$U_{\mathrm{dip}}(\mathbf{r},t) = -\frac{3\pi c^2\Gamma_j}{\omega_a^4} I(\mathbf{r},t) = -\alpha_{\mathrm{DC}}\frac{I(\mathbf{r},t)}{2\epsilon_0 c} \tag{5.6}$$

This is a so called Quasi-electrostatic trap (QUEST). The trap depth just depends on α_{DC}, which is the static polarizability of the atom. In this case the scattering rate is given by:

$$\Gamma_{\mathrm{sc}}(\mathbf{r},t) = \frac{6\pi c^2 \Gamma^2 \omega_l^3}{\hbar \omega_a^8} I(\mathbf{r},t). \tag{5.7}$$

In real atoms all transitions which optically couple to the ground state need to be considered to calculate the resulting optical dipole potential. This is further complicated by the presence of a fine- or hyperfine-splitting. If $\delta \gg \Delta_{\mathrm{FS}} > \Delta_{\mathrm{HFS}}$ then the presence of the (hyper)fine structure can be ignored, otherwise the line strengths Γ have to be modified to include the square of the relevant Clebsch-Gordon-coefficients for the selected polarization [85]. The total potential and scattering rate is now given by the summation over all coupled states:

$$U_{\mathrm{dip}}(\mathbf{r},t) = -\sum_j \frac{3\pi c^2 \Gamma_j}{2\omega_j^3} \left(\frac{1}{\omega_j - \omega_l} + \frac{1}{\omega_j + \omega_l} \right) I(\mathbf{r},t) \tag{5.8}$$

$$\Gamma_{\mathrm{sc}}(\mathbf{r},t) = \sum_j \frac{3\pi c^2 \Gamma_j^2}{2\hbar \omega_j^3} \left(\frac{\omega_l}{\omega_j} \right)^3 \left(\frac{1}{\omega_j - \omega_l} + \frac{1}{\omega_j + \omega_l} \right)^2 I(\mathbf{r},t), \tag{5.9}$$

where the transition wavelengths are given by ω_j and the corresponding linewidths by Γ_j.

The fundamental source for heating in an optical dipole trap stems from the scattering of trap photons. In the far-detuned case considered here, the scattering is completely elastic. This means that the energy of the scattered photon is determined by the frequency of the laser and not of the optical transition. Both the absorption and the spontaneous re-emission processes contribute to the total heating. Both contributions add up to an increase of the total thermal energy by $2E_{\mathrm{rec}}$ (where $E_{\mathrm{rec}} = \hbar^2 k^2 / 2m$ is the recoil energy) in a time $1/\Gamma_{\mathrm{sc}}$[21]. The heating power is directly related to the photon scattering rate by

$$P_{\mathrm{heat}} = 2E_{\mathrm{rec}} \Gamma_{\mathrm{sc}} = k_{\mathrm{B}} T_{\mathrm{rec}} \Gamma_{\mathrm{sc}} \,. \tag{5.10}$$

Approximating the dipole trap by a power-law potential, allows one to apply the virial theorem and express the previous equation as a heating rate

$$\dot{T} = \frac{2/3}{1+\kappa} T_{\mathrm{rec}} \Gamma_{\mathrm{sc}} \,, \tag{5.11}$$

[21] This seems intuitively clear, but on closer examination one realizes that the absorption process is anisotropic (in the direction of the dipole trap beam), while the re-emission is isotropic. A rigorous derivation [85] shows that the longitudinal direction is heated on average by $4E_{\mathrm{rec}}/3$ per scattering process and $E_{\mathrm{rec}}/3$ for the two transversal directions. Since the trap mixes the motional degrees on a time scale faster than or comparable to the heating, one can thus use a simple global heating of $2E_{\mathrm{rec}}$ per scattering event.

describing the corresponding increase of temperature with time. κ is the ratio of the potential and the kinetic energy and depends on the trap type ($\kappa = 1$ for a 3D harmonic trap, $\kappa = 0$ for an ideal 3D box potential). Due to the finite trap depth of an optical dipole trap, this heating process will lead to increased evaporation and thus atom loss.

The simplest realization of an optical dipole trap[22] is to use a red detuned Gaussian beam. The intensity distribution of a Gaussian beam which propagates in z-direction with Power P is given by [203]

$$I(r,z) = \frac{2P}{\pi w^2(z)} \exp\left(-\frac{2r^2}{w^2(z)}\right) \tag{5.12}$$

$$w(z) = w_0 \sqrt{1 + \left(\frac{z}{z_R}\right)^2} \tag{5.13}$$

$$z_R = \pi w_0^2 / \lambda_l, \tag{5.14}$$

In the case of ^{52}Cr-atoms and light with a wavelength of 1064 nm, the dipole potential depth and the scattering rate are related to the intensity by

$$U_{\mathrm{dip}}(r,z) = 2.74 \cdot 10^{-37} \frac{\mathrm{Jm}^2}{\mathrm{W}} \cdot I(r,z) \qquad \text{and} \qquad \Gamma_{\mathrm{str}}(r,z) = 5.3 \cdot 10^{-12} \frac{\mathrm{m}^2}{\mathrm{Ws}} \cdot I(r,z)\,. \tag{5.15}$$

In the trap center the dipole potential is approximately harmonic with trap frequencies

$$\omega_r = \sqrt{\frac{4U_{\mathrm{dip}}(0,0)}{m w_0^2}} \qquad \text{and} \qquad \omega_z = \sqrt{\frac{2U_{\mathrm{dip}}(0,0)}{m z_R^2}}. \tag{5.16}$$

The ratio of the radial and axial trap frequencies is given by

$$\frac{\omega_r}{\omega_z} = \frac{\sqrt{2}\pi}{\lambda} w_0, \tag{5.17}$$

and is a direct consequence of relation (5.14) for the shape of a Gaussian beam.

5.4.2 Optical dipole trap for ^{52}Cr

In the case of chromium the relevant levels which can optically couple to the ground state are listed in Table 5.2 on page 72 (see Fig. D.1 on page 144 for the complete level scheme). Since the detuning δ is much bigger than the existing fine-structure splitting Δ_{FS} we can safely ignore it. Therefore we have a very simple $s \rightarrow p$ transition, see

[22] Other realizations are also common, see [85] for a review.

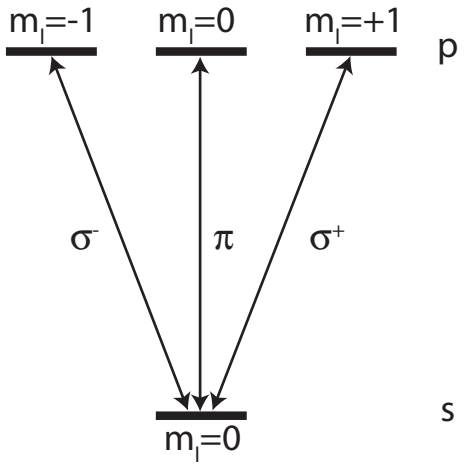

Figure 5.9: For very large detunings exceeding the fine-structure splitting $\delta \gg \Delta_{\mathrm{FS}}$ every transition listed in Table 5.2 reduces to a simple $s \rightarrow p$ transition. For any laser polarization it behaves like a two-level system.

Fig. 5.9. Such a transition behaves like a two-level atom with the full line strength for any laser polarization, and the ground state light shift is thus equal to the one of a two-level atom. The single ground state couples to the electronic spin in exactly the same way as it would do without light. In this simple case, all resulting magnetic sub-states acquire the light shift of the initial atomic s state.

Figure 5.10 shows the dependence of the depth of the dipole potential U_{dip} and the scattering rate Γ_{sc} on the trapping laser wavelength calculated according to Eq. (5.9), in the rotating wave approximation Eq. (5.4) and for the quasi electrostatic case Eq. (5.6). One clearly sees that the counter-rotating term in Eq. (5.9) cannot be neglected for very far detuned dipole traps.

5.4.3 Setup

The optical dipole trap is made up by two Gaussian beams of a Yb-fiber laser[23]. Such lasers can be bought in a wave-length range from 1030 nm to 1120 nm. We opted for a laser running at 1064 nm since this allows one to work with cheap, off the shelf optics for Nd:YAG lasers. The laser emits up to 20 W of linear polarized light with a beam quality $M^2 < 1.1$. Power fluctuations are specified to be <2.5% (rms) for a range of 1 kHz—20 MHz or <3% for the long-term stability. The line-width of the laser is $\Delta\lambda = 1.65$ nm from which the coherence length can be calculated to be $\lambda_c = \lambda^2/\Delta\lambda = 0.7$ mm. A longer coherence length would lead to the existence of

[23] IPG Photonics, PYL-20W-LP

transition	vacuum wavelength λ [nm]	Γ [$10^8\,\mathrm{s}^{-1}$]
a^7S-z^7P	427.193	$3.13 \cdot 10^{-1}$
a^7S-z^5P	373.364	$1.3 \cdot 10^{-3}$
a^7S-y^7P	359.198	1.52
a^7S-y^5P	336.517	$8.9 \cdot 10^{-4}$
a^7S-x^7P	236.707	$5.7 \cdot 10^{-2}$
a^7S-w^7P	209.664	$1.1 \cdot 10^{-2}$

Table 5.2: Possible optical transitions from the $^7S_3$ ground state for ^{52}Cr [166]. The transition a^7S-y^7P is the only other relevant transition besides the cooling transition at 427 nm. The contributions of the other transitions to the optical potential U_{dip} and the scattering rate Γ_{sc} can be safely neglected. All values given here are multiplett averaged values.

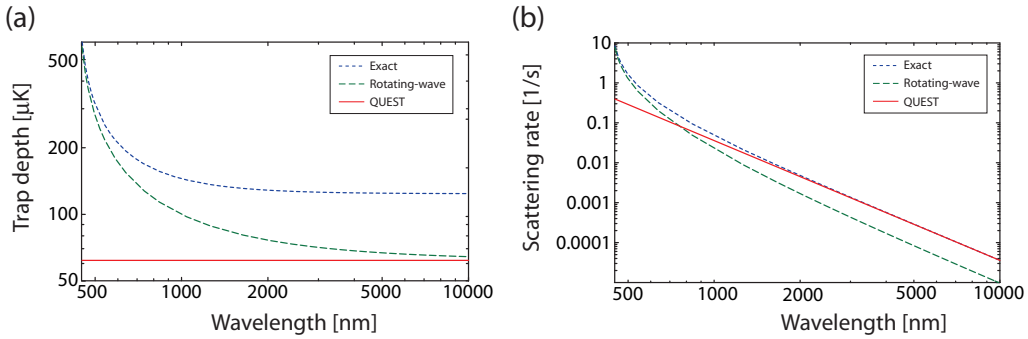

Figure 5.10: Dependence of (a) the depth of the dipole potential and (b) the scattering rate on the trapping laser wavelength. Shown are the full calculation Eq. (5.1), the rotating wave approximation Eq. (5.4) and the QUEST approximation Eq. (5.6). For this calculation we assumed a laser power of 10 W, a waist of 30 μm for the Gaussian beam and included all lines given in Table 5.2.

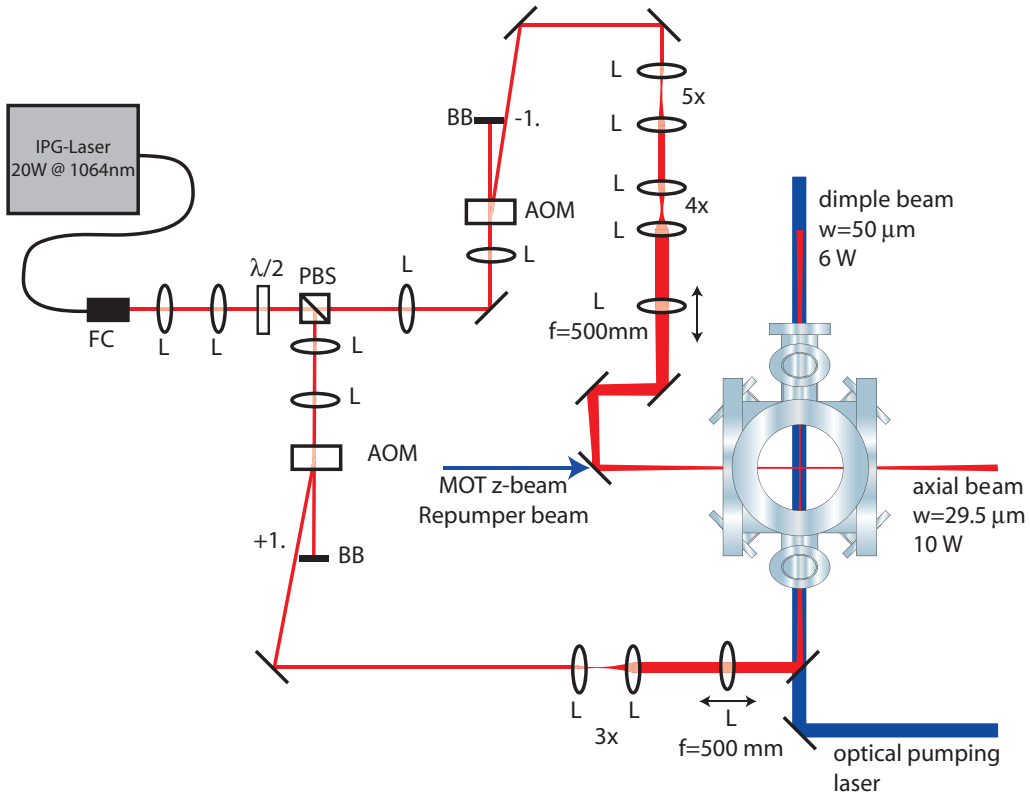

Figure 5.11: Setup of the laser system for the optical dipole trap. Sketch of the setup for the optical dipole trap. L: lens, $\lambda/2$, $\lambda/4$: half and quarter-wave plate, M: mirror, PBS: polarizing beam splitter, AOM: acousto-optic modulator, BB: Beam block, FC: Fiber coupler.

standing waves in our crossed dipole trap, which is not wanted. The setup of the dipole trap has changed considerably since the description in [100], to address the problems encountered previously.

An overview of the dipole laser system is given in Fig. 5.11. The laser power is divided into two beams using a $\lambda/2$-wave plate and a polarizing beam-splitter. Each beam then passes through an acousto-optic modulator[24] which allows to control the laser power independently in each beam[25]. Both beams are then expanded by one or more telescopes to Gaussian waists of w_0=6 mm and 3 mm respectively, before

[24] Crystal Technology, Model 3110-125 together with RF-Driver Model 1110AF-AIFO-2.0

[25] As can seen from Fig. 5.11 for one beam the +1 order and for the other the -1 order is used, thereby shifting the laser frequency between both beams by twice the RF-frequency of the AOMs of $2 \cdot 110$ MHz. This again ensures that there will be no standing waves in the crossed optical dipole trap.

being focused into the chamber by a 500 mm lens (diameter 2 inch)[26]. The last lens is mounted onto a translation stage to allow for precise control of the waist position in the chamber. The beam with more power is directed along the axial direction of the magnetic trap, which ensures good mode-matching between the magnetic and dipole trap. The second beam traverses the vacuum chamber in vertical direction, which may allow the magnetic levitation of atoms [245] in the optical dipole trap in the future. Both beam directions are already used by existing blue laser beams (for the z-beam of the MOT and for optical pumping), so we employed dichriotic mirrors[27] just before the chamber to overlap the beams.

5.4.4 Characterization

To reliably determine the physical properties of the atomic cloud from the camera pictures, a good knowledge about the properties of the dipole trap is needed. In particular a good knowledge about the dependency of the trap frequencies on the laser power is needed. Theoretically the trap frequencies are fully determined by Eqs. (5.16). But this is too shortsighted. It starts with the measurement of the power in the considered dipole beam. The beam power can only be measured outside the vacuum chamber, and the passage through the vacuum window introduces approximately 8% of losses due to reflections. Since the spot size on the power meter must not be to small, the beam power has to be measured even earlier in the beam path, introducing additional losses and uncertainties. The beam waist w_0 can be determined by imaging the beam on the CCD chip of a camera and searching for the smallest spot. The beam waist is given by twice the Gaussian width of the spot on the camera. The influence of the vacuum window on the beam waist is again unknown and leads to further uncertainty. By looking at the mode of our dipole beams with the help of the CCD-camera, we discovered that the beam mode outside the Rayleigh range $\pm z_R$ is not a Gaussian TEM_{00} mode any more, but shows contributions of higher order modes. These higher order modes may reduce the already low axial trap frequency even further. Due to all these uncertainties involved in the determination of the trap frequencies, we needed to carry out a in-situ measurement.

One in-situ possibility is to measure the temperature of an atomic sample using a time-of-flight temperature measurement and the in-trap size of the cloud to calculate the trap frequencies by the following equation:

$$\omega_{r,z} = \frac{1}{\sigma_{r,z}} \sqrt{\frac{k_\mathrm{B} T}{m}} \,. \tag{5.18}$$

Due to the uncertainties in the trap size and the temperature, the resulting error bars on the trap frequencies are huge and thus making this method inappropriate

[26] There is no need to use an achromat for the last lens, since due to a $f/\#$-number of 20 the imaging is not limited by the spherical aberration but is diffraction limited.

[27] HR 1064 nm and HT 425 nm from Lens Optics.

for our purposes. We finally settled the question of the trap frequencies by using a method commonly called "parametric heating" [72, 181, 193, 243].

When harmonic trap parameters, such as trap frequencies, or trap center position, are periodically modulated by external fields, the excitation spectrum shows narrow peaks at integer fractions of twice the trap frequency ω_0 [180]. This is most easily visualized for the modulation of the trap frequency. Atoms which reach their turning point at a time when the trap frequency is increased due to the modulation, will gain additional energy. If the modulation frequency is twice the trap frequency (or an integer fraction of it), they will reach their other outer turning point again in phase with the modulation. Atoms initially out of phase with the modulation will initially lose some energy until they come in phase with the modulation and are thus also heated. In our optical dipole trap the trap frequency can be modulated by changing the laser intensity. The increased temperature of the atomic sample becomes apparent through an increase in the size of the atomic cloud or due to the finite depth of the trap, the atoms will be lost from the dipole trap. The (classical) equation of motion for the atoms is given (to first order in the potential) by

$$\frac{d^2x(t)}{dt^2} + \omega_0^2\left[1+\epsilon(t)\right]x(t) = 0\,, \tag{5.19}$$

where $\epsilon(t) = \epsilon_0\cos(\omega t)$ for our case of harmonic modulation. This differential equation can then be written in the Mathieu canonical form

$$\frac{d^2x(t)}{dt^2} + \left[\alpha - 2q\cos(2z)\right]x(t) = 0\,, \tag{5.20}$$

with $z = \omega t/2$, $\alpha = (2\omega_0/\omega)^2$, and $q = \epsilon_0\alpha/2$. It is well known [2] that depending on the values of α and q, the solutions $x(t)$ are stable or unstable. In the context of parametric heating the transition curves which separate regions of stability and instability define the width of the corresponding resonance. For $q \ll \alpha$ the resonances are located at $\alpha \propto n^2$, i.e. $\omega = 2\omega_0/n$. The resonance at $\omega = 2\omega_0$ has a width[28] $\Delta_{2\omega_0} \propto \epsilon_0\omega_0/2$. That the width of the parametric resonance depends on modulation amplitude is obvious, because the atoms "sample" a potential whose trap frequency changes between $\omega_0(1\pm\epsilon)$. For $\omega = 2\omega_0$ the energy increases exponentially with a rate constant $\epsilon_0\omega_0$ [30, 73, 113, 207].

Figure 5.12 on the next page shows the results for a parametric heating measurement in a crossed optical dipole trap. Typical trap parameters for our optical dipole trap extrapolated from our trap frequency measurements can be found in Table 5.3. Figure 5.13 shows absorption images of a single beam and a crossed dipole trap.

[28] For deriving this dependency one needs to approximate the curves separating the unstable and stable regions by a power series for small q using, e.g. equation 20.2.25 of [2]. For the resonance $\omega = \omega_0$ one finds a width $\Delta_{\omega_0} \propto \epsilon_0^2\omega_0/4$. Since the width of this resonance is expected to be smaller, it would allow a much more accurate determination of the trap frequency. Unfortunately it is not as pronounced as the resonance at $2\omega_0$.

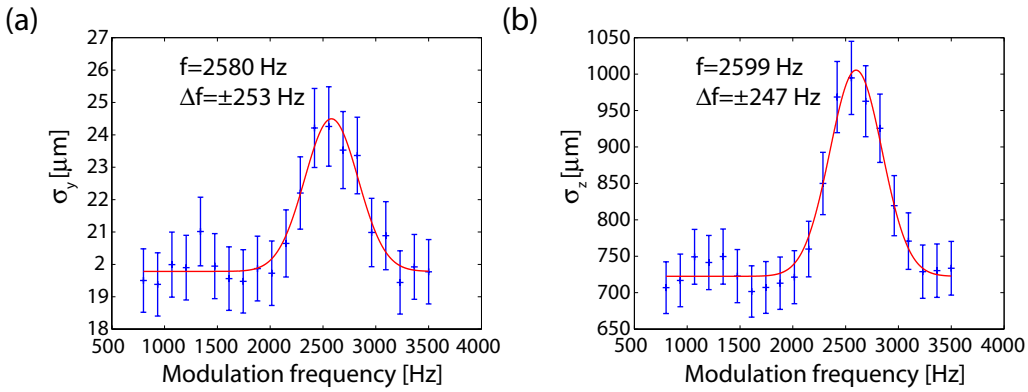

Figure 5.12: Measurement of the trap frequencies of a crossed optical dipole trap. We observe the heating of the sample through an increase in the size of our atomic cloud when the modulation frequency is twice the trap frequency. The modulation amplitude was approximately 5%.

	axial beam trap	radial beam trap	crossed trap
Laser power	P_z =8.25 W	P_x =5.25 W	P_z =8.25 W P_x =5.25 W
Beam waist	$\omega_0 = 29\,\mu$m	$\omega_0 = 50\,\mu$m	
Trap frequencies	$\omega_{ax} = 2\pi \cdot 12$ Hz	$\omega_{ax} = 2\pi \cdot 2$ Hz	$\omega_x = 2\pi \cdot 1604$ Hz
	$\omega_{rad} = 2\pi \cdot 1550$ Hz	$\omega_{rad} = 2\pi \cdot 415$ Hz	$\omega_y = 2\pi \cdot 1549$ Hz
			$\omega_z = 2\pi \cdot 416$ Hz
Trap depth U_0/k_B	125 μK	27 μK	152 μK
scattering rate Γ_{sc}	0.034 $^1/_s$	0.007 $^1/_s$	0.041 $^1/_s$

Table 5.3: Parameters for both optical dipole trap beams at typical beam powers. All parameters are calculated neglecting the gravitation. The radial beam, which is along the vertical direction, can not by itself trap atoms due to the gravitation.

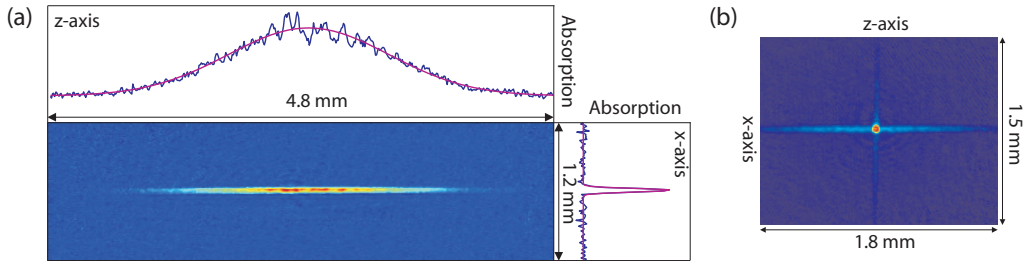

Figure 5.13: Typical absorption images for (a) a single beam optical dipole trap and (b) a crossed optical dipole trap. For both cross-sections and typical sizes are given.

5.5 Computer control

Many coordinated events must occur to prepare and detect a sample of ultracold atoms. Lasers have to be switched on and off at the right junctures, their frequency has to be changed several times, the currents through the magnetic coils have to be ramped up and down and RF fields have to be swept in frequency. Most experimental parameters can be easily controlled through digital and analog signals, while others (especially function generators) are controlled through the GPIB-Bus[29]. The timing accuracy required for all control signals is below $100\,\mu s$. This can be achieved using a computer control system. The control computer we use, is equipped with an AMD Athlon 1.2 GHz CPU, a 32 Channel digital input/output PCI card[30], two 8 channel, 12 bit analog output PCI cards[31] and a GPIB-Card[32]. The analog and digital cards are interconnected through the RTSI-Bus[33], which allows the synchronization of the output signals. The digital output signals are opto-coupled to a $50\,\Omega$ driver which can also be controlled manually. The analog output signals are rescaled to the required voltages levels to retain the 12 bit accuracy of the D/A converter. When necessary, an additional 1:1 isolation amplifier is employed to prevent grounding problems.

For the experiments a control software was developed. The control software should allow the easy programming of the experimental sequences using a graphical user interface. Some other design considerations were:

- Easy programming of analog output waveforms
- Support for loops in sequences, which allow to change an experimental parameter during each loop iteration (for statement)

[29] General Purpose Instrument Bus
[30] National Instruments, PCI-6533 (DIO-32-HS)
[31] National Instruments, PCI-6713
[32] National Instruments, PCI-GPIB
[33] Real-Time-System-Integration Bus

- Conditional execution of sequences (if statement)
- Subroutines allow to reuse common standard sequence parts
- Easy extensibility through external modules, to accommodate future requirements
- Usage of variables allows to easily change parameters in a sequence
- Close integration with the camera and data-evaluation software

The control software is implemented in LabView[34] and C++ [229]. The user interface and the programming of the I/O-cards were done in LabView, while the sample generation for the I/O-cards was implemented for performance reasons (among others) in C++.

The user interface of the control software is shown in Fig. 5.14. An experimental sequence is a concatenation of so called "words". Each word can serve different purposes. Most commonly a word defines the state of all digital and analog channels that last for a specified time (a so called output word). Other purposes a word can serve are:

- Start a for loop
- Start an if case
- End a loop/if
- Call a Sub-VI[35] with the supplied parameters
- Execute a sub-sequence

For each purpose the respective fields need to be filled in. All fields not only allow numerical values but also accept arbitrary mathematical expressions involving the most common mathematical functions and variables. The usage of variables instead of numerical values allows to easily change the experimental parameters in many words at the same time, which would otherwise need to be done by hand and would be quite tedious and error prone. The variable values can be set explicitly or through loop variables. In the value fields for the analog outputs, the variable t plays a special role. During the duration of an output word the value of t varies from 0 to 1. This allows for example to linearly change the value of an analog output channel in a word or even modulate it with a sinusoidal function.

[34] National Instruments

[35] VI stands for Virtual Instrument and is nothing more than a small sub-program written in LabView.

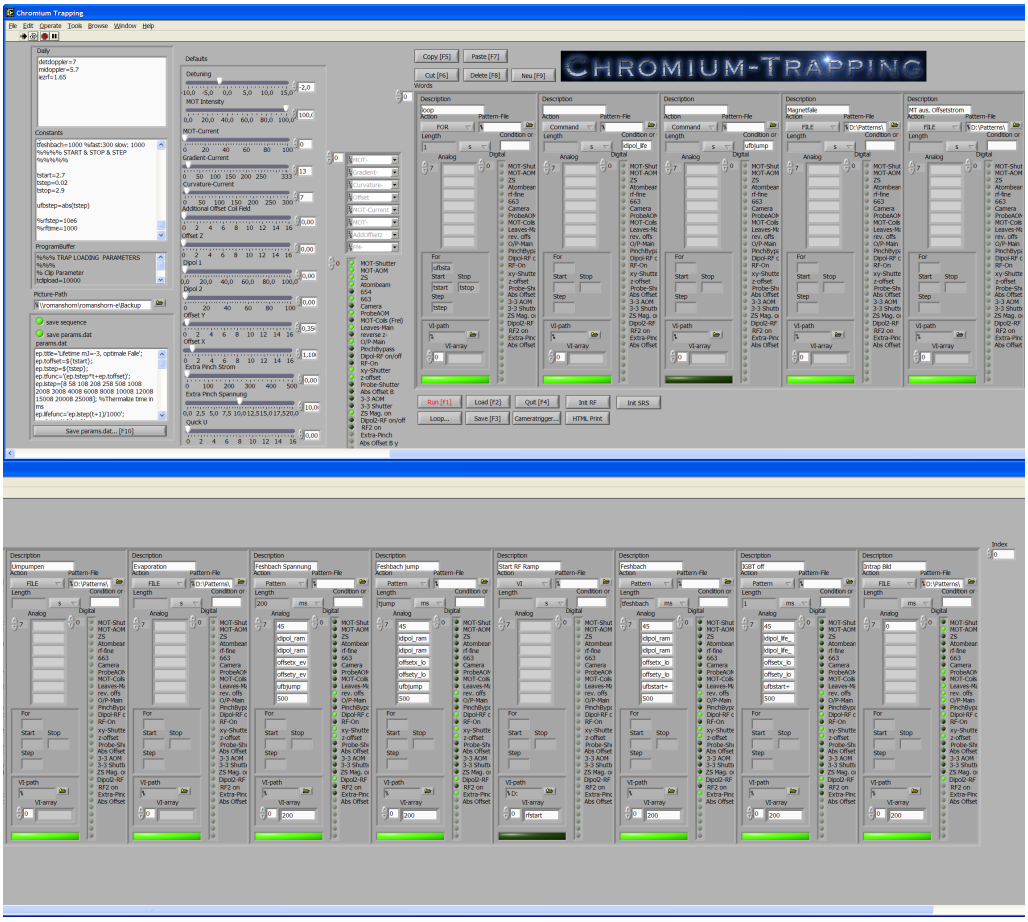

Figure 5.14: The user interface of the computer control software. Left top: Assignment of variables, left bottom: template for the information file which is used by the data evaluation software. Middle: Default values for all channels when no sequence is running. Right: Sequence of "words".

It is possible to call sub-VIs at certain times during the execution of a sequence, which can perform different tasks. One commonly used task is to program a function generator using the GPIB-Bus. To achieve the necessary timing accuracy a hardware counter on the I/O-cards is used to keep track of the time. This allows to execute the sub-VIs with a timing accuracy of $\pm 5\,\mathrm{ms}$[36].

After each experimental run, the sequence file is saved automatically to enforce the documentation. Additionally an information file is saved for the data evaluation

[36] A better timing accuracy could be achieved by using a Real-Time OS, i.e. LabView RT. But since the time-delay between the transmission of the GPIB command and the execution of the command is for many instruments of the same order (or even an order bigger!), this does not matter.

software, which contains the relevant experimental parameters. The format of this information file is defined by a template, where the expression `${variable name}` is replaced by the value of the variable used in the sequence.

5.5.1 Implementation

Since the software design of the computer control software is non-trivial, the key points of our implementation can only be highlighted in the following section.

When a sequence of words is executed, LabView converts the graphical representation of the sequence into source code of a specifically devised programming language. Due to historical reasons, the language resembles MATLAB[37] source code, but has been syntactically simplified and expanded with new commands to suit our needs. The two most important new commands are `pattern` (which defines the states of the digital and analog channels for a certain time) and `callvi` (which calls a LabView Sub-VI during the execution of a sequence). A short sample program is shown in Fig. 5.15. The source-code is then passed on to an interpreter, which was completely written in C++.

The job of the interpreter is to execute the program and thereby build up tables which contain the time and the values of the digital and analog channels when their state changes and the times when a Sub-VI needs to be executed. The information contained in these tables is the basis for the generation of the raw data which is sent to the cards. Before turning our attention to this step, we'll take a closer look at the design and the implementation of the interpreter.

In computer science a lot of literature exists about compiler[38] design and implementation (see Aho et al. [3] for an introduction). The operation of an interpreter is normally divided into three phases. The first phase is a so called "Lexer". The Lexer takes the source code, which is nothing else than a stream of characters and breaks the stream up into vocabulary symbols. For example the three characters `f o r` are turned into the vocabulary symbol *for* which is just an integer number and much more easily to handle computationally. In the second phase, the parser applies a grammatical structure to this stream of vocabulary symbols. The grammatical structure describes the order in which the vocabulary symbols are allowed to appear in the stream[39]. The generation of the source-code for these two phases can be easily automatized. Tools have been developed which take input files describing the vocabulary and the grammar of a language and output the necessary source-code. The two most well known tools for this task are LEX and YACC [133]. We decided

[37] The Mathworks

[38] An interpreter is a simpler form of a compiler.

[39] This is completely similar to the grammar in human languages, though the extent of the vocabulary in human languages is orders of magnitude bigger than for computer languages.

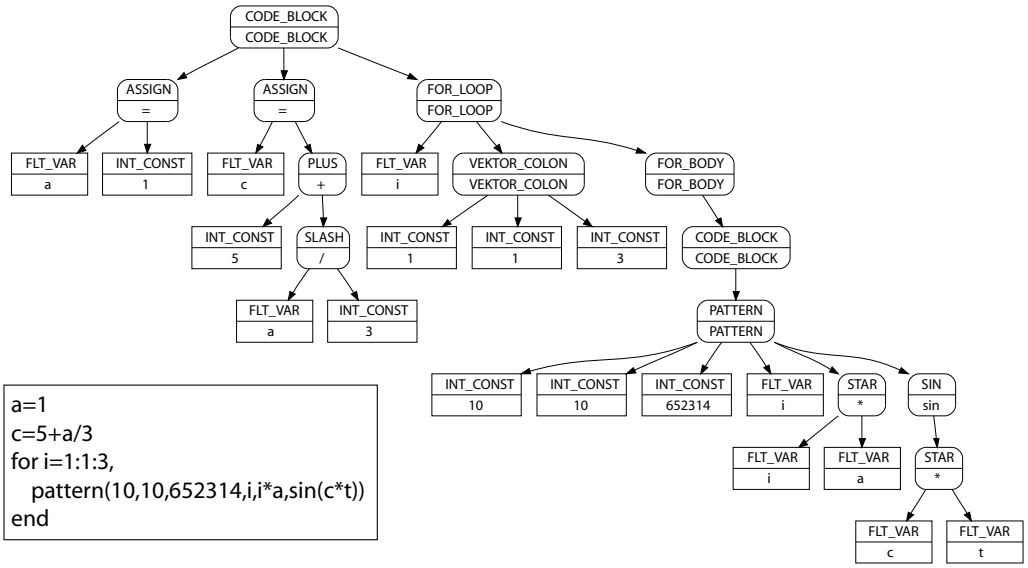

Figure 5.15: A simple sample program and the corresponding AST generated by the ANTLR Lexer and Parser. Nodes with rounded corners are non-terminals, while rectangular nodes are terminals. Each node is of a certain type (upper part) and can contain additional information (lower part). A tree walker is then used to execute the program. If it for examples encounters the sin node, it recurses down the tree to retrieve the argument of the sine. There it comes across a node of type STAR which can be evaluated by multiplying the values of the variables c and t.

to use a tool called ANTLR[40] because it can also generate much of the necessary source code for the third and last phase. The parsers generated by ANTLR not only check the grammatical structure of the program but also construct a so called AST[41], which is a tree representation of the program. For our small example program the corresponding AST is shown in Fig. 5.15. In the third phase a tree walker is employed. It starts with the top node of the tree and then recurses down the tree, while executing the necessary commands according to the type of the encountered non-terminal nodes. The complete and comprehensive definition of the grammar and the tree walker for our language can be found in Appendix E.

After the interpreter has done its job, all the necessary data is contained in the tables which are returned by the interpreter. LabView is now again used to initialize the cards, configure a master/slave configuration where the scan clock of one card (master, usually the digital card) is distributed over the RTSI-Bus to the other (slave) cards, thereby synchronizing all the cards. For each card a circular buffer (size about

[40] ANother Tool for Language Recognition, a predicated-LL(k) parser generator that handles lexers, parsers, and tree parsers [175].
[41] Abstract Syntax Tree

64000 samples) is set up and filled with the initial data. After the sample generation is started, the circular buffers are periodically refilled with new data. The data for the circular buffers is generated on the fly from the tables returned from the interpreter. The tables just contain for how many samples a certain state should be applied, while the cards need a stream of sample values which they output. To generate the sample values from the tables again C++ code is used for performance reasons. The stream of digital samples is obtained by copying the digital value only sufficiently often. The analog sample values are more complicated. They are given by a formula, which can still contain the variable t. The formula needs to be evaluated with t being a vector with values from zero to one. Since the size of t can be huge (commonly a few thousand elements) optimized assembler routines[42] are used for the vector calculations. As already mentioned, a hardware counter is configured to count the number of scan clock transitions which corresponds to the number of samples which have already been generated. The value of this hardware counter is periodically polled[43] and used to execute the Sub-VIs at the correct points in time. When a sequence is finished, the cards are cleared and the default values for the digital and analog channels are applied.

5.6 Imaging and data evaluation

All thermodynamic properties of an atomic ensemble can be obtained from images of its density and momentum distribution. For imaging we use a 12 bit digital progressive scan charge coupled device (CCD) camera[44], connected to a standard PC. The camera offers a high resolution of 1392x1024 pixel, with a pixel size of 6.45x6.45 μm^2 and a quantum efficiency of over 45% at 425 nm. The camera can be positioned to image the atomic cloud along the radial axis either in horizontal or vertical direction. In both positions it is possible to use 1:1 or 2.6:1 (reduction) imaging. The optical resolution of the 1:1 imaging system was determined using a USAF-1951 test target[45] to be 8 μm, which is consistent with the resolution limit of $\Delta x = 1.22\lambda f/\# = 6.2\,\mu$m. At both positions it is possible to do flourescence as well as absorption imaging. The remaining experimental setup for flourescence and absorption imaging is unchanged from [209] and all relevant theoretical aspects were covered already there in detail. For imaging atoms in the m_s =-3 state we changed the polarisation of our imaging light from σ^- to σ^+ by turning the $\lambda/4$-plate around, so the beam traverses it in the opposite direction. Also the detuning of the imaging light had to be adapted. The detuning was experimentally determined to give the

[42] We are using the Intel Integrated Performance Primitives and the Intel Math Kernel Library
[43] Unfortunately LabView does not seem to support an interrupt driven approach.
[44] PCO, model PixelFly QE
[45] Newport

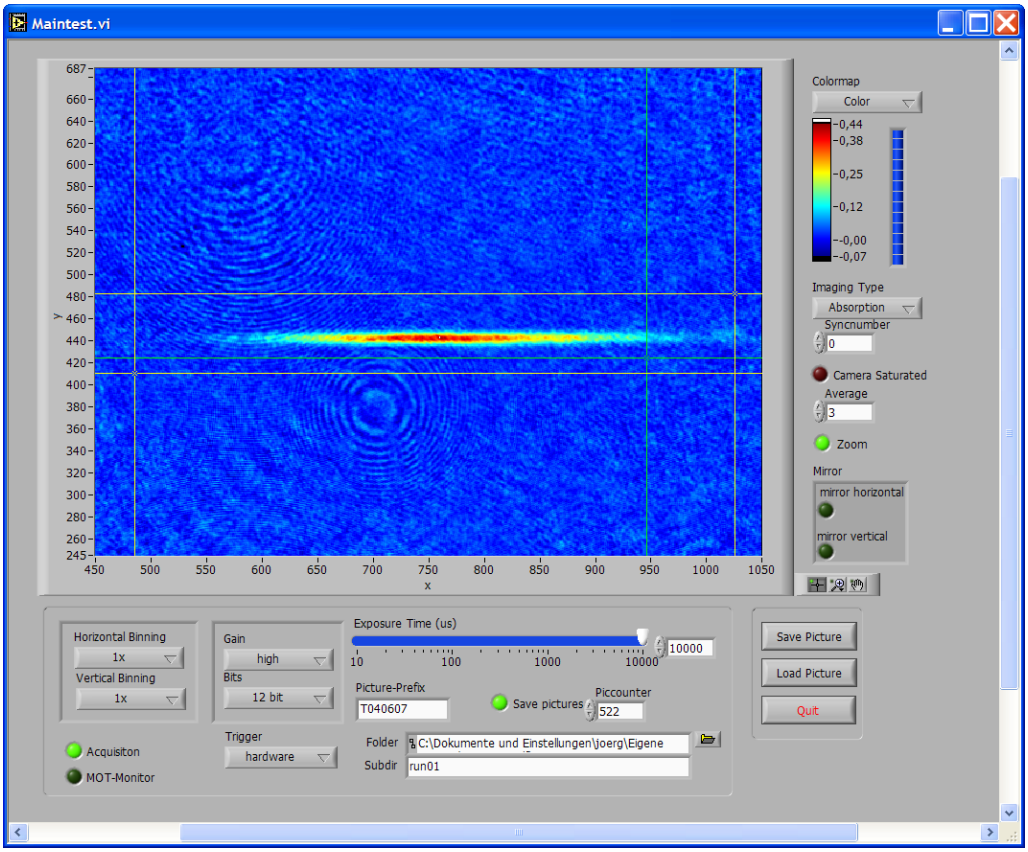

Figure 5.16: Screen shot of the camera program. Shown is an absorption image of a single beam dipole trap. The program calculates the resulting absorption image on the fly from three separate absorption images. As an additional post-processing step, it allows to apply an average.

highest number of atoms observed, which lead to a value of $\delta = -2.3\,\Gamma$ for m_s =-3 (compared to $\delta = +2.6\,\Gamma$ for m_s =+3).

A custom made LabView program is used to control all camera settings (e.g. exposure time, binning etc.) and to save the recorded images to the hard drive. It can also calculate the resulting column density distribution for fluorescence and absorption images on the fly. This allows to easily monitor the experimental runs. A screenshot of the user-interface is shown in Fig. 5.16.

The main purpose of the data evaluation is to extract from the CCD camera images the physical properties describing the atomic ensemble. The images represent the integrated density distribution of the atomic cloud along the direction of the camera. From these images and the knowledge of other experimental parameters (e.g. exposure time, laser wave-length, trap geometry, ballistic flight time...) one can extract the

number of atoms, density, size, temperature and phase-space density of the atomic sample. This is done using a home grown Matlab[46] script, which allows us to perform almost real-time data evaluation during an experimental run [209, 230].

[46]The Mathworks

Chapter 6

Feshbach resonances in ^{52}Cr

After laying all the necessary foundations in the previous chapters, this chapter gives a comprehensive account of the performed experimental Feshbach measurements. It starts by describing the steps involved in the preparation of the ultracold atomic sample of chromium atoms. The main part of this chapter is dedicated to the employed experimental techniques and the interpretation of the origin of the experimentally found Feshbach resonances. It comprises a review of relevant molecular levels and possible coupling mechanisms for the existence of Feshbach resonances in chromium. Then the experimental positions of the Feshbach resonances are used to determine precise values for the scattering lengths and C_6, C_8 coefficients of the molecular potentials through numerical multi-channel calculations. The precise knowledge of the potential allows to infer the outcome of several follow-up experiments which are investigated at the end of this chapter.

6.1 Sample preparation

To be able to investigate Feshbach resonances, the collision energy spread of the atoms needs to be smaller than the width of the Feshbach resonance one wants to observe. For ^{52}Cr a temperature below $10\,\mu$K is required to be able to observe resonances with a width of 100 mG. Additionally, densities above $10^{12}\,{}^{1}/_{\mathrm{cm}^3}$ are required for sufficiently high collision rates. Preparing atoms at such temperatures and densities requires employing laser- and evaporation-cooling techniques. These techniques were established during the last ten years and have become the standard tools for preparing ultracold and dense atomic gases. Due to the complicated level structure and the high magnetic moment of ^{52}Cr compared to the alkalis, some extra effort is involved in laser- and evaporatively cooling chromium into the ultracold regime. Many of the established technologies needed to be adapted or extended when applied to chromium. This section will give a short account of all the steps required to prepare our ultracold atomic chromium sample.

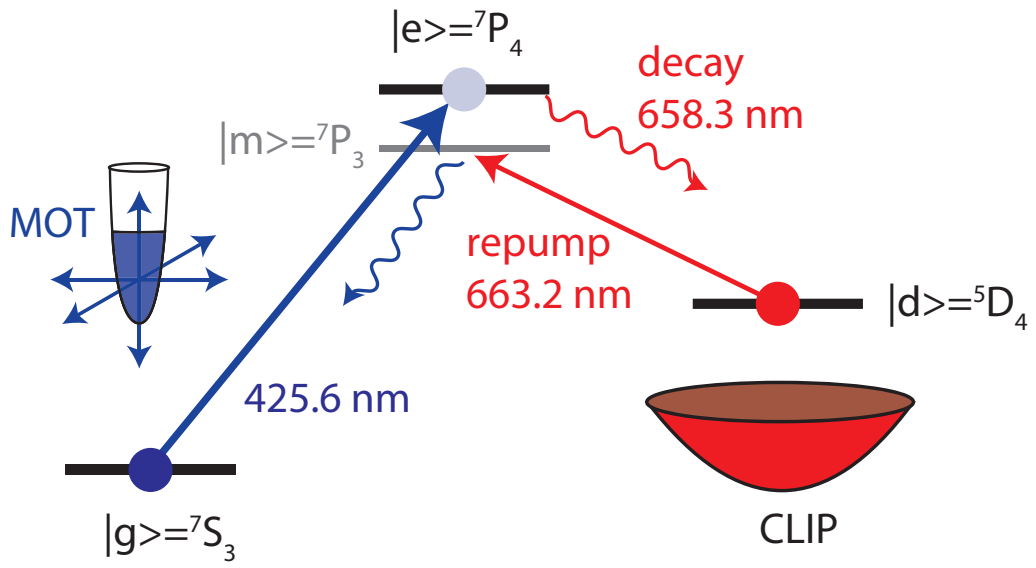

Figure 6.1: CLIP trap loading scheme. Shown are the relevant atomic levels and transitions for the implementation in ^{52}Cr. The magneto-optical trap is operated by driving the fast transition from $|\,g\,\rangle$ to $|\,e\,\rangle$. Transfer between MOT and CLIP trap is provided by radiative leakage from $|\,e\,\rangle$ to $|\,d\,\rangle$. Repumping the atoms via an intermediate state $|\,m\,\rangle$ allows to transfer the atoms to the ground state.

6.1.1 CLIP-Trap

The basic idea of the continuous loading scheme was developed and implemented for chromium in a 3D-quadrupole magnetic trap by Stuhler [230]. The idea was then extended to an Ioffe-Pritchard (IP) type trap by Schmidt [209]. The basic principle of operation of a CLIP-Trap is shown in Fig. 6.1 using a simplified level scheme for ^{52}Cr. On the strong dipole transition with linewidth Γ_{ge} which couples the ground state $|\,g\,\rangle = {}^7S_3$ and the excited state $|\,e\,\rangle = {}^7P_4$ we operate a modified magneto-optical trap. The light field configuration was chosen so that it is compatible with the magnetic field produced by an IP-trap and is similar to a 2D$^+$-MOT configuration [55]. Two orthogonal pairs of σ^+/σ^--polarized laser beams cool and trap the atoms radially. An additional pair of σ^+-polarized laser beams along the axial direction provide Doppler cooling and very weak confinement due to light pressure forces. The necessary radial gradient field, axial curvature field and offset field are generated by the IP-trap (see Chapter 5.3 on page 65). The non-vanishing offset field of the IP-trap prevents the Majorana spin-flip losses found in the 3D-quadrupole setup. The actual transition used for the chromium MOT is not closed. Atoms can undergo spontaneous emission to the long-lived metastable states $^5D_4$ and $^5D_3$ denoted by $|\,d\,\rangle$ with a rate of Γ_{ed}. The radiative leakage is the loading mechanism for the magnetic

trap. Due to the high magnetic moment of the $|\,d\,\rangle$-states (up to $6\mu_B$), atoms in the low-field seeking state of the $|\,d\,\rangle$ manifold can be trapped in the magnetic field of the IP-trap. Since typical magnetic field gradients in the CLIP-trap are around 5-10 $^{\mathrm{G}}/_{\mathrm{cm}}$, the magnetic trap is not very deep and only atoms which have been pre-cooled by cycling on the MOT transition will be captured. Due to the high branching ratio $\Gamma_{eg}/\Gamma_{ed} \approx 250\,000$ this condition is easily fulfilled, on the contrary it even limits the loading rate. The steady-state atom number in the $^5D_4$ and $^5D_3$ states is given by the ratio of the loading rate Γ_{ed} and the loss rate from these states.

After 10 s of loading the atom number in the $|\,d\,\rangle$-states has reached a steady-state and the MOT-beams are switched off. Due to the high inelastic losses which have been observed in the $|\,d\,\rangle$ states [230] the atoms are transferred back into the ground state via the intermediate state $|\,m\,\rangle$. The intermediate state $|\,m\,\rangle$ is used instead of the excited state $|\,e\,\rangle$, since it allows much faster repumping. The great advantage of the CLIP trap is that it removes the need for a transfer step from a 3D-quadrupole into an IP magnetic trap, thus greatly simplifying the preparation procedure. It can also be used as a source for loading a waveguide, a usage scenario which is also pursued by our group.

Using the CLIP trap we prepare $2 \cdot 10^8$ atoms in the magnetic trap with temperatures below 100 μK. In the following step we adiabatically compress the magnetic trap to increase the scattering rate. It turned out though, that it is still not sufficient to allow for efficient evaporative cooling. This is why we have to employ an additional Doppler cooling step to further increase the phase-space density.

6.1.2 Doppler cooling

Free-space one-dimensional Doppler cooling [132] is usually performed in a standing wave field created by a pair of counterpropagating laser beams with a frequency below the atomic transition. The cooling effect is due to preferential absorption of photons from the laser beam opposing the direction of motion of the atom. Subsequent spontaneous emission is centrally symmetric and on average does not change the momentum of the atom. Our group [211] showed that in optical dense clouds not only the direction along the laser beams is cooled down to the Doppler limit, but also the radial directions. Cooling in the radial directions can be explained by reabsorption of spontaneously emitted photons by the optically dense cloud. The Doppler cooling step is performed in a fully compressed magnetic trap. The corresponding offset field has a quite high value of 28 G, which ensures sufficient splitting of the Zeeman-levels and thereby suppressing unwanted depolarizing transitions. For cooling we use a retro-reflected σ^+ polarized laser beam along the axis of our magnetic trap. The laser frequency is tuned $7\,\Gamma$ above the $^7S_3 \leftrightarrow {}^7P_4$ transition in ^{52}Cr, which corresponds to an effective detuning of $-0.8\,\Gamma$ in the center of the magnetic trap. Applying the laser beams for approximately 200 ms with a mean intensity of $4 \cdot 10^{-3}\,I_{sat}$ leads to

an increase in the phase-space density to $\rho = 1 \cdot 10^{-7}$ or by a factor of 80. After adiabatically compressing the magnetic trap, the scattering rate is sufficiently high to start evaporative cooling.

6.1.3 Evaporative cooling

Evaporative cooling is a well known process, which occurs in many physical systems. The most well known example is a cup of coffee or tea which gets colder due to the evaporating water. Evaporative cooling is used in all experiments creating Bose-Einstein condensates or degenerate Fermi-gases as final cooling step. It has been proven to be very efficient and was used to prepare a sample of an atomic gas with a temperature as low as 500 pK [129].

Evaporative cooling of a trapped gas is based on the preferential removal of atoms with an energy higher than the average energy and on thermalization by elastic collisions. The general idea is to remove atoms with an energy E greater than a certain cut-off energy $\mathrm{E_c}$. Since this reduces the average energy of the atoms remaining in the trap, the gas will be driven by thermalizing interatomic collisions towards a new equilibrium state at a lower temperature. These collisions also promote atoms to energies higher than $\mathrm{E_c}$, thus keeping the evaporation going. As the temperature of the trapped gas drops, the number of atoms that are able to leave the trap is exponentially suppressed, approximately like $\exp(\mathrm{E_c}/k_\mathrm{B}T)$. Eventually the cooling rate is balanced by a competing heating mechanism, or becomes negligibly small. In order to force the cooling to proceed at a constant rate, the evaporation threshold $\mathrm{E_c}$ may be lowered as the gas cools. The optimal strategy of lowering the evaporation threshold to achieve the highest possible phase-space density is the topic many publications and thus will be not discussed here. A nice overview can be found by Ketterle and van Druten [120]. Hensler [100] applied the theoretical model from Luiten et al. [137] to ^{52}Cr.

Experimentally two different methods are commonly used for removing atoms with an energy higher than the cut-off energy, depending on the trap type. If the atoms are captured in a magnetic trap a method called rf-evaporation is used. Here rf is used to transfer the trapped atoms from the low-field seeking state into the high-field seeking state using a Landau-Zener transition. The resonance condition $m_j g_j \mu_\mathrm{B} B(r) = \hbar\omega_\mathrm{rf} = \mathrm{E_c}$ is only fulfilled for a sharp equipotential-surface. Any atom which has sufficient energy to cross the equipotential surface is removed from the trap. Another method commonly used in dipole-traps where rf-evaporation is not possible, is to lower the trap depth of the dipole-trap and thus lowering E_c. The disadvantage of this method is that with lowering the trap depth, also the trap frequencies go down. This decreases the density and the temperature of the trap and consequently lowers the collision rate, leading to slower evaporation [172]. Still the creation of a Bose-Einstein condensate in an optical dipole trap is possible [12, 33].

Evaporative cooling of ^{52}Cr in a magnetic trap allowed to increase the phase-space density by almost five orders of magnitude to $\rho = 0.03 \pm 0.01$ [100]. Still this was not enough to reach the required phase-space density $\rho > 1$ for the phase-transition to a Bose-Einstein condensate. The run-away regime, where the evaporation accelerates itself was never reached. Moreover the figure-of-merit for evaporative cooling, the ratio of good to bad collisions decreases dramatically when densities above $10^{12}\,{}^{1}/_{\mathrm{cm}^3}$ were reached. This decrease is due to the increased contribution of the dipolar relaxation process, with a rate constant of $\beta_{\mathrm{dr}} = 4 \cdot 10^{-12}\,{}^{\mathrm{cm}^3}/_{\mathrm{s}}$ at an offset field of 1 G (see Chapter 4.3). Since the dipolar relaxation rate scales with the magnetic offset field, performing the evaporation at lower offset fields should allow to suppress the dipolar relaxation. One cannot though choose arbitrary low offset fields, since at low offset fields additional losses stemming from Majorana-spin flips are introduced. The best values quoted above were obtained for an optimal offset field of approximately 130 mG. To be able to suppress the dipolar relaxation process completely, one has to transfer the atoms into the absolute ground state, the high-field seeking state m_s =-3. But atoms in a high-field seeking state cannot be trapped in a magnetic trap[1], so a transfer of the atoms into an optical dipole trap becomes necessary, which traps atoms independent of their magnetic sub-state.

6.1.4 Transfer into optical dipole trap

As introduced in the previous chapter the optical dipole trap consists out of two focused beams of a fiber laser. The beam with higher laser power and smaller spotsize is directed along the axial direction of the magnetic trap to allow for maximum overlap between the trap volumes of both trap types. The second, weaker and less focused beam is along the vertical direction. The axial beam is already switched on during the preparation of the atomic sample (i.e. already when the CLIP-trap is loading). We have not yet found any adverse effects of the dipole trap on the loading of the CLIP-trap or the Doppler cooling stage. The depth of the axial trap ($\approx$100 μK) is simply not sufficiently deep enough to already trap the atoms after Doppler cooling. Due to this, an evaporative cooling step is necessary. The atoms now see a hybrid-trap formed by the magnetic field and the optical dipole trap. The confinement of the optical trap in the axial direction is very weak compared to the magnetic trap, while in the radial directions the situation is reversed. Atoms oscillating in the radial direction thus see lower magnetic fields than atoms oscillating in the axial direction. For temperatures of the atomic sample below the depth of the dipole trap, the evaporation becomes one-dimensional and thus will not show the maximum possible efficiency. To avoid this situation we took care not to ramp below the trap depth during the last rf-evaporation step. The last evaporation ramps were optimized to obtain the maximum possible number of atoms in the dipole trap.

[1] It is not possible to generate static magnetic field maxima in free space [255].

To complete the transfer into the optical dipole trap the magnetic trap needs to be switched off. This cannot be done abruptly, due to the axial frequency of the magnetic trap being higher than the axial frequency of the dipole trap. A breathing mode would be created which in turn incurs a phase-space density loss. Abrupt switching also leads to uncontrollable transient fields, which are better avoided unless one wants to lose some atoms. To minimize these negative effects, the magnetic trap is switched off adiabatically in $\tau = 2\,\mathrm{s} > {}^{1}/_{\nu_{\mathrm{ax}}}$. Additional care has to be taken to ensure that the magnetic offset field never crosses zero during switching, since this would incur an additional atom loss. To prevent uncontrolled mixing of the magnetic sub-states a small homogeneous guiding field remains applied. In most of the experiments presented here, the second dipole beam is only switched on later in the experimental sequence. Alternatively, if not the optimum number of atoms is required, the atoms can be directly transferred from the magnetic trap into a crossed optical dipole trap, thereby shortening the experimental sequence.

Now that we have our atomic sample in an optical dipole trap, we can transfer all the atoms into the m_s =-3 state to completely suppress the dipolar relaxation.

6.1.5 Optical pumping

In the presence of a magnetic field the ground state $^7S_3$ of ^{52}Cr splits up into seven Zeeman sub-levels $m_s = +3 \ldots -3$. Our atomic sample is prepared in the low-field seeking state m_s =+3 in a magnetic trap. Due to the high dipolar interaction, during a collision of two chromium atoms in the m_s =+3 state, either one or both can spin-flip to the m_s =+2 state. Through this process they gain the Zeeman-energy, which in turn leads to heating of the whole sample and thus atoms are lost from the trap. This process continues until all the remaining atoms are in the m_s =-3 state, the energetically lowest possible state [100]. To prevent this atom loss, one has to actively transfer the atoms from the m_s =+3 state into the m_s =-3 state through optical pumping on the $^7S_3 \leftrightarrow {}^7P_3$ transition. This is achieved by applying a homogeneous magnetic field over the extent of the atomic sample and using a slightly red detuned, σ^- polarized, retro-reflected laser beam along the same direction as the magnetic field. Atoms in the $^7S_3$, $m_s = m$ state are then exited to the $^7P_3$, $m_s = m - 1$ state, from where they can then again spontaneously decay to the ground state with $m_s = m, m \pm 1$. The excitation probability, as well as the decay probabilities are given by the squares of the Clebsch-Gordon (CG) coefficients. The values for a $3 \leftrightarrow 3$ transition as in our case are shown in Fig. 6.2. Atoms which end up in the $^7S_3$, m_s =-3 state are in a so called "dark state" since this state is not coupled to the σ^- polarized laser light any more. This is also the reason why the $^7S_3 \leftrightarrow {}^7P_3$ transition is used for optical pumping, instead of the $^7S_3 \leftrightarrow {}^7P_4$ transition where this is not the case. In addition, one has to take care that the splitting of the Zeeman sub-levels is greater than the line width of the employed laser, otherwise

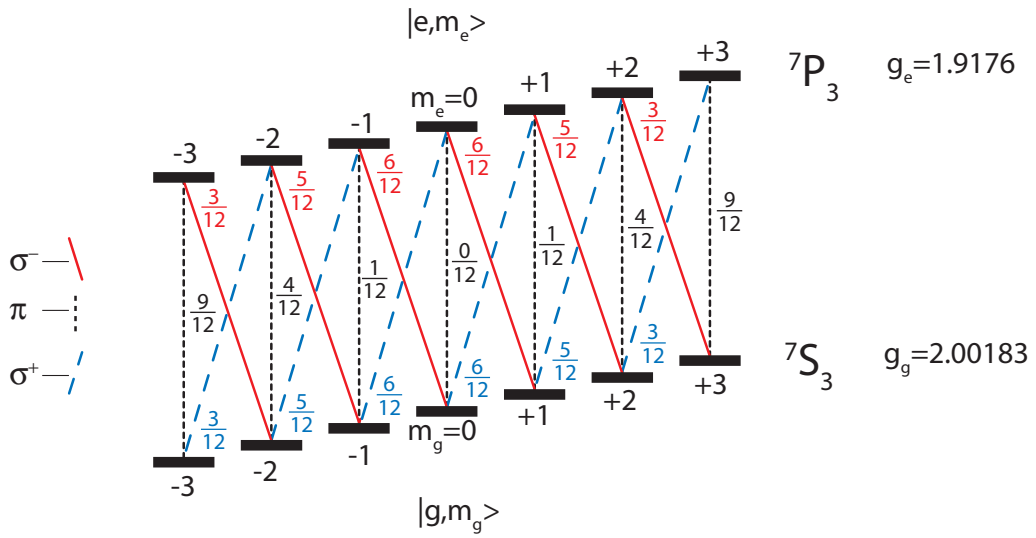

Figure 6.2: Level scheme for the optical pumping process on the $^7S_3 \leftrightarrow {}^7P_3$ transition. Each transition is color coded according to the transition type $\sigma^{\pm,0}$ and labeled with the corresponding Clebsch-Gordon coefficient squared.

impurities in the polarization of the laser beam can lead to sub-optimal optical pumping.

Optical pumping theory

The time evolution of the optical pumping process can be modeled theoretically. Assuming only σ^- polarized light, the change in the occupation probability $\dot{P}_m(t)$ for each state is given by following equation[2]:

$$\begin{aligned}\dot{P}_m(t) = {} & P_{m+1}(t)\,\Gamma_s({}^3_3CG^-_{m+1}\,s^-_{m+1})\,{}^3_3CG^0_m \\ & + P_{m+2}(t)\,\Gamma_s({}^3_3CG^-_{m+2}\,s^-_{m+2})\,{}^3_3CG^+_m \\ & - P_m(t)\,\Gamma_s({}^3_3CG^-_m\,s^-_m)({}^3_3CG^0_{m-1} + {}^3_3CG^+_{m-2})\,,\end{aligned} \tag{6.1}$$

where

$$\Gamma_s(s) = \frac{\Gamma}{2}\frac{s}{s+1} \tag{6.2}$$

is the photon scattering rate, which has a dependence on the saturation parameter s. The value of the saturation parameter s^-_m in this case depends on the magnetic quantum number m due to the different Zeeman-shift of the ground and the excited state. The saturation parameter is defined as [147]

$$s^-_m = \frac{I/I_S}{1 + 4\delta^2/\Gamma^2}\,, \tag{6.3}$$

[2]In the following we have shortened the notation for the magnetic quantum number m_s to m for readability.

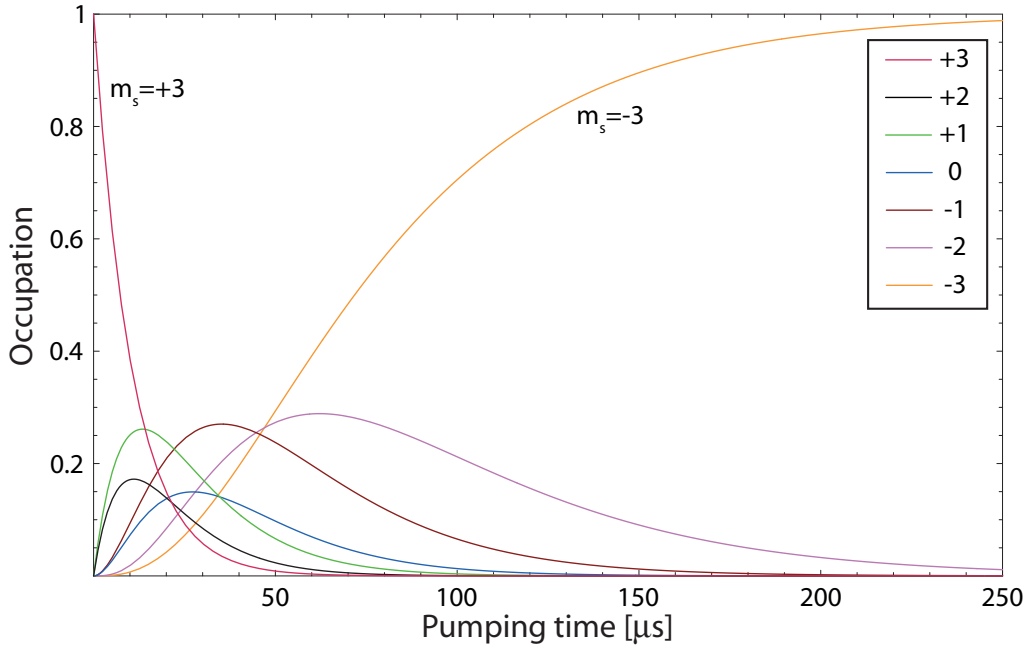

Figure 6.3: Theoretical calculation of the optical pumping process. Shown is the evolution of the occupation probability for each magnetic Zeeman sub-state separately. The experimental parameters used for this calculation were: applied magnetic offset field B=9.2 G, laser intensity $I = 1\,\mathrm{mW/cm^2}$ which corresponds to $I/I_{\mathrm{sat}} = 0.11$ and a detuning δ=-6.38 Γ.

where $I_S = {}^{\pi hc\Gamma}/_{3\lambda^3}$ is the two level saturation intensity and δ the detuning between the laser and the atomic transition. In addition we have to take into account the different Clebsch-Gordon coefficients CG[3]. We have thus seven coupled differential equations for the G_m [4] which can be solved numerically. Figure 6.3 shows the resulting time evolution of the occupation probability for an initially in the m_s =+3 polarized sample assuming our typical experimental parameters. After approximately 250 μs all the atoms are transferred from the m_s =+3 into the m_s =-3 state.

Optical pumping experiment

The required homogeneous magnetic offset field for the optical pumping was generated using one pair of the offset compensation coils. Its value of 9.2 G ensures

[3] ${}^{y}_{x}CG^{p}_{m}$ is the square of the Clebsch-Gordon coefficient for a p-type transition (where $p = +, 0, -$ corresponds to σ^+, π, σ^-) from a level with a magnetic quantum state m between $F = x \rightarrow F' = y$

[4] The nonexistent G_m for $|m| > 3$ have been set to zero.

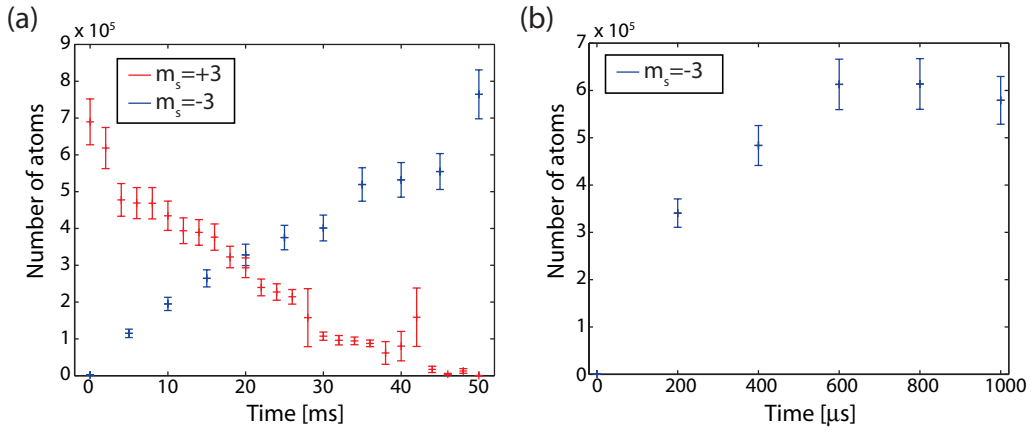

Figure 6.4: Measured number of atoms in the $m_s = \pm 3$ states after different optical pumping times, for (a) low I≈100 μW/cm² and (b) high I≈900 μW/cm² laser intensities.

sufficient splitting of the Zeeman-levels and thereby suppressing unwanted depolarizing transition due to impurities in the polarization of the optical pumping beam. The direction of the optical pumping beam (and thus the direction of the applied magnetic field) coincides with the direction of the second vertical (dimple) dipole beam (see Fig. 5.11). The optical pumping has to occur perpendicular to the elongation of the optical dipole trap, because along the direction of the dipole trap the optical density of the atomic cloud is greater than ten! This would prevent the optical pumping beam from penetrating the whole cloud at once, thus leading to much longer pumping times. In the perpendicular direction the optical density is much lower ($\lesssim 1$). The average laser power we used for optical pumping was 1 mW and the size of the laser beam at the position of the atoms was approximately 1 cm^2. The laser frequency was set to f=32 MHz below the resonance frequency. The resonance frequency was determined by tuning the laser wavelength so that our running MOT disappeared. This typically occurred at a vacuum wavelength of λ=427.6000(5) nm, which coincides with the value for this transition from the NIST Database [166] of λ=427.600 nm.

The efficiency of our optical pumping process was determined by measuring the number of atoms in the m_s =+3 and -3 states through σ^+/σ^--imaging after different optical pumping times. The results are shown in Fig. 6.4 for low and high intensities of the optical pumping laser. We see that for I≈900 μW/cm² after approximately 500 μs all atoms are transferred into the m_s =-3 state, which is consistent with our theory. One has to be careful though in interpreting the atom numbers, because we do not know if only atoms in the extreme states are imaged, or if also atoms in the intermediate magnetic sub-states contribute to the result. Theoretical calculations [100, §6.3] show that also atoms in the intermediate states contribute partly to

the result. Since our initial sample is not fully polarized, the detected initial atom number will be lower than the real number of atoms trapped. After optical pumping all atoms will be in the m_s =-3 state and will also be observed. This effect leads to the sometimes experimentally observed fact, that the atom number after optical pumping is higher than before the optical pumping process[5]. The temperature of our atomic sample seems also to be unchanged after optical pumping. Due to the finite trap depth the heating would immediately be reflected by an atom loss. All in all, we can conclude that optical pumping allows us to transfer close to 100% of the atoms into the m_s =-3 state without increasing the temperature.

A different method for transferring the atoms into the m_s =-3 state is to apply a Landau-Zener sweep[6] using radio-frequency [201, 264]. The Landau-Zener sweep is a coherent process and can thus only invert the population distribution, while optical pumping is due to the spontaneous emissions an incoherent process and can thus fully polarize a sample. Earlier investigations [100] have shown that applying a Landau-Zener sweep is indeed not as effective as optical pumping.

6.1.6 Evaporation in the optical dipole trap

Figure 6.5(a) is a logarithmic plot showing the evolution of the atom-number in the single beam optical dipole trap over time. The picture includes the data of a sample prepared in the m_s =+3 state and of a sample which has been optically pumped into the m_s =-3 state. We extract the lifetime from the exponential decay of the atom number. For the sample prepared in the m_s =+3 state we obtain a lifetime of only 6.3 s. Even when all magnetic fields are switched off, there are still stray magnetic fields present in our experimental chamber. Due to the dipolar relaxation the atoms can decay into the m_s =-3 sub-state, thereby gaining six times the Zeeman-splitting energy. Through collisions the gained energy is spread over all the atoms and thus leads to heating of the complete sample. Since the optical dipole trap is not very deep, every heating process leads to atom loss. The situation is completely different, when the atoms are optically pumped into the absolute ground state m_s =-3. Since in this case dipolar relaxation is not possible any more, the lifetime increases by a factor of 20 to 142 s. For either state, a strong non-exponential initial decay in the atom number can be observed. Due to the high initial temperature of the atoms and the limited depth of the dipole trap, atoms evaporate from the trap. This effect is

[5] During optical pumping the atoms can also decay into the $^5S_2$ state instead of the $^7S_3$ and are thus lost from the optical pumping process. The probability that a decay from the $^7P_3$ to the $^5S_2$ instead of the $^7S_3$ happens is 1:1000. Since we only need about ten photons for the transfer, this would mean a 1% loss which can be negelected.

The atoms in $^5S_2$ are still trapped in the optical dipole trap, but to get them back into the ground state a new laser system with a wavelength of 633 nm would be needed which does not exist yet.

[6] Also called rapid adiabatic passage.

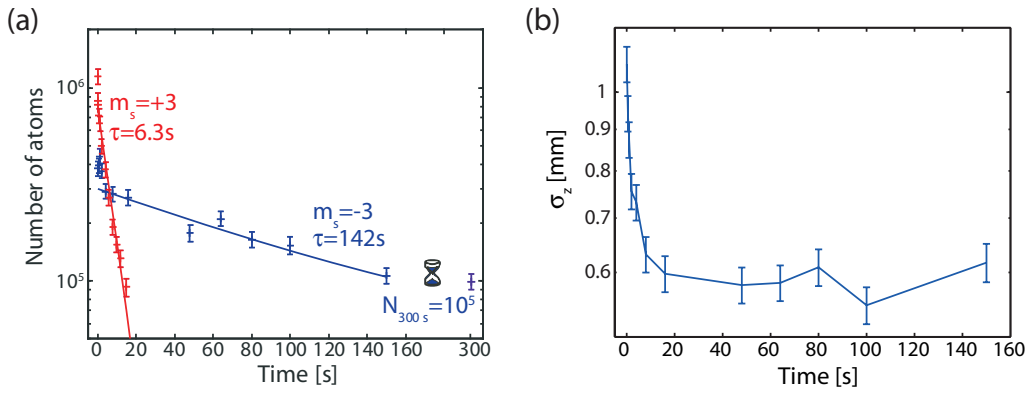

Figure 6.5: (a) The lifetime in the dipole trap increases from 6.3 s in the m_s =+3 state to 142 s after optical pumping all the atoms into the energetically lowest state m_s =-3. The fast initial decay in the first 10 s can be mainly attributed to atom loss due to an initial plain evaporation. This can be seen in figure (b) which shows σ_z, the elongation of the cloud in the z-direction.

called plain evaporation. As depicted in Fig. 6.5(a) a steady state is reached after about 10 s. This observation is supported by Fig. 6.5(b) which shows the evolution of the size of the atomic sample in the dipole-trap over time. From Eq. (5.18) we see that the size of the atomic cloud in the trap is proportional to its temperature, i.e. the temperature decreases during the first 10 s.

The next step is to slowly switch the second dipole trap beam on. Since the second dipole beam is perpendicular to the first one, a so called "dimple" potential is formed: The second beam provides additional strong confinement in the weak direction of the first dipole beam. The deformation of the trap potential by the dimple thus leads to an increase of the phase-space density [179, 218] which is determined by the ratio of the dimple volume to the trap volume and the depth of the dimple. To prepare a sample of up to 120 000 atoms at a temperature of 6 μK and a peak-density of $5 \cdot 10^{13}$ $1/\mathrm{cm}^3$ in a crossed optical dipole trap, we continue the evaporation by ramping down the intensity of the stronger of the two laser beams to 5 W.

6.2 Feshbach measurements

To locate the Feshbach resonances in ^{52}Cr [224] we look for an increase of atom loss by three-body recombination. As already explained in Chapter 3.4 the three-body loss rate L_3 is proportional to the scattering length to the power of four.

Before delving into the experimental details, we would like to develop a qualitative understanding of the behavior of the atom-number when the magnetic field crosses a

Feshbach resonance. The density of our sample is reduced over time due to collisions with the hot background gas (L_1) and two- and three-body losses (L_2, L_3):

$$\dot{n} = -L_1 n - L_2 n^2 - L_3 n^3 \,. \tag{6.4}$$

First of all we can safely neglect background gas collisions and two-body losses, since these only play a role on timescales much larger than those relevant for the Feshbach measurements (typically $< 1\,\mathrm{s}$). Since we are interested in the number of atoms and not in the density, we need to integrate over the trap volume. For a harmonic trap with average trap frequency $\bar{\omega}$ we get

$$\dot{N} = \int \dot{n}\,\mathrm{d}V = -L_3' \frac{N^3}{T^3} \text{ with } L_3' = \left(\frac{m\bar{\omega}^2}{2\pi k_\mathrm{B}}\right) \frac{1}{\sqrt{27}} L_3 \,. \tag{6.5}$$

The solution to this differential equation is

$$N(t) = \frac{T^{3/2}}{\sqrt{\frac{T^3}{N^2(0)} + 2L_3' t}} \,. \tag{6.6}$$

Substituting into the equation for L_3' the a^4 proportionality of L_3 (see Eq. (3.46)) and expressing the behavior of a near a Feshbach resonance through Eq. (3.30) gives

$$N(t) = \frac{T^{3/2}}{\sqrt{\frac{T^3}{N^2(0)} + \frac{n_l C \hbar m^2 t a_0^4 \left(1 - \frac{\Delta}{B - B_0}\right)^4 \bar{\omega}^6}{12\sqrt{3} k_\mathrm{B}^3 \pi^3}}} \,. \tag{6.7}$$

In Figure 6.6 the divergence of the scattering length a on a Feshbach resonance is shown together with the atom loss close to a resonance due to the increasing three-body recombination rate. For high positive values of the non-resonant scattering length, the incursion can show an asymmetry with a shallower slope for magnetic field values below the Feshbach resonance[7]. One should be aware though, that our model is quite simple. Theoretical calculations show that C is not constant, but will oscillate between C=0 and C=70 close to a Feshbach resonance [13, 23]. Additionally, we need to take the finite temperature of the atomic sample into account, this would require the convolution of Eq. 6.7 with the Maxwell-Boltzmann distribution. Due to the asymmetry of the Maxwell-Boltzmann distribution, the slope at lower magnetic fields is less steep.

After preparing a cool and dense atomic sample in our optical dipole trap we are set to start searching for Feshbach resonances. The necessary homogeneous offset field is generated using the pinch coils. We chose to employ the pinch coils instead of the

[7] If the non-resonant scattering length is negative, the shallower slope will be found above the resonance.

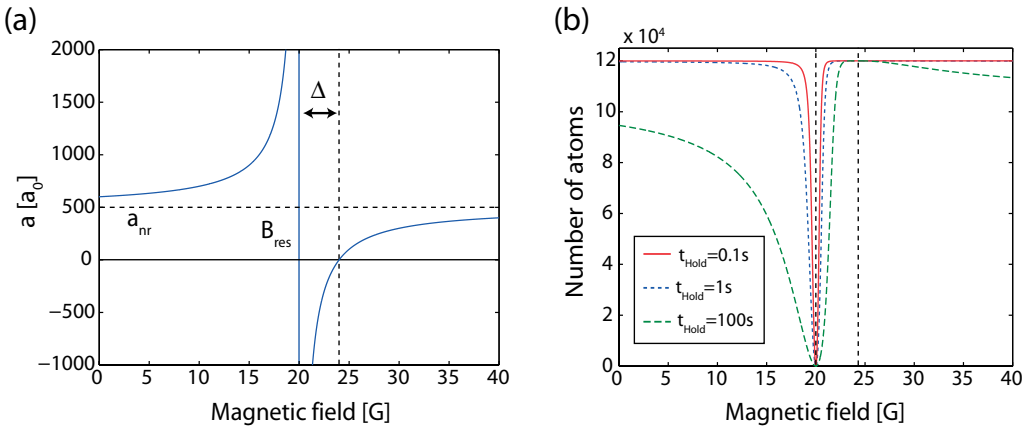

Figure 6.6: Theoretical calculation of the behavior of the scattering length (a) and the remaining number of atoms (b) with the magnetic field for different hold times. With increasing hold time the observed loss feature broadens. For $t_{\mathrm{Hold}} = 100\,\mathrm{s}$ we can also see that the inelastic losses are suppressed for $a = 0$. The plots were calculated under the following conditions: a_{nr} =500 a_0, $\Delta = 4\,\mathrm{G}$, B_0=20 G, N_0=120 000 atoms, T=6 μK and ω=2 400 Hz.

offset coils, even if the field generated by the pinch coils is not as homogeneous as the field generated by the offset coils due to their geometrical configuration. The pinch coils though, generate less residual eddy currents in the chamber and the vacuum copper seals, thus allowing shorter switching times of the magnetic field. Fast switching of the magnetic field is necessary to prevent atom loss when the magnetic field is passing over a lower lying Feshbach resonance. The inhomogeneity in the magnetic field leads to a variation across the cloud on the order of 50 mG. In the magnetic field region between 0-20 G we use the z-compensation field instead, since it allows a finer control of the magnetic field and the generated magnetic field is homogeneous due to the Helmholtz-configuration of the coils.

The search itself is performed by first sweeping the magnetic field strength in coarse steps on the order of 1 G–3 G from 0 G to 600 G. Smaller sweep ranges are then used in regions where atom loss was observed. To find the precise location of the resonances a different method is used. The magnetic field is ramped up to a value close to the resonance in about 5 ms. We hold the magnetic field for 2 s to let the current settle and to give our magnetic coils time to thermalize. Then the magnetic field is quickly ramped to the desired value and held there for a variable amount of time. The holding time is chosen to clearly resolve the resonance and lies between 100 ms and 10 s. Finally, the magnetic field is switched off and an absorption image is taken. The typical result of such a Feshbach measurement is shown in Fig. 6.7 on the next page. Shown are (a) the atom loss and (b) the temperature increase for magnetic fields close to a Feshbach resonance. The temperature increase is partly

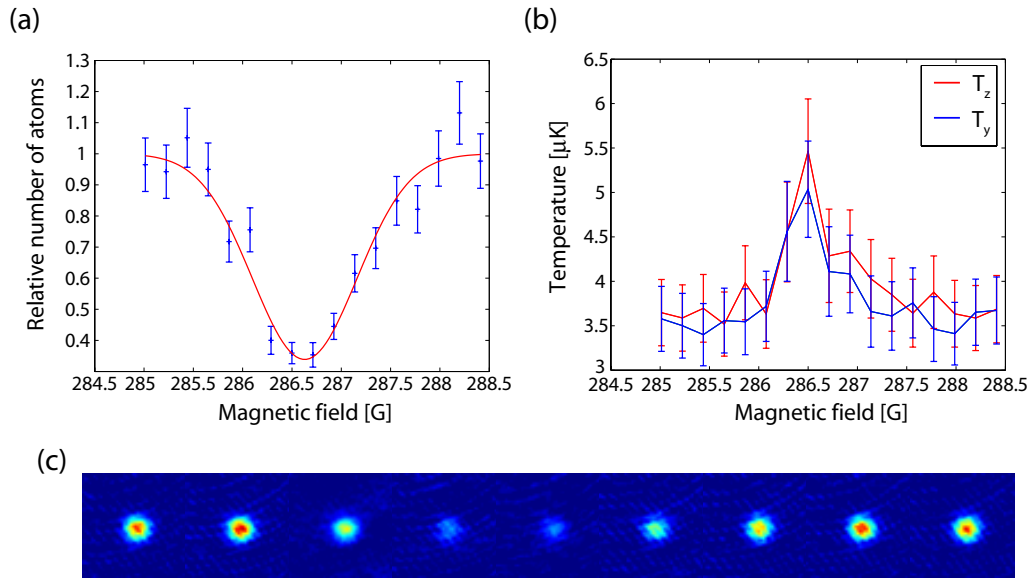

Figure 6.7: Feshbach resonance at 286.6 G. On a Feshbach resonance the atom number decreases, while the temperature increases. Shown are (a) the relative atom number and (b) the temperature over the magnetic field. (c) shows the corresponding absorption image pictures of the atomic cloud (every other picture has been omitted for space reasons).

due to the binding energy of the molecule which the third atom takes away and distributes it in the atomic sample through collisions. A second source for the heating is anti-evaporation.

The resolution limit of our measurements is below 100 mG at B=600 G. It is the result of three different contributions. We already mentioned the inhomogeneity of the magnetic field, which accounts for 50 mG. The finite temperature of our sample gives rise to an additional uncertainty in the resonance location that is of the same magnitude. The experimental noise of the magnetic field accounts for another 40 mG.

6.3 Calibration and data evaluation

The description of the basic fitting and data extraction methods from the absorption images was already covered by Schmidt [209] and will be not repeated here. We will concentrate on the additional steps necessary for extracting the required values for the Feshbach measurements. The positions and widths of all the observed loss features are determined by a gaussian fit to the data, see Fig. 6.8(a). We decided to use a gaussian instead of Eq. (6.5), since our measurements did not show an asymmetry and also for convenience. From the depths of these loss features though, one can estimate an upper limit for the three-body loss coefficient L_3 using Eq. (6.5).

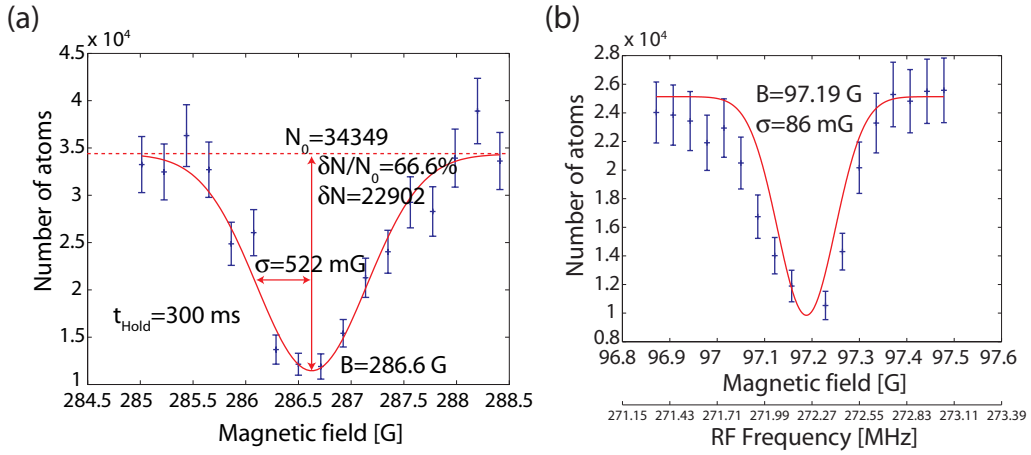

Figure 6.8: (a) An inverted gaussian is fitted to the atom number measurement of each loss feature. From this gaussian fit the following information is obtained: Position of the Feshbach resonance, width and depth of the loss feature, off-resonant number of atoms. Together with the off-resonant temperature and density of the atomic sample, the L_3 coefficient can be calculated. (b) Calibration of the magnetic field with rf-spectroscopy. The rf-frequency at which the loss feature occurs determines the magnetic field to which the atoms are exposed.

The intrap size was inferred from the size of the cloud after a certain time-of-flight and the trap frequencies. Eq. (5.18) allows then to calculate the temperature of the atoms. Together with the trap size and the trap frequencies, the calculation of the density is now easily done.

The magnetic field was calibrated separately slightly below and above each resonance using rf-spectroscopy: a radio-frequency sweep transfers the atoms into higher m_s-levels via adiabatic rapid passage. From there they can undergo dipolar relaxation processes and are thus lost from the trap. By changing the center frequency of the radio-frequency sweep and monitoring the atom-loss we can determine the value of the magnetic field with a one-standard deviation uncertainty of 100 mG (see Fig. 6.8(b)). The calibration of each resonance was done immediately after a measurement of the loss feature position, to preclude errors due to day-to-day changes of the laboratory/cooling-water temperature which influence the accuracy of the calibration. For the two highest resonances above 450 G this method was not applicable any more, since the irradiated rf-power by the employed rf-antenna was too low to drive transitions between different m_s states at frequencies above 1.2 GHz[8].

[8] We employed the same antenna which is also used for evaporative cooling. This antenna (and the whole rf-system) was designed for low frequencies. Due to the unknown impedance of the antenna at such high frequencies and the unknown losses in the coaxial cables we are not able to estimate the irradiated power in the chamber. To generate the required rf-frequencies we

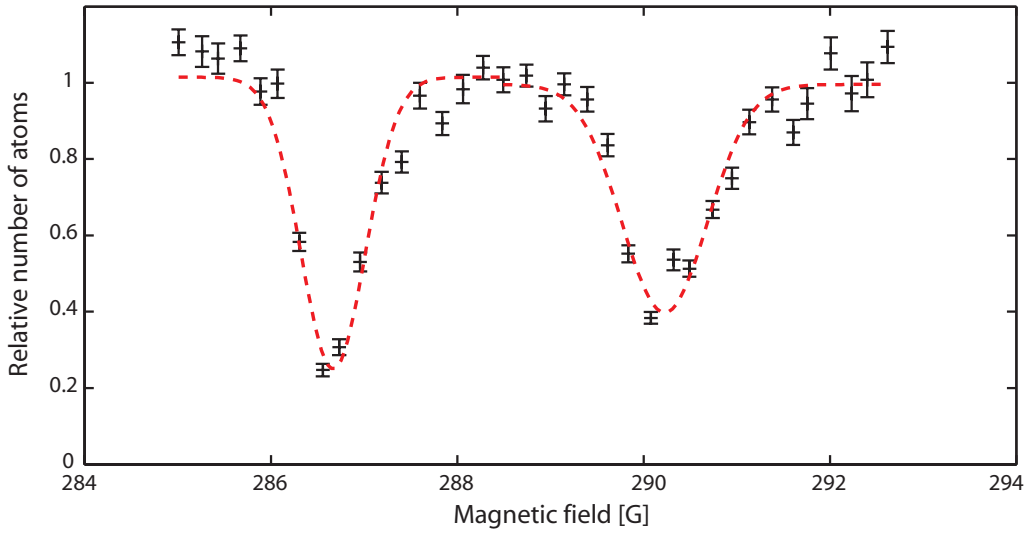

Figure 6.9: Inelastic loss measurement of the Feshbach resonances at 286.6 G and 290.3 G. The dashed lines are gaussian fits to the data and determine the position and width of the loss features. The experimental data points are averages over many experimental measurements. Each measurement was separately normalized to the offset of a gaussian fit to the data.

We thus had to resort to extrapolation of the applied magnetic field for these two resonances from three magnetic field calibrations at 270 G, 360 G and 440 G.

6.4 Experimental results

Using the techniques described above we were able to observe fourteen Feshbach resonances for magnetic fields below 600 G. All fourteen loss features are shown in Fig. 6.13 together with their position and width. These values are also tabulated in Table 6.2. If the loss feature was observed more than once, the given width and L_3 coefficient are the average of all measurements. The given positions stem only from calibrated measurements, which were only done once. Of all fourteen resonances we investigated the two loss features near 290 G more closely. This was done to see if two loss features are lying close to each other "by chance", or if it is one resonance which splits up into a multiplett (see Chapter 6.6.2). Figure 6.9 shows the result of thirteen measurements of these two resonances. Each measurement was separately normalized by fitting a gaussian to the data to determine the offset. Since not all measurements were done at the same field, we had to take an average over all points in approx. 100 mG wide bins. The error bars in the figure are mainly determined by

used a signal generator from Rohde & Schwarz, Model SMY02

the atom number fluctuation. For a multiplett to exist, we would have expected at least an additional third resonance, which we did not observe. We thus were able to conclude that the two resonances are close to each other just "by chance".

Even though searching for Feshbach resonances is quite tedious and time consuming it is a straightforward process. In addition to the knowledge of the resonance positions we need to identify which bound state is responsible for each Feshbach resonance. To be able to do this assignment, we need to take closer look at the origin of the interaction potentials, the possible couplings between the open and closed channels and the resulting selection rules.

6.5 Multi-channel calculations

From the experimentally measured positions of the Feshbach resonances one can deduce several characteristic values of the relevant interaction potentials. This is done by starting with a model-potential characterized by a handful of parameters. For this model-potential the Schrödinger equation needs to be solved. From the solution we can determine the position of the Feshbach resonances for this model potential. The theoretical positions are then compared to the experimental values to see if they coincide. If this is not the case the model-potential parameters are adjusted slightly and the whole process is repeated. Of critical importance for this method to work reliably is the interaction potential.

6.5.1 Modeling of the potential

In a quantum mechanical description of interaction processes between two atoms, one should in principle take into account the electric and magnetic forces between all electrons and nuclei involved in the process. Even for simple atoms, like alkalis, this turns out to be way to complex to calculate. It can be shown [130] that one is allowed to make two approximations which simplify the calculations immensely. The first one is the well known Born-Oppenheimer approximation. Due to the much higher mass of the nuclei their motion is much slower than the motion of the electrons. Thus the electrons can immediately follow the motion of the nuclei. This allows to separate the molecule wave function into a product of the nuclei wave function and the electronic wave function. The second is the Shizgal [213] approximation, which assumes that all spins are located at the position of their respective nucleus. Together this results in an interaction potential V, which only depends on the nuclei distance and the spin quantum numbers

$$V = \sum_{j=1}^{2} (V_j^{\mathrm{HF}} + V_j^{\mathrm{Z}}) + V^{\mathrm{C}} + V^{\mathrm{SS}} + V^{\mathrm{SO}} \,. \tag{6.8}$$

It is comprised out of the single-atom hyperfine V_j^{HF} and Zeeman term V_j^{Z} for each atom, a central two-atom interaction term V^{C} and the dipole-dipole interactions V^{SS} and V^{SO}.

Hyperfine interaction

The hyperfine interaction describes the coupling of the (valence) electron spin $\vec{s}$ and the nuclear spin $\vec{i}$ to the total spin $\vec{f}$. We will use lower case letters for single-atom spin operators and quantum numbers and reserve capital letters for two-atom spins. The hyperfine term V_j^{HF} is thus given by

$$V_j^{\mathrm{HF}} = \frac{a_j^{\mathrm{HF}}}{\hbar^2} \vec{s}_j \cdot \vec{i}_j \,, \tag{6.9}$$

where a_j^{HF} is the hyperfine splitting constant. Since ^{52}Cr has no nuclear spin, the hyperfine interaction can be omitted from Eq. (6.8).

Zeeman interaction

The Zeeman interaction of the atoms with an external magnetic field is essential for magnetically induced Feshbach resonances. It has the familiar form

$$V_j^{\mathrm{Z}} = -\vec{\mu}_j \cdot \vec{B} = \frac{\mu_{\mathrm{B}}}{\hbar} g_s \vec{s}_j \cdot \vec{B} = \frac{\mu_{\mathrm{B}}}{\hbar} g_s m_{s,j} B \,, \tag{6.10}$$

where g_s is the Landé-factor for the electron and m_s the projection of $\vec{s}$ on the magnetic field direction. The value of the Landé-factor for ^{52}Cr was determined by Childs and Goodman [35] to be $g_s = 2.00183$, which is close to the value of the electron g factor of[9] $g_s = 2.002319$.

Central interaction

The central interaction V^{C} depends only on the quantum number S associated with the magnitude of the total electronic spin $\vec{S} = \vec{s}_1 + \vec{s}_2$ which can be between 0 and 6 for ^{52}Cr. It consists out of two contributions

$$V^{\mathrm{C}} = V^{\mathrm{ex}} + V^{\mathrm{disp}} \,, \tag{6.11}$$

where V^{ex} is the electronic exchange interaction and V^{disp} is the dispersion interaction. The exchange interaction stems from the overlap of both electron clouds and is short-ranged due to its exponential behavior [99, 153, 227]. If the two atoms are very

[9] Brix et al. [26] gives some possible explanations for this discrepancy.

close they will repel each other due to the Pauli principle. At intermediate distances, where the inner electron shells do not overlap any more, the relative spin orientation of the valence electrons determines the position and depth of the potential minimum. Are the spins aligned, the potential will be very shallow, since both atoms repel each other. Is this not the case, they will attract each other due to the covalent binding and the resulting potential will be deep. The dispersion interaction dominates at long range and describes the attractive interaction between the induced electric multipoles. It is given by

$$V^{\mathrm{disp}} = -\frac{\mathrm{C}_6}{r^6} - \frac{\mathrm{C}_8}{r^8} - \frac{C_{10}}{r^{10}} - \dots \,, \tag{6.12}$$

where C_6, C_8 and C_{10} are the dispersion coefficients.

Magnetic dipole-dipole interaction

In elements with a high magnetic moment, like ^{52}Cr the spin-spin or dipole-dipole interaction term V^{SS} becomes relevant. It leads to a long-ranged potential of the form

$$V^{\mathrm{SS}} = \frac{\mu_0 (g_s \mu_\mathrm{B})^2}{4\pi} \frac{\vec{s}_1 \cdot \vec{s}_2 - 3(\vec{s}_1 \cdot \hat{R})(\vec{s}_2 \cdot \hat{R})}{R^3} \,. \tag{6.13}$$

Here $\vec{s}_{1,2}$ are the electron spin of each atom and $\vec{S} = \vec{s}_1 + \vec{s}_2$ the resulting total electronic spin. $\hat{R}$ and R are the orientation of the internuclear axis and internuclear separation, respectively. V^{SS} is not spherical symmetric, so the angular momentum ℓ is not conserved. The dipole-dipole interaction thus allows the redistribution of angular momentum between the spin $\vec{S}$ and the orbital angular momentum ℓ.

Another way of writing this interaction that isolates the spin and partial-wave operators is

$$V^{\mathrm{SS}} = \frac{\mu_0 (g_s \mu_\mathrm{B})^2 \sqrt{6}}{4\pi R^3} \sum_{q=-2}^{q=2} (-1)^q T^2_q (s_1 \otimes s_2)^2_{-q} \,. \tag{6.14}$$

Here T^2_q is a reduced spherical harmonic that depends on the relative orientation of the atoms, and $(s_1 \otimes s_2)^2_{-q}$ is the second rank tensor formed from the rank-1 spin operators [40, Section $\mathrm{B_{XI}}$]. Each term of the sum stands for a different physical process. For $q = \pm 2$ both spins are flipped, for $q = \pm 1$ one of the spins is flipped up or down. $q = 0$ describes elastic scattering where no spins flip. Since the total angular momentum has to be conserved m_ℓ has to change accordingly, i.e. $\Delta m_s + \Delta m_\ell = 0$. This can also be easily seen from the matrix element for V^{SS}

$$\langle\, \ell m_\ell \,|\, V^{\mathrm{SS}} \,|\, \ell' m'_\ell \,\rangle \propto \int Y_{\ell'}^{m'_\ell *}(\theta,\varphi) Y_2^q(\theta,\varphi) Y_\ell^{m_\ell}(\theta,\varphi) \mathrm{d}\Omega \tag{6.15}$$

which according to the properties of the spherical harmonic functions $Y_\ell^{m_\ell}$ is different from zero only for $\ell' = \ell, \ell-2, \ell+2$, $m'_\ell = m_\ell + q$ with the exception of $\ell = \ell' = 0$ which vanishes by symmetry. The possible values for Δm_ℓ can thus vary between $-2 \ldots + 2$.

Spin-Orbit interaction

In addition to the spin-spin interaction there is another interaction which allows to redistribute angular momentum between spin and orbital angular momentum, the second-order spin-orbit interaction V^{SO} [153]. It originates when the atomic charge clouds overlap as a molecule is formed, and the interaction between the ground state spins are modified due to couplings mediated through distant excited electronic states of the molecule. These interactions are well known in molecular spectroscopy and mimic the direct spin-spin coupling [130] due to the same tensor structure. The spin-orbit interaction decays exponentially (similar to the exchange interaction) and is thus short-ranged, while the spin-spin interaction shows a $1/R^3$ behavior. Note, that the signs of V^{SO} and V^{SS} are different, so they can compensate each other. For heavy species like Rb and Cs these indirect terms can be much larger than the V^{SS} term at short distances and strongly influence the spin-relaxation rate [153].

Let's now apply the above knowledge to ^{52}Cr. The isotropic interactions between two ground state ^{52}Cr atoms can be described by Hund's case (a) $^{2S+1}\Sigma^+_{g/u}$ Born-Oppenheimer potentials[10]. The large number of valence electrons leads to seven Born-Oppenheimer potentials instead of two for ground state alkali-metal atoms. For ^{52}Cr even (odd) S implies g (u) symmetry, respectively.

Theoretical *ab-initio* calculations [7, 176] exist but are extremely challenging for ^{52}Cr. Figure 6.10 shows the resulting potentials of the *ab-initio* calculations by Pavlovic et al. [176]. On the experimental side conventional spectroscopic data only exists for the ground state $^1\Sigma^+_g$ potential [31].

We construct $^{2S+1}\Sigma^+_{g/u}$ Born-Oppenheimer potentials V_S by smoothly joining a short-range $R \leq R_x$ model potential with the well-known long-range dispersion potential $\sum_n -C_n/R^n$, in which we only retain the $n = 6$ and 8 terms. The connection point

[10] Hund's case (a) is applicable when the interaction of the nuclear rotation with the electronic motion(spin as well as orbital) is very weak, whereas the electronic motion itself is coupled very strongly to the line joining the nuclei [105]. This means that L the orbital angular momentum of the electrons couples to the electrostatic field produced by the nuclei along to the internuclear axis, with Λ being the projection onto the internuclear axis. S the total electronic spin couples then to the magnetic moment produced by L (with Λ being the projection along the internuclear axis). Finally adding the nuclear rotation R results in the total molecular angular momentum J. The notation for Hund's case (a) is $^{2S+1}\Lambda^\sigma_{\pi_e}$. $\Lambda = 0, 1, 2, 3, \ldots$ is denoted by $\Sigma, \Pi, \Delta, \Phi, \ldots$. σ is the symmetry upon reflection at a plane through the internuclear axis (either + or -) and π_e the parity of the wave function (g/u which stands for *gerade/ungerade*)

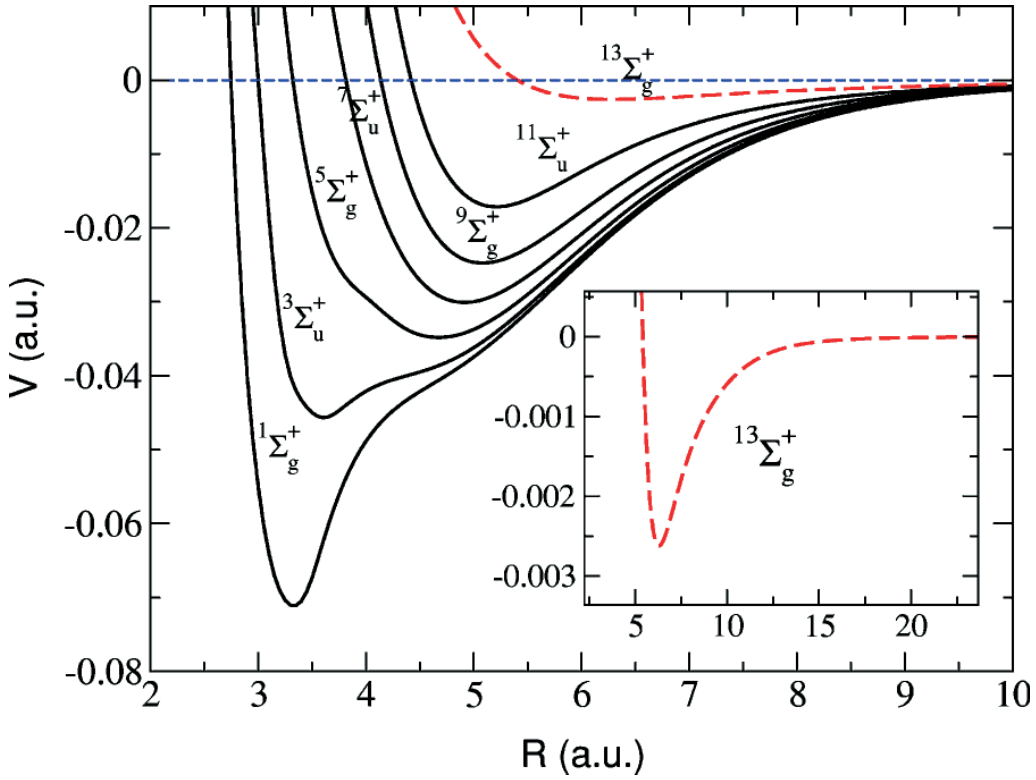

Figure 6.10: Potential curves for the ground state manifold of Cr_2 computed with the CASSCF/CASPT2 method. The maximally spin-stretched electronic state $^{13}\Sigma_g^+$is shown as a dashed line and in detail in the inset. Figure taken from [176].

$R_x = 17.5\ a_0$ is chosen such that each V_S can be well represented by its long-range form beyond R_x and its value at R_x is much larger than the collision and bound-state energies of interest here. The inner wall and dissociation energy of the model potentials approximately agree with Pavlovic et al. [176]. Details of the short-range potentials are unimportant at ultracold temperatures. We allow for variation of C_n and include short-range corrections near the minimum of each potential curve. This allows us to independently tune C_n and the s-wave scattering lengths a_S of V_S to fit the experimental data. The number of bound states of V_S is uncertain to ± 10 for the deeper potentials.

6.5.2 Quantum numbers and selection rules

When the atoms are far apart, the eigenstates of the dimer are $|\, SM_S; \ell m_\ell \,\rangle$, in which M_S and m_ℓ are projections of $\vec{S}$ and $\vec{\ell}$ along $\vec{B}$. The total projection $M = m_\ell + M_S$ and parity $(-1)^\ell$ are conserved during the collision. As the nuclei of the atoms are

	1^{st} order	2^{nd} order
$\Delta\ell$	$0, \pm 2$	$0, \pm 2, \pm 4$
Δm_ℓ	0^a, $\pm 1, \pm 2$	$0, \pm 1, \pm 2, \pm 3, \pm 4$
ΔS	$0, \pm 2$	$0, \pm 2, \pm 4$

[a] not allowed for $\ell = 0 \rightarrow \ell' = 0$!

Table 6.1: Selection rules for a dipole-dipole transition to 1^{st} and 2^{nd} order.

identical only states with $(-1)^{S+\ell} = 1$ exist due to the symmetrization. In absence of an interaction, the Hamiltonian conserves $\vec{\ell}$ and $\vec{S}$ as well.

When looking at the different contributions to the potential operator discussed in the previous section, it turns out that only the Coulomb, spin-spin and spin-orbit terms provide the necessary coupling for the existence of Feshbach resonances. In alkalis the Coulomb interaction is the dominating interaction, while the spin-spin and spin-orbit interactions are much weaker [142]. The situation in ^{52}Cr is quite different. The Coulomb interaction also exists, but due to the selection rule $\Delta M_S = 0$ the incoming and the bound state will exhibit the same magnetic moment and can thus not be tuned relative to each other[11]. Due to the much higher magnetic moment of ^{52}Cr of $6\,\mu_B$, the spin-spin interaction is a factor of 36 higher than for alkalis which typically have a magnetic moment of $1\,\mu_B$. The contribution of the spin-orbit interaction can be neglected for ^{52}Cr, since it is much weaker than the spin-spin interaction. This has to be contrasted with the situation in the heavier alkalis like Rb and Cs, where spin-spin and spin-orbit interaction can be of the same order. This has two reasons: First, the lower magnetic moment of Rb and Cs and second, due to being heavier the spin-orbit interaction is more pronounced. We will see later on, from the results of our calculations that neglecting the spin-orbit interaction is really justified. The only relevant interaction for ^{52}Cr is thus the spin-spin interaction and it thus determines the relevant selection rules for the possible Feshbach resonances.

As we have seen in the previous section, the anisotropic spin-spin dipole interaction couples states with $\Delta S = 0, 2$ and $\Delta\ell = 0, 2$ with $\ell = 0 \rightarrow \ell' = 0$ transitions forbidden. In Table 6.1 we have compiled an overview over the possible changes in the quantum numbers for first and second-order spin-spin transitions. This is further complicated by the the fact, that due to the conservation of the total projection $\Delta M = \Delta m_\ell + \Delta M_S = 0$ every change in m_ℓ has to be reflected in

[11] In alkalis which exhibit a Hyperfine-splitting the selection rule is accordingly $\Delta M_F = 0$ and a Feshbach resonance is possible between states with different F but same M_F. Due to the different F both states can exhibit different magnetic moments.

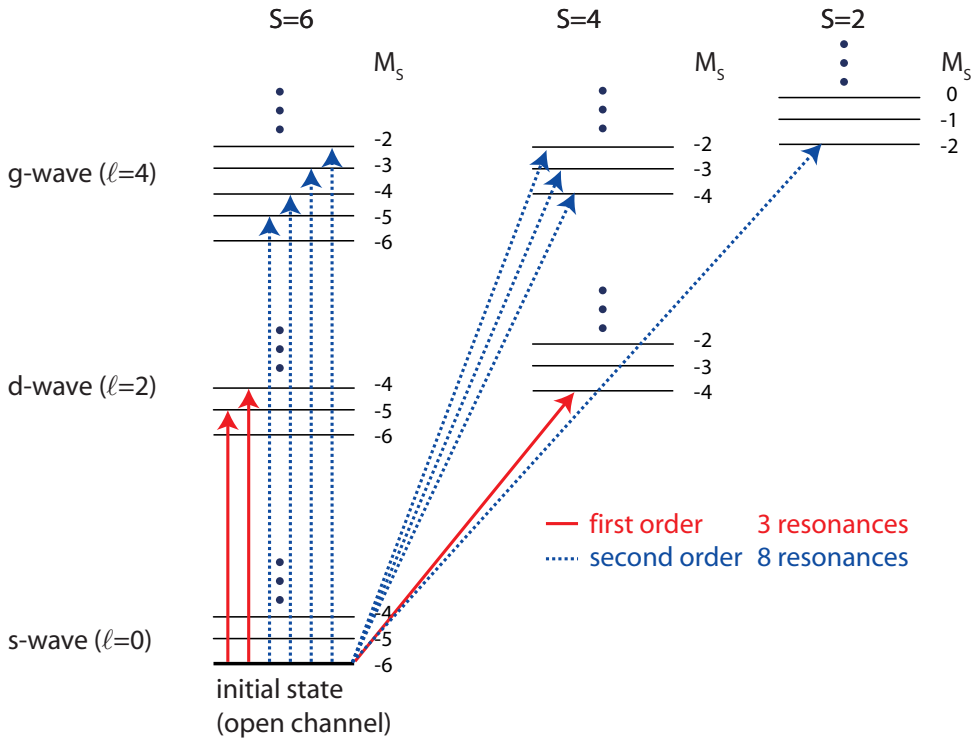

Figure 6.11: Shown are all possible transitions from the open channel $|\, S = 6, M_S = -6; \ell = 0, m_\ell = 0 \,\rangle$ according to the selection rules for the dipole-dipole interaction up to second-order. For a better overview the different Born-Oppenheimer potentials have been grouped in columns, while the different angular momenta $\ell = 0, 2, 4$ form the rows. The position of a state does not necessarily reflect its energy

M_S. This rules out some possibilities due to the violation of other selection rules. Our sample is spin polarized, so that the incoming state has quantum numbers $|\, S = 6, M_S = -6; \ell = 0, m_\ell = 0 \,\rangle$ by straightforward angular momentum addition. Figure 6.11 shows graphically all possible transitions to first and second-order for our incoming state.

6.5.3 Assignment of the Feshbach resonances

Now that we have determined our model potential and the possible coupling mechanism, we can turn our attention to the task of assigning quantum numbers to the experimentally observed Feshbach resonances. This is done by calculating the molecular bound state energies for each basis state $|\, SM_S; \ell m_\ell \,\rangle$ separately. For this we use the Hamiltonian of a pair of $^7S_3$ chromium atoms in an external magnetic field $\vec{B}$ which includes the seven isotropic Born-Oppenheimer potentials, the nuclear

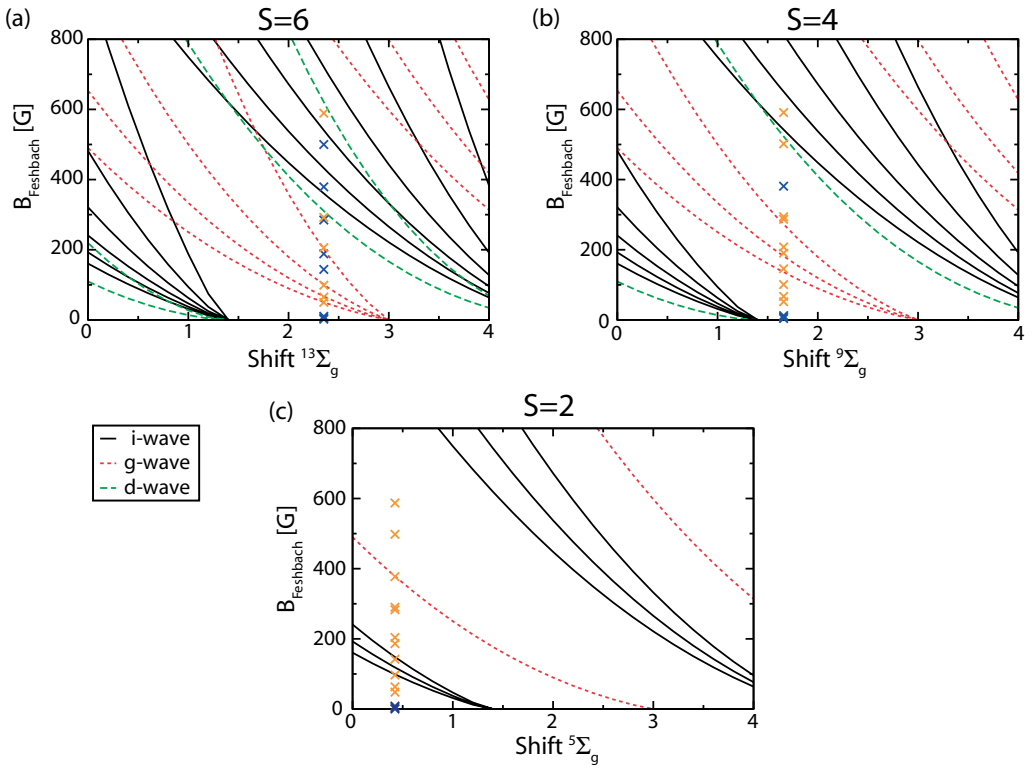

Figure 6.12: Theoretical calculations of the bound state energy for S=6,4,2 depending on the depth of the relevant model potential (denoted as shift). Also shown are the experimental values for the observed Feshbach resonances. The assignment of the resonances is done by locating the depth of the potential for which most of the experimental data points can be reproduced. This is first done for S=6 and then S=4 and 2. Already assigned experimental data points are shown in orange, while still unassigned points are drawn in blue.

rotational energy $\hbar^2\vec{\ell}^2/(2\mu R^2)$ where $\vec{\ell}$ is the orbital angular momentum of the nuclei and μ the reduced mass of the diatom and the Zeeman interaction with the magnetic field. For now we neglect the spin-spin interaction. By solving the Schrödinger equation using the DVR method described in Chapter 3.3.2 on page 44 we obtain the energies of all bound states[12]. Since we know the magnetic moment of each basis state, we can infer the magnetic field which is necessary for the bound state to come into resonance with the incoming channel $|\, S=6, M_S=-6; \ell=0, m_\ell=0\,\rangle$. As we do not know exactly the real depth of our potential, we need to vary the depth of our model potentials and see how the positions of the Feshbach resonances behave. Figure 6.12 shows this behavior for $S=6,4,2$ and the accordingly allowed ℓ values. Now we are set to do the assignment. For each spin-state $S=6,4,2$ separately we

[12]The resulting energies are listed in Appendix A.2.

need to find a potential depth, where the theoretically predicted Feshbach resonance position matches as many experimental positions as possible. During matching we also need to take into account the strength of the coupling. On the theory side we know that a first order coupling is stronger than a second-order coupling. Experimentally a stronger resonance will exhibit a broader width and a higher L_3 coefficient. In Fig. 6.12 the crosses with the experimental values of the Feshbach resonances show the chosen assignment. The resulting assignment of S, M_S, ℓ, and m_ℓ to each experimentally observed resonance from this approximate model are shown in Table 6.2.

We find that, in addition to the incoming state, states with $\ell = 2$ and 4 (d and g) partial waves and $S = 2, 4$, and 6 have to be coupled together in order to explain the 11 strongest observed features of Table 6.2. Even though no term in the molecular Hamiltonian directly couples $\ell = 4$ states to the $\ell_i = 0$ state, second-order mixing in the spin-spin dipole interaction via $\ell = 2$ states is relevant in ^{52}Cr.

So far, we have focused on incoming $\ell_i = 0$ s-wave scattering and thus assumed $M = -6$. We do observe resonances due to collisions from $\ell_i = 2$ partial d waves with $M = -4, \ldots, -8$ corresponding to different orientations of the internuclear axis. The pair near 4 G and 8 G is due to such collisions. These additional features are strongly suppressed at our temperatures and we are only able to detect them at fields $B < 20$ G where we have larger atom numbers and an optimal control of the magnetic field strength. We are not able to infer from our data a conclusive assignment of the weakest observed resonance at 6.1 G. A complete overview over all the experimentally observed resonances and their assignment is shown in Fig. 6.13 on the next page.

When the spin-spin dipole interaction is neglected — as we did up to now — a simple resonance-pattern for the Feshbach resonances is expected. Scattering is then independent of m_ℓ and the resonances occur at $B_{\text{res}} = E_B/(g_s\mu_B(M_S + 6))$ (see Fig. 6.14, where E_B is one of the zero-field binding energies of the potential $V_S(R) + \hbar^2\ell(\ell+1)/(2\mu R^2)$). From Fig. 6.14 on page 112 we see that the theoretical resonance structure qualitatively reproduces the experimental data, but quantitatively we still observe deviations as large as ≈ 10 G. As we will see in the next section this will be remedied by the inclusion of the spin-spin dipole interaction.

6.5.4 Position of the Feshbach resonances

Now, that we know the assignment and more importantly the approximate depth of our model potentials, we can tackle the challenge to calculate the exact positions of the Feshbach resonances. The theoretical analysis now uses the same Hamiltonian as before, but now comprises also the anisotropic spin-spin dipole interaction. We do not include the second-order spin-orbit or spin-rotation interactions [130]. The

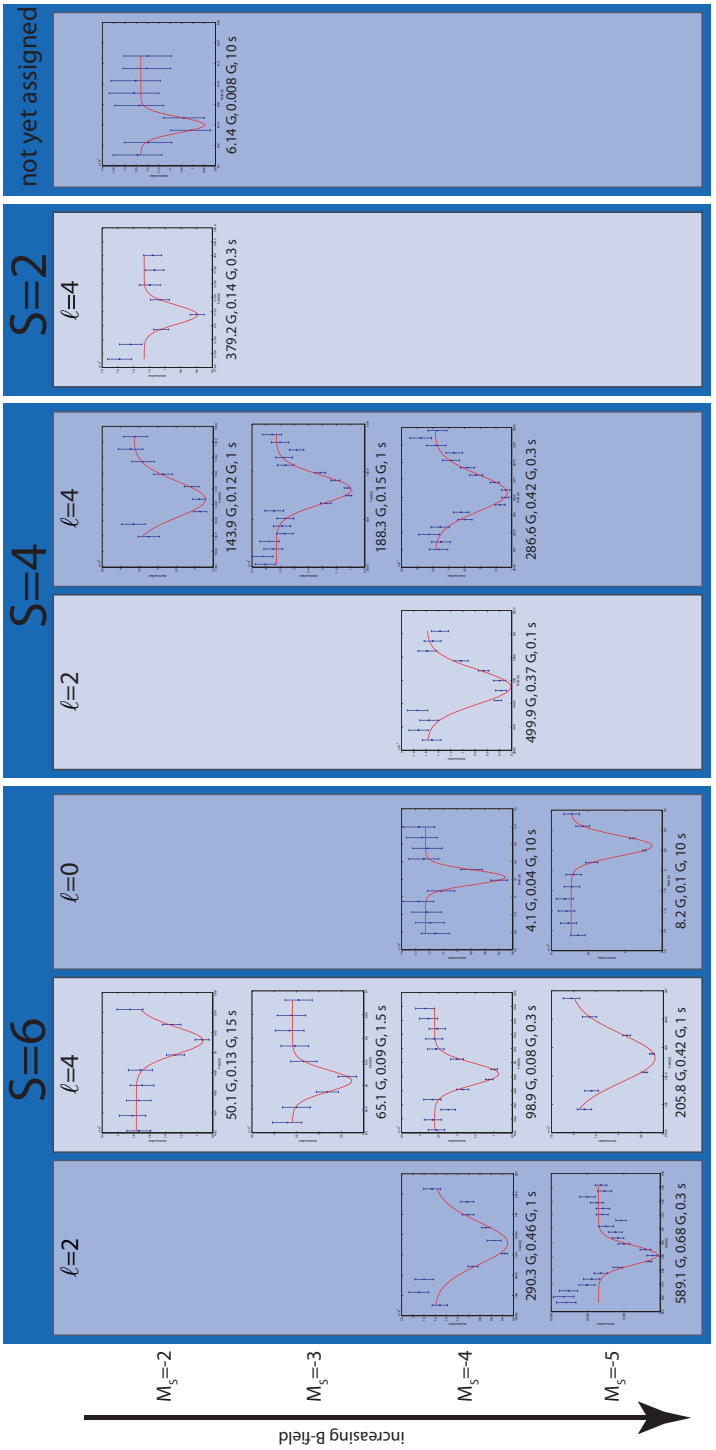

Figure 6.13: Overview over all fourteen resonances found in ^{52}Cr. They are grouped according to the quantum numbers of the bound state which couples to the incoming channel. Of special interest is the vertical grouping according to the magnetic sub-state M_S. The position of the resonance should behave according to $B_{\mathrm{res}} = 1/(M_S + 6)$. For each resonance the position, width and hold time is given.

Exp. Pos. [G]	Theo. Pos. [G]	Exp. Width ($1/\sqrt{e}$) [mG]	Theo. Δ [mG]	L_3 [cm^6/s]	$\ell_i; SM_S; \ell m_\ell$
4.1	4.0	40	...	$3 \cdot 10^{-28}$	2; 6, -4; 0 , 0
6.1	...	8	...	$8 \cdot 10^{-29}$	...
8.2	8.1	100	...	$4 \cdot 10^{-27}$	2; 6, -5; 0 , 0
50.1	50.1	140	$< 1 \cdot 10^{-3}$	$2 \cdot 10^{-26}$	0; 6, -2; 4, -4
65.1	64.9	90	$6 \cdot 10^{-3}$	$5 \cdot 10^{-26}$	0; 6, -3; 4, -3
98.9	98.5	90	0.30	$1 \cdot 10^{-24}$	0; 6, -4; 4, -2
143.9	143.2	120	0.12	$1 \cdot 10^{-26}$	0; 4, -2; 4, -4
188.3	187.9	150	0.22	$4 \cdot 10^{-26}$	0; 4, -3; 4, -3
205.8	205.6	420	12	$4 \cdot 10^{-24}$	0; 6, -5; 4, -1
286.6	288.0	430	12	$6 \cdot 10^{-25}$	0; 4, -4; 4, -2
290.3	290.7	470	51	$1 \cdot 10^{-25}$	0; 6, -4; 2, -2
379.2	379.2	140	0.42	$1 \cdot 10^{-25}$	0; 2, -2; 4, -4
499.9	499.2	370	81	$1 \cdot 10^{-24}$	0; 4, -4; 2, -2
589.1	589.2	680	1700	$3 \cdot 10^{-24}$	0; 6, -5; 2, -1

Table 6.2: Compendium of positions and strengths of the observed loss features, the theoretical positions, widths, initial partial wave, and assignment of the resonances. Theoretical calculations use a collision energy of $E = k_B T$ and parameters as described in the text. The one standard deviation uncertainty of the experimental resonance position is below 100 mG.

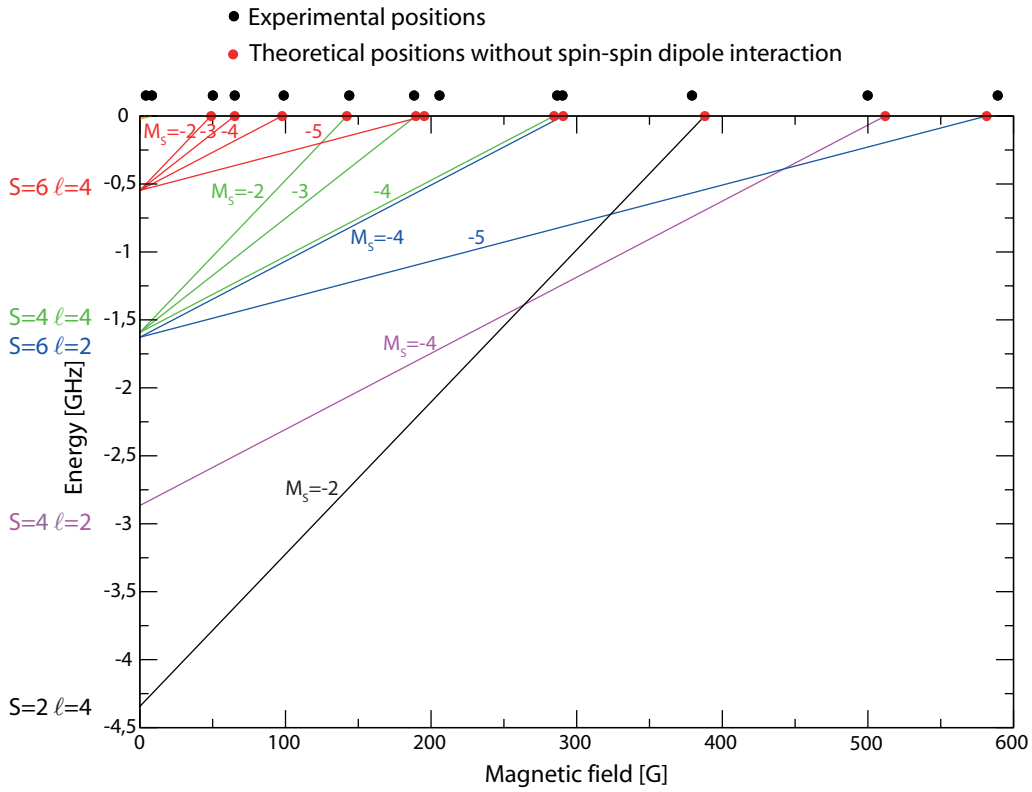

Figure 6.14: Dependence of the position of the bound states on the applied magnetic field. Every time a bound state reaches $E = 0$ a Feshbach resonance occurs. In this diagram also the origin of the different series of resonances can be seen. The open channel can for example couple to the bound state $S = 6$ $\ell = 4$ (shown in red) which splits due to the applied magnetic field into a series of four resonances for M_S =-2,-3,-4,-5. The bound state calculations were done disregarding the dipole-dipole interactions, which explains the deviation between the predicted and experimentally observed positions.

temperature of our sample, T≈6 μK, is small compared to the $\ell \geq 2$ centrifugal barrier[13] such that incoming $\ell_i = 0$ collisions dominate the scattering cross sections. As we saw in the assignment section though, we also need to consider $\ell_i = 2$ to reproduce two of the weakest resonances. For the numerical solution of the Schrödinger equation we now used Gordon's method as described in section 3.3.1.

The locations of the maxima in the experimental three-body loss rate are compared with locations of peaks in the elastic two-body cross section calculated by full quantum-scattering methods. We perform a global χ^2-minimization with parameters $a_{2,4,6}$, C_6 and C_8. Our best-fit parameters with one standard deviation are a_2=-7(20) a_0, a_4=58(6) a_0, a_6=112(14) a_0, C_6 =733(70) a.u., and $C_8 = 75^{+90}_{-75} \cdot 10^3$ a.u..

[13]The threshold temperatures are for $\ell = 2, 4$: $T_{\ell=2} \approx 1.1\,\mathrm{mK}$ and $T_{\ell=4} \approx 6.8\,\mathrm{mK}$

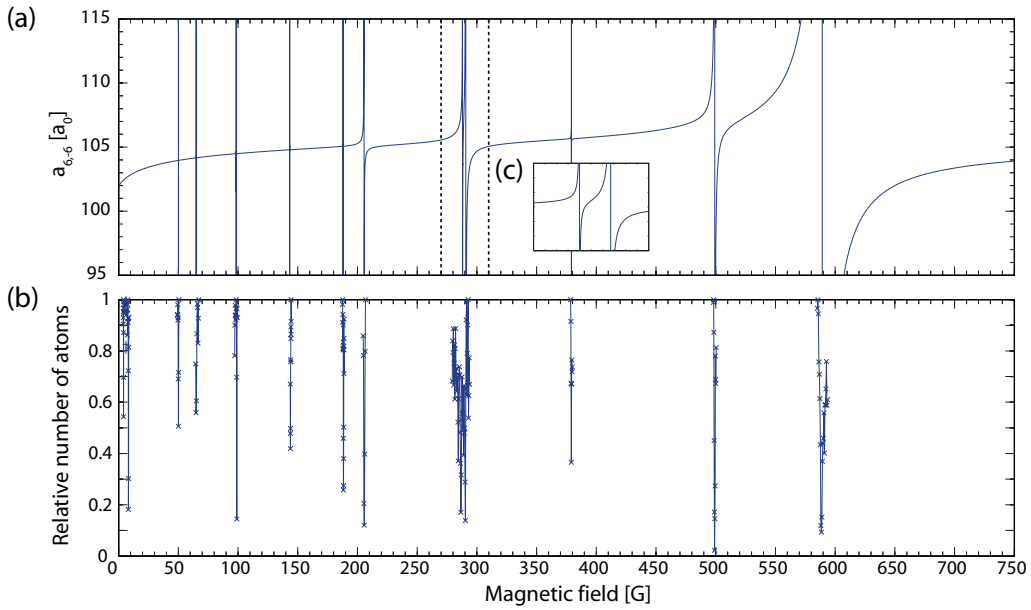

Figure 6.15: (a) Experimentally accessible s-wave scattering length a_{S,M_S} calculated for two colliding $s = 3$, $m_s = -3$ ($|\, S = 6, M_S = -6; \ell = 0, m_\ell = 0 \,\rangle$) atoms as a function of magnetic field for our best-fit parameters a_6=111.56 a_0, a_4=57.61 a_0, a_2=-7.26 a_0, C_6 = 733 a.u. and $C_8 = 75 \cdot 10^3$ a.u.. (b) Plot of the positions of the experimental loss features (c) The feature near 290 G is a pair of nearly degenerate Feshbach resonances (see Fig. 6.9 for details).

Here 1 a.u. is $E_h a_0^n$ for C_n and $E_h = 4.359744 \cdot 10^{-18}$ J is a Hartree. The minimization procedure provides only a weak upper bound on the C_8. The $^{13}\Sigma_g^+$ scattering length a_6 is in reasonable agreement with Ref. [212] and the C_6 coefficient is consistent with that of Ref. [176, 177]. The average difference between theoretical and experimental resonance positions is only ≈ 0.6 G.

Figure 6.15 shows the experimentally accessible s-wave scattering length a_{S,M_S} of two colliding $s = 3$, $m_s = -3$ ($|\, S = 6, M_S = -6; \ell = 0, m_\ell = 0 \,\rangle$) atoms as a function of magnetic field for our best-fit parameters. For comparison also the experimental data is shown. Unlike the a_S, this scattering length a_{S,M_S} depends on the spin-spin dipole interaction. The off-resonant scattering length is approximately 105 a_0. Near each Feshbach resonance, the scattering length both diverges and crosses zero. The difference in magnetic field between these two locations defines the resonance width. The theoretical resonance width Δ [239] is listed together with the experimental $^1/_e$ magnetic field width and the experimental L_3 coefficient in Table 6.2.

Our theoretical calculations of the scattering lengths from the measured positions of the loss features were independently verified by Pavlovic et al. [177].

Looking at the data in Table 6.2 and Fig. 6.16(a), we see that smaller experimental

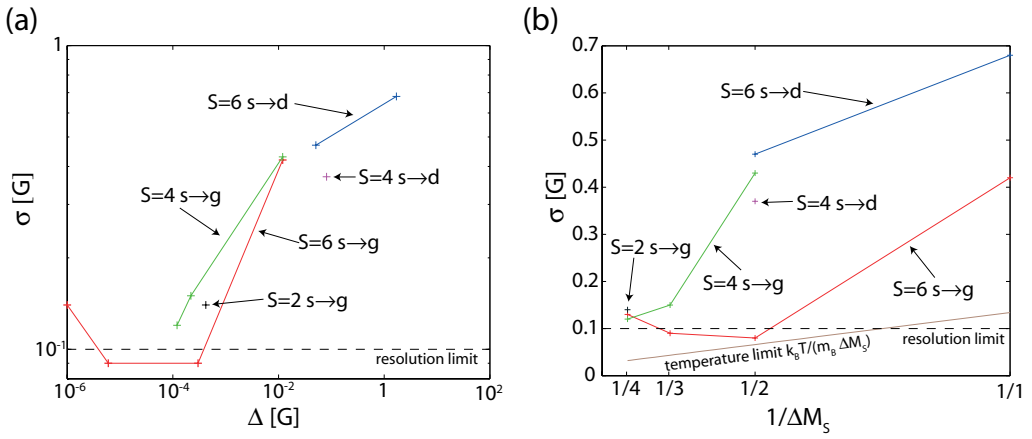

Figure 6.16: Shown are the dependence of the experimentally measured width of the loss features on (a) $1/\Delta M_S$ and (b) the theoretically predicted width. Resonances belonging to the same series, are connected by straight lines. Since the theoretical values cover eight orders of magnitudes, we employed a log-log plot for (b).

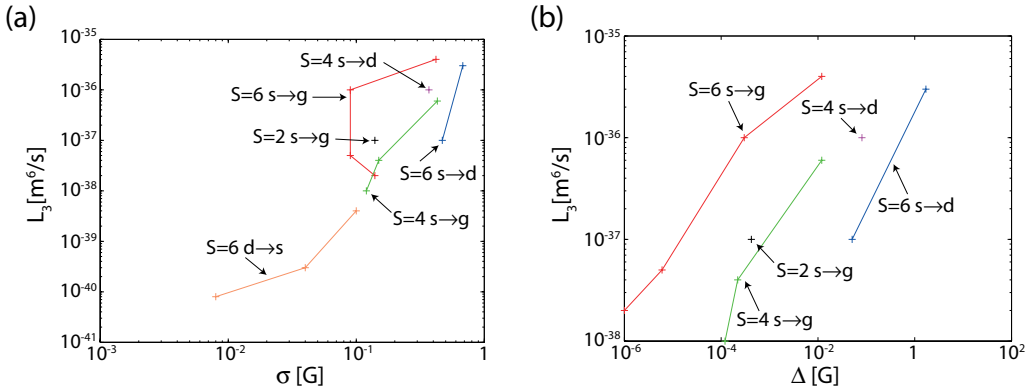

Figure 6.17: As seen in both figures, the loss-rate L_3 is correlated to the (a) experimentally observed width σ and (b) the theoretically predicted width Δ.

widths correspond to smaller theoretical widths, up to the point where we are limited by our experimental resolution of[14] 100 mG. The discrepancy between the theoretical and experimental widths of more than two orders of magnitude can be rectified by the following argument: While the theoretical width Δ is the "real" width of the resonance feature (as defined in Eq. (3.32)), the experimental value σ is the $1/\sqrt{e}$-width of the loss feature. The width of the loss feature is determined by the theoretical width Δ of the resonance and additionally by the hold time at the applied

[14]The resolution limit we are using was deduced using the uncertainty of our experimental parameters. As seen from the figures we seem to have a slightly higher resolution.

magnetic field. For typical hold times on the order of seconds, the resulting width is much larger, see Eq. (6.7) and Fig. 6.6. Figure 6.16(b) shows the dependence of the experimental width on $1/\Delta M_S$ for series of resonances with constant S and ℓ. Here ΔM_S is the difference of M_S between the incoming and the closed channel. We again observe a trend to smaller widths for increasing ΔM_S. This is to be expected, since a bound state with a bigger ΔM_S crosses the incoming channel faster for increasing magnetic field, thus leading to a smaller width of the resonance. We also see from this figure, that our measured widths are all above the minimum thermal width of $k_B T/\mu_B \Delta M_S$, where we assumed a typical temperature of T=6 μK.

Even though models for a theoretical determination of L_3 do not exist, we know from Eq. (3.47) that the three-body loss rate is proportional to the width of the Feshbach resonance[15]. A careful comparison of the theoretical width Δ or the experimental width σ and L_3 shows correlations as seen in Fig. 6.17. That is for resonances of a given S and ℓ, increasing theoretical widths coincide with higher experimental L_3 values[16]. The on-resonance loss rate we measure is comparable or smaller, respectively, than the ones observed in ^{23}Na [225], Cs [246] and ^{85}Rb [197] but larger than the ones observed in ^{87}Rb [143]. Consequently, this will allow for sufficient lifetimes for experiments in the vicinity of the resonance.

6.6 Significance of our results

The observation of Feshbach resonances in ^{52}Cr allowed the first precise determination of the potential parameters for the $^{13,9,5}\Sigma_g^+$ states. This is significant in a number of ways. On the experimental side the now known background scattering length of 105 a_0 should allow the creation of a Bose-Einstein condensate. The existence of Feshbach resonances enables us to experimentally tune the scattering length to arbitrary values and to create Cr_2 molecules. On the theoretical side, the precise knowledge of the potentials may lead to a better understanding of the bonding mechanisms of the chromium dimer, which is not yet fully understood [200]. In addition it is possible to predict the scattering lengths for different collision channels of interest and other chromium isotopes. To get a better understanding of the consequences of our measurements lets take a look at some of the aforementioned points in some more detail.

[15] An exact value for L_3 cannot be calculated since Γ_e, the width for the formation of a molecule is unknown.

[16] For Feshbach resonances with a width comparable to our experimental resolution of 100 mG, we may underestimate the absolute value of the L_3 coefficient. This is due to the fluctuations in the magnetic field, which may lead to an averaging of the L_3 value over the whole width of the resonance.

	$a_{6,-6}$ $[a_0]$	a_6 $[a_0]$	a_4 $[a_0]$	a_2 $[a_0]$
^{50}Cr	29	32	254	209

Table 6.3: Scattering lengths obtained for ^{50}Cr by mass-scaling the ^{52}Cr potential.

6.6.1 Scattering length of ^{50}Cr

Now that we know the scattering length for ^{52}Cr we can predict the scattering lengths for other isotopes, through a method called mass-scaling. The interatomic potential is independent of the mass, and thus the same for all isotopes. From the Feshbach measurements and the corresponding theory we now know the interatomic potential. So we simply need to calculate the solution of the previously used Schrödinger equation with the same potential but different reduced masses. Table 6.3 shows the scattering lengths we obtained for ^{50}Cr. We can see that the value $a_{6,-6}$ for ^{50}Cr is consistent with the value of $40 \pm 15\,a_0$ we found by mass-scaling the less precise potential obtained from cross-dimensional relaxation measurements.

6.6.2 Observation of multipletts

In section 6.5.1 we derived the matrix element for the dipole-dipole interaction, see Eq. (6.15). Ticknor et al. [237] observed that for fixed q the strength of the interaction depends on m_ℓ. The fact that the dipole-dipole interaction does not contribute equally to all values of m_ℓ means that bound states with different m_ℓ have different energies. This implies that Feshbach resonances with different values of m_ℓ couple to distinct bound states and thus have different magnetic field dependencies.

It is best to discuss the implications of this using our resonance at 589.2 G as an example. It results from the coupling between the incoming state $|\, S = 6, M_S = -6, \ell = 0, m_\ell = 0 \,\rangle$ and the bound state $|\, S' = 6, M'_S = -5, \ell' = 2, m'_\ell = -1 \,\rangle$. Since we have s-wave scattering ($\ell = 0$), m_ℓ is required to be 0 and thus this bound state is the only one we can couple to. The situation changes for $\ell \geq 2$. Lets discuss what happens if we are incoming in d-waves ($\ell = 2$). m_ℓ can now vary between -2 and 2, so $M = M_S + m_\ell$ can range from -8 to -4. Figure 6.18 shows the possible transitions due to the selection rule $\Delta M = 0$ and assuming $\Delta M_S = +1$[17]. In addition to the observed $s \rightarrow d$ resonance, four $d \rightarrow d$ resonances are possible. The transition with $M = -6$ couples to the same bound state as the $s \rightarrow d$ transition, so it will occur at exactly the same field and cannot be observed. The other three transitions will

[17] There are also possible transitions with $\Delta M_S = +2$, but those will end in a bound state with $M_S = +4$ and thus will form the multiplett which belongs to a different Feshbach resonance.

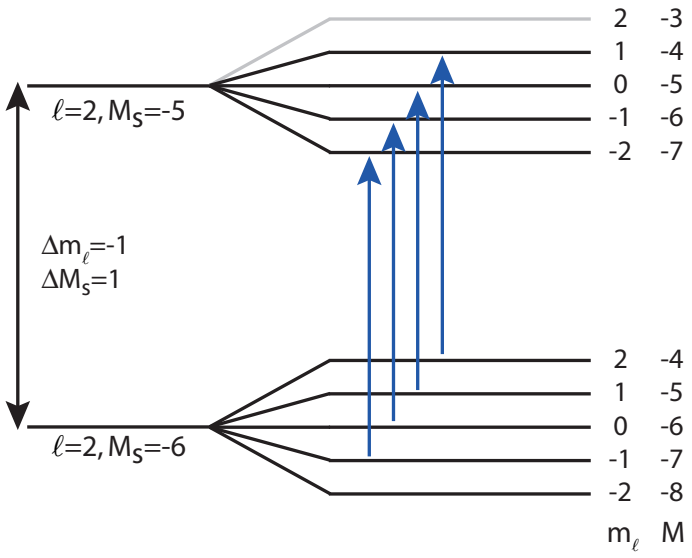

Figure 6.18: Due to the anisotropy of the dipole-dipole interaction the degeneracy of a Feshbach resonance is lifted and it splits up into a multiplett. This is only possible for collisions with $\ell \geq 2$ because then $m_\ell \neq 0$. Different m_ℓ lead to shifts in the resonance positions due to different contributions of the matrix element $\int Y_{\ell'}^{m'_\ell *}(\theta,\varphi) Y_2^q(\theta,\varphi) Y_\ell^{m_\ell}(\theta,\varphi) \mathrm{d}\Omega$.

S'	M'_S	ℓ'	M	m'_ℓ	B [G]
6	-5	2	-6	-1	589.209
6	-5	2	-4	1	591.722
6	-5	2	-7	-2	565.66
6	-5	2	-5	0	593.779

Table 6.4: Results from the multi-channel scattering calculations for the corresponding $d \rightarrow d$ transitions of the $s \rightarrow d$ resonance at 589.2 G. The first $d \rightarrow d$ resonance is at the same position as the $s \rightarrow d$ resonance and thus hidden by the latter one. When neglecting the spin-spin dipole interaction the resonance is found at 581.0 G. The spin-spin dipole interaction then spreads the multiplett by up to 13 G in both directions.

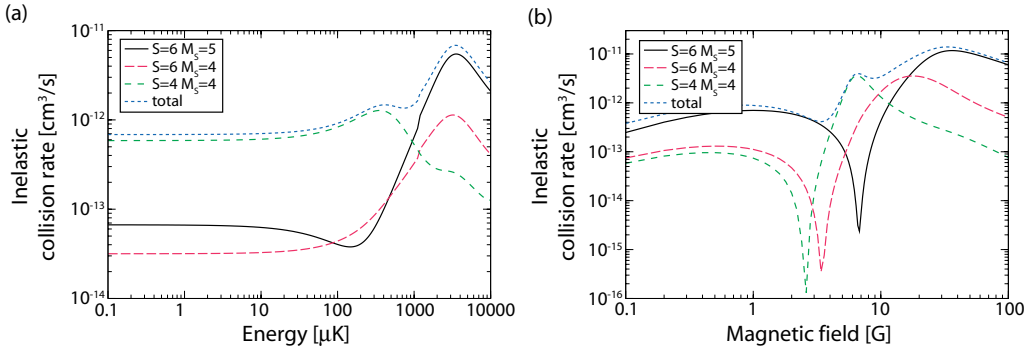

Figure 6.19: Dependence of the inelastic collision rate for different dipolar relaxation processes on (a) the energy and (b) the magnetic field. For the plot over the energy a magnetic field of B=5 G assumed, while for the magnetic field plot an energy of E=10 μK was used [216].

couple to slightly shifted bound states (due to their different m'_ℓ) and will thus occur at different magnetic fields. It is experimentally challenging to observe these resonances, since the coupling is very weak and so is their strength. This is the case for all resonances with $\ell \geq 2$, because the colliding atoms have to tunnel through the centrifugal barrier before they can couple to the bound state. As we are able to observe resonances with $\ell = 2$ at low fields, using a magnetic field stabilization should allow the observation of these multipletts. Table 6.4 shows the predicted positions of these resonances from our multi-channel calculations [216]. Neglecting the spin-spin dipole interaction the resonance position is at approximately 581.0 G (see Fig. 6.14). The spin-spin dipole interaction spreads the multiplett by approximately 13 G in both directions. This has to be compared to a splitting of only 0.5 G in alkalis, which has been observed in ^{40}K [189]. In contrast to Ref. [237] we also do not expect a $|m_\ell|$ degeneracy, because in our case the scattering is not elastic (T_0), but the coupling flips a spin ($T_{\pm 1}$). Due to the properties of the spherical harmonic functions in Eq. (6.15) the symmetry is broken and thus the $|m_\ell|$ degeneracy is lifted.

6.6.3 Predictions for inelastic collisions in the m_s =+3 state

From the exact knowledge of the relevant potential parameters we can also make predictions about inelastic collisions between atoms in the m_s =+3 state. Figure 6.19(a) shows the inelastic collision rate over the collision energy, while 6.19(b) shows the dependence on the applied magnetic field. The dipolar relaxation allows the incoming state $|\, S = 6, M_S = 6 \,\rangle$ to decay to the states $|\, S' = 6, M'_S = 5 \,\rangle$, $|\, S' = 6, M'_S = 4 \,\rangle$ and $|\, S' = 4, M'_S = 4 \,\rangle$. Looking at the energy dependence first, we see that up to 10 μK the inelastic collision rate stays constant and then starts to increase. It peaks

around 4 mK. Below 10 μK only s-wave scattering contributes to the scattering rate. For values above 10 μK a d-wave shape resonance is responsible for the existence of the peak. For even higher energies some more shape resonances are expected as seen in Ref. [177, Fig. 1]. This low lying shape resonance may be the reason, why buffer gas cooling below a few mK is not possible due to the experienced high inelastic dipolar losses [49, 50, 249]. Another interesting feature is seen in Fig. 6.19(b). For certain values of the magnetic field the inelastic collision rate is sharply suppressed. This behavior is due to the zero crossing of the wave function for positive scattering lengths (see Fig. 2.4). The value of the matrix element for the dipole-dipole interaction Eq. 6.15 is mainly determined by the region around $r \sim 1/k_f$, and becomes minimal for $1/k_f \sim a$. Because this happens for each possible channel at a different magnetic field, the total scattering rate will average out this drastic behavior.

Chapter 7

Summary and perspectives

In this Chapter, I give a summary of the results presented in this thesis and discuss their consequence for future investigations. Prospects for exciting experiments involving the recently realized Bose-Einstein condensate and the Feshbach resonances conclude this chapter.

7.1 Summary

The properties of degenerate quantum gases are governed by the interactions between the atoms. The main interaction is the contact interaction which arises from s-wave scattering. For atoms which exhibit a high magnetic moment — like chromium — the dipole-dipole interaction becomes significant. In contrast to the contact interaction, the dipole-dipole interaction is anisotropic and long-range. These features are expected to alter the properties of a degenerate quantum gas and will lead to new phenomena. An exact knowledge of the interactions between two atoms is an important premise to be able to study these new phenomena. The observation of Feshbach resonances, together with a theoretical model allows one to deduce the exact interaction potentials.

In this thesis, I reported the first observation of magnetically induced Feshbach resonances in an ultracold gas of ^{52}Cr atoms. Chapters 2 and 3 were devoted to presenting the theory which is used to describe Feshbach resonances. We followed the approach of Feshbach since it is the most accessible to the reader. It is though using the framework of "formal" scattering theory which we thus needed to introduce first. Following the formal derivation was a "hands-on" calculation of a model Feshbach resonance using two square-well potentials. This simple example already reproduces all relevant aspects of a Feshbach resonance. Most importantly, we saw that the resonance position is shifted according to the coupling strength. Since the Schrödinger equation for real interaction potentials cannot be solved analytically any more, one

needs to resort to numerical methods. Two common methods were presented, the classical Gordon's method and the more recent discrete variable representation method. The theoretical part of this thesis is concluded by an overview over the different possibilities to experimentally detect the variation of the scattering length due to a Feshbach resonance.

Chapter 4 started with a presentation of the physical, electronic and spectroscopic properties of ^{52}Cr relevant for this thesis. It also contains a detailed look at the results of previous measurements performed by our group. These measurements dealt with determining the ^{52}Cr and ^{50}Cr scattering lengths in a magnetic trap through cross-dimensional relaxation measurements and the measurement of the dipolar relaxation rate from the m_s =+3 state. These results had two important consequences for our experiment: Even though the scattering length for ^{52}Cr is positive and large enough for creating a Bose-Einstein condensate, this goal was defeated by the existence of a high loss rate due to the dipolar relaxation.

The dipolar relaxation losses can be suppressed by transferring the atoms into the m_s =-3 state, which is the energetically lowest state. Since atoms in the m_s =-3 state cannot be trapped in a magnetic trap, the atoms need to be loaded into an optical dipole trap first, before the could be optically pumped into the m_s =-3 state. These steps required setting up an optical dipole trap for ^{52}Cr and a new laser system for optical pumping of the atoms into the energetically lowest state. These two laser systems and the computer control system were newly implemented during this thesis and are thus covered in some detail in Chapter 5 which treats the experimental setup. The remaining parts of our setup were also described, but only very concise and with pointers to the relevant publications.

This brings us to Chapter 6 which contains the Feshbach measurements. Before delving into the details of the Feshbach measurements, the chapter starts with recounting the steps involved in the preparation of our atomic sample and the reasoning behind each step. Some more time has been spent on developing a theory for the optical pumping process and comparing it with the experimental results. We achieve a transfer efficiency of close to 100% without incuring any measurable heating. After the transfer we further cool down our sample by taking advantage of the existing plain evaporation followed by a short forced evaporation. After all these preparation steps, we end up with about 120 000 atoms at a temperature of 6 μK and a peak density of $5 \cdot 10^{13}\,{}^{1}/_{\mathrm{cm}^3}$ in the crossed optical dipole trap, which are close to optimal conditions for observing Feshbach resonances.

Fourteen resonances were located by measuring the inelastic loss of ^{52}Cr in the energetically lowest Zeeman sub-state m_s =-3 as a function of the applied offset field (4 to 600 G). A calibration of the magnetic field was done for each observed resonance slightly above and below the resonance using rf-spectroscopy. This allowed us to determine the positions of the resonances with an accuracy of below 100 mG.

From the obtained data we were also able to extract the width of the inelastic loss features and an upper bound for the three-body loss-rate L_3 at the resonance.

Using quantum-scattering calculations we identified thirteen of the fourteen observed resonances and assigned the relevant quantum numbers. The eleven strongest Feshbach resonances build a complete set of all possible resonances up to second-order in the magnetic dipole-dipole coupling for the deca-triplett s-wave entrance channel. The two remaining identified resonances are resonances with a d-wave entrance channel and are thus much weaker. We were not yet able to identify the weakest resonance at 6.1 G.

Positions and widths extracted from quantum-scattering calculations are in good agreement with the experimental data. The average difference between theoretical and experimental resonance positions is only ≈ 0.6 G. The inclusion of the spin-spin dipole interaction into our calculations was essential for a quantitative understanding of the experimental spectrum. From our calculations we obtained the following best-fit parameters for the different potentials (given with one standard deviation): a_2=-7(20) a_0, a_4=58(6) a_0, a_6=112(14) a_0, C_6 =733(70) a.u., and $C_8 = 75^{+90}_{-75} \cdot 10^3$ a.u.. We have improved the accuracy of the previous collisional measurements [212] and provided a determination of the $^{9,5}\Sigma_g^+$ scattering lengths, together with the corresponding C_6 and C_8. Our results are the most precise determination of the chromium interaction potentials up-to-date.

Finally, due to the absence of the hyperfine-structure, ^{52}Cr forms an ideal candidate for the theoretical investigation of Feshbach resonances; it is an ideal "text-book" example for discussing Feshbach resonances.

7.2 Perspectives

We already discussed some of the more immediate consequences from the exact knowledge of the ^{52}Cr interaction potentials at the end of the previous chapter. There we investigated some predictions about the scattering lengths of other chromium isotopes and inferred the scattering lengths in the m_s =+3 state. We also looked at the existence of a multiplett structure of Feshbach resonances in nonzero partial waves. Now we will focus onto the more far-reaching perspectives opened up by the precise knowledge of the interaction potentials, some of which were already realized during the time this thesis was written.

7.2.1 Improved control over the short-range scattering properties

In this thesis we concentrated on observing the magnetic field position of a Feshbach resonance through inelastic loss measurements. Even though the width of the inelastic

loss features gives an indication of the real width Δ of a Feshbach resonance, for future measurements the exact behavior of the scattering length close to a Feshbach resonance needs to be determined. Of special interest is the position of the zero-crossing of the scattering length, because it allows to completely switch of the contact interaction. This can be done by using two of the methods presented in Chapter 3.4: Using a Bose-Einstein condensate we can measure the mean-field energy during the expansion of the BEC. Or we can determine this position by varying the scattering length during the evaporation. If the sample cannot thermalize due to a vanishing scattering length, this process becomes very inefficient and no increase in the phase space density is expected. Furthermore, these measurements will enable us to optimize our evaporation strategy. In a single beam trap, where the density is low a large scattering length is desired, while in a crossed dipole trap with a higher density a smaller scattering length is preferable to avoid three-body losses.

7.2.2 Creation of a dipolar Bose-Einstein condensate

The measured off-resonant scattering length of approximately $105\,a_0$, together with the suppression of the dipolar relaxation in the m_s =-3 state, should allow the creation of a Bose-Einstein condensate (BEC) due to the much better ratio between thermalizing collisions and losses. Shortly after the Feshbach measurements were concluded, our group finally accomplished this goal [84]. By further lowering the power in the stronger axial beam we increased the phase-space density above the critical value of $\rho \approx 1$. We were able to create a pure BEC with approximately 50 000 atoms. The critical temperature, at which the phase-transition occurs is around 700 nK. ^{52}Cr is the first element which was condensed, where the dipole-dipole interaction is strong enough to be visible. Compared with the contact interaction its strength is approximately $1/10$ of the contact interaction. This is already enough to manifest itself in a well pronounced modification of the condensate expansion that depends on the orientation of the magnetic moments [78]. Only recently our group was able to observe this effect [231]. Tuning the contact interaction between ^{52}Cr atoms close to zero using one of the observed Feshbach resonances will allow us to realize a dipolar BEC [9] in which the dipole-dipole interaction is the dominant interaction. In this way, many predicted dipole-dipole phenomena can be investigated experimentally. These include the occurrence of a Maxon-Roton in the excitation spectrum of a dipolar BEC [206] or new kinds of quantum phase transitions [91, 261] as well as the stability and the ground state of dipolar BECs [88, 171, 205].

7.2.3 Tuning the dipole-dipole interaction

In addition to tuning the contact interaction also the dipole-dipole interaction can be tuned [77]. This is done by applying a rotating magnetic field to the dipoles as

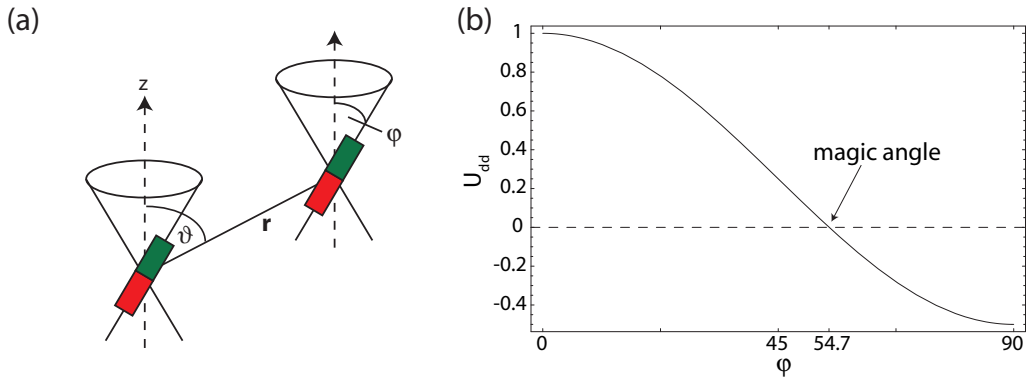

Figure 7.1: Tunability of the magnetic dipole interaction. (a) Using time-varying magnetic fields, the dipoles are rapidly rotated around the z axis. (b) The angle φ between the dipole orientation and the z axis determines the strength and sign of the effective interaction. $\varphi = 0$: the magnetic dipoles are polarized along the z direction. $\varphi = \pi/2$: the sign of the effective interaction is inverted and the absolute value is only half of the polarized case. $\varphi = 54.7°$ (magic angle): the dipolar interaction averages to zero.

shown in Fig. 7.1(a). The interaction strength then depends on the rotation angle φ and allows to tune the dipole-dipole interaction from attraction to repulsion, or even to zero at the so called magic angle of 54.7° (see Fig. 7.1(b)). The rotation frequency ω_{spin} of the radial field has to be chosen such that $\omega_{\text{trap}} \ll \omega_{\text{spin}} \ll \omega_{\text{Larmor}}$. In our case $\omega_{\text{trap}} \approx 2\pi \cdot 200\,{}^1/_{\text{s}}$ and $\omega_{\text{Larmor}}/B = 2\pi \cdot 8.3 \cdot 10^6\,{}^1/_{\text{G·s}}$, and thus the required rotation frequency lies in a well accessible range. Together with tuning the contact interaction by using a Feshbach resonance a degenerate quantum gas with adjustable long- and short-range interactions can be realized.

7.2.4 Creation of ultracold molecules

Almost ten years after the first creation of a BEC with rubidium [6], there are now many groups working with BECs of various elements. The next big challenge to tackle was now the creation of a sample of ultracold molecules. Quantum gases of molecules would allow very precise molecular spectroscopy, they are very good candidates for matter-wave interferometers and they could contribute to a better understanding of the formation of Cooper-pairs and thus superconductivity. But how can a molecular quantum gas be produced? One idea was to do it the same way as it is done with atoms. It turns out though, that laser cooling of molecules is complex. Unlike in atoms in molecules there are no closed transitions due the many decay channels from the vibrational and rotational levels. A second approach is to use buffer-gas loading and evaporative cooling of paramagnetic molecules [122]. The third possibility is to slow polar molecules in inhomogenic electrical fields [14]. Both

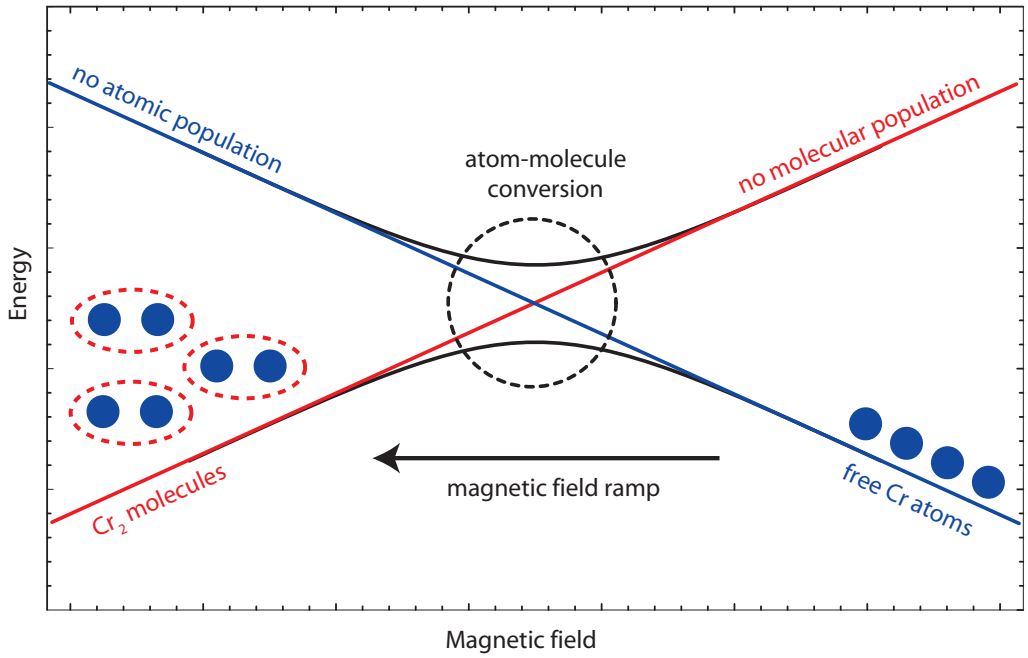

Figure 7.2: Due to the dipole-dipole interaction, a coupling exists between the free atomic and the molecular state. This turns the crossing of these two levels into a so called avoided crossing. By slowly ramping the magnetic field above the crossing point, one can adiabatically convert atoms into molecules and back again.

methods offer the advantage that they can be applied to a whole class of molecules but also in both cases the degenerate regime was not yet reached.

The problems with the direct cooling of molecules can be circumvented by associating the molecules from already ultracold atoms. A very popular method to do this is photoassociation [164, 165], though the formed dimers tend to be distributed over a range of very high vibrational states, thus reducing the phase-space density. There is another, astonishing simple method to generate ultracold molecules from atoms, which involves Feshbach resonances. In this thesis we already discussed the creation of molecules through three-body-recombination close to a Feshbach resonance (see section 3.4). But there is also the possibility to use a Feshbach resonance to coherently produce dimers in one highly excited vibrational state. To understand how this works we need to recall, that due to the dipole-dipole interaction the crossing of the energy of the molecular state and the energy of the free colliding atoms is turned into a so called avoided crossing or Landau-Zener [264] transition. This is depicted in Fig. 7.2. Thus, if we ramp the magnetic field slowly enough above the resonance (coming from higher values), we can adiabatically transfer two free atoms into a molecule. This works both ways: by ramping upwards again, we can dissociate the molecules again into atoms. Since this is a coherent process an atomic BEC will be

turned into a coherent molecular sample [58]. Using a degenerate sample of fermions even a molecular BEC can be achieved [82, 116].

Using one of the Feshbach resonances found in this thesis, it should be possible to create an ultracold sample of chromium molecules. From the fourteen available resonances the ones at 290.3 G, 499.9 G and 589.1 G seem to be the most promising candidates for creating molecules. All three of them are first order resonances and thus display a strong coupling. This has important consequences: The stronger coupling allows to ramp the magnetic field much faster above the resonance, i.e. the generation of molecules is much more efficient. As these resonances are also at least an order of magnitude wider, the experimental control over the magnetic fields needs to be not as accurate as for the other resonances[1]. A ramp of the magnetic field is easily implemented experimentally. The experimental challenge is the detection of the molecules. Imaging with a laser beam is not possible, because no closed transition exists. A simple solution is to perform the experiment in a weak vertical dipole trap, where the atoms are levitated against the gravitation by a gradient field. The molecules have a different, lower magnetic moment, so they will slowly drop. If the magnetic field ramp is now reversed, the molecules are converted back to atoms again and will appear at a lower position when imaging occurs.

We are interested in the dependence of the efficiency of this molecule formation process and the lifetime of the molecules at different resonances. A prediction of the lifetimes is currently not possible. We expect to obtain very precise values for the resonance widths from the energy gain of the atoms during dissociation [61]. More challenging will be precision spectroscopy on Cr_2 molecules. Predominantly, these measurements will increase the knowledge of the molecular potentials.

7.2.5 Improved continuous loading scheme

Doing experiments with a higher number of atoms decreases the signal-to-noise ratio and thus the experimental error. In the following we will look at a possible improvement of our continuous loading scheme which should increase the number of atoms available in our experiment. We saw already in Chapter 6.1.1 that the steady state atom number in the $^5D_4$ state is given by the ratio of the decay rate into this state compared to the loss rate. If we thus find another state which is magnetically trappable and which has a higher loading rate to decay rate ratio, we would be able to load more atoms into the magnetic trap. The $^5S_2$ is such a state. By applying our optical pumping laser, we intent to populate the $^7P_3$ state during laser cooling. The decay from this state into the $^5S_2$ state is 200 times faster than the decay from $^7P_4$ state into the $^5D_4$ state (see figure 7.3 on the next page) and should improve

[1] The figure of merit here is the ratio between the width and the absolute position of the Feshbach resonance.

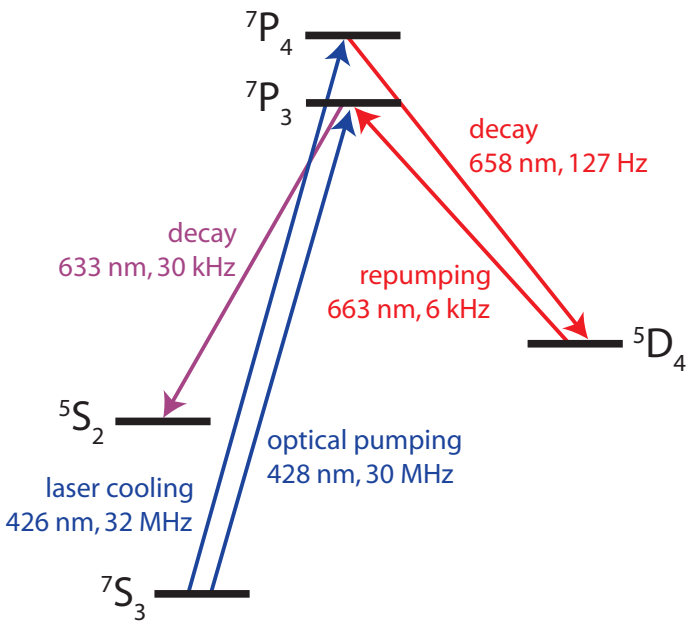

Figure 7.3: In future experiments we intent to use an different intermediate state in our loading scheme. The fast decay rate into the $^5S_2$ states exceeds the decay rate into the $^5D_4$ states and therefore improves the loading rate into the magnetic trap. The wavelengths and the widths of the relevant transitions are indicated.

the loading scheme. By changing the intensity of the optical pumping laser we can control the amount of atoms transferred into the $^5S_2$ state. The $^5S_2$ state also has a lower magnetic moment of $4\,\mu_B$, leading to less volume overlap between the magnetic trap and the magneto-optical trap. Thereby inelastic losses due to collisions between atoms in the two trap types are reduced. One disadvantage of the lower magnetic moment of the $^5S_2$ state is that only atoms with a lower temperature than for the $^5D_4$ trap are retained. After loading, the magnetically trapped atoms have to be transferred back to the ground state. For this purpose a new laser system with a wavelength of 633 nm is necessary.

7.2.6 Spin dynamics in classical and quantum degenerate gases

Due to the very different values of the scattering lengths of the $^{13,9,5}\Sigma_g^+$ molecular potentials, the elastic spin-changing collision rates for collisions between these states exceed the inelastic rates by about two orders of magnitude. This makes studies of spin-dynamics and of the magnetic ground state in zero magnetic field in a Bose-Einstein condensate possible. These measurements will help to determine the scattering length of the $^1\Sigma_g^+$ ground state potential. Due to its seven magnetic

sub-states and the absence of a quadratic Zeeman effect our system is in particular suitable for exploring this kind of physics.

We already outlined that the preparation of dense atomic samples is not possible for atoms in the m_s =+3 state in a magnetic trap, due to the high dipolar relaxation rates. The dipolar relaxation couples the kinetic to the spin reservoir, i.e. when a spin-flip occurs we convert (potential) spin energy into kinetic energy, the sample heats up and becomes depolarized. But what happens if we are able to reverse this process? If we for example start in an optical dipole trap in the m_s =-3 state and a small homogeneous magnetic field $k_{\mathrm{B}}T \gg \mu B$ is applied, the relaxation process reverses the energy transfer. Kinetic energy will be transferred to the spin reservoir, i.e. the sample will be cooled. Analogous to the experiments in nuclear physics [48, 76], where adiabatic demagnetization enables researchers to cool their samples to a small fraction of their initial temperature, we expect a reduction in the kinetic temperature depending on the applied offset field [103]. In combination with an optical pumping process this might be an efficient cooling process which is enabled by inelastic dipolar collisions.

Appendix A

Overview over the observed Feshbach resonances in ^{52}Cr

A.1 Raw experimental data

Position [G]	$1/\sqrt{e}$-Width [mG]	L_3 [cm^6/s]	reference data
4.1	40	$3 \cdot 10^{-28}$	30.08.2004, run18
6.1	8	$8 \cdot 10^{-29}$	30.08.2004, run21
8.2	101	$4 \cdot 10^{-27}$	30.08.2004, run15
8.2	110	$4 \cdot 10^{-27}$	02.09.2004, run01
50.1	140	$2 \cdot 10^{-26}$	25.08.2004, run15
65.1	80	$3 \cdot 10^{-26}$	25.08.2004, run11
65.1	110	$7 \cdot 10^{-26}$	25.08.2004, run23
98.9	90	$3 \cdot 10^{-24}$	20.08.2004, run03
98.9	80	$1 \cdot 10^{-24}$	20.08.2004, run04
98.9	90	$1 \cdot 10^{-24}$	23.08.2004, run02
98.9	70	$1 \cdot 10^{-24}$	30.08.2004, run02
143.9	130	$1 \cdot 10^{-26}$	10.09.2004, run07

continued on next page

continued from previous page

Position [G]	$1/\sqrt{e}$-Width [mG]	L_3 [cm^6/s]	reference data
143.9	110	$1 \cdot 10^{-26}$	10.09.2004, run08
188.3	150	$4 \cdot 10^{-26}$	10.09.2004, run11
205.8	420	$4 \cdot 10^{-24}$	19.06.2004, run04
286.6	440	$2 \cdot 10^{-24}$	27.08.2004, run23
286.6	330	$1 \cdot 10^{-24}$	06.09.2004, run18
286.6	420	$2 \cdot 10^{-25}$	08.09.2004, run03
286.6	530	$1 \cdot 10^{-25}$	08.09.2004, run04
290.3	160	$2 \cdot 10^{-24}$	27.08.2004, run23
290.3	530	$1 \cdot 10^{-25}$	06.09.2004, run15
290.3	550	$2 \cdot 10^{-25}$	06.09.2004, run17
290.3	400	$1 \cdot 10^{-25}$	08.09.2004, run03
290.3	330	$1 \cdot 10^{-25}$	08.09.2004, run06
290.3	734	$1 \cdot 10^{-25}$	08.09.2004, run07
379.2	140	$1 \cdot 10^{-25}$	03.09.2004, run17
499.9	370	$1 \cdot 10^{-24}$	03.09.2004, run11
589.1	683	$3 \cdot 10^{-24}$	03.09.2004, run05

Table A.1: Compilation of all Feshbach resonance measurements results.

A.2 Calculated bound state energies

Potential	1^{st}	2^{nd}	3^{rd}	4^{th}	5^{th}
$S = 6, \ell = 0$	$-2.72 \cdot 10^{-9}$	$-3.23 \cdot 10^{-7}$	$-1.81 \cdot 10^{-6}$	$-5.31 \cdot 10^{-6}$	$-1.16 \cdot 10^{-5}$
$S = 6, \ell = 2$	$-2.47 \cdot 10^{-7}$	$-1.67 \cdot 10^{-6}$	$-5.12 \cdot 10^{-6}$	$-1.13 \cdot 10^{-5}$	$-2.08 \cdot 10^{-5}$
$S = 6, \ell = 4$	$-8.31 \cdot 10^{-8}$	$-1.36 \cdot 10^{-6}$	$-4.66 \cdot 10^{-6}$	$-1.07 \cdot 10^{-5}$	$-2.01 \cdot 10^{-5}$
$S = 4, \ell = 0$	$-1.87 \cdot 10^{-8}$	$-5.22 \cdot 10^{-7}$	$-2.41 \cdot 10^{-6}$	$-6.60 \cdot 10^{-6}$	$-1.39 \cdot 10^{-5}$
$S = 4, \ell = 2$	$-4.36 \cdot 10^{-7}$	$-2.27 \cdot 10^{-6}$	$-6.40 \cdot 10^{-6}$	$-1.37 \cdot 10^{-5}$	$-2.49 \cdot 10^{-5}$
$S = 4, \ell = 4$	$-2.42 \cdot 10^{-7}$	$-1.94 \cdot 10^{-6}$	$-5.93 \cdot 10^{-6}$	$-1.31 \cdot 10^{-5}$	$-2.42 \cdot 10^{-5}$
$S = 2, \ell = 0$	$-1.03 \cdot 10^{-7}$	$-1.02 \cdot 10^{-6}$	$-3.67 \cdot 10^{-6}$	$-8.98 \cdot 10^{-6}$	$-1.78 \cdot 10^{-5}$
$S = 2, \ell = 2$	$-5.31 \cdot 10^{-8}$	$-9.09 \cdot 10^{-7}$	$-3.50 \cdot 10^{-6}$	$-8.76 \cdot 10^{-6}$	$-1.76 \cdot 10^{-5}$
$S = 2, \ell = 4$	$-6.60 \cdot 10^{-7}$	$-3.11 \cdot 10^{-6}$	$-8.23 \cdot 10^{-6}$	$-1.69 \cdot 10^{-5}$	$-2.99 \cdot 10^{-5}$

Table A.2: Calculated energy for the five highest bound states. The energy is given in atomic units.

Appendix B

Derivation of the Green's Operator

To formally derive Green's Operator, we investigate the scattering problem in the interaction picture [40]. We are only interested in the quantum states long before ($t \to -\infty$) and long after ($t \to \infty$) the scattering event, where the influence of the potential is negligible and the full solution coincides with the free solution. In the interaction picture the time evolution of a state is given by

$$|\,\phi(t)\,\rangle = \hat{U}(t,t')|\,\phi(t')\,\rangle \tag{B.1}$$

and the time evolution operator $\hat{U}(t,t')$ is given by

$$\hat{U}(t,t') = e^{\frac{i}{\hbar}\hat{H}_0 t} e^{-\frac{i}{\hbar}\hat{H}(t-t')} e^{-\frac{i}{\hbar}\hat{H}_0 t'} \tag{B.2}$$

We now define the Møller operators as

$$\hat{\Omega}^{(\pm)} = \hat{U}(0, \mp\infty)\,. \tag{B.3}$$

To get an explicit form of $\hat{\Omega}^{(\pm)}$ we need to apply the limiting procedure of Gell-Mann and Goldberger [74]. It is defined by

$$\lim_{t\to-\infty} f(t) = \lim_{\epsilon\to 0^+} \epsilon \int_{-\infty}^{0} e^{\epsilon t'} f(t')\,\mathrm{d}t'\,, \tag{B.4a}$$

and

$$\lim_{t\to\infty} f(t) = \lim_{\epsilon\to 0^+} \epsilon \int_{0}^{\infty} e^{-\epsilon t'} f(t')\,\mathrm{d}t'\,. \tag{B.4b}$$

We use the last two equations now to rewrite $\hat{\Omega}^{(\pm)}$

$$\begin{aligned}
\hat{\Omega}^{(\pm)} &= \lim_{t\to\pm\infty} U(0,t) \\
&= \lim_{t\to\mp\infty} e^{\frac{i}{\hbar}\hat{H}t} e^{-\frac{i}{\hbar}\hat{H}_0 t}\,\mathrm{d}t \\
&= \lim_{\epsilon\to 0^+} \mp\epsilon \int_{0}^{\mp\infty} e^{\pm\epsilon t} e^{\frac{i}{\hbar}\hat{H}t} e^{-\frac{i}{\hbar}\hat{H}_0 t}\,\mathrm{d}t\,.
\end{aligned} \tag{B.5}$$

Assuming that the states $|\,\phi_\alpha\,\rangle$ form a complete set, we can use the completeness relation to write

$$\hat{\Omega}^{(\pm)} = \lim_{\epsilon\to 0^+} \mp\epsilon \sum_\alpha \int_0^{\mp\infty} e^{\pm\epsilon t} e^{\frac{i}{\hbar}\hat{H}t} |\,\phi_\alpha\,\rangle\langle\,\phi_\alpha\,| e^{-\frac{i}{\hbar}E_\alpha t}\,\mathrm{d}t\,. \tag{B.6}$$

Performing the integration results in

$$\hat{\Omega}^{(\pm)} = \lim_{\epsilon\to 0^+} \sum_\alpha \frac{\pm i\epsilon}{E_\alpha - \hat{H} \pm i\epsilon} |\,\phi_\alpha\,\rangle\langle\,\phi_\alpha\,|\,, \tag{B.7}$$

or multiplied with $|\,\phi_\alpha\,\rangle$ from the right

$$|\,\psi_\alpha^{(\pm)}\,\rangle = \hat{\Omega}^{(\pm)}|\,\phi_\alpha\,\rangle = \lim_{\epsilon\to 0^+} \frac{\pm i\epsilon}{E_\alpha - \hat{H} \pm i\epsilon} |\,\phi_\alpha\,\rangle\,. \tag{B.8}$$

Since $\hat{H}_0|\,\phi_\alpha\,\rangle = E_\alpha|\,\phi_\alpha\,\rangle$ and $\hat{H} = \hat{H}_0 + \hat{V}$ we may also write the result as

$$\begin{aligned} |\,\psi_\alpha^{(\pm)}\,\rangle = \hat{\Omega}^{(\pm)}|\,\phi_\alpha\,\rangle &= \lim_{\epsilon\to 0^+} \frac{1}{E_\alpha - \hat{H} \pm i\epsilon}(E_\alpha - \hat{H}_0 - \hat{V} + \hat{V} \pm i\epsilon)|\,\phi_\alpha\,\rangle \\ &= |\,\phi_\alpha\,\rangle + \lim_{\epsilon\to 0^+} \frac{1}{E_\alpha - \hat{H} \pm i\epsilon}\hat{V}|\,\phi_\alpha\,\rangle = (1 + \hat{G}^{(\pm)}\hat{V})|\,\phi_\alpha\,\rangle\,, \end{aligned} \tag{B.9}$$

which retrieves our original definition of the Møller operators from equation 2.19 in section 2.2. There we have also shown that this solution is equivalent to

$$|\,\psi^{(\pm)}\,\rangle = |\,\phi\,\rangle + \hat{G}_0^{(\pm)}\hat{V}|\,\psi^{(\pm)}\,\rangle\,. \tag{B.10}$$

Appendix C

Publication in PRL

We published the results of this thesis also in Physical Review Letters. It appeared in Volume 94, Number 18, Article 183201 and is reproduced here on the following pages.

PRL **94,** 183201 (2005) PHYSICAL REVIEW LETTERS week ending 13 MAY 2005

Observation of Feshbach Resonances in an Ultracold Gas of ^{52}Cr

J. Werner, A. Griesmaier, S. Hensler, J. Stuhler, and T. Pfau*
5. Physikalisches Institut, Universität Stuttgart, 70550 Stuttgart, Germany

A. Simoni and E. Tiesinga
National Institute of Standards and Technology, Gaithersburg, Maryland 20899-8423, USA
(Received 2 December 2004; published 9 May 2005)

We have observed Feshbach resonances in collisions between ultracold ^{52}Cr atoms. This is the first observation of collisional Feshbach resonances in an atomic species with more than one valence electron. The zero nuclear spin of ^{52}Cr and thus the absence of a Fermi-contact interaction leads to regularly spaced resonance sequences. By comparing resonance positions with multichannel scattering calculations we determine the s-wave scattering length of the lowest $^{2S+1}\Sigma_g^+$ potentials to be 112(14) a_0, 58(6) a_0, and $-7(20)$ a_0 for $S = 6$, 4, and 2, respectively, where $a_0 = 0.0529$ nm.

DOI: 10.1103/PhysRevLett.94.183201 PACS numbers: 34.50.-s, 03.65.Nk, 31.10.+z

With the development of laser cooling and trapping techniques, atomic collisional properties in the ultracold regime have become directly accessible. Today, these properties play a crucial role in experiments with quantum degenerate bosonic and fermionic gases. In the ultracold regime, elastic collisions between most neutral atoms are dominated by isotropic interaction potentials, which only depend on the internuclear separation R and can be characterized by a single length, the s-wave scattering length a. This type of interaction is responsible for many of the fascinating phenomena observed in Bose-Einstein condensates (BEC's) (for a review see [1]) and two-species degenerate Fermi gases [2–5].

In alkali-metal gases, the effect of the isotropic potentials and, consequently, the value of the scattering length can be controlled by magnetically tunable Feshbach resonances [6]. Feshbach resonances appear when the energy of the incoming atoms equals the energy of a bound molecular level of a higher-lying molecular potential and can be used to change the sign and magnitude of a [7]. Recently, Feshbach resonances have been exploited to study the strong interaction regime in ultracold atomic gases or even to produce molecular Bose-Einstein condensates [7]. Feshbach resonances between different atomic species have also been theoretically predicted [8], and experimentally observed [9,10].

The spins of the six electrons in the $3d$ and $4s$ valence shells of the $^7S_3$ ground state of ^{52}Cr are aligned. This gives rise to a magnetic moment as large as $\mu = 6\mu_B$, where μ_B is the Bohr magneton. This large magnetic moment is responsible for a very strong anisotropic spin-spin dipole interaction between two $^7S_3$ ^{52}Cr atoms. In fact, when compared to alkali-metal atoms, which have a maximum magnetic moment of 1 μ_B, it is 36 times stronger.

For atomic ^{52}Cr the effects of the *anisotropic* and *long-range* spin-spin dipole interaction can add a new twist to the field of ultracold quantum gases. In particular, the expansion of a BEC of ^{52}Cr is expected to depend on the orientation of the magnetic dipoles [11]. The anisotropic interaction can be changed by time-varying magnetic fields [12], while the isotropic interaction can be tuned using a Feshbach resonance. This allows one to arbitrarily adjust the ratio of the isotropic and anisotropic interactions. One can thus create a so called dipolar quantum gas, in which the dipole-dipole interaction is dominant.

Isotropic interactions between two ground-state ^{52}Cr atoms can be described by Hund's case (a) $^{2S+1}\Sigma_{g/u}^+$ Born-Oppenheimer potentials. The large number of valence electrons leads to seven Born-Oppenheimer potentials instead of two for ground-state alkali-metal atoms. Conventional spectroscopic data only exists for the ground-state $^1\Sigma_g^+$ potential. Theoretical *ab initio* calculations [13,14] exist but are extremely challenging for ^{52}Cr.

Using a cross-dimensional relaxation technique, our group was able to determine the decatriplet $^{13}\Sigma_g^+$ s-wave scattering length of ^{52}Cr to be 170(39) a_0 and of ^{50}Cr to be 40(15) a_0 where $a_0 = 0.0529$ nm [15]. The uncertainty in parenthesis is a one standard deviation uncertainty combining statistical and systematic errors.

In this Letter, we report the observation of magnetic Feshbach resonances in a gas of ultracold ^{52}Cr atoms. We locate 14 resonances through inelastic loss measurements between magnetic-field values of 0 and 60 mT. The broadest observed feature has a $1/e$ width of 96 μT. By comparing the experimental data with theoretical multichannel calculations, we are able to identify the resonances and to determine the scattering lengths of the $^{13,9,5}\Sigma_g^+$ Born-Oppenheimer potentials, the van der Waals dispersion coefficient C_6, and C_8, which are the same for all seven Born-Oppenheimer potentials.

The details of our cooling scheme are presented in [16]. After Doppler cooling in a clover-leaf-type magnetic trap [16] and evaporative cooling, we load the atoms into a crossed optical dipole trap. The dipole trap is realized using an Yb-fiber laser with a wavelength of 1064 nm.

The two trapping beams have a waist of 30 and 50 μm and a power of 11 and 6 W, respectively. To suppress dipolar relaxation, we optically pump the atoms from the $m_s = +3$ Zeeman sublevel of the $^7S_3$ state to the energetically lowest $m_s = -3$ level [22]. The lifetime in the optical dipole trap increases from 7 s in the $m_s = +3$ state to 140 s in the $m_s = -3$ state and is limited by dipolar relaxation in the former and by the finite background gas pressure in the latter case. The optical pumping field of about 0.9 mT is left on, in order to prevent thermal reoccupation of higher m_s levels through dipolar collision processes. During the first 5 s after optical pumping, we see a fast initial decay in the atom number and a decrease in temperature, which we ascribe to plain initial evaporation in the optical dipole trap. To prepare a sample of up to 120 000 atoms at a temperature of 6 μK and a peak density of 5×10^{19} m^{-3} in a crossed optical dipole trap, we continue the evaporation by ramping down the intensity of the stronger of the two laser beams to 5 W.

We look for an increase of atom loss by three-body recombination to locate the Feshbach resonances [17]. This is done by first sweeping the magnetic-field strength in coarse steps on the order of 0.1–3 mT from 0 to 60 mT. Smaller sweep ranges are then used in regions where atom loss is observed. To find the precise location of the resonances a different method is used. The magnetic field is ramped up to a value close to the resonance in about 5 ms. We hold the magnetic field for 2 s to let the current settle and to give our magnetic coils time to thermalize. Then the magnetic field is quickly ramped to the desired value and held there for a variable amount of time. The holding time is chosen to clearly resolve the resonance and lies between 100 ms and 10 s. Finally, the magnetic field is switched off and an absorption image is taken.

The magnetic field is calibrated both slightly below and above each resonance using rf-spectroscopy. We are able to determine the value of the magnetic field with a one standard deviation uncertainty of 10 μT.

Figure 1 shows our data for two loss features near 29 mT. The position and widths of all the observed loss features are determined by a Gaussian fit, which we used for convenience. From the depth of these loss features, one can estimate an upper limit for the three-body loss coefficient L_3 [18]. The error bars in the figure are obtained from repeated measurements of atom loss and are mainly determined by number fluctuation. All resonance parameters are tabulated in Table I. In addition to atom loss, we also observe heating near most resonances, like in [18]. The resolution limit of our measurements is 14 μT at B = 60 mT.

Our experimental resonance positions can determine the scattering lengths of the Born-Oppenheimer potentials with high accuracy. The theoretical analysis uses the Hamiltonian of a pair of $^7S_3$ chromium atoms in an external magnetic field $\vec{B}$ and includes the seven isotropic Born-Oppenheimer potentials, the nuclear rotational energy $\hbar^2\vec{\ell}^2/(2\mu R^2)$ where $\vec{\ell}$ is the orbital angular momentum of the nuclei and μ the reduced mass of the diatom, the Zeeman interaction with the magnetic field, and the anisotropic spin-spin dipole interaction. For this Letter, we do not include second-order spin-orbit or spin-rotation interactions [19].

We construct $^{2S+1}\Sigma^+_{g/u}$ Born-Oppenheimer potentials V_S by smoothly joining a short-range $R \leq R_x$ model potential with the well-known long-range dispersion potential $\sum_n -C_n/R^n$, in which we only retain the $n = 6$ and 8 terms. The connection point $R_x = 17.5\ a_0$ is chosen such that each V_S can be well represented by its long-range form beyond R_x and its value at R_x is much larger than the collision and bound-state energies of interest here. The inner wall and dissociation energy of the model potentials approximately agree with Ref. [14]. Details of the short-range potentials are unimportant at ultracold temperatures. We allow for variation of C_n and include short-range corrections near the minimum of each potential curve. This allows us to independently tune C_n and the s-wave scattering lengths a_S of V_S to fit the experimental data. The number of bound states of V_S is uncertain to ± 10 for the deeper potentials.

When the atoms are far apart, the eigenstates of the dimer are $|SM_S; \ell m_\ell\rangle$, in which M_S and m_ℓ are projections of $\vec{S}$ and $\vec{\ell}$ along $\vec{B}$. The total projection $M = m_\ell + M_S$ and parity $(-1)^\ell$ are conserved during the collision. As the nuclei of the atoms are identical, only states with $(-1)^{S+\ell} = 1$ exist. In absence of the spin-spin interaction, the Hamiltonian conserves $\vec{\ell}$ and $\vec{S}$ as well. The anisotropic spin-spin dipole interaction couples states with $\Delta S = 0, 2$ and $\Delta\ell = 0, 2$; with $\ell = 0 \rightarrow \ell' = 0$ transitions forbidden.

Our sample is spin polarized, so that the incoming state has quantum numbers $S = -M_S = 6$ by straightforward angular momentum addition. Moreover, the temperature of the sample, $T \approx 6\ \mu$K, is small compared to the $\ell \geq 2$

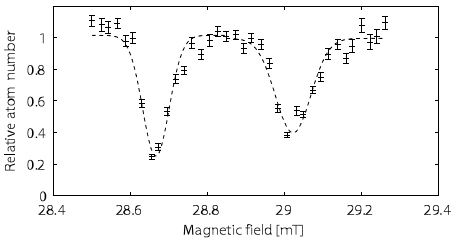

FIG. 1. Inelastic loss measurement of the Feshbach resonances at 28.66 and 29.03 mT. The dashed lines are Gaussian fits to the data and determine the position and width of the loss features. The experimental data points are averages over many experimental measurements. Each measurement was separately normalized to the offset of a Gaussian fit to the data.

PRL **94,** 183201 (2005) PHYSICAL REVIEW LETTERS week ending 13 MAY 2005

TABLE I. Compendium of positions and strengths of the observed loss features L_3, the theoretical positions, widths Δ, initial partial wave ℓ_i, and assignment of the resonances. Theoretical calculations use a collision energy of $E = k_B T$ and parameters as in Fig. 2. The one standard deviation uncertainty of the experimental resonance position is below 14 μT (see text).

Exp. Pos. [mT]	Theo. Pos. [mT]	Theo. Δ [μT]	Upper limit for Exp. L_3 [m^6/s]	ℓ_i; SM_S; ℓm_ℓ
0.41	0.40	...	3×10^{-40}	2; 6, −4; 0, 0
0.61	...	...	8×10^{-41}	...
0.82	0.81	...	4×10^{-39}	2; 6, −5; 0, 0
5.01	5.01	$<1 \times 10^{-4}$	2×10^{-38}	0; 6, −2; 4, −4
6.51	6.49	6×10^{-4}	5×10^{-38}	0; 6, −3; 4, −3
9.89	9.85	0.030	1×10^{-36}	0; 6, −4; 4, −2
14.39	14.32	0.012	1×10^{-38}	0; 4, −2; 4, −4
18.83	18.79	0.022	4×10^{-38}	0; 4, −3; 4, −3
20.58	20.56	1.2	4×10^{-36}	0; 6, −5; 4, −1
28.66	28.80	1.2	6×10^{-37}	0; 4, −4; 4, −2
29.03	29.07	5.1	1×10^{-37}	0; 6, −4; 2, −2
37.92	37.92	0.042	1×10^{-37}	0; 2, −2; 4, −4
49.99	49.92	8.1	1×10^{-36}	0; 4, −4; 2, −2
58.91	58.92	170	3×10^{-36}	0; 6, −5; 2, −1

centrifugal barrier such that incoming $\ell_i = 0$ collisions dominate the scattering cross sections. We find that, in addition to the incoming state, states with $\ell = 2$ and 4 (d and g) partial waves and $S = 2, 4$, and 6 have to be coupled together in order to explain the 11 strongest observed features of Table I. Even though no term in the molecular Hamiltonian directly couples $\ell = 4$ states to the $\ell_i = 0$ state, second-order mixing in the spin-spin dipole interaction via $\ell = 2$ states is relevant in ^{52}Cr. All these states have a total projection $M = -6$. Two of the weakest $B <$ 1 mT resonances in Table I must be explained with incoming $\ell_i = 2$ d-wave collisions and $M \neq -6$.The resonance at 0.61 mT, the weakest observed resonance, could not be assigned.

The locations of the maxima in the experimental three-body loss rate are compared with locations of peaks in the elastic two-body cross section calculated by full quantum-scattering methods. We perform a global χ^2-minimization with parameters $a_{2,4,6}$, C_6, and C_8. Our best-fit parameters with one standard deviation are $a_2 = -7(20)\ a_0$, $a_4 = 58(6)\ a_0$, $a_6 = 112(14)\ a_0$, $C_6 = 733(70)$ a.u., and $C_8 = 75^{+90}_{-75} \times 10^3$ a.u. Here 1 a.u. is $E_h a_0^n$ for C_n and $E_h = 4.359\,744 \times 10^{-18}$ J is a Hartree. The minimization procedure provides only a weak upper bound on the C_8. The $^{13}\Sigma_g^+$ scattering length a_6 is in reasonable agreement with the C_6 coefficient is consistent with that of Ref. [14]. The average difference between theoretical and experimental resonance positions is only ≈ 0.06 mT.

Figure 2 shows the experimentally accessible s-wave scattering length a_{S,M_S} of two colliding $s = 3$, $m_s = -3$, ($S = -M_S = 6$) atoms as a function of magnetic field for our best-fit parameters. The theoretical resonance width Δ [6] is given in Table I. The experimental $1/e$ magnetic-field width of all observed features is on the order of 12–96 μT. Smaller experimental widths correspond to smaller theoretical widths, up to the point where we are limited by our experimental resolution of 14 μT. For resonances of a given S, increasing theoretical widths coincide with higher experimental L_3 values. The on-resonance loss rate we measure is comparable or smaller, respectively, than the ones observed in ^{23}Na [20] and ^{87}Rb [21]. This will allow for sufficient lifetimes for experiments in the vicinity of the resonance.

The nature of ^{52}Cr Feshbach resonances can be understood through approximate calculations of molecular bound states. We find that calculations of eigenstates of a reduced Hamiltonian limited to a single basis state $|SM_S; \ell m_\ell\rangle$ locates the resonances to within 0.25 mT from the scattering calculation. Our assignment S, M_S, ℓ, and m_ℓ from this approximate model is shown in Table I. An alternative assignment in which the quantum numbers of the nearly degenerate pair near 29.0 mT are interchanged is consistent with our best-fit parameters.

In the limit of vanishing spin-spin dipole interaction a simple resonance pattern is expected. Scattering is then independent of m_ℓ and the resonances occur at $B_{\text{res}} = E_B/[g_s \mu_B (M_S + 6)]$, where E_B is one of the zero-field binding energies of the potential $V_S(R) + \hbar^2 \ell(\ell + 1)/(2\mu R^2)$. Inclusion of the spin-spin dipole interaction gives rise to observable deviations from this pattern, as large as ≈ 1 mT. Such shifts are an order of magnitude larger than the 0.06 mT discrepancies that remain after our least-squares fit. Moreover, the 0.06 mT agreement strongly suggests that the spin-spin dipole interaction is the dominant relativistic interaction in ultracold ^{52}Cr.

In conclusion, we have observed Feshbach resonances in an ultracold gas of ^{52}Cr atoms held in an optical dipole trap. Resonances were located by measuring the inelastic loss of ^{52}Cr in the energetically lowest Zeeman substate. Positions and widths extracted from quantum-scattering

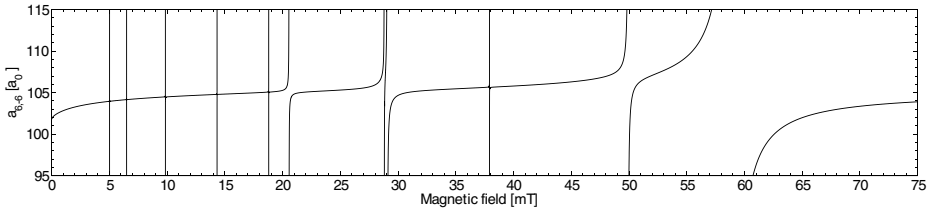

FIG. 2. Calculated scattering length of two $m_s = -3$ ^{52}Cr atoms versus magnetic field, for model parameters $a_6 = 111.56\ a_0$, $a_4 = 57.61\ a_0$, $a_2 = -7.26\ a_0$, $C_6 = 733$ a.u., and $C_8 = 75 \times 10^3$ a.u. The feature near 29 mT is a pair of nearly degenerate Feshbach resonances (see Fig. 1 for the corresponding experimental data).

calculations are in good agreement with the experimental data. The spin-spin dipole interaction is essential for a quantitative understanding of the experimental spectrum. We have improved the accuracy of the previous collisional measurements and provided a determination of the $^{9,5}\Sigma_g^+$ scattering lengths [15].

The resonances can be used to control the relative strength of isotropic and anisotropic interactions. Together with the BEC of ^{52}Cr we recently realized [22], this makes the spin-spin dipole interaction in degenerate quantum gases experimentally accessible. Moreover, the formation of Cr_2 molecules via Feshbach resonances is now envisaged.

This work is supported within the priority programme SPP 1116 of the DFG and the European RTN "Cold Quantum Gases" under Contract No. HPRN CT-2000-00125. We would like to thank A. Görlitz and S. Giovanazzi for many fruitful discussions.

*Electronic address: t.pfau@physik.uni-stuttgart.de

[1] K. Bongs and K. Sengstock, Rep. Prog. Phys. **67**, 907 (2004).
[2] C. Chin, M. Bartenstein, A. Altmeyer, S. Riedl, S. Jochim, J. H. Denschlag, and R. Grimm, Science **305**, 1128 (2004).
[3] T. Bourdel, L. Khaykovich, J. Cubizolles, J. Zhang, F. Chevy, M. Teichmann, L. Tarruell, S. J. J. M. F. Kokkelmans, and C. Salomon, Phys. Rev. Lett. **93**, 050401 (2004).
[4] M. Greiner, C. A. Regal, and D. Jin, Nature (London) **426**, 537 (2003).
[5] M. W. Zwierlein, C. A. Stan, C. H. Schunck, S. M. F. Raupach, A. J. Kerman, and W. Ketterle, Phys. Rev. Lett. **92**, 120403 (2004).
[6] E. Tiesinga, B. J. Verhaar, and H. T. C. Stoof, Phys. Rev. A **47**, 4114 (1993).
[7] R. A. Duine and H. T. C. Stoof, Phys. Rep. **396**, 115 (2004); and references therein.
[8] A. Simoni, F. Ferlaino, G. Roati, G. Modugno, and M. Inguscio, Phys. Rev. Lett. **90**, 163202 (2003).
[9] C. A. Stan, M. W. Zwierlein, C. H. Schunck, S. M. F. Raupach, and W. Ketterle, Phys. Rev. Lett. **93**, 143001 (2004).
[10] S. Inouye, J. Goldwin, M. L. Olsen, C. Ticknor, J. L. Bohn, and D. S. Jin, Phys. Rev. Lett. **93**, 183201 (2004).
[11] S. Giovanazzi, A. Görlitz, and T. Pfau, J. Opt. B **5**, S208 (2003).
[12] S. Giovanazzi, A. Görlitz, and T. Pfau, Phys. Rev. Lett. **89**, 130401 (2002).
[13] K. Andersson, Chem. Phys. Lett. **237**, 212 (1995).
[14] Z. Pavloviç, B. O. Roos, R. Côté, and H. R. Sadeghpour, Phys. Rev. A **69**, 030701 (2004).
[15] P. O. Schmidt, S. Hensler, J. Werner, A. Griesmaier, A. Görlitz, and T. Pfau, Phys. Rev. Lett. **91**, 193201 (2003).
[16] P. O. Schmidt, S. Hensler, J. Werner, T. Binhammer, A. Görlitz, and T. Pfau, J. Opt. Soc. Am. B **20**, 960 (2003).
[17] J. Stenger, S. Inouye, M. R. Andrews, H.-J. Miesner, D. M. Stamper-Kurn, and W. Ketterle, Phys. Rev. Lett. **82**, 2422 (1999).
[18] T. Weber, J. Herbig, M. Mark, H.-C. Nagerl, and R. Grimm, Phys. Rev. Lett. **91**, 123201 (2003).
[19] H. Lefebvre-Brion and R. W. Field, *Perturbations in the Spectra of Diatomic Molecules* (Academic, London, 1986).
[20] J. Stenger, S. Inouye, M. R. Andrews, H.-J. Miesner, D. M. Stamper-Kurn, and W. Ketterle, Phys. Rev. Lett. **82**, 2422 (1999).
[21] J. L. Roberts, N. R. Claussen, S. L. Cornish, and C. E. Wieman, Phys. Rev. Lett. **85**, 728 (2000).
[22] A. Griesmaier, J. Werner, S. Hensler, J. Stuhler, and T. Pfau, Phys. Rev. Lett. **94**, 160401 (2005).

Appendix D

Properties of Chromium

element	mass [au]	abundance [%]	nuclear spin	statistics
chromium	50	4.35	0^+	boson
	52	83.79	0^+	boson
	53	9.5	$^3/_2{}^+$	fermion
	54	2.36	0^+	boson

Table D.1: Natural abundance and nuclear spin of stable chromium isotopes.

vacuum wavelength	λ	$=$	$\frac{2\pi}{k}$	$=$	$425.554\,\mathrm{nm}$
natural linewidth	Γ	$=$	$\frac{1}{\tau}$	$=$	$31.5 \cdot 10^6\,{}^1/_\mathrm{s}$
				$=$	$2\pi \cdot 5.02\,\mathrm{MHz}$
saturation intensity	I_sat	$=$	$\frac{\pi h c \Gamma}{3\lambda^3}$	$=$	$8.52\,{}^\mathrm{mW}/_\mathrm{cm^2}$
absorption cross-section	σ_λ	$=$	$6\pi\bar{\lambda}^2$	$=$	$8.65 \cdot 10^{-10}\,\mathrm{cm}^2$
Doppler temperature	T_Doppler	$=$	$\frac{1}{k_B}\,\hbar\frac{\Gamma}{2}$	$=$	$124\,\mu\mathrm{K}$
recoil temperature	T_rec	$=$	$\frac{1}{k_B}\,\frac{(\hbar k)^2}{2m}$	$=$	$1.02\,\mu\mathrm{K}$
recoil velocity	v_rec	$=$	$\frac{\hbar k}{m}$	$=$	$1.80\,{}^\mathrm{cm}/_\mathrm{s}$

Table D.2: Properties of the cooling and trapping transition ${}^7\mathrm{S}_3 \leftrightarrow {}^7\mathrm{P}_4$

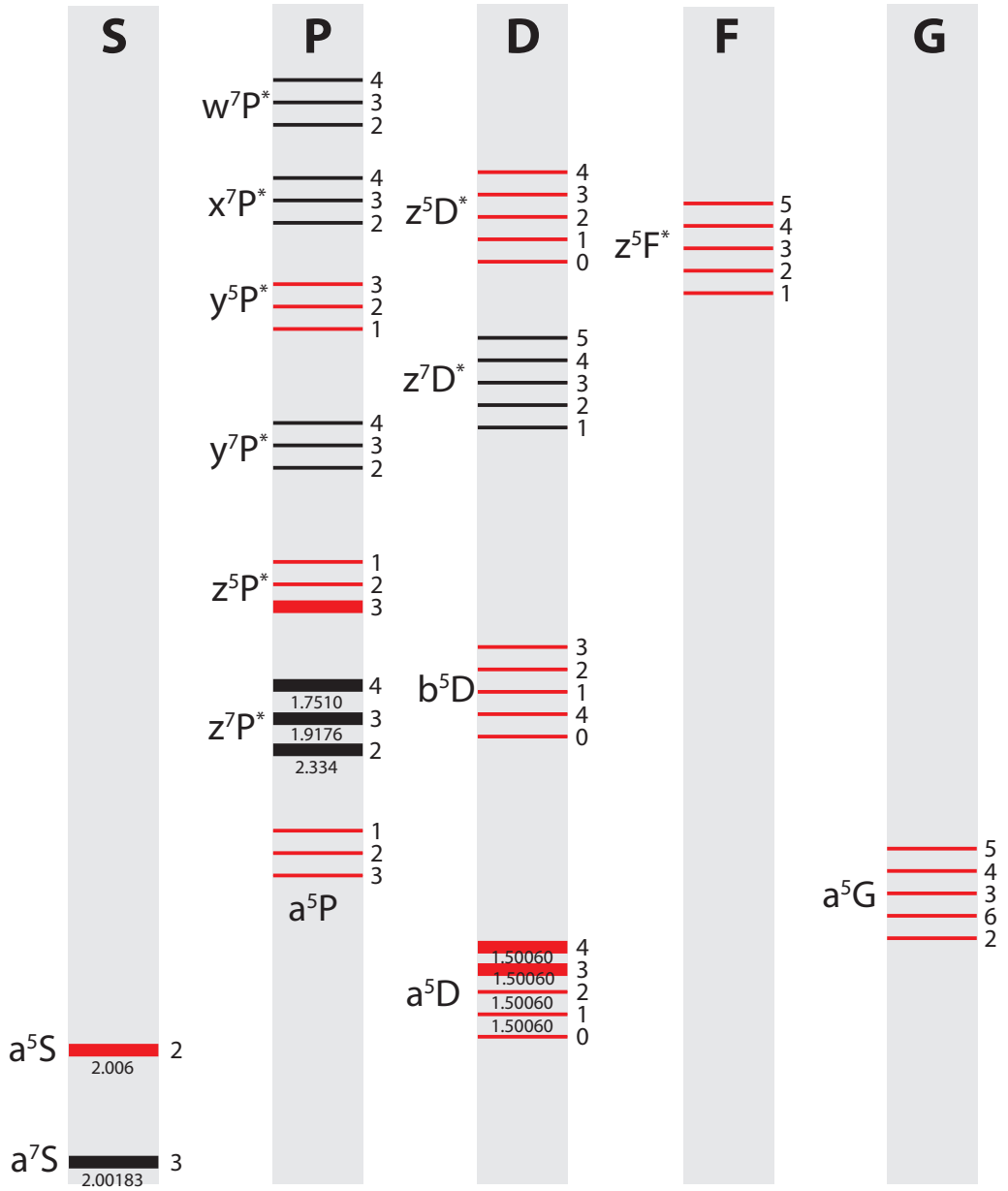

Figure D.1: Grotrian diagram of ^{52}Cr. Septett states are drawn in black, while quintett states appear in red. States marked by an asterisk have odd parity.

transition	vacuum wavelength	natural linewidth	ref
$^7S_3 \leftrightarrow {}^7P_4$	425.554 nm	$\Gamma = 31.5 \cdot 10^6\,s^{-1}$	[166]
$^7S_3 \leftrightarrow {}^7P_3$	427.600 nm	$\Gamma = 30.7 \cdot 10^6\,s^{-1}$	[166]
$^5S_2 \leftrightarrow {}^7P_3$	633.185 nm	$\Gamma = 29 \cdot 10^3\,s^{-1}$	[166]
$^5D_4 \leftrightarrow {}^7P_4$	658.2740(2) nm	$\Gamma = (127 \pm 14)\,s^{-1}$	[230]
$^5D_4 \leftrightarrow {}^7P_3$	663.1846(2) nm	$\Gamma = 6 \cdot 10^3\,s^{-1}$	[166, 230]
$^5D_3 \leftrightarrow {}^7P_4$	649.1978(2) nm	$\Gamma = (42 \pm 6)\,s^{-1}$	[230]
$^5D_3 \leftrightarrow {}^7P_3$	653.9727(2) nm	-	[230]

Table D.3: Vacuum wavelengths and natural linewidths of the most important ^{52}Cr transitions.

Appendix E

Grammar of the experiment control language

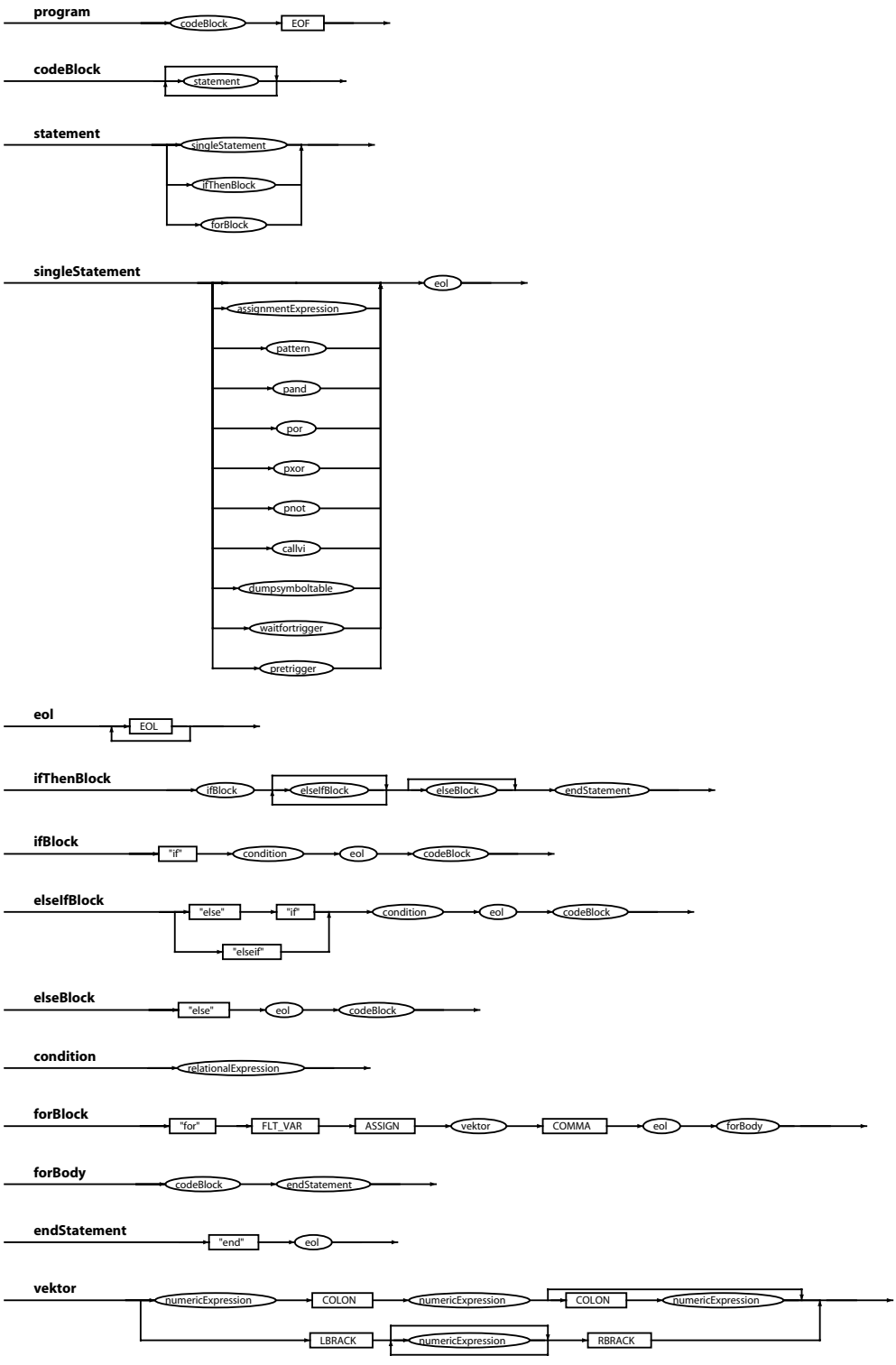

Figure E.1: Pattern Parser (1/3)

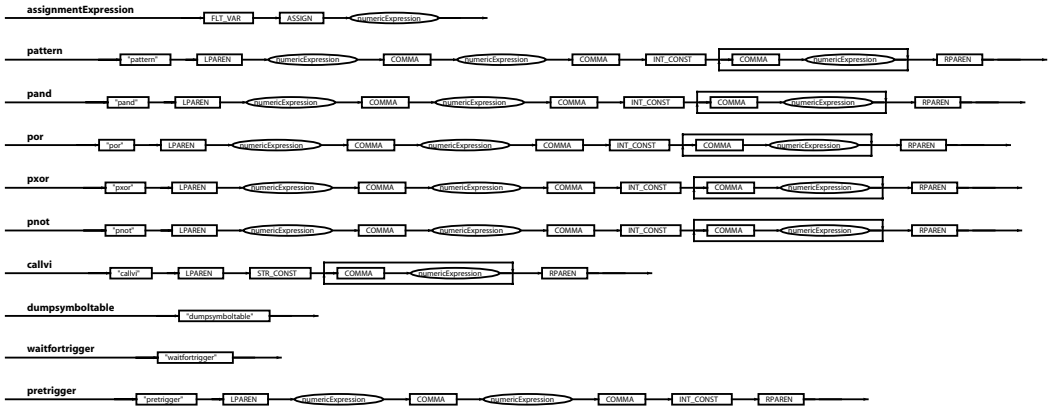

Figure E.2: Pattern Parser (2/3)

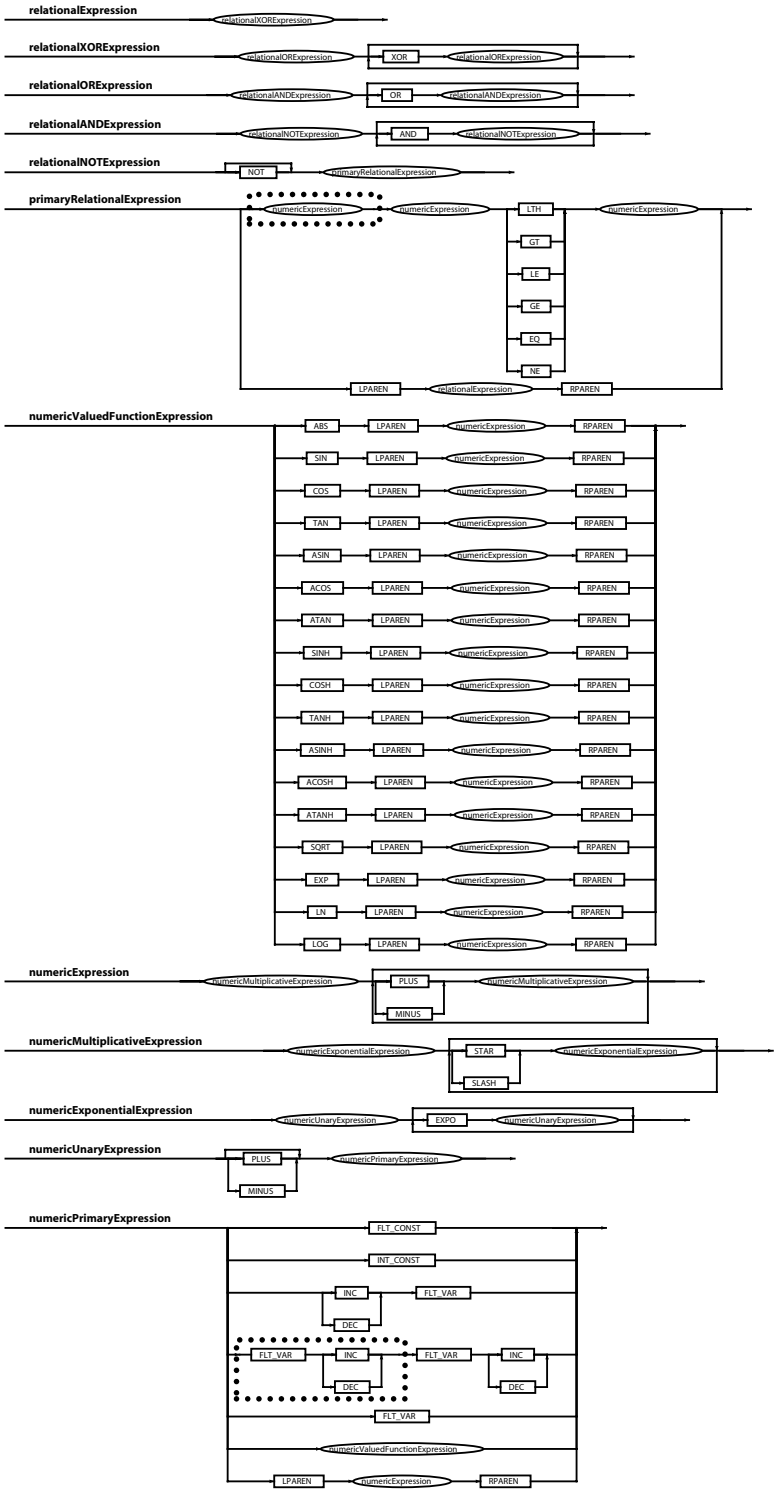

Figure E.3: Pattern Parser (3/3)

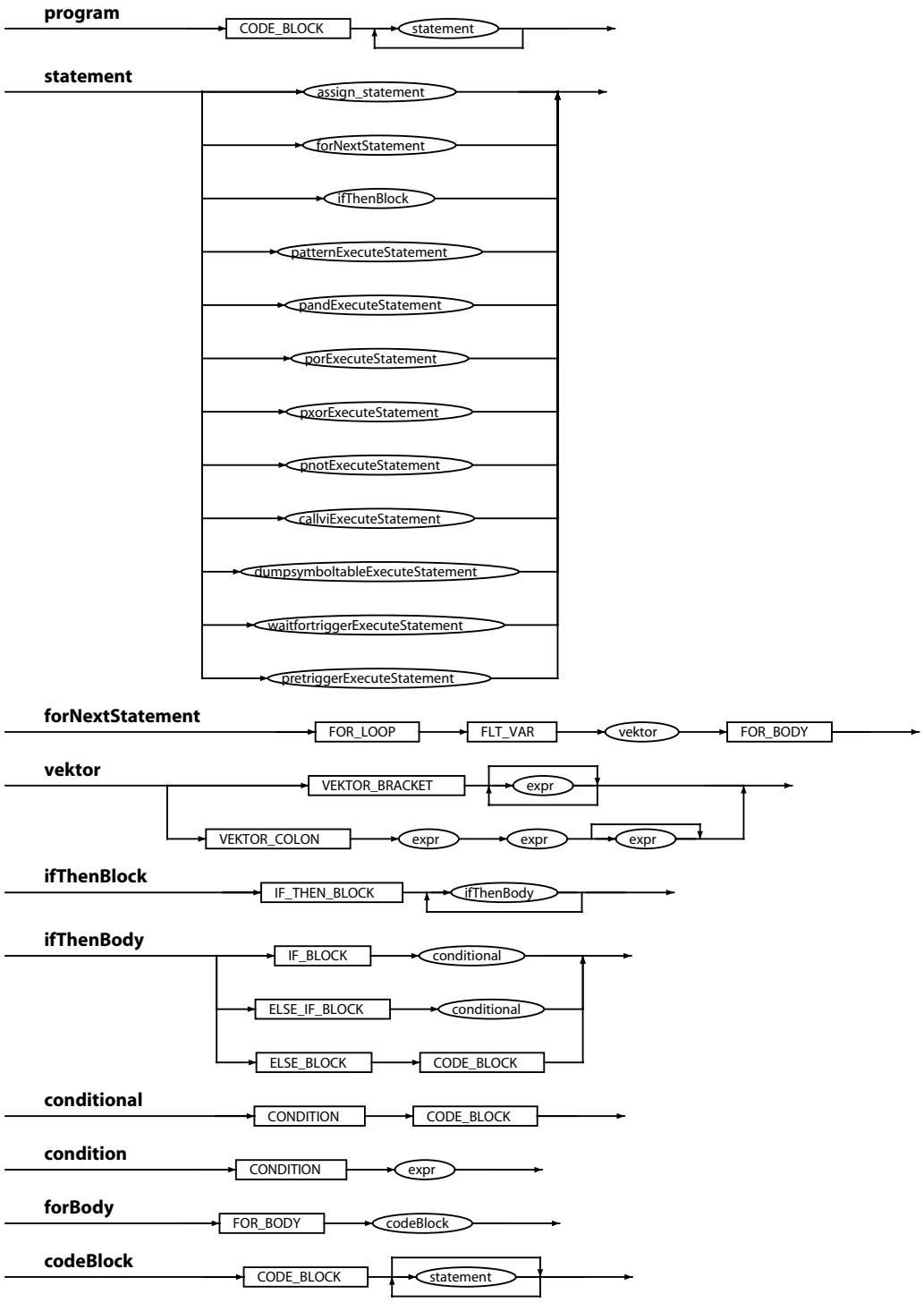

Figure E.4: Pattern Walker (1/3)

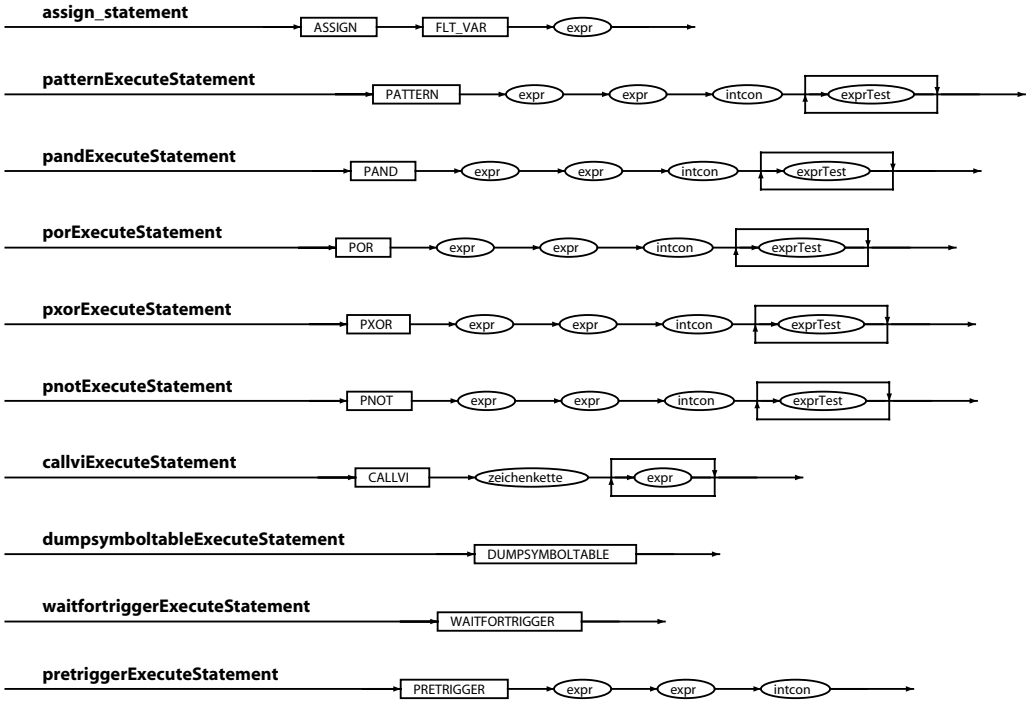

Figure E.5: Pattern Walker (2/3)

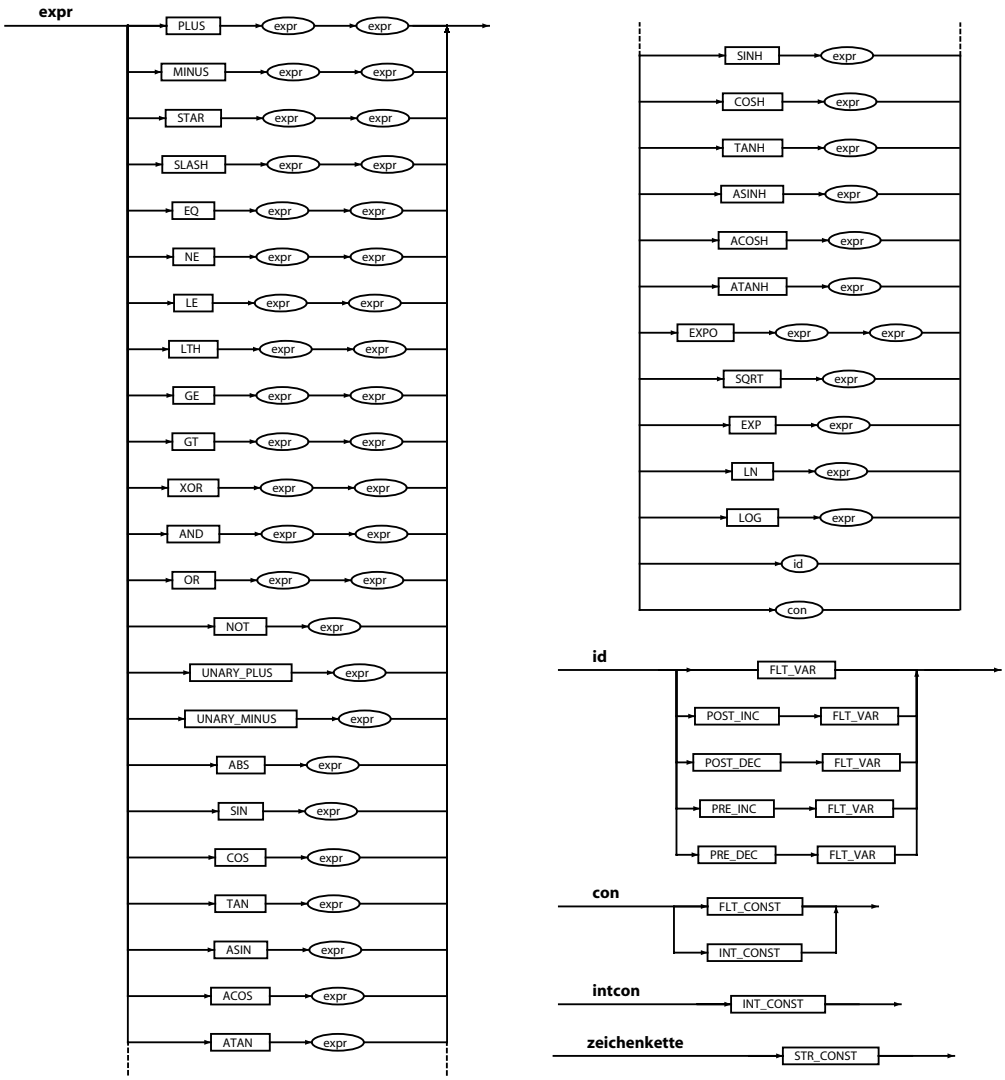

Figure E.6: Pattern Walker (3/3)

Bibliography

[1] J. R. Abo-Shaeer, C. Raman, J. M. Vogels, and W. Ketterle. Observation of Vortex Lattices in Bose-Einstein Condensates. *Science*, 292(5516):476–479, 2001. URL http://www.sciencemag.org/cgi/content/abstract/292/5516/476.

[2] M. Abramowitz and I. A. Stegun. *Handbook of Mathematical Functions with Formulas, Graphs, and Mathematical Tables*. Dover, New York, ninth dover printing, tenth gpo printing edition, 1964. ISBN 0-486-61272-4.

[3] A. Aho, R. Sethi, and J. Ullman. *Compilers: Principles, Techniques and Tools*. Addison-Wesley, Boston, 1986.

[4] B. P. Anderson and M. A. Kasevich. Macroscopic Quantum Interference from Atomic Tunnel Arrays. *Science*, 282(5394):1686–1689, 1998. URL http://www.sciencemag.org/cgi/content/abstract/282/5394/1686.

[5] B. P. Anderson, P. C. Haljan, C. A. Regal, D. L. Feder, L. A. Collins, C. W. Clark, and E. A. Cornell. Watching Dark Solitons Decay into Vortex Rings in a Bose-Einstein Condensate. *Physical Review Letters*, 86(14):2926–2929, 2001. URL http://link.aps.org/abstract/PRL/v86/p2926.

[6] M. H. Anderson, J. R. Ensher, M. R. Matthews, C. E. Wieman, and E. A. Cornell. Observation of Bose-Einstein Condensation in a Dilute Atomic Vapor. *Science*, 269(0):198, July 1995.

[7] K. Andersson. The electronic spectrum of Cr_2. *Chemical Physics Letters*, 237: 212–221, 1995.

[8] M. Arndt, M. B. Dahan, D. Guéry-Odelin, M. W. Reynolds, and J. Dalibard. Observation of a Zero-Energy Resonance in Cs-Cs Collisions. *Physical Review Letters*, 79(4):625–628, July 1997. URL http://link.aps.org/abstract/PRL/v79/p625.

[9] M. Baranov, L. Dobrek, K. Góral, L. Santos, and M. Lewenstein. Ultracold Dipolar Gases — a Challenge for Experiments and Theory. *Physica Scripta*, T102:74–81, 2002. and references therein.

[10] M. A. Baranov, M. S. Mar'enko, V. S. Rychkov, and G. V. Shlyapnikov. Superfluid pairing in a polarized dipolar Fermi gas. *Physical Review A (Atomic, Molecular, and Optical Physics)*, 66(1):013606, 2002. URL http://link.aps.org/abstract/PRA/v66/e013606.

[11] J. Barnes, editor. *Early Greek Philosophy*. Penguin Classics, November 2002.

[12] M. D. Barrett, J. A. Sauer, and M. S. Chapman. All-Optical Formation of an Atomic Bose-Einstein Condensate. *Physical Review Letters*, 87(1):010404, 2001. URL http://link.aps.org/abstract/PRL/v87/e010404.

[13] P. F. Bedaque, E. Braaten, and H.-W. Hammer. Three-body Recombination in Bose Gases with Large Scattering Length. *Physical Review Letters*, 85(5): 908–911, 2000. URL http://link.aps.org/abstract/PRL/v85/p908.

[14] H. L. Bethlem, G. Berden, and G. Meijer. Decelerating Neutral Dipolar Molecules. *Physical Review Letters*, 83(8):1558–1561, 1999. URL http://link.aps.org/abstract/PRL/v83/p1558.

[15] H. L. Bethlem, F. M. H. C. Giel Berden, R. T. Jongma, and A. J. A. van Roij Gerard Meijer. Electrostatic trapping of ammonia molecules. *Nature*, 406: 491–494, 2001.

[16] I. Bloch, T. W. Hansch, and T. Esslinger. Atom Laser with a cw Output Coupler. *Physical Review Letters*, 82(15):3008–3011, 1999. URL http://link.aps.org/abstract/PRL/v82/p3008.

[17] I. Bloch, M. Greiner, O. Mandel, T. W. Hänsch, and T. Esslinger. Sympathetic cooling of ^{85}Rb and ^{87}Rb. *Physical Review A (Atomic, Molecular, and Optical Physics)*, 64:021402, 2001.

[18] J. L. Bohn and P. S. Julienne. Prospects for influencing scattering lengths with far-off-resonant light. *Physical Review A (Atomic, Molecular, and Optical Physics)*, 56(2):1486–1491, 1997. URL http://link.aps.org/abstract/PRA/v56/p1486.

[19] K. Bongs and K. Sengstock. Physics with coherent matter waves. *Reports on Progress in Physics*, 67(6):907–963, June 2004.

[20] S. Bose. Plancks Gesetz und Lichtquantenhypothese. *Zeitschrift für Physik*, 26 (3):178, 1924.

[21] T. Bourdel, J. Cubizolles, L. Khaykovich, K. M. F. Magalhaes, S. J. J. M. F. Kokkelmans, G. V. Shlyapnikov, and C. Salomon. Measurement of the Interaction Energy near a Feshbach Resonance in a Li Fermi Gas. *Physical Review*

Letters, 91(2):020402, 2003. URL http://link.aps.org/abstract/PRL/v91/e020402.

[22] E. Braaten and H. Hammer. Universality in Few-body Systems with Large Scattering Length, Oct. 2004. URL arXiv:cond-mat/0410417.

[23] E. Braaten and H.-W. Hammer. Three-Body Recombination into Deep Bound States in a Bose Gas with Large Scattering Length. *Physical Review Letters*, 87 (16):160407, 2001. URL http://link.aps.org/abstract/PRL/v87/e160407.

[24] C. C. Bradley, C. A. Sackett, J. J. Tollett, and R. G. Hulet. Evidence of Bose-Einstein Condensation in an Atomic Gas with Attractive Interactions. *Physical Review Letters*, 75(9):1687–1690, Aug. 1995. URL http://link.aps.org/abstract/PRL/v75/p1687. *ibid.* **79**, 1170 (1997).

[25] C. C. Bradley, C. A. Sackett, J. J. Tollett, and R. G. Hulet. Evidence of Bose-Einstein Condensation in an Atomic Gas with Attractive Interactions. *Physical Review Letters*, 75(9):1687–1690, 1995. URL http://link.aps.org/abstract/PRL/v75/p1687.

[26] P. Brix, J. T. Eisinger, H. Lew, and G. Wessel. The Zeeman Effect of the Cr Ground State. *Physical Review*, 92:647, 1953.

[27] S. Burger, K. Bongs, S. Dettmer, W. Ertmer, K. Sengstock, A. Sanpera, G. V. Shlyapnikov, and M. Lewenstein. Dark Solitons in Bose-Einstein Condensates. *Physical Review Letters*, 83(25):5198–5201, 1999. URL http://link.aps.org/abstract/PRL/v83/p5198.

[28] S. Burger, F. S. Cataliotti, C. Fort, F. Minardi, M. Inguscio, M. L. Chiofalo, and M. P. Tosi. Superfluid and Dissipative Dynamics of a Bose-Einstein Condensate in a Periodic Optical Potential. *Physical Review Letters*, 86(20): 4447–4450, 2001. URL http://link.aps.org/abstract/PRL/v86/p4447.

[29] E. A. Burt, R. W. Ghrist, C. J. Myatt, M. J. Holland, E. A. Cornell, and C. E. Wieman. Coherence, Correlations, and Collisions: What One Learns about Bose-Einstein Condensates from Their Decay. *Physical Review Letters*, 79(3): 337–340, July 1997. URL http://link.aps.org/abstract/PRL/v79/p337.

[30] E. I. Butikov. Parametric excitation of a linear oscillator. *European Journal of Physics*, 25(4):535–554, 2004. URL http://stacks.iop.org/0143-0807/25/535.

[31] S. M. Casey and D. G. Leopold. Negative ion photoelectron spectroscopy of chromium dimer. *J. Phys. Chem.*, 97(4):816–830, 1993.

[32] Y. Castin. *Coherent atomic matter waves*, volume 72 of *Les Houches Summer school*, chapter 1. Springer-Verlag GmbH, 2001.

[33] G. Cennini, G. Ritt, C. Geckeler, and M. Weitz. All-Optical Realization of an Atom Laser. *Physical Review Letters*, 91(24), 2003.

[34] A. P. Chikkatur, A. Görlitz, D. M. Stamper-Kurn, S. Inouye, S. Gupta, and W. Ketterle. Suppression and Enhancement of Impurity Scattering in a Bose-Einstein Condensate. *Physical Review Letters*, 85(3):483–486, 2000. URL http://link.aps.org/abstract/PRL/v85/p483.

[35] W. J. Childs and L. S. Goodman. Electronic g Factors fo Low-Lying Levels of Fe I, Cr I, and Mn I. *Physical Review A (Atomic, Molecular, and Optical Physics)*, 140:A447, 1965.

[36] C. Chin, V. Vuletic, A. J. Kerman, and S. Chu. High Resolution Feshbach Spectroscopy of Cesium. *Physical Review Letters*, 85(13):2717–2720, 2000. URL http://link.aps.org/abstract/PRL/v85/p2717.

[37] C. Chin, A. J. Kerman, V. Vuletić, and S. Chu. Sensitive Detection of Cold Cesium Molecules Formed on Feshbach Resonances. *Physical Review Letters*, 90 (3):033201, 2003. URL http://link.aps.org/abstract/PRL/v90/e033201.

[38] C. Chin, M. Bartenstein, A. Altmeyer, S. Riedl, S. Jochim, J. H. Denschlag, and R. Grimm. Observation of the Pairing Gap in a Strongly Interacting Fermi Gas. *Science*, page 1100818, 2004. URL http://www.sciencemag.org/cgi/content/abstract/1100818v1.

[39] S. Chu. Nobel Lecture: The manipulation of neutral particles. *Review of Modern Physics*, 70(3):685–706, 1998. URL http://link.aps.org/abstract/RMP/v70/p685.

[40] C. Cohen-Tannoudji, B. Diu, and F. Laloe. *Quantum Mechanics*. Wiley-Interscience, 1977.

[41] C. Cohen-Tannoudji, J. Dupont-Roc, and G. Grynberg. *Atom-photon interactions*. John Wiley & Sons, 1 edition, 1992.

[42] C. N. Cohen-Tannoudji. Nobel Lecture: Manipulating atoms with photons. *Review of Modern Physics*, 70(3):707–719, 1998. URL http://link.aps.org/abstract/RMP/v70/p707.

[43] D. T. Colbert and W. H. Miller. A novel discrete variable representation for quantum mechanical reactive scattering via the S-matrix Kohn method. *Journal of Chemical Physics*, 96(3):1982–1991, 1992. URL http://link.aip.org/link/?JCP/96/1982/1.

[44] W. N. Cottingham and D. A. Greenwood. *An Introduction to the Standard Model of Particle Physics*. Cambridge University Press, November 1998.

[45] P. Courteille, R. S. Freeland, D. J. Heinzen, F. A. van Abeelen, and B. J. Verhaar. Observation of a Feshbach Resonance in Cold Atom Scattering. *Physical Review Letters*, 81(1):69–72, 1998. URL http://link.aps.org/abstract/PRL/v81/p69.

[46] F. Dalfovo, S. Giorgini, L. P. Pitaevskii, and S. Stringari. Theory of Bose-Einstein condensation in trapped gases. *Review of Modern Physics*, 71(3):463, Apr. 1999.

[47] K. B. Davis, M.-O. Mewes, and W. Ketterle. An analytical model for evaporative cooling of atoms. *Applied Physics B*, 60:155, 1995.

[48] P. Debeye. *Annalen der Physik*, 81:1154, 1926.

[49] R. deCarvalho and J. Doyle. Evaporative cooling at low trap depth. *Physical Review A (Atomic, Molecular, and Optical Physics)*, 70(5):053409, 2004. URL http://link.aps.org/abstract/PRA/v70/e053409.

[50] R. deCarvalho, C. I. Hancox, and J. M. Doyle. Enhanced inelastic scattering rates of cold atomic chromium. *Journal of the Optical Society of America B: Optical Physics*, 20(5):1131–1134, 2003. URL http://www.opticsinfobase.org/abstract.cfm?URI=JOSAB-20-5-1131.

[51] B. DeMarco and D. S. Jin. Onset of Fermi Degeneracy in a Trapped Atomic Gas. *Science*, 285(5434):1703, Sept. 1999.

[52] D. DeMille. Quantum Computation with Trapped Polar Molecules. *Physical Review Letters*, 88(6):067901, 2002. URL http://link.aps.org/abstract/PRL/v88/e067901.

[53] W. Demtröder. *Laserspektroskopie*. Springer Verlag, 1991.

[54] J. Denschlag, J. E. Simsarian, D. L. Feder, C. W. Clark, L. A. Collins, J. Cubizolles, L. Deng, E. W. Hagley, K. Helmerson, W. P. Reinhardt, S. L. Rolston, B. I. Schneider, and W. D. Phillips. Generating Solitons by Phase Engineering of a Bose-Einstein Condensate. *Science*, 287:97, Jan. 2000.

[55] K. Dieckmann, R. J. C. Spreeuw, M. Weidemüller, and J. T. M. Walraven. Two-dimensional magneto-optical trap as a source of slow atoms. *Physical Review A (Atomic, Molecular, and Optical Physics)*, 58(5):3891–3895, Nov. 1998. URL http://link.aps.org/abstract/PRA/v58/p3891.

[56] K. Dieckmann, C. A. Stan, S. Gupta, Z. Hadzibabic, C. H. Schunck, , and W. Ketterle. Decay of an Ultracold Fermionic Lithium Gas near a Feshbach Resonance. *Physical Review Letters*, 89:203201, 2002.

[57] K. Dieckmann, C. A. Stan, S. Gupta, Z. Hadzibabic, C. H. Schunck, and W. Ketterle. Decay of an Ultracold Fermionic Lithium Gas near a Feshbach Resonance. *Physical Review Letters*, 89(20):203201, 2002. URL http://link.aps.org/abstract/PRL/v89/e203201.

[58] E. A. Donley, N. R. Claussen, S. T. Thompson, and C. E. Wieman. Atom-molecule coherence in a Bose-Einstein condensate. *Nature*, 417:529, May 2002.

[59] R. W. P. Drever, J. L. Hall, F. V. Kowalski, J. Hough, G. M. Ford, A. J. Munley, and H. Ward. Laser phase and frequency stabilization using an optical resonator. *Applied Physics B*, 31(2):97, 1983.

[60] R. A. Duine and H. T. C. Stoof. Atom-molecule coherence in Bose gases. *Physics Reports*, 396(3):115–195, June 2004.

[61] S. Dürr, T. Volz, A. Marte, and G. Rempe. Observation of Molecules Produced from a Bose-Einstein Condensate. *Physical Review Letters*, 92(2):020406, 2004. URL http://link.aps.org/abstract/PRL/v92/e020406.

[62] A. Einstein. Quantentheorie des einatomigen idealen Gases. Zweite Abhandlung. *Sitzungber. Preuss. Akad. Wiss.*, 1925:3, Jan. 1925.

[63] M. Erhard, H. Schmaljohann, J. Kronjager, K. Bongs, and K. Sengstock. Measurement of a mixed-spin-channel Feshbach resonance in ^{87}Rb. *Physical Review A (Atomic, Molecular, and Optical Physics)*, 69(3):032705, 2004. URL http://link.aps.org/abstract/PRA/v69/e032705.

[64] B. D. Esry, C. H. Greene, and J. James P. Burke. Recombination of Three Atoms in the Ultracold Limit. *Physical Review Letters*, 83(9):1751–1754, 1999. URL http://link.aps.org/abstract/PRL/v83/p1751.

[65] T. Esslinger, I. Bloch, and T. W. Hänsch. Bose-Einstein condensation in a quadrupole-Ioffe-configuration trap. *Physical Review A (Atomic, Molecular, and Optical Physics)*, 58(4):R2664, Oct. 1998.

[66] F. K. Fatemi, K. M. Jones, and P. D. Lett. Observation of Optically Induced Feshbach Resonances in Collisions of Cold Atoms. *Physical Review Letters*, 85(21):4462–4465, 2000. URL http://link.aps.org/abstract/PRL/v85/p4462.

[67] P. O. Fedichev, Y. Kagan, G. V. Shlyapnikov, and J. T. M. Walraven. Influence of Nearly Resonant Light on the Scattering Length in Low-Temperature Atomic Gases. *Physical Review Letters*, 77(14):2913–2916, 1996. URL http://link.aps.org/abstract/PRL/v77/p2913.

[68] P. O. Fedichev, M. W. Reynolds, U. M. Rahmanov, and G. V. Shlyapnikov. Inelastic decay processes in a gas of spin-polarized triplet helium. *Physical Review A (Atomic, Molecular, and Optical Physics)*, 53(3):1447–1453, 1996. URL http://link.aps.org/abstract/PRA/v53/p1447.

[69] P. O. Fedichev, M. W. Reynolds, and G. V. Shlyapnikov. Three-Body Recombination of Ultracold Atoms to a Weakly Bound s Level. *Physical Review Letters*, 77(14):2921–2924, 1996. URL http://link.aps.org/abstract/PRL/v77/p2921.

[70] H. Feshbach. A Unified Theory of Nuclear Reactions. II. *Annalen der Physik*, 19:287, 1962.

[71] T. Fließbach. *Elektrodynamik*. Spektrum, Akademischer Verlag, 2. edition, 1997.

[72] S. Friebel, C. D'Andrea, J. Walz, M. Weitz, and T. W. Hänsch. CO_2-laser optical lattice with cold rubidium atoms. *Physical Review A (Atomic, Molecular, and Optical Physics)*, 57(1):R20–R23, 1998. URL http://link.aps.org/abstract/PRA/v57/pR20.

[73] M. E. Gehm, K. M. O'Hara, T. A. Savard, and J. E. Thomas. Dynamics of noise-induced heating in atom traps. *Physical Review A (Atomic, Molecular, and Optical Physics)*, 58(5):3914–3921, Nov. 1998. URL http://link.aps.org/abstract/PRA/v58/p3914.

[74] M. Gell-Mann and M. L. Goldberger. The Formal Theory of Scattering. *Physical Review*, 91:398–408, 1953.

[75] J. M. Gerton, D. Strekalov, I. Prodan, and R. G. Hulet. Direct observation of growth and collapse of a Bose-Einstein condensate with attractive interactions. *Nature*, 408:692, Dec. 2000.

[76] W. F. Giauque. A thermodynamic treatment of certain magnetic effects. A proposed method of producing temperatures considerably below 1° absolute. *J. Am. Chem. Soc.*, 49(1864), 1927.

[77] S. Giovanazzi, A. Görlitz, and T. Pfau. Tuning the Dipolar Interaction in Quantum Gases. *Physical Review Letters*, 89(13):130401, 2002. URL http://link.aps.org/abstract/PRL/v89/e130401.

[78] S. Giovanazzi, A. Görlitz, and T. Pfau. Ballistic expansion of a dipolar condensate. *Journal of Optics B: Quantum Semiclassical Optics*, 5:S208–S211, 2003.

[79] R. G. Gordon. New Method for Constructing Wavefunctions for Bound States and Scattering. *Journal of Chemical Physics*, 51(1):14–25, 1969. URL http://link.aip.org/link/?JCP/51/14/1.

[80] Y. V. Gott, M. S. Ioffe, and V. G. Telkovsky. . *Nuclear Fusion, 1962 Suppl., Pr. 3 (International Atomic Energy Agency, Vienna, 1962)*, page 1045–1049, 1962.

[81] M. Greiner, O. Mandel, T. Esslinger, T. W. Hänsch, and I. Bloch. Quantum phase transition from a superfluid to a Mott insulator in a gas of ultracold atoms. *Nature*, 415:39, Jan. 2002.

[82] M. Greiner, C. A. Regal, and D. Jin. Emergence of a molecular Bose-Einstein condensate from a Fermi gas. *Nature*, 426:537–540, 2004.

[83] A. Griesmaier. *Aufbau einer kombinierten magneto-optischen Falle für Chrom und Rubidium*. Diploma thesis, 5. Physikalisches Institut, Universität Stuttgart, 2002.

[84] A. Griesmaier, J. Werner, S. Hensler, J. Stuhler, and T. Pfau. Bose-Einstein Condensation of Chromium. *Physical Review Letters*, 94(16):160401, 2005. URL http://link.aps.org/abstract/PRL/v94/e160401.

[85] R. Grimm, M. Weidemüller, and Y. B. Ovchinnikov. Optical dipole traps for neutral atoms. *Advances in Atomic, Molecular, and Optical Physics*, 42:95–170, 2000.

[86] D. Guéry-Odelin, J. Söding, P. Desbiolles, and J. Dalibard. Is Bose-Einstein condensation of atomic cesium possible? *Europhysics Letters*, 44(1):26, Oct. 1998.

[87] K. Góral and L. Santos. Ground state and elementary excitations of single and binary Bose-Einstein condensates of trapped dipolar gases. *Physical Review A (Atomic, Molecular, and Optical Physics)*, 66(2):023613, 2002. URL http://link.aps.org/abstract/PRA/v66/e023613.

[88] K. Góral and L. Santos. Ground state and elementary excitations of single and binary Bose-Einstein condensates of trapped dipolar gases. *Physical Review A (Atomic, Molecular, and Optical Physics)*, 66(2):023613, 2002. URL http://link.aps.org/abstract/PRA/v66/e023613.

[89] K. Góral, K. Rzążewski, and T. Pfau. Bose-Einstein condensation with magnetic dipole-dipole forces. *Physical Review A (Atomic, Molecular, and Optical Physics)*, 61(5):051601, 2000. URL http://link.aps.org/abstract/PRA/v61/e051601.

[90] K. Góral, M. Gajda, and K. Rzążewski. Thermodynamics of an interacting trapped Bose-Einstein gas in the classical field approximation. *Physical Review A (Atomic, Molecular, and Optical Physics)*, 66(5):051602, 2002. URL http://link.aps.org/abstract/PRA/v66/e051602.

[91] K. Góral, L. Santos, and M. Lewenstein. Quantum Phases of Dipolar Bosons in Optical Lattices. *Physical Review Letters*, 88(17):170406, 2002. URL http://link.aps.org/abstract/PRL/v88/e170406.

[92] A. Görlitz, T. L. Gustavson, A. E. Leanhardt, R. Löw, A. P. Chikkatur, S. Gupta, S. Inouye, D. E. Pritchard, and W. Ketterle. Sodium Bose-Einstein Condensates in the $F = 2$ State in a Large-Volume Optical Trap. *Physical Review Letters*, 90(9):090401, Mar. 2003. URL http://link.aps.org/abstract/PRL/v90/e090401.

[93] E. W. Hagley, L. Deng, M. Kozuma, J. Wen, K. Helmerson, S. L. Rolston, and W. D. Phillips. A Well-Collimated Quasi-Continuous Atom Laser. *Science*, 283:1706, Mar. 1999.

[94] H. Haken and H. C. Wolf. *The Physics of Atoms and Quanta*. Springer, October 2000.

[95] D. S. Hall, M. R. Matthews, J. R. Ensher, C. E. Wieman, and E. A. Cornell. Dynamics of Component Separation in a Binary Mixture of Bose-Einstein Condensates. *Physical Review Letters*, 81(8):1539–1542, 1998. URL http://link.aps.org/abstract/PRL/v81/p1539.

[96] D. S. Hall, M. R. Matthews, C. E. Wieman, and E. A. Cornell. Measurements of Relative Phase in Two-Component Bose-Einstein Condensates. *Physical Review Letters*, 81(8):1543–1546, 1998. URL http://link.aps.org/abstract/PRL/v81/p1543.

[97] D. O. Harris, G. G. Engerholm, and W. D. Gwinn. Calculation of Matrix Elements for One-Dimensional Quantum-Mechanical Problems and the Application to Anharmonic Oscillators. *Journal of Chemical Physics*, 43(5):1515–1517, 1965. URL http://link.aip.org/link/?JCP/43/1515/1.

[98] L. V. Hau, B. D. Busch, C. Liu, Z. Dutton, M. M. Burns, and J. A. Golovchenko. Near-resonant spatial images of confined Bose-Einstein condensates in a 4-Dee

magnetic bottle. *Physical Review A (Atomic, Molecular, and Optical Physics)*, 58(1):R54, July 1998.

[99] D. J. Heinzen. Ultracold atomic interactions. In M. Inguscio, S. Stringari, and C. E. Wieman, editors, *Proceedings of the International School of Physics - Enrico Fermi*, page 351. IOS Press, 1999.

[100] S. Hensler. *Wechselwirkungen in ultrakalten dipolaren Gasen*. Phd thesis, 5. Physikalisches Institut, Universität Stuttgart, Pfaffenwaldring 57, 70550 Stuttgart, 2004.

[101] S. Hensler. *Eine magneto-optische Falle mit Chromatomen*. Diploma thesis, Universität Konstanz, Lehrstuhl J. Mlynek, 1999.

[102] S. Hensler, J. Werner, A. Griesmaier, P. O. Schmidt, A. Görlitz, T. Pfau, and K. R. S. Giovanazzi. Dipolar Relaxation in an ultra-cold gas of magnetically trapped chromium atoms. *Applied Physics B*, 77:765–772, 2003.

[103] S. Hensler, A. Greiner, J. Stuhler, and T. Pfau. Depolarisation cooling of an atomic cloud. *ArXiv Quantum Physics e-prints*, May 2005.

[104] J. Herbig, T. Kraemer, M. Mark, T. Weber, C. Chin, H.-C. Nägerl, and R. Grimm. Preparation of a Pure Molecular Quantum Gas. *Science*, 301(5639): 1510–1513, 2003.

[105] G. Herzberg. *Molecular spectra and molecular structure. Vol.1: Spectra of diatomic molecules*, volume 1. Van Nostrand Reinhold, New York, 2nd edition, 1950.

[106] S. A. Hopkins, S. Webster, J. Arlt, P. Bance, S. Cornish, O. Marago, and C. J. Foot. Measurement of elastic cross section for cold cesium collisions. *Physical Review A (Atomic, Molecular, and Optical Physics)*, 61:032707, 2000.

[107] M. Houbiers, H. T. C. Stoof, W. I. McAlexander, and R. G. Hulet. Elastic and inelastic collisions of ^{6}Li atoms in magnetic and optical traps. *Physical Review A (Atomic, Molecular, and Optical Physics)*, 57(3):R1497–R1500, 1998. URL http://link.aps.org/abstract/PRA/v57/pR1497.

[108] S. Inouye, M. R. Andrews, J. Stenger, H.-J. Miesner, D. M. Stamper-Kurn, and W. Ketterle. Observation of Feshbach resonances in a Bose-Einstein condensate. *Nature*, 392(0):151, Mar. 1998.

[109] S. Inouye, T. Pfau, S. Gupta, A. P. Chikkatur, A. Görlitz, D. E. Pritchard, and W. Ketterle. Phase-coherent amplification of atomic matter waves. *Nature*, 402:641, Dec. 1999.

[110] S. Inouye, S. Gupta, T. Rosenband, A. P. Chikkatur, A. Görlitz, T. L. Gustavson, A. E. Leanhardt, D. E. Pritchard, and W. Ketterle. Observation of Vortex Phase Singularities in Bose-Einstein Condensates. *Physical Review Letters*, 87(8):080402, 2001. URL http://link.aps.org/abstract/PRL/v87/e080402.

[111] S. Inouye, J. Goldwin, M. L. Olsen, C. Ticknor, J. L. Bohn, and D. S. Jin. Observation of Heteronuclear Feshbach Resonances in a Mixture of Bosons and Fermions. *Physical Review Letters*, 93(18):183201, 2004.

[112] J. D. Jackson. *Classical Electrodynamics*. John Wiley & Sons, New York, 2. edition, 1975.

[113] R. Jauregui. Nonperturbative and perturbative treatments of parametric heating in atom traps. *Physical Review A (Atomic, Molecular, and Optical Physics)*, 64(5):053408, 2001. URL http://link.aps.org/abstract/PRA/v64/e053408.

[114] C. J. Joachain. *Quantum collision theory*. North-Holland publishing company, Amsterdam, 1975.

[115] S. Jochim, M. Bartenstein, A. Altmeyer, G. Hendl, C. Chin, J. H. Denschlag, and R. Grimm. Pure Gas of Optically Trapped Molecules Created from Fermionic Atoms. *Physical Review Letters*, 91(24):240402, 2003. URL http://link.aps.org/abstract/PRL/v91/e240402.

[116] S. Jochim, M. Bartenstein, A. Altmeyer, G. Hendl, S. Riedl, C. Chin, J. Hecker Denschlag, and R. Grimm. Bose-Einstein Condensation of Molecules. *Science*, 302(5653):2101–2103, 2003.

[117] T. Junglen, T. Rieger, S. A. Rangwala, P. W. H. Pinkse, and G. Rempe. Two-Dimensional Trapping of Dipolar Molecules in Time-Varying Electric Fields. *Physical Review Letters*, 92(22):223001, 2004. URL http://link.aps.org/abstract/PRL/v92/e223001.

[118] Y. Kagan, B. V. Svistunov, and G. V. Shlyapnikov. Effect of Bose condensation on inelastic processes in gases. *Sov. Phys. JETP Lett.*, 42(4):209, Aug. 1985.

[119] G. M. Kavoulakis, C. J. Pethick, and H. Smith. Collisional relaxation in diffuse clouds of trapped bosons. *Physical Review A (Atomic, Molecular, and Optical Physics)*, 61(5):053603, Apr. 2000. URL http://link.aps.org/abstract/PRA/v61/e053603.

[120] W. Ketterle and N. J. van Druten. Evaporative Cooling of Trapped Atoms. *Adv. At. Mol. Opt. Phys.*, 37(0):181, 1996.

[121] W. Ketterle, D. S. Durfee, and D. M. Stamper-Kurn. Making, probing and understanding Bose-Einstein condensates. In M. Inguscio, S. Stringari, and C. E. Wieman, editors, *Proceedings of the International School of Physics - Enrico Fermi*, page 67. IOS Press, 1999.

[122] J. Kim, B. Friedrich, D. P. Katz, D. Patterson, J. D. Weinstein, R. deCarvalho, and J. M. Doyle. Buffer-gas loading and magnetic trapping of atomic europium. *Physical Review Letters*, 78(19):3665–3668, May 1997. URL http://link.aps.org/abstract/PRL/v78/p3665.

[123] D. Kleppner. Professor Feshbach and his resonance. *Physics Today*, page 12–13, August 2004.

[124] V. Kokoouline, J. Vala, and R. Kosloff. Tuning the scattering length on the ground triplet state of Cs_2. *Journal of Chemical Physics*, 114(7):3046–3050, 2001. URL http://link.aip.org/link/?JCP/114/3046/1.

[125] M. Kozuma, L. Deng, E. W. Hagley, J. Wen, R. Lutwak, K. Helmerson, S. L. Rolston, and W. D. Phillips. Coherent Splitting of Bose-Einstein Condensed Atoms with Optically Induced Bragg Diffraction. *Physical Review Letters*, 82 (5):871–875, 1999. URL http://link.aps.org/abstract/PRL/v82/p871.

[126] M. Kozuma, Y. Suzuki, Y. Torji, T. Sugiura, T. Kuga, E. W. Hagley, and L. Deng. Phase–Coherent Amplification of Matter Waves. *Science*, 286:2309, 1999.

[127] L. D. Landau and E. M. Lifshitz. *Quantum Mechanics*, volume 3 of *Course of theoretical physics*. Butterworth-Heinemann, Oxford, United Kingdom, 3 edition, 1977.

[128] R. H. Landau. *Quantum mechanics II: a second course in quantum theory*. John-Wiley & Sons, Inc., New York, 1990.

[129] A. E. Leanhardt, T. A. Pasquini, M. Saba, A. Schirotzek, Y. Shin, D. Kielpinski, D. E. Pritchard, and W. Ketterle. Cooling Bose-Einstein Condensates Below 500 Picokelvin. *Science*, 301(5639):1513–1515, 2003. URL http://www.sciencemag.org/cgi/content/abstract/301/5639/1513.

[130] H. Lefebvre-Brion and R. W. Field. *Perturbations in the Spectra of Diatomic Molecules*. Academic Press, Inc, London, 1986.

[131] P. J. Leo, C. J. Williams, and P. S. Julienne. Collision Properties of Ultracold ^{133}Cs Atoms. *Physical Review Letters*, 85(13):2721–2724, 2000. URL http://link.aps.org/abstract/PRL/v85/p2721.

[132] P. D. Lett, W. D. Phillips, S. L. Rolston, C. E. Tanner, R. N. Watts, and C. I. Westbrook. Optical molasses. *Journal of the Optical Society of America B*, 6: 2084–2107, 1989.

[133] J. Levine, T. Mason, and D. Brown. *Lex & Yacc*. O'Reilly and Associates, Boston, 1986.

[134] J. C. Light and T. Carrington. Discrete-variable representations and their utilization. *Adv. Chem. Phys.*, 114:263–310, 2000.

[135] J. C. Light, I. P. Hamilton, and J. V. Lill. Generalized discrete variable approximation in quantum mechanics. *Journal of Chemical Physics*, 82(3): 1400–1409, 1985. URL http://link.aip.org/link/?JCP/82/1400/1.

[136] J. V. Lill, G. A. Parker, and J. C. Light. The discrete variable–finite basis approach to quantum scattering. *Journal of Chemical Physics*, 85(2):900–910, 1986. URL http://link.aip.org/link/?JCP/85/900/1.

[137] O. J. Luiten, M. W. Reynolds, and J. T. M. Walraven. Kinetic theory of the evaporative cooling of a trapped gas. *Physical Review A (Atomic, Molecular, and Optical Physics)*, 53(1):381–389, 1996. URL http://link.aps.org/abstract/PRA/v53/p381.

[138] H. Mabuchi, E. S. Polzik, and H. J. Kimble. Blue-light-induced infra red absorption in $KNbO_3$. *Journal of the Optical Society of America B*, 11(10): 2023, 1994.

[139] K. W. Madison, F. Chevy, W. Wohlleben, and J. Dalibard. Vortex Formation in a Stirred Bose-Einstein Condensate. *Physical Review Letters*, 84(5):806–809, 2000. URL http://link.aps.org/abstract/PRL/v84/p806.

[140] O. M. Marago, S. A. Hopkins, J. Arlt, E. Hodby, G. Hechenblaikner, and C. J. Foot. Observation of the Scissors Mode and Evidence for Superfluidity of a Trapped Bose-Einstein Condensed Gas. *Physical Review Letters*, 84(10): 2056–2059, 2000. URL http://link.aps.org/abstract/PRL/v84/p2056.

[141] M. Marinescu and L. You. Controlling Atom-Atom Interaction at Ultralow Temperatures by dc Electric Fields. *Physical Review Letters*, 81(21):4596–4599, 1998. URL http://link.aps.org/abstract/PRL/v81/p4596.

[142] A. Marte. *Feshbach-Resonanzen bei Stößen ultrakalter Rubidiumatome*. Phd thesis, Technische Universität München, Max-Planck-Institut für Quantenoptik, 2003.

[143] A. Marte, T. Volz, J. Schuster, S. Dürr, G. Rempe, E. G. M. van Kempen, and B. J. Verhaar. Feshbach Resonances in Rubidium 87: Precision Measurement and Analysis. *Physical Review Letters*, 89(28):283202, 2002. URL http://link.aps.org/abstract/PRL/v89/e283202.

[144] M. R. Matthews, B. P. Anderson, P. C. Haljan, D. S. Hall, M. J. Holland, J. E. Williams, C. E. Wieman, and E. A. Cornell. Watching a Superfluid Untwist Itself: Recurrence of Rabi Oscillations in a Bose-Einstein Condensate. *Physical Review Letters*, 83(17):3358–3361, 1999. URL http://link.aps.org/abstract/PRL/v83/p3358.

[145] M. R. Matthews, B. P. Anderson, P. C. Haljan, D. S. Hall, C. E. Wieman, and E. A. Cornell. Vortices in a Bose-Einstein Condensate. *Physical Review Letters*, 83(13):2498–2501, 1999. URL http://link.aps.org/abstract/PRL/v83/p2498.

[146] C. Maus. *Frequenzverdopplung eines Titan-Saphir-Ringlasers für die Spektroskopie an Chromatomen*. Diploma thesis, Universität Konstanz, Lehrstuhl J. Mlynek, 1994.

[147] H. Metcalf and P. van der Straten. *Laser Cooling and Trapping*. Springer, New York, 1999.

[148] M.-O. Mewes, M. R. Andrews, N. J. van Druten, D. M. Kurn, D. S. Durfee, and W. Ketterle. Bose-Einstein Condensation in a Tightly Confining dc Magnetic Trap. *Physical Review Letters*, 77(3):416, 1996.

[149] M.-O. Mewes, M. R. Andrews, N. J. van Druten, D. M. Kurn, D. S. Durfee, C. G. Townsend, and W. Ketterle. Collective Excitations of a Bose-Einstein Condensate in a Magnetic Trap. *Physical Review Letters*, 77(6):988–991, Aug. 1996. URL http://link.aps.org/abstract/PRL/v77/p988.

[150] M.-O. Mewes, M. R. Andrews, D. M. Kurn, D. S. Durfee, C. G. Townsend, and W. Ketterle. Output Coupler for Bose-Einstein Condensed Atoms. *Physical Review Letters*, 78(4):582–585, Jan. 1997. URL http://link.aps.org/abstract/PRL/v78/p582.

[151] P. Meystre. *Atom Optics*. Springer Verlag, 2001.

[152] F. H. Mies. Molecular Theory of Atomic Collisions: Calculated Cross Sections for H^++F(^{2}P). *Physical Review A (Atomic, Molecular, and Optical Physics)*, 7 (3):957–967, 1973. URL http://link.aps.org/abstract/PRA/v7/p957.

[153] F. H. Mies, C. J. Williams, P. S. Julienne, and M. Krauss. Estimating Bounds on Collisional Relaxation Rates of Spin-Polarized ^{87}Rb Atoms at Ultracold Temperatures. *J. Res. Natl. Inst. Stand. Technol.*, 101(4):521, July 1996.

[154] H.-J. Miesner, D. M. Stamper-Kurn, J. Stenger, S. Inouye, A. P. Chikkatur, and W. Ketterle. Observation of Metastable States in Spinor Bose-Einstein Condensates. *Physical Review Letters*, 82(11):2228–2231, Mar. 1999. URL http://link.aps.org/abstract/PRL/v82/p2228.

[155] A. J. Moerdijk, B. J. Verhaar, and A. Axelsson. Resonances in ultracold collisions of ^{6}Li, ^{7}Li, and ^{23}Na. *Physical Review A (Atomic, Molecular, and Optical Physics)*, 51(6):4852–4861, 1995. URL http://link.aps.org/abstract/PRA/v51/p4852.

[156] A. J. Moerdijk, B. J. Verhaar, and T. M. Nagtegaal. Collisions of dressed ground-state atoms. *Physical Review A (Atomic, Molecular, and Optical Physics)*, 53 (6):4343–4351, 1996. URL http://link.aps.org/abstract/PRA/v53/p4343.

[157] C. R. Monroe, E. A. Cornell, C. A. Sackett, C. J. Myatt, and C. E. Wieman. Measurement of Cs-Cs Elastic Scattering at $T = 30\mu$K. *Physical Review Letters*, 70(4):414–417, Jan. 1993. URL http://link.aps.org/abstract/PRL/v70/p414.

[158] N. F. Mott and H. S. W. Massey. *The Theory of Atomic Collisions*, volume 1. Oxford University Press, Oxford, United Kingdom, 3 edition, 1965.

[159] C. J. Myatt, E. A. Burt, R. W. Ghrist, E. A. Cornell, and C. E. Wieman. Production of Two Overlapping Bose-Einstein Condensates by Sympathetic Cooling. *Physical Review Letters*, 78(4):586–589, Jan. 1997. URL http://link.aps.org/abstract/PRL/v78/p586.

[160] N. R. Newbury, C. J. Myatt, E. A. Cornell, and C. E. Wieman. Gravitational Sisyphus Cooling of ^{87}Rb in a Magnetic Trap. *Physical Review Letters*, 74 (12):2196–2199, Mar. 1995. URL http://link.aps.org/abstract/PRL/v74/p2196.

[161] N. R. Newbury, C. J. Myatt, and C. E. Wieman. S-wave elastic collisions between cold ground-state ^{87}Rb atoms. *Physical Review A (Atomic, Molecular, and Optical Physics)*, 51(4):R2680, Apr. 1995.

[162] R. G. Newton. *Scattering Theory of Waves and Particles*. McGraw-Hill, New-York, 1966.

[163] E. Nielsen and J. H. Macek. Low-Energy Recombination of Identical Bosons by Three-Body Collisions. *Physical Review Letters*, 83(8):1566–1569, 1999. URL http://link.aps.org/abstract/PRL/v83/p1566.

[164] A. N. Nikolov, E. E. Eyler, X. T. Wang, J. Li, H. Wang, W. C. Stwalley, and P. L. Gould. Observation of Ultracold Ground-State Potassium Molecules.

Physical Review Letters, 82(4):703–706, 1999. URL http://link.aps.org/abstract/PRL/v82/p703.

[165] A. N. Nikolov, J. R. Ensher, E. E. Eyler, H. Wang, W. C. Stwalley, and P. L. Gould. Efficient Production of Ground-State Potassium Molecules at Sub-mK Temperatures by Two-Step Photoassociation. *Physical Review Letters*, 84(2): 246–249, 2000. URL http://link.aps.org/abstract/PRL/v84/p246.

[166] NIST. Atomic Spectra Databases, 2005. URL http://physics.nist.gov/PhysRefData/ASD/lines_form.html.

[167] W. Nolting. *Quantenmechanik, Teil 2: Methoden und Anwendungen*, volume 5 of *Grundkurs: Theoretische Physik*. Zimmermann-Neufang, Antoniusstraße 9, D-56766 Ulmen, 2 edition, 1994.

[168] B. Numerov. *Publ. Observatoire Central Astrophys. Russ.*, 2:188, 1933.

[169] D. O'Dell, S. Giovanazzi, G. Kurizki, and V. M. Akulin. Bose-Einstein Condensates with $1/r$ Interatomic Attraction: Electromagnetically Induced "Gravity". *Physical Review Letters*, 84(25):5687–5690, June 2000. URL http://link.aps.org/abstract/PRL/v84/p5687.

[170] D. H. J. O'Dell, S. Giovanazzi, and G. Kurizki. Rotons in Gaseous Bose-Einstein Condensates Irradiated by a Laser. *Physical Review Letters*, 90(11): 110402, 2003. URL http://link.aps.org/abstract/PRL/v90/e110402.

[171] D. H. J. O'Dell, S. Giovanazzi, and C. Eberlein. Exact Hydrodynamics of a Trapped Dipolar Bose-Einstein Condensate. *Physical Review Letters*, 92(25): 250401, 2004. URL http://link.aps.org/abstract/PRL/v92/e250401.

[172] K. M. O'Hara, M. E. Gehm, S. R. Granade, and J. E. Thomas. Scaling laws for evaporative cooling in time-dependent optical traps. *Physical Review A (Atomic, Molecular, and Optical Physics)*, 64:051403, 2001.

[173] K. M. O'Hara, S. L. Hemmer, S. R. Granade, M. E. Gehm, J. E. Thomas, V. Venturi, E. Tiesinga, and C. J. Williams. Measurement of the zero crossing in a Feshbach resonance of fermionic ^{6}Li. *Physical Review A (Atomic, Molecular, and Optical Physics)*, 66:041401(R), Oct. 2002.

[174] C. Orzel, A. K. Tuchman, M. L. Fenselau, M. Yasuda, and M. A. Kasevich. Squeezed States in a Bose-Einstein Condensate. *Science*, 291:2386–2389, 2001.

[175] T. Parr. ANTLR. URL http://www.antlr.org.

[176] Z. Pavlovic, B. O. Roos, R. Cote, and H. R. Sadeghpour. Collisional properties of trapped cold chromium atoms. *Physical Review A (Atomic, Molecular, and Optical Physics)*, 69(3):030701, 2004.

[177] Z. Pavlovic, R. V. Krems, R. Cote, and H. R. Sadeghpour. Magnetic Feshbach resonances and Zeeman relaxation in bosonic chromium gas with anisotropic interaction. *Physical Review A (Atomic, Molecular, and Optical Physics)*, 71 (6):061402, 2005. URL http://link.aps.org/abstract/PRA/v71/e061402.

[178] W. D. Phillips. Laser cooling and trapping of neutral atoms. *Review of Modern Physics*, 70(3):721, July 1998.

[179] P. W. H. Pinkse, A. Mosk, M. Weidemüller, M. W. Reynolds, T. W. Hijmans, and J. T. M. Walraven. Adiabatically Changing the Phase-Space Density of a Trapped Bose Gas. *Physical Review Letters*, 78(6):990–993, Feb. 1997. URL http://link.aps.org/abstract/PRL/v78/p990.

[180] A. B. Pippard. *The physics of vibration*. Cambridge: Cambridge University Press, 1989, Revised edition, 1989.

[181] N. Poli, R. J. Brecha, G. Roati, and G. Modugno. Cooling atoms in an optical trap by selective parametric excitation. *Physical Review A (Atomic, Molecular, and Optical Physics)*, 65(2):021401, 2002. URL http://link.aps.org/abstract/PRA/v65/e021401.

[182] W. H. Press, S. A. Teukolsky, W. T. Vetterling, and B. P. Flannery. *Numerical recipes in C: The art of scientific computing*. Cambridge University Press, Cambridge, UK, 2 edition, 1997.

[183] D. E. Pritchard. Cooling Neutral Atoms in a Magnetic Trap for Precision Spectroscopy. *Physical Review Letters*, 51(15):1336–1339, Oct. 1983. URL http://link.aps.org/abstract/PRL/v51/p1336.

[184] H. Pu, W. Zhang, and P. Meystre. Ferromagnetism in a Lattice of Bose-Einstein Condensates. *Physical Review Letters*, 87(14):140405, 2001.

[185] C. Raman, M. Köhl, R. Onofrio, D. S. Durfee, C. E. Kuklewicz, Z. Hadzibabic, and W. Ketterle. Evidence for a Critical Velocity in a Bose-Einstein Condensed Gas. *Physical Review Letters*, 83(13):2502–2505, Sept. 1999. URL http://link.aps.org/abstract/PRL/v83/p2502.

[186] G. H. Rawitscher, B. D. Esry, E. Tiesinga, J. P. Burke, Jr., and I. Koltracht. Comparison of numerical methods for the calculation of cold atom collisions. *Journal of Chemical Physics*, 111(23):10418–10426, 1999. URL http://link.aip.org/link/?JCP/111/10418/1.

[187] C. A. Regal and D. S. Jin. Measurement of Positive and Negative Scattering Lengths in a Fermi Gas of Atoms. *Physical Review Letters*, 90(23):230404, June 2003. URL http://link.aps.org/abstract/PRL/v90/e230404.

[188] C. A. Regal, C. Ticknor, J. L. Bohn, and D. S. Jin. Creation of ultracold molecules from a Fermi gas of atoms. *Nature*, 424:47, July 2003.

[189] C. A. Regal, C. Ticknor, J. L. Bohn, and D. S. Jin. Tuning p-Wave Interactions in an Ultracold Fermi Gas of Atoms. *Physical Review Letters*, 90(5):053201, 2003. URL http://link.aps.org/abstract/PRL/v90/e053201.

[190] C. A. Regal, M. Greiner, and D. S. Jin. Observation of Resonance Condensation of Fermionic Atom Pairs. *Physical Review Letters*, 92(4):040403, 2004. URL http://link.aps.org/abstract/PRL/v92/e040403.

[191] M. W. Reynolds, I. Shinkoda, R. W. Cline, and W. N. Hardy. Observation of inverse predissociation of spin-polarized atomic hydrogen at low temperatures. *Physical Review B (Condensed Matter)*, 34(7):4912–4915, 1986. URL http://link.aps.org/abstract/PRB/v34/p4912.

[192] L. Ricci, M. Weidemüller, T. Esslinger, A. Hemmerich, C. Zimmermann, V. Vuletić, W. König, and T. W. Hänsch. A compact grating-stabilized diode laser system for atomic physics. *Optics Communications*, 117:541–549, 1995.

[193] G. Roati, W. Jastrzebski, A. Simoni, G. Modugno, and M. Inguscio. Optical trapping of cold fermionic potassium for collisional studies. *Physical Review A (Atomic, Molecular, and Optical Physics)*, 63:052709, 2001.

[194] A. Robert, O. Sirjean, A. Browaeys, J. Poupard, S. Nowak, D. Boiron, and C. W. A. Aspect. A Bose-Einstein Condensate of Metastable Atoms. *Science*, 292:461–464, 2001.

[195] J. L. Roberts, N. R. Claussen, J. P. Burke, Jr., C. H. Greene, E. A. Cornell, and C. E. Wieman. Resonant Magnetic Field Control of Elastic Scattering in Cold Rb. *Physical Review Letters*, 81(23):5109–5112, 1998. URL http://link.aps.org/abstract/PRL/v81/p5109.

[196] J. L. Roberts, N. R. Claussen, J. P. Burke, Jr., C. H. Greene, E. A. Cornell, and C. E. Wieman. Resonant Magnetic Field Control of Elastic Scattering of Cold ^{85}Rb. *Physical Review Letters*, 81(23):5109–5112, Dec. 1998. URL http://link.aps.org/abstract/PRL/v81/p5109.

[197] J. L. Roberts, N. R. Claussen, S. L. Cornish, and C. E. Wieman. Magnetic Field Dependence of Ultracold Inelastic Collisions near a Feshbach Resonance. *Physical Review Letters*, 85(4):728–731, 2000. URL http://link.aps.org/abstract/PRL/v85/p728.

[198] J. L. Roberts, J. P. Burke, Jr., N. R. Claussen, S. L. Cornish, E. A. Donley, and C. E. Wieman. Improved characterization of elastic scattering near a Feshbach resonance in ^{85}Rb. *Physical Review A (Atomic, Molecular, and Optical Physics)*, 64(2):024702, 2001. URL http://link.aps.org/abstract/PRA/v64/e024702.

[199] J. L. Roberts, N. R. Claussen, S. L. Cornish, E. A. Donley, E. A. Cornell, and C. E. Wieman. Controlled Collapse of a Bose-Einstein Condensate. *Physical Review Letters*, 86(19):4211–4214, 2001. URL http://link.aps.org/abstract/PRL/v86/p4211.

[200] B. O. Roos. The Ground State Potential for the Chromium Dimer Revisited. *Collect. Czech. Chem. Commun.*, 68:265, 2003.

[201] J. R. Rubbmark, M. M. Kash, M. G. Littman, and D. Kleppner. Dynamical effects at avoided level crossings: A study of the Landau-Zener effect using Rydberg atoms. *Physical Review A (Atomic, Molecular, and Optical Physics)*, 23:3107, 1981.

[202] J. J. Sakurai. *Modern Quantum Mechanics*. Addison–Wesley, Redwood City, CA, 1 edition, 1985.

[203] B. E. A. Saleh and M. C. Teich. *Fundamentals of Photonics*. Wiley series in pure and applied optics. A Wiley-Interscience publication, 1991.

[204] F. P. D. Santos, J. Léonard, J. Wang, C. J. Barrelet, F. Perales, E. Rasel, C. S. Unnikrishnan, M. Leduc, and C. Cohen-Tannoudji. Bose-Einstein Condensation of Metastable Helium. *Physical Review Letters*, 86:3459–3462, 2001.

[205] L. Santos, G. V. Shlyapnikov, P. Zoller, and M. Lewenstein. Bose-Einstein Condensation in Trapped Dipolar Gases. *Physical Review Letters*, 85(9): 1791–1794, 2000. URL http://link.aps.org/abstract/PRL/v85/p1791.

[206] L. Santos, G. V. Shlyapnikov, and M. Lewenstein. Roton-Maxon Spectrum and Stability of Trapped Dipolar Bose-Einstein Condensates. *Physical Review Letters*, 90(25):250403, 2003. URL http://link.aps.org/abstract/PRL/v90/e250403.

[207] T. A. Savard, K. M. O'Hara, and J. E. Thomas. Laser-noise-induced heating in far-off resonance optical traps. *Physical Review A (Atomic, Molecular, and Optical Physics)*, 56(2):R1095, Aug. 1997.

[208] H. Schmaljohann, M. Erhard, J. Kronjager, M. Kottke, S. van Staa, L. Cacciapuoti, J. J. Arlt, K. Bongs, and K. Sengstock. Dynamics of F = 2 Spinor Bose-Einstein Condensates. *Physical Review Letters*, 92(4):040402, 2004. URL http://link.aps.org/abstract/PRL/v92/e040402.

[209] P. O. Schmidt. *Scattering properties of ultra-cold chromium atoms*. Phd thesis, Universität Stuttgart, 5. Phys. Institut, 2003.

[210] P. O. Schmidt. *Lichtmasken in der Atomlithographie*. Diploma thesis, Universität Konstanz, Lehrstuhl J. Mlynek, 1998.

[211] P. O. Schmidt, S. Hensler, J. Werner, T. Binhammer, A. Görlitz, and T. Pfau. Doppler cooling of an optically dense cloud of trapped atoms. *Journal of the Optical Society of America B*, 20(5):960–967, 2003.

[212] P. O. Schmidt, S. Hensler, J. Werner, A. Griesmaier, A. Görlitz, T. Pfau, and A. Simoni. Determination of the s-Wave Scattering Length of Chromium. *Physical Review Letters*, 91(19):193201, 2003. URL http://link.aps.org/abstract/PRL/v91/e193201.

[213] B. Shizgal. Kinetic-theory calculation of NMR relaxation-time of dilute He-3 gas. *Journal of Chemical Physics*, 58:3424, 1973.

[214] B. W. Shore. *The Theory of coherent atomic excitation*. J. Wiley & Sons, Inc., 1990.

[215] I. F. Silvera, H. P. Godfried, E. R. Eliel, J. G. Brisson, J. D. Gillaspy, J. C. Mester, and C. Mallardeau. Magnetic-field dependence of resonance recombination in spin-polarized atomic hydrogen. *Physical Review B (Condensed Matter)*, 37(4):1520–1524, 1988. URL http://link.aps.org/abstract/PRB/v37/p1520.

[216] A. Simoni. private communication, 2005.

[217] A. Simoni, F. Ferlaino, G. Roati, G. Modugno, and M. Inguscio. Magnetic Control of the Interaction in Ultracold K-Rb Mixtures. *Physical Review Letters*, 90(16):163202, 2003. URL http://link.aps.org/abstract/PRL/v90/e163202.

[218] D. M. Stamper-Kurn, H.-J. Miesner, A. P. Chikkatur, S. Inouye, J. Stenger, and W. Ketterle. Reversible Formation of a Bose-Einstein Condensate. *Physical Review Letters*, 81(11):2194–2197, Sept. 1998. URL http://link.aps.org/abstract/PRL/v81/p2194.

[219] D. M. Stamper-Kurn, H.-J. Miesner, S. Inouye, M. R. Andrews, and W. Ketterle. Collisionless and Hydrodynamic Excitations of a Bose-Einstein Condensate. *Physical Review Letters*, 81(3):500–503, July 1998. URL http://link.aps.org/abstract/PRL/v81/p500.

[220] D. M. Stamper-Kurn, A. P. Chikkatur, A. Görlitz, S. Inouye, S. Gupta, D. E. Pritchard, and W. Ketterle. Excitation of Phonons in a Bose-Einstein Condensate by Light Scattering. *Physical Review Letters*, 83(15):2876–2879, Oct. 1999. URL http://link.aps.org/abstract/PRL/v83/p2876.

[221] D. M. Stamper-Kurn, H.-J. Miesner, A. P. Chikkatur, S. Inouye, J. Stenger, and W. Ketterle. Quantum Tunneling across Spin Domains in a Bose-Einstein Condensate. *Physical Review Letters*, 83(4):661–665, July 1999. URL http://link.aps.org/abstract/PRL/v83/p661.

[222] C. A. Stan, M. W. Zwierlein, C. H. Schunck, S. M. F. Raupach, and W. Ketterle. Observation of Feshbach Resonances between Two Different Atomic Species. *Physical Review Letters*, 93(14):143001, 2004. URL http://link.aps.org/abstract/PRL/v93/e143001.

[223] B. Steinheil. *Aufbau eines frequenzverdoppelten Diodenlaser-Systems zur Untersuchung ultrakalter Chromatome*. Diploma thesis, 5. Physikalisches Institut, Universität Stuttgart, Pfaffenwaldring 57, 70550 Stuttgart, 2003.

[224] J. Stenger, S. Inouye, M. R. Andrews, H.-J. Miesner, D. M. Stamper-Kurn, and W. Ketterle. Strongly Enhanced Inelastic Collisions in a Bose-Einstein Condensate near Feshbach Resonances. *Physical Review Letters*, 82(12):2422–2425, Mar. 1999. URL http://link.aps.org/abstract/PRL/v82/p2422.

[225] J. Stenger, S. Inouye, M. R. Andrews, H.-J. Miesner, D. M. Stamper-Kurn, and W. Ketterle. Strongly Enhanced Inelastic Collisions in a Bose-Einstein Condensate near Feshbach Resonances. *Physical Review Letters*, 82(12):2422–2425, 1999. URL http://link.aps.org/abstract/PRL/v82/p2422.

[226] J. Stenger, S. Inouye, D. M. Stamper-Kurn, H.-J. Miesner, A. P. Chikkatur, and W. Ketterle. Spin domains in ground-state Bose-Einstein condensates. *Nature*, 396:345, Nov. 1999.

[227] H. T. C. Stoof, J. M. V. A. Koelman, and B. J. Verhaar. Spin-exchange and dipole relaxation rates in atomic hydrogen: Rigorous and simplified calculations. *Physical Review B (Condensed Matter)*, 38(7):4688, 1988.

[228] K. E. Strecker, G. B. Partridge, A. G. Truscott, and R. G. Hulet. Formation and propagation of matter-wave soliton trains. *Nature*, 417:150, May 2002.

[229] B. Stroustrup. *The C++ Programming Language, Special Edition*. Addison-Wesley, Boston, 2000.

[230] J. Stuhler. *Kontinuierliches Laden einer Magnetfalle mit lasergekühlten Chromatomen*. Phd thesis, Universität Konstanz, Lehrstuhl J. Mlynek, Ufo-Verlag, Allensbach, 2002.

[231] J. Stuhler, A. Griesmaier, T. Koch, M. Fattori, T. Pfau, S. Giovanazzi, P. Pedri, and L. Santos. Observation of dipole-dipole interaction in a degenerate quantum gas. *Physical Review Letters*, 95(15):150406, 2005. URL http://link.aps.org/abstract/PRL/v95/e150406.

[232] W. C. Stwalley. Stability of spin-aligned hydrogen at low temperatures and high magnetic fields: New field-dependent scattering resonances and predissociations. *Physical Review Letters*, 37(24):1628–1631, 1976. URL http://link.aps.org/abstract/PRL/v37/p1628.

[233] H. Sully and E. Brandes. *Metallurgy of The Rarer Metals-1, Chromium*. London Butterworths, 2 edition, 1967.

[234] Y. Takasu, K. Maki, K. Komori, T. Takano, K. Honda, M. Kumakura, T. Yabuzaki, and Y. Takahashi. Spin-Singlet Bose-Einstein Condensation of Two-Electron Atoms. *Physical Review Letters*, 91(4):040404, July 2003. URL http://link.aps.org/abstract/PRL/v91/e040404.

[235] J. R. Taylor. *Scattering Theory: The Quantum Theory on Nonrelativistic Collisions*. John-Wiley & Sons, Inc., New York, 1972.

[236] M. Theis, G. Thalhammer, K. Winkler, M. Hellwig, G. Ruff, R. Grimm, and J. H. Denschlag. Tuning the Scattering Length with an Optically Induced Feshbach Resonance. *Physical Review Letters*, 93(12):123001, 2004. URL http://link.aps.org/abstract/PRL/v93/e123001.

[237] C. Ticknor, C. A. Regal, D. S. Jin, and J. L. Bohn. Multiplet structure of Feshbach resonances in nonzero partial waves. *Physical Review A (Atomic, Molecular, and Optical Physics)*, 69(4):042712, 2004. URL http://link.aps.org/abstract/PRA/v69/e042712.

[238] E. Tiesinga, A. Moerdijk, B. J. Verhaar, and H. T. C. Stoof. Conditions for Bose-Einstein condensation in magnetically trapped atomic cesium. *Physical Review A (Atomic, Molecular, and Optical Physics)*, 46(3):R1167, Aug. 1992.

[239] E. Tiesinga, B. J. Verhaar, and H. T. C. Stoof. Threshold and resonance phenomena in ultracold ground-state collisions. *Physical Review A (Atomic, Molecular, and Optical Physics)*, 47(5):4114–4122, May 1993. URL http://link.aps.org/abstract/PRA/v47/p4114.

[240] F. A. van Abeelen and B. J. Verhaar. Time-Dependent Feshbach Resonance Scattering and Anomalous Decay of a Na Bose-Einstein Condensate. *Physical Review Letters*, 83(8):1550–1553, 1999. URL http://link.aps.org/abstract/PRL/v83/p1550.

[241] J. M. Vogels, C. C. Tsai, R. S. Freeland, S. J. J. M. F. Kokkelmans, B. J. Verhaar, and D. J. Heinzen. Prediction of Feshbach resonances in collisions of ultracold rubidium atoms. *Physical Review A (Atomic, Molecular, and Optical Physics)*, 56(2):R1067, Aug. 1997.

[242] T. Volz, S. Durr, S. Ernst, A. Marte, and G. Rempe. Characterization of elastic scattering near a Feshbach resonance in ^{87}Rb. *Physical Review A (Atomic, Molecular, and Optical Physics)*, 68(1):010702, 2003. URL http://link.aps.org/abstract/PRA/v68/e010702.

[243] V. Vuletić, C. Chin, A. Kerman, and S. Chu. Degenerate Raman Sideband Cooling of Trapped Cesium Atoms at Very High Atomic Densities. *Physical Review Letters*, 81:5768, 1998.

[244] V. Vuletić, A. J. Kerman, C. Chin, and S. Chu. Observation of Low-Field Feshbach Resonances in Collisions of Cesium Atoms. *Physical Review Letters*, 82(7):1406–1409, Feb. 1999. URL http://link.aps.org/abstract/PRL/v82/p1406.

[245] T. Weber, J. Herbig, M. Mark, H.-C. Nägerl, and R. Grimm. Bose-Einstein Condensation of Cesium. *Science*, 299:232–235, 2003.

[246] T. Weber, J. Herbig, M. Mark, H.-C. Nägerl, and R. Grimm. Three-Body Recombination at Large Scattering Lengths in an Ultracold Atomic Gas. *Physical Review Letters*, 91(12):123201, 2003. URL http://link.aps.org/abstract/PRL/v91/e123201.

[247] J. Weinstein, R. deCarvalho, J. Kim, D. Patterson, B. Friedrich, and M. Doyle. Magnetic trapping of atomic chromium. *Physical Review A (Atomic, Molecular, and Optical Physics)*, 57(5):3173–3175, 1998.

[248] J. D. Weinstein, R. deCarvalho, T. Guillet, B. Friedrich, and J. M. Doyle. Magnetic trapping of calcium monohydride molecules at millikelvin temperatures. *Nature*, 395(6698):148, Sept. 1998.

[249] J. D. Weinstein, R. deCarvalho, C. I. Hancox, and J. M. Doyle. Evaporative cooling of atomic chromium. *Physical Review A (Atomic, Molecular, and Optical Physics)*, 65(2):021604, 2002. URL http://link.aps.org/abstract/PRA/v65/e021604.

[250] J. Werner. *Kontinuierliches Laden einer Magnetfalle mit lasergekühlten Chromatomen*. Diploma thesis, Universität Konstanz, Juni 2000.

[251] E. P. Wigner and L. Eisenbud. Higher Angular Momenta and Long Range Interaction in Resonance Reactions. *Physical Review*, 72(1):29–41, 1947. URL http://link.aps.org/abstract/PR/v72/p29.

[252] J. Williams, R. Walser, J. Cooper, E. Cornell, and M. Holland. Nonlinear Josephson-type oscillations of a driven, two-component Bose-Einstein condensate. *Physical Review A (Atomic, Molecular, and Optical Physics)*, 59(1):R31, Jan. 1999.

[253] J. Williams, R. Walser, J. Cooper, E. A. Cornell, and M. Holland. Excitation of a dipole topological state in a strongly coupled two-component Bose-Einstein condensate. *Physical Review A (Atomic, Molecular, and Optical Physics)*, 61(3): 033612, Feb. 2000. URL http://link.aps.org/abstract/PRA/v61/e033612.

[254] J. E. Williams and M. J. Holland. Preparing topological states of a Bose-Einstein condensate. *Nature*, 401:568, Oct. 1999.

[255] W. H. Wing. On neutral particle trapping in quasistatic electromagnetic fields. *Prog. Quant. Electr.*, 8:181, 1984.

[256] A. Witte, T. Kisters, F. Riehle, and J. Helmcke. Laser cooling and deflection of a calcium atomic beam. *Journal of the Optical Society of America B*, 9:1030, 1992.

[257] H. Wu and C. J. Foot. Direct simulation of evaporative cooling. *Journal of Physics B: Atomic Molecular and Optical Physics*, 29:L321, 1996.

[258] R. Wynar, R. S. Freeland, D. J. Han, C. Ryu, and D. J. Heinzen. Molecules in a Bose-Einstein Condensate. *Science*, 287:1016, Feb. 2000.

[259] K. Xu, T. Mukaiyama, J. R. Abo-Shaeer, J. K. Chin, D. E. Miller, and W. Ketterle. Formation of Quantum-Degenerate Sodium Molecules. *Physical Review Letters*, 91(21):210402, 2003. URL http://link.aps.org/abstract/PRL/v91/e210402.

[260] S. Yi and L. You. Probing dipolar effects with condensate shape oscillation. *Physical Review A (Atomic, Molecular, and Optical Physics)*, 66(1):013607, 2002. URL http://link.aps.org/abstract/PRA/v66/e013607.

[261] S. Yi, L. You, and H. Pu. Quantum Phases of Dipolar Spinor Condensates. *Physical Review Letters*, 93(4):040403, 2004. URL http://link.aps.org/abstract/PRL/v93/e040403.

[262] V. A. Yurovsky and A. Ben-Reuven. Three-body loss of trapped ultracold ^{87}Rb atoms due to a Feshbach resonance. *Physical Review A (Atomic, Molecular, and Optical Physics)*, 67(5):050701, 2003. URL http://link.aps.org/abstract/PRA/v67/e050701.

[263] V. A. Yurovsky, A. Ben-Reuven, P. S. Julienne, and C. J. Williams. Atom loss and the formation of a molecular Bose-Einstein condensate by Feshbach resonance. *Physical Review A (Atomic, Molecular, and Optical Physics)*, 62(4): 043605, 2000. URL http://link.aps.org/abstract/PRA/v62/e043605.

[264] C. Zener. Non-Adiabatic Crossing of Energy Levels. *Proc. R. Soc. London, Ser. A*, 137:696, 1932.

[265] W. Zhang, H. Pu, C. Search, and P. Meystre. Spin Waves in a Bose-Einstein–Condensed Atomic Spin Chain. *Physical Review Letters*, 88(6):060401, 2002.

[266] M. W. Zwierlein, C. A. Stan, C. H. Schunck, S. M. F. Raupach, A. J. Kerman, and W. Ketterle. Condensation of Pairs of Fermionic Atoms near a Feshbach Resonance. *Physical Review Letters*, 92(12):120403, 2004. URL http://link.aps.org/abstract/PRL/v92/e120403.

Acknowledgments

This work would not have been possible without support from many people. First and foremost, I would like to thank my advisor Tilman Pfau. He offered me the possibility to continue working on the chromium experiment after finishing my diploma thesis. It was an exhilarating experience to follow the course of the experiment from the early beginnings in Konstanz to finally reaching our long sought goal of creating a Bose-Einstein condensate. Your suggestions and ideas were one of the key factors to the success of the experiment. I'm also awed by the broad physical knowledge you not only have, but were also always patiently enough to convey to your PhD and diploma students. On a personal note, I will never forget your support during the time I became a father.

The results presented in this thesis are not my own accomplishments, but are rather a group effort. I'm heavily indebted to the help of the following co-workers:

- My former senior PhD Student Jürgen Stuhler, who returned to "his" Chromium experiment after finishing his post-doc in Italy. He spent many, many nights with us in the lab fighting with the experiment. He also managed to motivate me again when nothing was working and never ran out of good suggestions.

- Piet Schmidt who shaped the experiment like no one else. He not only introduced the CLIP-trap and the Doppler cooling step, but also did the first scattering length measurements. I always enjoyed the common trips home with the S-Bahn, where we talked about other stuff than physics.

- Sven Hensler for his never-ceasing good mood. He really manged to get our diode lasers to lock reliably. It was also his feat to design and build the next generation vacuum chamber which allowed us to perform our experiments. During all the years I couldn't dissuade him that my children are not so well behaved as he was always saying.

- Axel Griesmaier for the many hours and nights spent together in the lab, trying to Bose condense chromium or searching for Feshbach resonances.

- Andrea Simoni and Eite Tiesinga for doing all the scattering theory calculations. They really kept pace with identifying the Feshbach resonances we were discovering every other night. In the end, they even predicted two of the low field Feshbach resonances in advance. I have to especially thank Andrea for coming to visit us for a week in Stuttgart and taking the time to explain me the details of the numerical scattering calculations. All the errors in the presentation of the numerical calculations are mine and not yours.

- Our diploma students Thomas Binhammer for setting up the first version of our magnetic trap and Bernd Steinheil for constructing the optical pumping laser.

I'd also like to thank all the other PhD and diploma students of the Institute for supporting me and for their good mood. Countless times I was able to "borrow" some urgently needed parts from the other labs, only to integrate them forever into our setup. Jürgen Schoser and Robert Löw returned this favor by eating all the sweets from my desk drawer, thinking I wouldn't notice. Robert deserves a positive mention though, for always organizing the Institute breakfast.

Our two secretaries, first Karin Otter and then Sylvia Tassy relieved us of the more "mundane" tasks, so we could fully concentrate us on physics. Especially Karin kept an eye on all of us so we didn't lose touch with reality completely.

We couldn't have done our experiments without the help of the mechanics and electronics workshop which realized many special designs in a timely manner.

I'd like to especially thank Jürgen Stuhler and Sven Hensler for careful proof-reading of the manuscript.

Finally I have to thank my wife Brigitte for supporting me during the whole time of my PhD thesis. Without you this thesis wouldn't have been possible. Last but certainly not least I thank my children Lena-Sophie and Simon Per for putting a smile on my face each day.